United States
Environmental Protection
Agency

Atmospheric Sciences Research
Laboratory
Research Triangle Park NC 27711

EPA/600/3-85/069
Jan. 1986

Research and Development

EPA

EPA Complex Terrain Model Development:

Fifth Milestone Report—1985

EPA/600/3-85/069

EPA COMPLEX TERRAIN MODEL DEVELOPMENT
Fifth Milestone Report - 1985

by

Donald C. DiCristofaro
David G. Strimaitis
Benjamin R. Greene
Robert J. Yamartino
Akula Venkatram
Daniel A. Godden
Thomas F. Lavery
Bruce A. Egan

ENVIRONMENTAL RESEARCH & TECHNOLOGY, INC.
696 Virginia Road, Concord, Massachusetts 01742

Contract No. 68-02-3421

Project Officer

Peter L. Finkelstein
Meteorology and Assessment Division
Atmospheric Sciences Research Laboratory
Research Triangle Park, North Carolina 27711

ATMOSPHERIC SCIENCES RESEARCH LABORATORY
OFFICE OF RESEARCH AND DEVELOPMENT
U.S. ENVIRONMENTAL PROTECTION AGENCY
RESEARCH TRIANGLE PARK, NORTH CAROLINA 27711

NOTICE

The information in this document has been funded by the United States Environmental Protection Agency under Contract No. 68-02-3421 to Environmental Research and Technology, Inc. It has been subject to the Agency's peer and administrative review, and it has been approved for publication as an EPA document.

Mention of trade names or commercial products does not constitute endorsement or recommendation for use.

PREFACE

The Atmospheric Sciences Research Laboratory (ASRL) conducts intramural and extramural research programs in the physical sciences to detect, define, and quantify air pollution and its effects on urban, regional, and global atmospheres and the subsequent impact on water quality and land use. The Laboratory is responsible for planning, implementing, and managing research and development programs designed to quantify the relationships between emissions of pollutants for all types of sources with air quality and atmospheric effects, and to uncover and characterize hitherto unidentified air pollution problems. Information from ASRL programs and from the programs of other government agencies, private industry, and the academic community are integrated by the Laboratory to develop the technical basis for air pollution control strategies for various pollutants.

The Complex Terrain Model Development (CTMD) program is designed to develop reliable atmospheric dispersion models that are applicable to large pollutant sources located in complex terrain. Three major field studies were conducted during this six-year program. The first field measurements were collected at Cinder Cone Butte near Boise, Idaho during the fall of 1980. The second experiment was conducted at the Hogback Ridge near Farmington, New Mexico in October 1982. The third series of experiments were conducted in November 1983 and August 1984 at the Tracy Power Plant near Reno, Nevada. Data from these field studies along with measurements of fluid modeling simulations performed in the EPA Fluid Modeling Facility are being used to quantify the effects of terrain obstacles on stable plume dispersion. A series of annual milestone reports have been issued to describe the development of the Complex Terrain Dispersion Model (CTDM) to contrast the performance evaluation of the CTDM against existing complex terrain dispersion models. This Fifth Milestone Report describes the August 1984 field experiment. It discusses the continuing development of the CTDM and evaluates model performance using impingement data sets from the three experiment sites.

ABSTRACT

The Complex Terrain Model Development (CTMD) project is being sponsored by the U.S. Environmental Protection Agency to develop atmospheric dispersion models to simulate air pollutant concentrations in complex terrain that result from emissions from large sources. The emphasis of the program is to develop models with known accuracy and limitations for simulating 1-hour concentrations in complex terrain during stable conditions.

This Fifth Milestone Report documents work accomplished from June 1984 through May 1985. It describes in detail the August 1984 Full Scale Plume Study, including its setting, the experimental design, and the resulting data base. The FSPS produced a 128-hour data set of SF_6 and CF_3Br concentrations, ground-based and airborne lidar measurements, photographs, 8-mm movies, videotapes, and extensive meteorological data. The highest ten SF_6 and CF_3Br concentrations and a modeling analysis of 14 hours are discussed in this report.

The refinement of the HBR meteorological data base is essentially complete. The HBR data have been used to show that the path of the oil-fog plume centerline was predicted well by assuming the layer of air below the dividing streamline to be "dead" and by incorporating the effects of temperature stratification. Boundary layer similarity relationships simulated satisfactorily the winds and temperature measured at CCB and HBR up to an altitude of about 10L (ten times the Monin-Obukov length).

This milestone report also discusses the highest ground-level tracer concentrations measured at the CCB, HBR, and FSPS sites. The meteorological characteristics of the concentration events and the differences among the sites are discussed.

The further development of CTDM is described. Mathematical descriptions of the modifications to the model are presented. The latest version of the model has been tested using a subset of impingement hours from the CCB, HBR, and FSPS data bases. The initial 14-hour FSPS data base was also used to test four existing complex terrain models--COMPLEX I and II, Valley, and RTDM.

An EPA Fluid Modeling Facility report describing towing tank simulations to characterize the effects of stability on the horizontal and vertical deflections around an isolated hill is included as an appendix.

This report was submitted in partial fulfillment of contract 68-02-3421 by Environmental Research & Technology, Inc. under the sponsorship of the U.S. Environmental Protection Agency. This report covers the period June 2, 1984 to June 1, 1985.

CONTENTS

FIGURES

FIGURES (Continued)

FIGURES (Continued)

FIGURES (Continued)

FIGURES (Continued)

FIGURES (Continued)

FIGURES (Continued)

FIGURES (Continued)

FIGURES (Continued)

TABLES

TABLES

LIST OF SYMBOLS AND ABBREVIATIONS

SYMBOL	
a	Ratio of σ_w to u_* (Subsection 3.3)
a(z)	Radius of an ideal hill circular in horizontal cross-section
a'	Separation distance of source/sink pair
A	Height of hill
α	Relaxation scale factor for decrease in terrain effect away from hill (Section 6)
α	Boundary layer profile parameter (Subsection 3.3)
α	First derivative of wind speed profile (Subsection 3.2)
α_w	Wind direction at infinity
ß	Boundary layer profile parameter (Subsection 3.3)
ß	Second Derivative of wind speed profile (Subsection 3.2)
ß	Rotation angle (Subsection 5.1)
C	Concentration
C_m	Mean concentration from many "filament" plumes
C_o	Observed concentration
C_P	Modeled concentration
χ	Concentration
d	Downwind distance of sampler (Section 4)
d	Distance from the centerline of the plume to the stagnation streamline associated with the mean wind direction (Section 6)
d_s	Stack diameter
D	Diffusivity
D_m	Mean diffusivity over the interval $s-s_o$
δ	Scale factor for LIFT-WRAP transition zone (Section 6)
δ	Streamline deflection (Subsection 3.2.2)
δ_z	Vertical deflection of the plume streamline
δH_c	Scale of transition zone
δ_Q	Streamline deflection due to stratification only
$\Delta h, \Delta z$	Plume height change due to buoyancy of emission
Δw	Vertical velocity perturbation
Δz	Plume height above H_c (Section 4)

SYMBOL	
$\Delta(x-x')$	Dirac delta function
ϵ	Error or residual
f	Shape of terrain
f(x)	Distance function
F	Buoyancy flux
Fr	Froude number based on hill height
Fr(Hc)	Bulk hill Froude number above H_c
F_z	Vertical distribution factor
g	Acceleration due to gravity
γ	Scale factor for the "stable" mixing length
Γ	Scale factor for the "neutral" mixing length
h	Terrain elevation above a reference elevation
h_o	Height of the zero-plane above the elevation defined as zero in the coordinate system being used
h(x)	Terrain function
H	Initial streamline height (Subsection 3.2.1 and Section 4)
H	Hill height (crest)
H_c	Critical dividing-streamline height
H_*	Effective hill height
η	Height of plume centroid above terrain
η_{obs}	Average observed streamline height
i_x, i_y, i_z	Turbulence intensities alongwind, crosswind, and vertical
k	x wavenumber (Section 6)
k	Wave number along flow (Subsection 3.2.2)
k	von Karman Constant (Subsection 3.1)
K	Diffusivity
K_F	Diffusivity in the absence of terrain
K_H	Eddy diffusivity for heat
K_m, K'_m	Mean diffusivity over the interval $s-s_o$. Prime denotes mean diffusivity in altered flow.

SYMBOL	
K_z	Eddy diffusivity for momentum
θ	Wind direction (Section 4)
θ	Potential temperature (Subsection 3.3)
θ_*	Scaling temperature
θ_m	Mean wind direction of approach flow
θ_r	Direction from effective receptor position to source
θ_r^*	Mean wind direction that carries the deflected plume centerline over the receptor
$\theta_r^{*'}$	Value of θ_r^* after being shifted to simulate the LIFT/WRAP transition region
θ_s	Direction of the stagnation streamline
ℓ	Mixing length (Subsection 3.3)
ℓ	y wavenumber (Section 6)
ℓ	Ratio of Brunt-Vaisala frequency to the wind speed (Subsection 3.2)
ℓ	Along-wind breadth of ellipse (Subsection 3.2.1)
ℓ_n	Neutral mixing length
ℓ_s	Stable mixing length
L	Monin-Obukhov length (Subsection 3.3)
L	Horizontal Scale of hill (Subsection 3.2)
L_c	Hill length approximation
λ	Wavelength of disturbances generated by the hill
λ	Aspect ratio of hill (Subsection 3.2)
m	Slope
m	Vertical wave number (Subsection 3.2.2)
m_a	Arithmetic mean
m_g	Geometric mean
M	Kummer Function
μ, ν	Elliptical coordinates
μ_o	Value of μ on boundary of ellipse
$\tilde{\mu}_s, \nu_s$	Elliptical coordinates
N	Brunt-Vaisala frequency
N_b	Bulk Brunt-Vaisala frequency for a layer

SYMBOL	
p	Power for wind speed profile power law
p	Trial function (Subsection 3.2)
p	Hill shape profile exponent (Subsection 5.1)
p'	Pressure fluctuation
$P(\theta)$	Wind direction probability distribution function
$P(H_c')$	H_c probability distribution function
P	Pressure
ϕ_h	Nondimensional potential temperature gradient
ϕ_m	Nondimensional wind speed gradient
Q	Source strength (mass flow rate)
ρ	Density
r	Distance from source to hill center
r	Correlation coefficient (Subsection 3.2)
R	Ratio of the plume centerline height above the ground to the spread of the plume in the vertical
Ri	Gradient Richardson number
Ri_b	Bulk Richardson number
s	Ratio of Brunt-Vaisala frequency times hill length approximation to the wind speed (Subsection 6.1)
(s,ℓ,h)	General point in a Cartesian coordinate system with s-axis aligned with the mean flow, where s is the distance from the source
s_a	Arithmetic standard deviation
s_b	Distance from the source to the base of the hill
s_g	Geometric standard deviation
s_m	Mean of s and s_o
s_o	Distance along wind direction from source to terrain at the elevation of H_c for the LIFT domain; distance to terrain at the elevation of the receptor for the WRAP domain
s_r	Distance from source to receptor
S	Wind speed
S_β	Component of speed that lies along the x_β-axis

SYMBOL	
$S_{s\beta}$	Component of speed along x_β-axis at the source position
S_∞	Wind speed far from hill
$S_{\beta\infty}$	Component of speed far from hill which lies along the x_β-axis
ψ, ψ_s	Source stream function
σ	Standard deviation
σ_{Hc}	Standard deviation of H_c
σ_u	Standard deviation of alongwind velocity fluctuations about the mean wind
σ_v	Standard deviation of crosswind velocity fluctuations about the mean wind
$\sigma_{v\tau}$	σ_v value obtained for a sampling duration τ
$\sigma_{v\infty}$	σ_v value obtained for an infinite sampling duration
σ_w	Standard deviation of vertical velocity fluctuations
σ_y, σ_z	Crosswind horizontal and vertical standard deviation of tracer concentrations
σ_y^*, σ_z^*	σ_y and σ_z for a plume from point source element for the interval $s-s_o$
σ_{yo}, σ_{zo}	Value of σ_y and σ_z at $s = s_o$
σ_{ye}, σ_{ze}	Effective σ_y and σ_z after accounting for all terrain effects up to the location of the model receptor
σ_{ym}	Standard deviation of the horizontal meander component of the wind fluctuations
σ_{yT}	Total σ_y including terrain effects (σ_{ye}) on the "filament" plume and meander
σ_{zT}	Total σ_z including terrain effects (σ_{ze}) on the "filament" plume and H_c variations
σ_{zu}	Plume spread above plume centerline height
$\sigma_{z\ell}$	Plume spread below plume centerline height
σ_{zb}	σ_z resulting from entrainment during the rise of a buoyant plume
σ_θ	Standard deviation of wind direction
t	Time

SYMBOL	
t_b	Time of travel from stack to the point at which σ_{zb} is measured
t_ℓ	Time of travel below plume centerline height
t_m	Time of travel to the midpoint of the interval $s-s_o$
t_o	Initial time of travel
t_u	Time of travel above plume centerline height
t_v	Virtual time
T	Temperature (Subsection 3.1)
T	Time plus virtual time (Subsection 3.5)
T_a	Ambient temperature
T_h, T_{ho}	Terrain factor for streamline distortion in the vertical direction; subscript o denotes value at crest
T_{iy}, T_{iz}	Terrain factors for turbulence intensity
$T_\ell, T_{\ell o}$	Terrain factor for streamline distortion in the lateral direction; subscript o denotes value at crest
$\overline{T}_\ell^x$	Average of T_ℓ along the trajectory of the plume
$\overline{T}_\ell^y$	Average of T_ℓ across the flow from the streamline that passes over the center of the hill to the streamline that passes through the source
T_m	Time scale of molecular mixing
T_u	Terrain factor for plume transport speed
T_y, T_z	Ratios of streamline distortion factor to diffusivity factor
T_E	Eulerian time scale
T_L	Lagrangian time scale
T_{LT}	Lagrangian time scale of the transverse correlogram
T_p	Partial height factor (terrain factor)
T_*	Scaling temperature
$T_{\sigma w}$	Factor for the change in mean turbulence in the interval
$T_{\sigma y}, T_{\sigma z}$	Terrain factors for diffusivity
τ	Time of travel
u	Generic wind speed

SYMBOL

u_r	Wind speed at release height
u_T	Total wind speed (incident flow plus perturbation)
$u_T(z')$	Total wind speed (incident flow plus perturbation) at z'
u'	Downstream velocity perturbation
u_*	Friction velocity
u_∞	Wind speed far from hill
V_{ex}	Exit velocity
(x,y,z)	General Cartesian coordinates
x_c	Distance from estimated height of streamline to hill center
$x_{o\beta}$	Position of the impingement point along the x_β-axis
x_r, y_r, z_r	Tracer release coordinates
$x_{r\beta}$	Position of the receptor along the x_β-axis
x_{sep}	Distance of flow separation point from hill crest
$x_{s\beta}$	Position of the source along the x_β-axis
x_v	Virtual source distance
x_R, y_R, z_R	Receptor coordinates
z_c	Height of streamline above H_c at x_c
z_g	Geometric mean height
Z_{max}	Sampler elevation of maximum concentration
z_r	Plume release height
z_r*	Plume centerline height after accounting for wind shear
z'	Height above surface

ABBREVIATIONS

AC	Alternating Current
ARLFRD	Air Resources Laboratory Field Research Division
ASRL	Atmospheric Sciences Research Laboratory
ATDL	Atmospheric Turbulence and Diffusion Laboratory
CF_3Br	Freon 13B1

ABBREVIATIONS

CCB	Cinder Cone Butte
CTDM	Complex Terrain Dispersion Model
CTMD	Complex Terrain Model Development
CW	Clockwise
DEC	Digital Equipment Corporation
EPA	U.S. Environmental Protection Agency
EPRI	Electric Power Research Institute
ERT	Environmental Research & Technology, Inc.
EWS	Electronic Weather Station
FFT	Fast Fourier Transform
FMF	Fluid Modeling Facility
FSPS	Full Scale Plume Study
GC	Gas Chromatograph
HBR	Hogback Ridge
IBM	International Business Machines
LASL	Los Alamos Scientific Laboratory
LMF	Linear Mass Flow Meter
MCO	Maximum observed concentration
MCP	Maximum predicted concentration
MDA	Modelers' Data Archive
MDT	Mountain Daylight Time
MRI	Meteorology Research, Inc.
MSE	Mean Square Error
MSI	Meteorological Standards Institute
MSL	Mean Sea Level
MW	Megawatts
$\mu s/m^3$	Micro-seconds per cubic meter
NOAA	National Oceanic and Atmospheric Administration
ppb	Parts per billion by volume
ppt	Parts per trillion by volume
PC	Personal Computer

ABBREVIATIONS

PDF	Probability Distribution Function
PDT	Pacific Daylight Time
PG	Pasquill-Gifford
PNM	Public Service Company of New Mexico
PPC	Plume Path Coefficient
PROM	Programmable Read-Only Memory
PST	Pacific Standard Time
PVC	Polyvinyl Chloride
RABAL	Radar-tracked Balloons
RTD	Resistance Thermometric Device
RTDM	Rough Terrain Diffusion Model
RTI	Research Triangle Institute
SF_6	Sulfur hexafluoride
SHIS	Small Hill Impaction Study
SRI	Stanford Research Institute International
TPP	Tracy Power Plant
TRC	TRC Environmental Consultants, Inc.
VAC	Volt Alternating Current
WPL	Wave Propagation Laboratory
YAG	Yttrium-Aluminum-Garnet

ACKNOWLEDGEMENTS

Continuing progress in the EPA CTMD program has resulted from the dedicated efforts of several scientists from several organizations. The success of the August 1984 Full Scale Plume Study (FSPS), in particular, reflects the cooperation of people from ERT, EPA, Morrison-Knudsen, Inc., the NOAA Air Resources Lab Field Research Division and Wave Propagation Lab and, of course, Sierra Pacific Power Company who let us release tracers from their Tracy Power Plant.

Many people--far too many, in fact, to acknowledge here individually--contributed their talents and energies over the years to make the CTMD project successful. In particular, we gratefully acknowledge the special contribution of the following individuals who helped with the FSPS or the preparation of this milestone report:

- Aaron Mann of Sierra Pacific Power who assisted us throughout the FSPS;
- Ray Dickson and his staff at NOAA ARLFRD who were responsible for the flow visualization and tracer experiments and extensive meteorological measurements;
- Wynn Eberhard and his colleagues at the Wave Propagation Laboratory who have supplied the lidar data and many meteorological measurements;
- Norm Ricks of Morrison-Knudsen who managed the photography program;
- Steve Andersen and Chris Johnson of ERT in Fort Collins who operated the 150-m meteorological tower and were responsible for all CTMD logistics at the Tracy Power Plant;
- Prakash Karamchandani, Cynthia Burkhart, and Elizabeth Rosentel of ERT who performed many of the analyses and model calculations presented in this report;
- Bill Snyder and his colleagues at the EPA Fluid Modeling Facility who have performed many towing tank and wind tunnel simulations in support of the modeling; and
- Julian Hunt for his ideas and recommendations on modeling stable conditions in complex terrain and with whom we have had many useful discussions.

Finally, we give special thanks to Frank Schiermeier, George Holzworth, and Peter Finkelstein (EPA) for their support and encouragement. Throughout, they have willingly shared with us the difficult times, and should share in our successes as well.

SECTION 1

INTRODUCTION

The Complex Terrain Model Development (CTMD) project is being sponsored by the U.S. Environmental Protection Agency (EPA) to develop, evaluate, and refine practical plume models for calculating ground-level air pollutant concentrations that would result from emission sources located in hilly or mountainous terrain. The primary objective of the project is to develop models to simulate 1-hour average concentrations during stable atmospheric conditions.

These models are to be used in a wide variety of applications, such as the siting of new energy development facilities and other sources of air pollution, regulatory decision making, and environmental planning. Therefore, the models should be easy to understand, easy to use, and of known accuracy and limitations. The CTMD project will recommend the types and extent of meteorological measurements needed to derive input to the models.

The objectives of the program were described by Holzworth (1980) and generally follow the recommendations of the participants of the EPA-sponsored workshop to consider the issues and problems of simulating air pollutant dispersion in complex terrain (Hovind et al. 1979). The program was subsequently designed to include model development efforts based on physical modeling, field experiments, and theoretical work.

The CTMD project was begun in June 1980. Four major field experiments have been completed during the last five years to collect data for development and evaluation of various modeling approaches. The first field experiment, Small Hill Impaction Study No. 1 (SHIS #1), was conducted during the fall of 1980 at Cinder Cone Butte (CCB), Idaho. CCB is a roughly axisymmetric, isolated 100-m tall hill located in the broad Snake River Basin near Boise, Idaho. SHIS #2 was performed during October 1982 at the Hogback Ridge (HBR) near Farmington, New Mexico. HBR is a long, 90-m tall ridge located on the Colorado Plateau near the western slopes of the San Juan Mountains. Both small hill studies consisted of flow visualization and tracer experiments conducted during stable flow conditions with supporting meteorological, lidar, and photographic measurements. At these sites the tracer gases were released from mobile cranes or a tower.

The third and fourth field experiments were conducted at the Tracy Power Plant (TPP) located next to the Truckee River east of Reno, Nevada. The third experiment, performed in November 1983, was

undertaken as a feasibility and design study for the Full Scale Plume Study (FSPS). It was co-sponsored by the Electric Power Research Institute (EPRI). The November experiment not only demonstrated the feasibility of conducting the FSPS at the TPP, but with the expanded scope made possible by EPRI's participation, it also produced a data base that itself is useful for modeling purposes. The FSPS was performed at Tracy in August 1984. It is described in detail in Section 2 of this milestone report.

The data bases compiled from the CCB, HBR, and November Tracy experiments are available from the EPA Project Officer. The FSPS data base will be available in late 1985. The data bases compiled from each of the experiments include the following components:

- Source information: emission rates, locations, and heights of SF_6, CF_3Br, and oil-fog releases.
- Meteorological data: measurements of the approach flow as well as information on flow and dispersion near the terrain.
- Tracer gas concentrations: data from more than 50,000 individual samples collected during the experiments from as many as 100 sampler locations in each experiment.
- Lidar data (archived at WPL): sections across the plume characterizing the trajectory and growth of the plume upwind of, interacting with, and sometimes in the lee of key terrain features.
- Photographic data: still photographs taken from fixed locations, aerial photographs taken at CCB and Tracy from an aircraft flying overhead, and (occasional) 16-mm and 8-mm movies and videotapes.

During the course of the CTMD project, four Milestone Reports (Lavery et al. 1982; Strimaitis et al. 1983; Lavery et al. 1983; and Strimaitis et al. 1984) have been published. These reports (EPA-600/3-82-036, EPA-600/3-83-015, EPA-600/3-83-101, and EPA-600/3-84-110), which are available from EPA, describe the progress in developing and evaluating complex terrain models using the CCB and HBR data bases. They also describe in detail the two small hill studies, the November Tracy study, and a series of towing tank and wind tunnel studies performed at the EPA Fluid Modeling Facility (FMF) in support of the modeling.

This phase of the CTMD project will end in December 1986. An initial, partially validated model will be delivered to the Project Officer by October 1, 1985. A workshop will be held in early 1986 to present to the scientific community results from the field experiments, model development activities, and related work done both within and outside the CTMD project. The final stable plume impingement model(s) will be delivered in late 1986. A project report will be published in December 1986.

This Fifth Milestone Report documents work accomplished from June 1984 through May 1985. It describes in detail the FSPS, including its setting, the experimental design, and the resulting data base. The FSPS was successful. It produced a 128-hour data set of SF_6 and CF_3Br concentrations, ground-based and airborne lidar measurements, photographs, 8-mm movies, videotapes, and extensive meteorological data. The highest ten SF_6 and CF_3Br concentrations and a modeling analysis of 14 selected hours are discussed later in this milestone report.

The refinement of the HBR meteorological data is complete. Five-minute and one-hour averaged values of meteorological measures have been calculated from the corrected 1-sec data.

HBR lidar data have been used to compare measured oil-fog plume centerline heights upwind and over the crest of HBR to streamline heights calculated from (1) potential flow theory and from (2) a linearized perturbation analysis. The comparisons suggest that for releases above H_c at HBR a substantial portion of the streamline deflection near the crest can be explained by potential flow of the air above H_c, i.e., by assuming the ridge was "cut-off" above H_c. The perturbation analysis shows some improvement in the simulation of the streamline height when stratification is included in the calculations.

Stable boundary layer similarity relationships were used to predict wind and temperature data at 40 m and 150 m from data obtained at 10 m and 2 m. The predictions were compared to measurements taken at CCB and HBR. They indicate that the similarity relationships reproduce the observations fairly well to elevations less than about 10L (ten times the Monin-Obukhov length). Above 10L the predictions have little reliability.

The Complex Terrain Dispersion Model (CTDM) formula for σ_z was tested using lidar estimates of σ_z taken from a 14-hour subset of the FSPS data base. The predicted σ_z values were all within a factor of 2 of the lidar estimates although they generally overestimated the observations.

This milestone report also discusses the highest ground-level tracer concentrations measured at the CCB, HBR, and FSPS sites. The meteorological characteristics of the concentration events and the differences among the sites are discussed.

The further development of CTDM is described. Mathematical descriptions of the modifications to the model are presented. The latest version of the model has been tested with a subset of impingement hours from the CCB, HBR, and FSPS data bases. The initial 14-hour FSPS data base was also used to test four existing complex terrain models--COMPLEX I and II, Valley, and RTDM.

This report consists of seven sections and one appendix. Section 2 provides a description of the FSPS. Various data refinements and analyses are presented in Section 3. Section 4 provides an analysis of the highest tracer concentrations measured at each site. Progress in developing CTDM and an evaluation of the model for impingement hours are discussed in Section 5. Future improvements and modifications to CTDM are discussed in Section 6. Section 7 presents the summary, conclusions, and recommendations for future work. The Appendix contains a report prepared by the EPA FMF describing a series of neutral and stratified flow experiments to determine streamline trajectories over a three-dimensional hill.

SECTION 2

FULL SCALE PLUME STUDY

2.1 Geographic and Meteorological Setting

The Tracy Power Plant east of Reno, NV, was selected as the site of the Full Scale Plume Study (FSPS) after an extensive survey of all power plants in the western United States located in settings that could qualify as complex terrain. In its favor were the following considerations:

- Unit 3 at Tracy is maintained in warm standby status when it is not in fact producing power for the grid.
- Sierra Pacific Power Co., the owner and operator, was very cooperative.
- The plant is surrounded by complex terrain, the elevations of the mountains affording opportunities for plume impact in many directions.
- The area is very sparsely populated and nearly devoid of trees.
- It is near a city with good commercial air service, lodging, and other logistical support.

The principal drawbacks to Tracy were that it is currently gas-fired so that its plume cannot be tracked by lidar and that its 120-megawatt capacity and common standby status did not make it representative of large new sources undergoing regulatory review.

The first of these drawbacks was overcome by production of "smoke" with corvus oil as had been done in the two CTMD Small Hill Impaction Studies. Augmentation of the particulate emissions at any power plant would have been necessary if photographic data were to be taken, as was ERT's intention. The feasibility of producing an artificially smokey plume was demonstrated by tests performed by ARLFRD at Tracy in July 1983. The size of Unit 3 at Tracy was not regarded as disqualifying for the purposes of CTMD for several reasons: New power-generation units in the West were tending to fall into the 250-MW range rather than the 600-MW range more common in the previous decade; the majority of sources undergoing regulatory review are better represented by Tracy than a larger power plant at full load; and the scale of the Tracy stack effluent required less tracer gas to keep sample concentrations within an analytical range yielding good chromatographic precision.

The Tracy site is in the Truckee River valley about 17 miles east of Reno. (See Figure 1). The plant has three units, but only Unit 3 with 120-MW capacity and a 300-foot (91.4 m) stack is operating. Geographically the site has merit in that stable flows from the west are fairly common at night. The Sierra Nevada to the west of Reno and the Pah Rah Mountains to the east define the Truckee Meadows basin in which the Reno-Sparks urban area lies. The Truckee River has cut a canyon through the Pah Rah range and drops approximately 200 feet from Sparks to Tracy. Large-scale downslope winds off the Sierra at night flow through the canyon and reinforce the drainage down the river. Photographs of the wood smoke plume from Sparks showed this to be the case.

At the plant site (Figure 2), the valley broadens to the north towards the Pah Rah Mountains. To the south, Clark Mountain rises almost 3,000 feet (910 m) above the stack base in seven km. At about 4.5 km east of the plant, the river swings sharply north through a narrow gorge between two large obstacles, "Beacon Hill" (5232 ft. MSL, or about 300 m above stack base) to the west of the gorge and "Target Mountain" (5764 ft. MSL or about 460 m above stack base) to the east. These two terrain elements were the principal "target" areas in the anticipated westerly winds. Figure 3 is a photograph looking east from the "Old Lonesome" camera site that shows the relationship of the plant to these two features.

2.2 Preliminary Experiment

A preliminary experiment was performed at Tracy in November 1983; it is described in the Fourth Milestone Report (Strimaitis et al., 1984) and will only be briefly summarized here.

The objectives of the preliminary experiment were to assess the feasibility of the site for the FSPS and to gather information to assist in the experimental design. As originally conceived, the November experiment involved only a handful of tracer samplers for estimation of dilution factors to determine appropriate tracer release rates. Typical flow patterns were to be investigated by personal observation and photographs of the oil-fog plume released from the 300-ft stack. The scope of this study was expanded substantially by the co-sponsorship of the Electric Power Research Institute (EPRI), however, and this "preliminary" experiment yielded a database useful for model development and evaluation in its own right. EPRI's contractors from the Plume Model Validation and Development program provided sampling at 53 sites, necessary helicopter service, the tracer concentration analyses and archiving, quality assurance audits of the tracer and meteorological components of the study, two pibal teams and equipment, and airborne lidar data by means of the ALPHA-1 system.

ERT erected CTMD's 150-m meteorological tower instrumented at four levels and supplied a data acquisition system for the tower, two electronic weather stations, two carbon arc lamps and operators, cameras and observers, technical and logistical management, and coordination with Sierra Pacific. The National Oceanic and

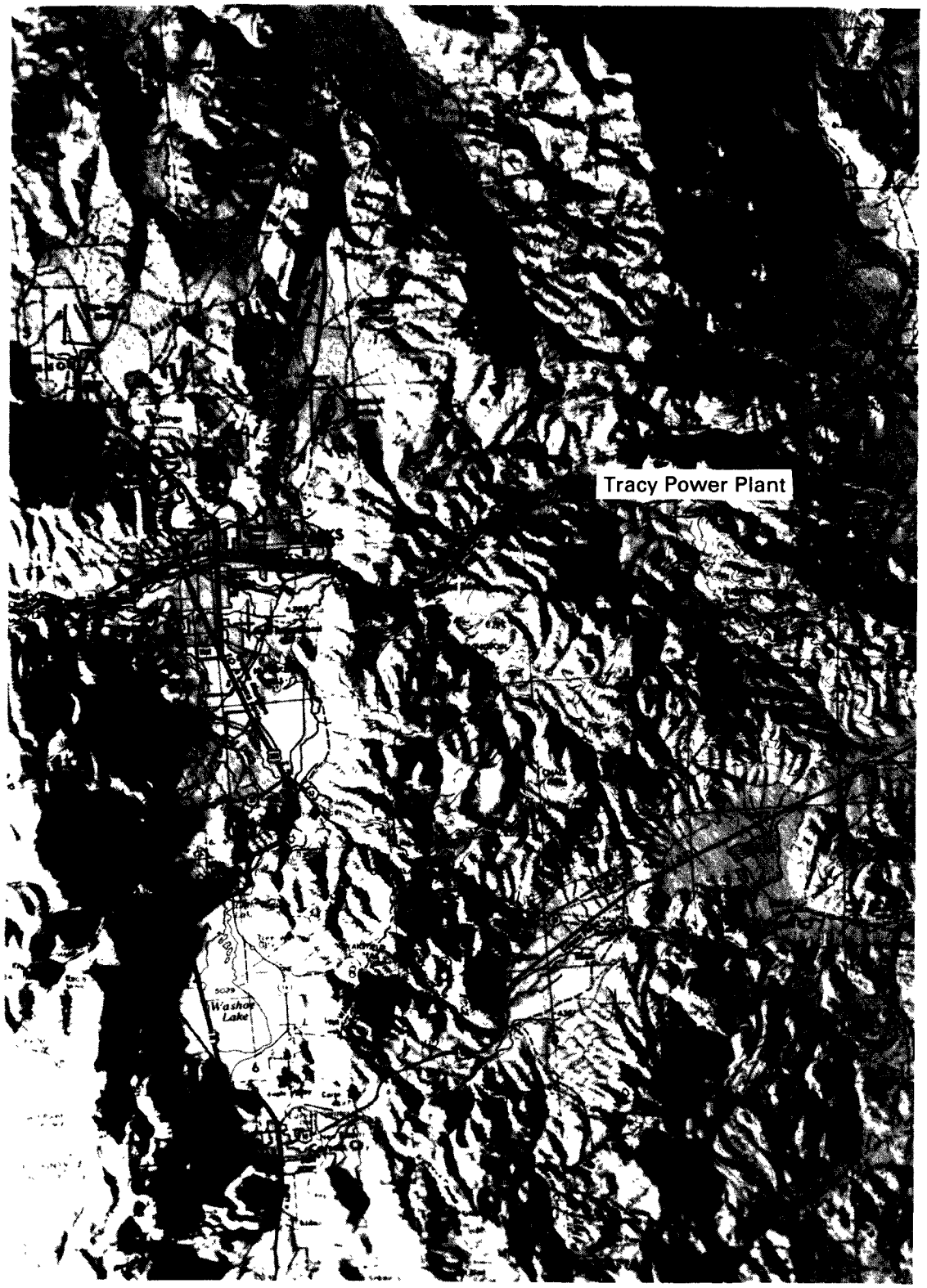

Figure 1. The region around the Tracy Power Plant.

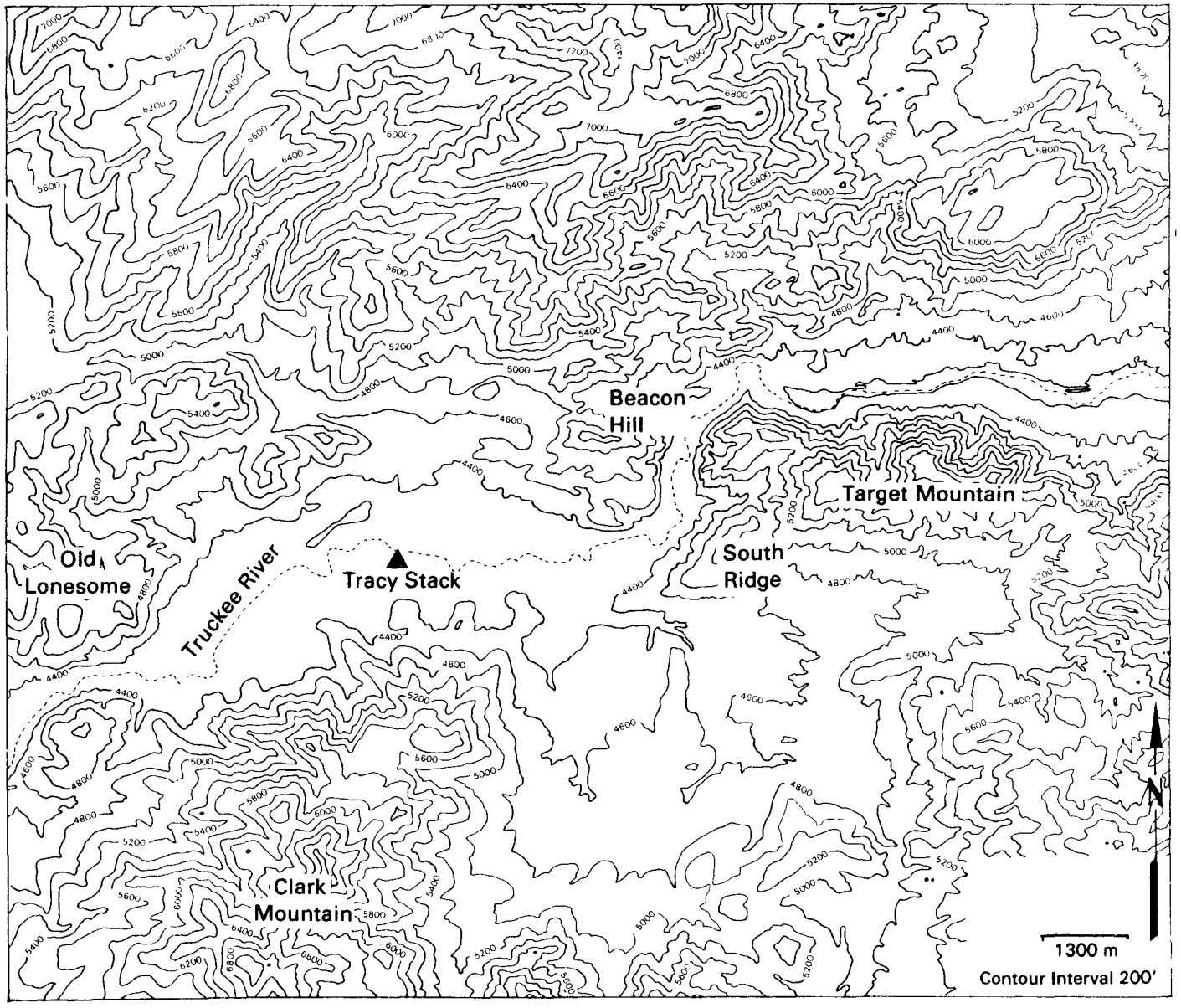

Figure 2. Plant site.

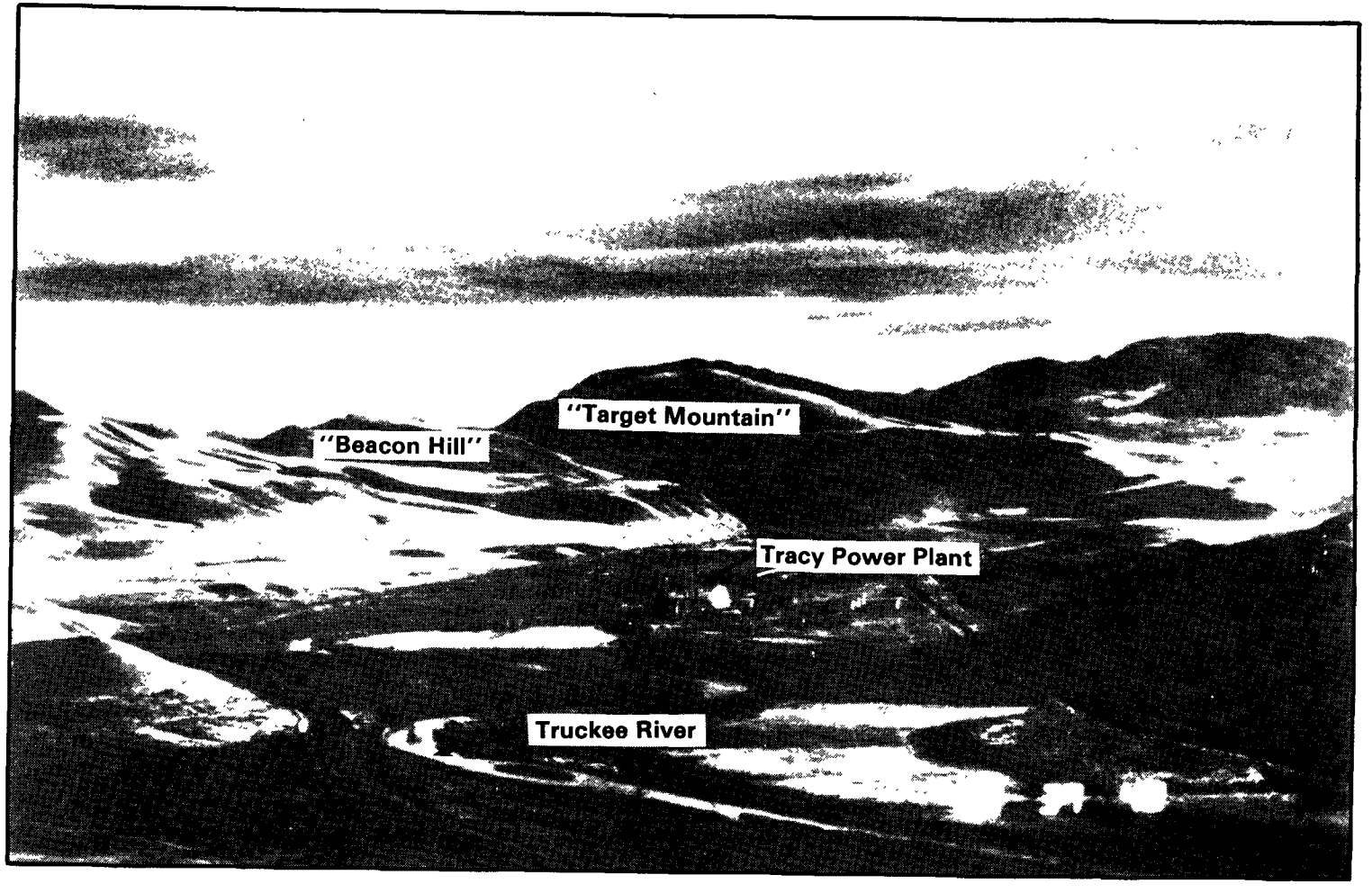

Figure 3. View of the Tracy Power Plant looking east from "Old Lonesome." "Target Mountain" and "Beacon Hill" can be seen at the eastern end of the valley.

Atmospheric Administration's Air Resources Laboratory Field Research Division (ARLFRD) and Wave Propagation Laboratory (WPL) were the principal participants on the EPA/CTMD team. ARLFRD was responsible for SF_6 and oil-fog tracer releases, two 10-m towers on promontories and associated telemetry and data logging, one tethersonde, radio voice communications, and subcontracted photographers. WPL provided a second tethersonde, two optical anemometers, a doppler acoustic sounder, and two monostatic acoustic sounders, all with necessary operational personnel. ERT produced the master data archive and distributed it to the participants.

The 150-m tower was maintained until after the FSPS to obtain almost a year of meteorological data as part of ERT's obligations under CTMD.

The preliminary experiment yielded 68 hours of tracer concentrations under a variety of nocturnal and morning conditions. Over half of these hours appear useful for modeling purposes.

The experiment also fulfilled the informational requirements of CTMD. Tracy was shown to be an appropriate site for the FSPS, and the plume often interacted with the terrain. But the drainage flow from the west proved to be neither as reliable nor as persistent as had been hoped. Not only was the flow influenced by several migrating weather systems, some accompanied by snow, but also in conditions of weak gradient winds, the motion in the valley at plume height often appeared oscillatory with a period on the order of two hours. Because of this sloshing, the FSPS sampling array was extended to cover areas to the west and northwest of the plant. The tracer releases into the breaching of Unit 3 were shown to be satisfactory, and the effluent flux from the stack with the plant in warm standby with the forced draft fan on was sufficient to prevent stack-top downwash in the light wind conditions that normally prevailed during stable hours. The spatial and temporal variability of the winds in the study area indicated the necessity for extensive meteorological instrumentation.

2.3 FSPS Experimental Design

The components of the FSPS were basically the same as those used in the Small Hill Impaction Studies. Two tracers, SF_6 and CF_3Br (Freon 13B1), were released simultaneously from two different locations to give twice the dispersion information at a small increase in cost. A "smoke" plume was produced by evaporation of corvus oil in a small jet aircraft engine exhausted into the side of the duct leading from the power boiler to the stack. SF_6 was injected into the same gas stream through a sampling port just upstream of the breaching into the flue. CF_3Br was released from one of three heights on the 150-m tower.

One-hour samples of ground-level tracer concentrations were obtained at more than 100 locations in two-liter Tedlar bags. Three additional samplers were mounted on the tall tower. Analysis of tracer concentrations was done by gas chromatography with electron-capture detection.

Ground-based lidar made vertical transects through the oil-fog plume, usually at five distances downwind, to measure the location and dimensions of the plume and its proximity to terrain.

The ALPHA-1 airborne lidar tracked the plume to greater distances. Color photographs of the plume were taken routinely every five minutes from five locations, and video-tapes were made during daylight hours. Two carbon-arc lamps panned along the plume for illumination when natural light was insufficient. ERT's scientist-observers took additional color slides and, after dawn, 8-mm time-lapse movies as well.

Meteorological measurements were made from the 150-m tower, four 10-m towers, two electronic weather stations, two tethersondes, and one monostatic and two doppler sodars. Two radar-tracking balloon sounding systems were also used. Figure 4 shows the locations of the various meteorological sensors, the lidar, and the Command Center.

As at HBR, principal participants in FSPS were ERT, NOAA/Wave Propagation Laboratory (WPL), and NOAA/Air Resources Laboratory Field Research Division (ARLFRD). Under subcontracts to ERT, Meteorological Standards Institute of Fox Island, WA, performed external audits of the meteorological tower instrumentation and the gas chromatography laboratory, and Morrison Knudsen Co., Inc., of Boise, ID, provided five photographers, 35-mm cameras, a video camera, film, an arc-lamp, and operators for both arc-lamps. Vara Systems, Inc., of Newbury Park, CA, surveyed the experiment area and produced a topographic map under contract to ARLFRD. SRI International made airborne lidar transects with the ALPHA-1 under the sponsorship of the Electric Power Research Institute.

Responsibilities of the principal participants are summarized in Tables 1 to 3.

2.3.1 Tracer Data

Tracer Release

Artificial smoke produced by evaporation of corvus oil in the exhaust of a small jet aircraft engine made the plume from the plant stack visible for lidar scans, photography, and observers. The jet-fogger vaporized approximately 60 gallons of oil per hour and injected it into the duct leading from Unit 3's boiler to the 91.4-m stack just downstream of the air preheater section. The boiler's forced draft fan maintained a steady flow of air through the duct regardless of generating load, and the plume downwashed at the top of the stack only on the infrequent occasions when the wind at stack-top exceeded about 6 m/s. There were apparent periods of building-induced downwash as well during strong winds at the beginning of a few experiments; these times are identifiable from observer comments, lidar data, and photographs.

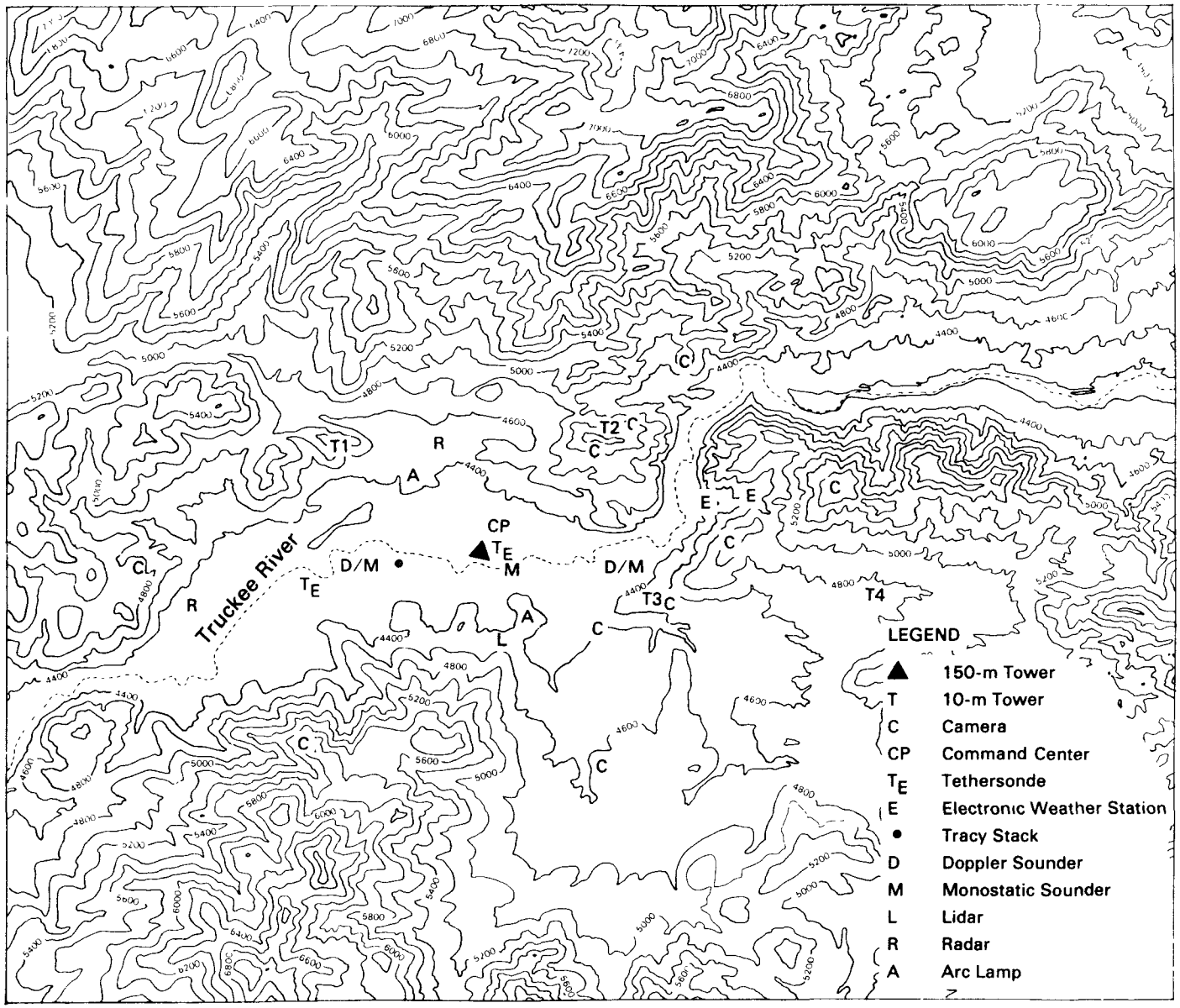

Figure 4. FSPS field experiment layout.

TABLE 1. SUMMARY OF ERT FSPS RESPONSIBILITIES

- Experimental Design (with other participants)
- Preparation of Quality Assurance Plan
- 150-Meter Meteorological Tower Reconfiguration
  1. Installation of additional levels and sensors
  2. Installation of sonic anemometers and temperature sensors
  3. Installation of tracer release system to release CF_3Br from three heights -- 102.1, 127.4, and 142.1 m
  4. Pre/Post-experiment system calibrations and tests
- Field Logistics and Site Preparation
  1. NOAA/ARLFRD equipment supply (meteorological systems)
  2. Command Center supply and installation
  3. Telephone and dataline arrangements
  4. Command Center power supply
  5. Subcontractor support coordination
  6. Lidar siting support
  7. Area landowners and lease-holder access authorization
  8. Agency notifications
- Data Collection System for 150-m Tower
  1. Design, code, and test data acquisition system for 150-m tower meteorological data
  2. Install Data General C330 computer system in Command Center
  3. Install IBM PC/XT and Intel computers in tower shelter
  4. Set-up data line for sonic anemometer computer/Command Center interface
  5. Perform and document control tests for meteorological data collection system
- Field Operations
  1. 150-meter meteorological tower maintenance
  2. Remote electronic weather station (EWS) installation, calibration, and maintenance
  3. Takedown and installation of tower-mounted tracer samplers after each experiment
  4. Field observations, smoke releases (candles), and photography

TABLE 1 (Continued)

5. Site security
6. Portable toilet services
7. General field support

- Project Takedown
  1. 150-meter meteorological tower takedown, inventory, and shipping
  2. Remote EWS (2) removal and shipping
  3. EWS data reduction and reporting
  4. Site decommissioning and restoration
  5. Complete project equipment inventory
  6. EPA equipment refurbishing (as needed)
  7. Shipping EPA equipment to FRD
- Archive of 150-m Tower Data
- Development and Distribution of Data Base
- Overall Direction of Experiment Operations
- Provision of Quality Assurance Auditor

TABLE 2. SUMMARY OF NOAA ARLFRD FSPS RESPONSIBILITIES

- Provide an initial quality assurance plan to ERT.
- Complete preliminary field site preparation and equipment installation and checkouts. Primary contributions were to:
  1. Survey sites for ground-level sampling, tower bases, tethersondes, lidar observations, roadways, and all other locations pertinent to the experiment; provide surveyed contour map of experiment site.
  2. Erect and provide electrical power for the 10-m towers.
  3. Attach temperature and wind sensors on the 10-m towers.
  4. Provide voice communications for FRD and ERT operations center(s), lidar crew, chief photographer, and scientific observers.
  5. Purchase oil, kerosene, SF_6, and CF_3Br.
  6. Provide for release of oil-fog and gaseous tracers from the 300-ft stack and the 150-m tower.
  7. Provide chairs, tables, refrigerator, and other equipment for NOAA ARL and ERT Command Center from available NOAA ARL resources.
  8. Deploy sequential tracer samplers at 107 pre-selected locations.
  9. Provide all telemetry equipment for the 10-m towers.
- Participate in the field measurement program by:
  1. Being ready for the initial test on August 6, 1984.
  2. Releasing oil-fog and two gaseous tracers provided by FRD.
  3. Sampling 128 hours of gaseous tracer releases at 107 predesignated ground-level sites and the 150-m tower.
  4. Trucking bags to Idaho Falls for GC analysis.
  5. Analyzing about 440 whole air samples of gaseous tracers for each of two shakedown experiments.
  6. Analyzing about 1,100 whole air samples of gaseous tracers for each of 12 tracer release test days. Preparing maps of tracer gas concentrations within about 48 hours.
  7. Conducting tethersonde soundings of pressure, temperature, humidity, wind speed, and direction.
  8. Supplying two radars and taking rabal winds, with the data provided to the command post in real-time during the experiments.

TABLE 2 (Continued)

- Submit a final record of all meteorological and tracer data on 9 track, 1600 bpi magnetic tape.
- Provide a final report on participation in the field measurement program, including a description of the surveyed sampling grid and measurement platform sites, the date and times of field measurement activities, and the information needed to allow correct understanding of the character and quality of these measurements.

TABLE 3. *SUMMARY OF NOAA WPL FSPS RESPONSIBILITIES*

- Provide an initial quality assurance plan to ERT.
- Complete field site preparation and equipment installation and checkouts. Work included:
  1. Preparation of the site and installation of power for the lidar system.
  2. Work with ERT on the installation of the sonic anemometer systems, including the data acquisition component.
  3. Installation of the doppler and monostatic acoustic sounder systems.
- Participate in the FSPS by:
  1. Having all equipment in place, ready for the initial experiment on August 6, 1984.
  2. Sampling the oil-fog plume with the lidar system.
  3. Operating the sonic systems and providing 20-min average data in real-time to the ERT command center.
  4. Operating two doppler acoustic sounders, with data transmitted to the command center upon request.
  5. Operating three monostatic acoustic sounders.
  6. Conducting tethersonde soundings of temperature, relative humidity, wind speed, and direction. Data transmitted routinely to the command center.
- Supply a final record of all numerical meteorological data on 9 track, 1600 bpi magnetic tape.
- Submit tapes of processed lidar data. Also, submit narrative interpretation of simultaneous monostatic sounder data.

The smoke plume could generally be tracked visually at least until its first interaction with terrain except in strong wind, neutral conditions. The lidars could track it even when it was invisible to the eye.

SF_6 was injected into the stack plume through a sampling port in the side of the duct work a few feet upstream of the stack. The second tracer gas, CF_3Br or Freon 13B1, was released from the 150-m tower at one of three levels -- 102.1, 127.4 and 142.1 m above the ground. The tracer was injected into the side of a Climatronics aspirated temperature shield with the fan motor mounted backwards so that the air was blown out the nozzle extension of the aspirator. The intent of this system was to dilute the heavy tracer with a relatively large volume of air, both to alleviate problems of negative buoyancy and to force the tracer away from the tower's three elevated samplers, located at 43.7, 104.8, and 145.4 m above the ground. This system seems to have worked since only eight of 128 hours of tracer concentration data have an abnormally high CF_3Br reading at the sampler near the release point. The nozzles of the aspirators were aimed to the east in anticipation of predominantly westerly flow during the experiments.

Both tracers were released from cylinders of "pure" gas stored at the ground. ARLFRD's release metering systems were those used at HBR and the preliminary FSPS and have been described in the Third Milestone Report (Lavery et al., 1983). SF_6 was piped to the port in the breaching by garden hose; CF_3Br was transported up the tower to the aspirators in PVC tubing. Each tower release point was fitted with an electrically controlled valve activated from the ground that directed the flow to the selected height.

Tracer Sampling

Tracer concentrations were sampled at 110 sites, including the three elevated samplers on the 150-m tower and one at its base, by the modified AQS-III bag samplers used at the CCB and HBR experiments. All samplers operated in the 1-hour mode and filled 2-liter Tedlar bags. Figure 5 is a map of the sampler sites.

Because of the rugged terrain and size of the network, a helicopter was necessary to ferry the sampler crew and bags around the network. ARLFRD arranged the loan of a large Bell helicopter and 2-man crew from another branch of NOAA for the duration of the experiment.

Tracer Analysis

Chromatographic analysis for SF_6 and CF_3Br in the sample bags was done by ARLFRD in their laboratory in Idaho Falls, ID. The analytical procedures and equipment were basically identical to those used in the lab in Farmington, NM.

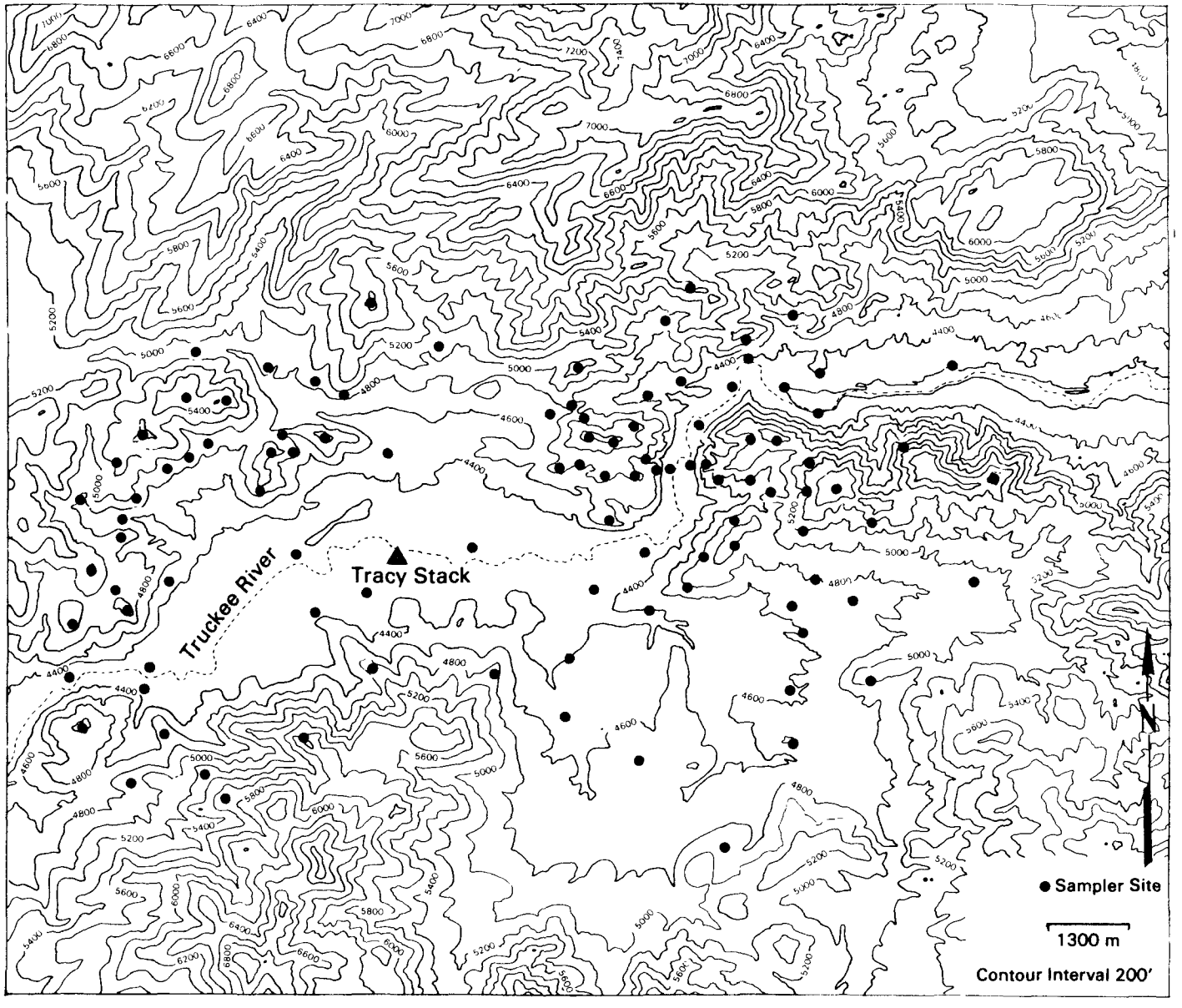

Figure 5. Tracer gas sampling sites.

Boxes of sample bags were shipped to Idaho Falls by contracted trucks. Analysis was generally completed within 48 hours of the end of each experiment.

2.3.2 Meteorological Data

Meteorological data were collected from instruments on the 150-m tower and four 10-m towers, from two tethersondes, two radar-tracked balloon (RABAL) systems, and one monostatic and two doppler acoustic sounders. ERT was responsible for the installation and maintenance of the 150-m tower instruments and data acquisition, archive, and display of their outputs with analytical presentations like those at CCB and HBR. ARLFRD was responsible for the same functions with respect to the four 10-m towers, although no real-time display or analysis were required; they also provided and operated the two RABAL systems and one tethersonde. WPL operated one tethersonde and installed, maintained, and archived data from three sonic anemometers on the 150-m tower and the acoustic systems.

150-m Tower Data

The data acquisition for the sensors on the 150-m tower was an improved version of the system used at CCB (Greene and Heisler, 1982). It provided onsite analysis and two media for local recording of reduced data. A block diagram of the system is shown in Figure 6.

The polling of the analog (voltage) outputs of the sensors, conversion to digital values, and the calculation of 5-min and 1-hr values of average data and turbulence quantities were done by ERT DS-00 "data stations," devices designed and coded by ERT and based on Intel microprocessors. These units, which were used at CCB, were located in the shelter at the tower base in the same pair of instrument racks as the Climatronics signal-conditioning equipment in order to limit the length of wires between the instrument outputs and the data acquisition equipment in the interest of noise suppression. The instruments were scanned four times per second by the Intels.

The two "types" of data stations used are distinguished by the coding of the PROM: a Type 2 device is designed for speed and direction inputs, as from Climatronics F460 cup-and-vane systems, and a Type 3 for UVW inputs, as from triaxial propeller anemometers. At each data sample, the Type 2 resolves speed and direction into U and V components. From then on, the two types operate in the same fashion for calculation of turbulence intensities and vector-resultant wind speeds and directions. (No vertical wind component is measured by the Type 2.) Additionally the microprocessors serving the F460s calculate scalar mean speeds and directions and σ_θ. Two microprocessors of each type were required for this installation.

Each Intel microprocessor updated its 1-hr and 5-min average calculations each minute. The measures available at each level of the tower are displayed in Table 4, and Table 5 indicates the meaning of the various measure codes.

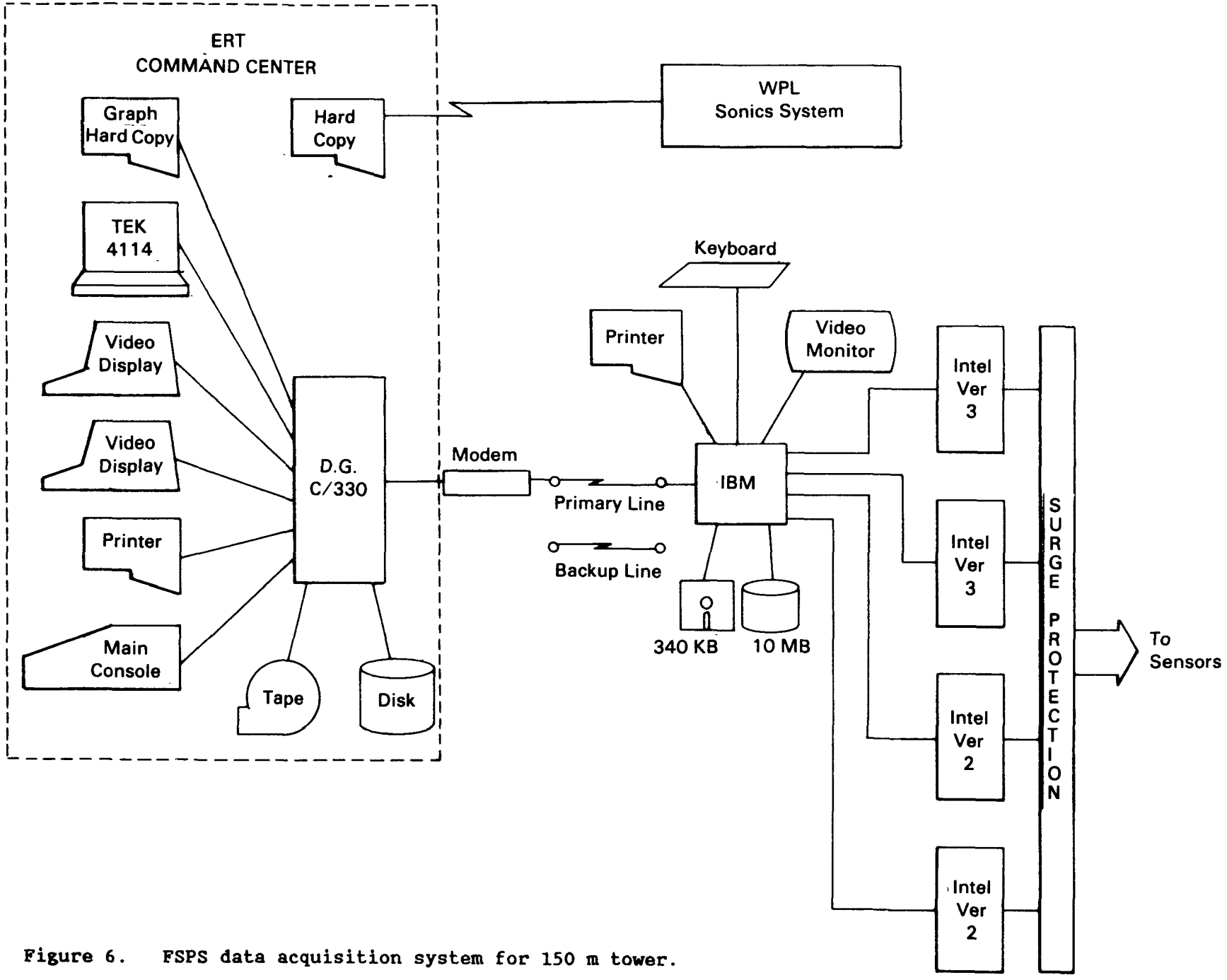

Figure 6. FSPS data acquisition system for 150 m tower.

TABLE 4. 150-M TOWER SENSOR LOCATIONS AND MEASURES

	1	10	50	75	100	125	150
Tower Level (m)							
U,V,W propeller anemometer		*	*		*	*	*
Cup and vane sets		*		*	*		*
Temperature		*					
Temperature difference		*	*	*	*	*	*
Pyranometer	*						
Net radiometer	*						
U,V,W sonic anemometer		*			*		*
Measures							
U,V,W		o	o		o	o	o
IXP, IYP, IZP		o	o		o	o	o
SPV, DPV		x	x		x	x	x
UCV, VCV					o		o
UCS, VCS		o		o	o		o
SCV, DCV					o		o
SCS		o		o	o		o
DCS		x		x	x		x
IXC, IYC					o		o
SDR		x		x	x		x
IYS		o		o	o		o
T		o					
TD			o	o	o	o	o
TC			x	x	x	x	x
SDS				o	o		o
DVS		o		o	o		o
SDV		o		o	o		o
FVC		o					
SVC		o					
SR	o						
NR	o						

* Indicates a sensor that was scanned four times per second.
o Indicates a "direct" measure calculated by microprocessors from instrument voltage outputs.
x Indicates a "derived" measure calculated by C330 computer from direct measures.

Note: The sonic data were archived via a separate data acquisition system provided by WPL. Averaged data were available on a printer in the command post.

TABLE 5. DEFINITION OF MEASURES

Measure Code	Definition	Units
U, V, W	Vector average wind components - props	m/s
UCV, VCV	Vector average wind components - cup and vane	m/s
UCS, VCS	Scalar average wind components - cup and vane	m/s
SPV	Vector average wind speed - props	m/s
DPV	Vector average wind direction - props	degrees
SCV	Vector average wind speed - cup and vane	m/s
DCV	Vector average wind direction - cup and vane	degrees
SCS	Scalar average wind speed - cups	m/s
DCS	Scalar average wind direction - vane	degrees
IXP*, IYP**, IZP***	Alongwind, crosswind, vertical intensities of turbulence - props	percent
IXC*, IYC**	Alongwind, crosswind intensities of turbulence - cup and vane	percent
IYS+	Scalar crosswind intensity of turbulence - vane	percent
SDR	Standard deviation of wind direction - vane	degrees
T	Ambient air temperature - encapsulated platinum wire	°C
TD	Temperature difference - encapsulated platinum wire	°C
TC	Calculated temperature, TC = T + TD	°C
SDS	Standard deviation of wind speed - cups	m/s

TABLE 5 (Continued)

Measure Code	Definition	Units
DVS	Scalar average of vane output signal	degrees
SDV	Standard deviation of vane output signal	degrees
FVC	Fixed voltage constant	volts
SVC	Standard deviation of fixed voltage constant	volts
SR	Solar radiation - pyranometer	langleys/min
NR	Net radiation - net radiometer	langleys/min

$$^{*}\ IX = \left\{\frac{1}{N}\left[\frac{(\Sigma u)^2\,\Sigma u^2 + (\Sigma v)^2\,\Sigma v^2 + 2\Sigma u\Sigma v\Sigma uv}{(\Sigma u)^2 + (\Sigma v)^2} - \frac{(\Sigma u)^2 + (\Sigma v)^2}{N}\right]\right\}^{1/2} \div \bar{U}$$

$$^{**}\ IY = \left\{\frac{1}{N}\left[\Sigma u^2 + \Sigma v^2 - \frac{(\Sigma u)^2\,\Sigma u^2 + (\Sigma v)^2\,\Sigma v^2 + 2\Sigma u\Sigma v\Sigma uv}{(\Sigma u)^2 + (\Sigma v)^2}\right]\right\}^{1/2} \div \bar{U}$$

$$^{***}\ IZ = \left\{\frac{\Sigma w^2 - (\Sigma w)^2}{N}\right\}^{1/2} \div \bar{U},$$

where $\bar{U} = \frac{[(\Sigma v)^2 + (\Sigma v)^2]^{1/2}}{N}$ is the vector resultant mean wind speed, N is the number of samples in the calculations, u and v are the instantaneous wind component speeds from the propeller anemometers or cup and vane, and w is the vertical instantaneous wind component speed from the propeller anemometer.

$$^{+}\ IYS = SDR \cdot \frac{\pi}{180} \cdot 100$$

The digital outputs of the Intels were in turn polled by a "data concentrator" computer, an IBM PC/XT desk-top computer located in the instrument shelter. This unit served as the "controller" of the Intel microprocessors. Its crystal-driven clock determined when the scans for 5-min and 1-hr averaged direct measures were performed, and it could store on disk more than 12 hours of tower data in the form of 5-min and 1-hr averages of the direct measures from the Intels. This archival function was invoked automatically whenever the IBM determined that communication with the computer in the control center office was not possible. The IBM was equipped with a CRT console as well as a line printer, on which messages were printed indicating problems with data collection or transmission.

After the IBM data concentrator completed a 5-min (or 5-min and 1-hr) scan of the direct measures from the Intels, it interrupted the central data collector in the experiment control trailer. The data collector was a Data General C330, a multi-tasking mini-computer that received the values of the direct measures from the IBM, calculated the indirect measures, flagged measures that fell outside prescribed reasonable ranges, and archived all measures on a 25-megabyte hard disk. Its other functions were tabulation of selected measures on hard copy as they were received or calculated, production of profiles of temperature and wind speed and direction by spline-under-tension algorithms, calculation of flow parameters such as Froude numbers and heights of critical streamlines, and production of plots of time histories or profiles on the Tektronix 4114 plotter. Software developed for the two previous field studies was used by the C330 with a few modifications to allow incorporation of doppler acoustic and/or tethersonde data into the profiles.

Communication between the IBM PC in the shelter and the C330 in the trailer was over a dedicated telephone line about 400 m long. The accuracy of data transmission was tested by a check-sum on each record.

At the end of each experiment, the data archived on disk was dumped to two 9-track tapes, one of which was shipped directly to ERT's office in Concord, MA, while the other remained in the Reno area.

Selected instrument outputs were recorded on strip chart recorders in the instrument shelter. The chart-recorded measurements included the following:

150-m W-propeller
150-m F460 speed and direction
100-m F460 speed and direction
10-m F460 speed and direction
10-m temperature
10- to 150-m temperature difference
10- to 100-m temperature difference

10-m Tower Data

The four 10-m towers were powered by high energy (approximately 400 amp-hrs) 12-volt storage batteries charged by solar panels. Instrument output from Towers 1, 2, and 3 was telemetered continuously to a Monitor Labs data logger in the Command Center via Communitronics radio links powered by the same batteries. The data logger controlled the sampling of the instrument outputs at 4-sec intervals and recorded these raw data on 9-track tape. The tape data were processed after the experiments were completed by FRD in their offices in Idaho Falls; 5-min and 1-hr averages of wind speed and direction and temperature as well as standard deviations of speed and direction were calculated. Additionally, 5-min averages could be printed on paper tape on request during calibration, system checks, and audit periods; but this function could not be performed during experiments because of CPU time constraints. All measurements from Towers 1, 2, and 3 were recorded on strip charts in the Command Center.

Tower 4, the easternmost tower, was inaccessible by the radio telemetry system, and the data from its instruments were recorded locally by a battery-powered Mars data logger.

Platinum temperature probes in aspirated radiation shields, cup anemometers, and wind vanes were mounted at 10 m on Towers 1, 2, and 3. Cups and vanes and aspirated temperatures were deployed at both 1 and 10 m on Tower 4.

Electronic Weather Stations (Target Mt. Draw)

ERT's two Climatronics Electronic Weather Stations were installed with their cups, vanes, and temperature probes mounted at about 1 m above the terrain to examine the flow in the large draw on the west end of the "target" mountain. Data from these instruments were recorded on multiple-trace chart recorders.

Sonic Anemometers

Sonic anemometer systems, comprising UVW components and very fast response platinum wire thermistors, were installed by WPL and ERT at 10, 100, and 150 m on the big tower. These instruments were sampled 20 times per second. Vector resultant wind speeds and directions and alongwind, crosswind, and vertical turbulence (σ_u, σ_v, and σ_w) were calculated for 5-min and 1-hour averaging periods. Additional flow parameters, including Monin-Obukhov length, friction velocity, vertical "temperature flux," and standard deviation of temperature, have been calculated as well. WPL was responsible for collection and archival of sonic data; their computer was housed in a van near the instrument shelter at the base of the tower. Selected averaged data were transmitted by cable to a line printer in the Command Center.

Tethersondes

Two tethersondes manufactured by A.I.R., Inc., were flown during experimental periods, one operated by ARLFRD about 0.8 km west of the stack and one operated by WPL near the big tower about 1.5 km east of the stack. These sondes were flown to give wind and temperature profiles upwind and downwind of the stack and were helpful as complements to the acoustic sounders nearby. The tethersonde data were printed on roll paper. The WPL tethersonde data were also recorded on cassette tapes.

Acoustic Sounders

WPL set up and operated three acoustic sounding systems; two were doppler sodars in monostatic configuration and one a monostatic sounder. One doppler was a few hundred meters west of the stack and one at the east end of the valley. The monostatic system was set up near the Command Center.

Each sounder had its own data acquisition system, the doppler's being mini-computer based with hard-copy digital output of 20-min wind and turbulence profiles. All three systems recorded monostatic-mode analog output on facsimile charts.

RABALS

ARLFRD operated two radar-tracked balloon (RABAL) systems north of the river to obtain wind profiles up to a few thousand meters altitude. Each had its own computerized data acquisition system that calculated wind speed and direction from azimuth, elevation angle, and range. Balloons were released and tracked every half hour at both sites.

2.3.3 Smoke Plume Data

Lidar

WPL operated their lidar system from the base of Clark Mountain about 2.2 km east-southeast of the plant. The lidar was basically the same as that used at HBR with the yttrium-aluminum-garnet (YAG) crystal doped with neodymium. It made vertical transects of the plume, usually at five azimuths ranging from near the stack to the "target" areas to the east when flow was from the west. When the plume blew towards the west, it was hidden from the lidar by terrain after a few kilometers; when the plume blew towards the high terrain to the northwest, the lidar sections were almost along the axis of the smoke.

A series of transects was made approximately every 5 mins, the data being recorded on 9-track tape for later processing. Improved real-time display of the signal returns gave feed-back on plume behavior for experimental guidance and understanding.

Photography Program

Under subcontract to ERT, Norman Ricks of Morrison-Knudsen Company, Inc., was responsible for the photography program, as he had been at HBR. He and five associates took photographs routinely every 5 mins from five positions in the high terrain and operated the arc lamp. A second arc lamp and its operator were contracted by Morrison-Knudsen. Each photographer had two cameras, using one for the routine 5-minute exposures and one for capturing interesting images of smoke from their viewpoints. In addition, video-tapes were made of the plume from the camera position near Tower 3 after dawn.

Airborne Lidar

EPRI sponsored the ALPHA-1 airborne downward-facing lidar at FSPS as they had in the preliminary experiment at Tracy in November 1983. This system, developed for EPRI by SRI International, was operated by SRI scientists during FSPS. The aircraft was typically flown in a ladder pattern back and forth across the plume, making transects from near the source to about 8 or 10 km distance. The signal returns were recorded on both tape and facsimile charts.

2.4 Preliminary Evaluation of FSPS and Database

The FSPS comprised 14 tests or experiments and a total of 128 hours of data collection. Table 6 lists the dates and durations of the 14 experiments. Experiment hours encompassed a variety of meteorological conditions ranging from very stable with very light winds to morning inversion breakup and fumigation. On several evenings early in an experiment, strong winds from the west produced near-neutral flow in the valley. Prolonged periods of stable plume impaction on the targeted elevations to the east frequently occurred.

Some light-wind, stable periods may be difficult to model because the flow at some levels alternated between going down the valley to the east and up the valley to the west with a typical period of more than an hour. The dynamics of this "sloshing" motion have not yet been studied in the database, but the oscillation appeared sometimes to lift the plume bodily and then let it subside. One effect of this sloshing was the advection of layers of old plume in the "approach flow" of subsequent periods. These layers may then have contributed "background" to sampled concentrations that were in large part caused by more direct impact of the source plume on receptors.

A tracer concentration database has been received from ARLFRD containing 11,609 concentrations for either tracer gas. This indicates a preliminary data capture of 82.5 percent based on 128 possible hours of sampling by 110 samplers.

Most of the meteorological instrumentation performed well and data capture is good. There were three systems with known problems however--the eastern doppler sodar, the western tethersonde, and the

TABLE 6. FSPS EXPERIMENT HOURS OF TRACER RELEASE AND CONCENTRATIONS

Experiment	Date (Aug 84)	Time (PDT)	Release			Concentrations	
			Oil-Fog	SF_6	CF_3Br	SF_6	CF_3Br
1	6	03-07	4	4	4	4	
2	7	03-07	4	4	4	4	4
3	9-10	20-06	8	10	10	10	10
4	10-11	20-06	10	10	10	10	10
5	11-12	20-06	8	10	9	10	10
6	15-16	22-08	10	10	10	10	10
7	16-17	22-08	10	10	10	10	10
8	17-18	22-08	5	11	11	10	10
9	20-21	22-08	10	10	10	10	10
10	21-22	23-09	7	10	10	10	10
11	22-23	23-09	10	10	10	10	10
12	25	00-10	10	10	10	10	10
13	26	00-10	10	10	10	10	10
14	27	00-10	9	10	10	10	10
TOTAL			115	129	128	128	128

Notes: Preliminary assessment pending receipt of final data.
Only whole hours counted.
Tracer releases often began 1/2 hour before start of sampling.

sonic anemometers, all of which suffered from difficulties with data acquisition systems. ALPHA-1 gave airborne lidar coverage during 75 experiment hours. WPL's lidar operated reliably except for a few brief periods.

Four of the five meteorological towers, the two electronic weather stations, and the tracer analysis laboratory in Idaho Falls were audited by Meteorological Standards Institute of Fox Island, WA, under subcontract to ERT. The meteorological systems checked out very well except for a few correctible problems with instrument alignments. The results of the audits of the GC lab were also excellent provided that the instrument responses were calibrated with polynomials to account for non-linearities. One potential problem was revealed by the audit in regard to the Mars data logger that had to be used at the No. 4 10-m tower: when this portable system was used to take data during the audit, it showed apparent inaccuracies in analog-to-digital conversion. Unfortunately, Tower 4 was not audited because of time constraints, and the impact of the A-D conversion problem on the measurements was therefore not evaluated. Estimates of the quality of data from this tower will have to be largely subjective for these reasons.

Very high CF_3Br concentrations were sometimes measured in samples from the base of the 150-m tower; only rarely did they occur aloft at the tower-mounted samplers. This pattern suggests the possibility that sometimes Freon leaked from the release system somewhere near the ground. However, an initial examination of CF_3Br concentrations sampled throughout the grid indicated no apparent effect from Freon leaks.

The photography contractor has submitted an archive of more than 11,700 35-mm color slides and 14 VHS videotapes.

Examples of initial analyses of the tracer concentration, photographic, and meteorological data from 20 FSPS hours are given in Section 4. Initial modeling of 14 FSPS hours is described in Section 5.

SECTION 3

DATA ANALYSIS

3.1 Refinement of HBR Meteorological Tower Data

In September 1983, ARLFRD submitted to ERT a database of 1-hr and 5-min values from the tower data acquisition system. The meteorological measurements in this database contained noise. The problems of noise in the raw 1-sec data have been described by Lavery et al. (1983); and the consistent and direction-dependent differences between wind speeds and directions derived from collocated cup-and-vane and propeller anemometer sets have been shown by Strimaitis et al. (1984). In October 1984, ERT decided to process the data using the results of wind tunnel studies of propeller anemometer calibrations and corrections for non-cosine response (Strimaitis et al., 1984) to see if some of the apparent biases could be alleviated at the same time instrument outputs were corrected for alignment errors revealed by the audit performed by TRC Environmental Consultants at HBR. These refinements and examples of their results are discussed here.

3.1.1 Filtering and Flagging Raw Data

ERT filtered and flagged the raw counts data in an effort to reduce the effects of noise on the calculated measurements. The following noise identification procedures were used:

1) Channel-skipping. If the output (in counts) of channels 15 and 16 of a 16-channel multiplexer were the same in a scan, a channel-skip was suspected, and a procedure was invoked to find the channel (from 1 to 15) at which the skip started. This involved calculating the sum of squares of differences between counts in the current scan and the previous scan channel-by-channel, assuming that the skip started at channel 15, then 14, then 13, etc., and finding the channel for which the sum is a minimum. The data were then moved sequentially one channel number higher. The datum from the channel at which the skip started was lost, set to -1 count, and flagged "L."

2) "Reasonable" limits. The range limits of reasonable instantaneous values of instrument outputs are listed in Table 7. This filter captured big spikes.

TABLE 7. FILTER LIMITS FOR TOWER MEASUREMENTS

Instrument type	Range Limits: Lower Limit Counts	Lower Limit Units	Upper Limit Counts	Upper Limit Units	Rate-of-change Limit Counts	Rate-of-change Limit Units
U, V prop	880	-14.0 m/s	3120	14.0 m/s	85	1.06 m/s
W prop	1400	-3.0 m/s	2800	4.0 m/s	100	0.50 m/s
F460 cups	10	0.13 m/s	1120	14.0 m/s	45	0.56 m/s
F460 vane	0	0 degs	4000	540 degs	130	17.55 deg
Fast thermistor	1100	-8.0° C	3100	32.0° C	40	0.80° C
Temperature (RTD)	1100	-8.0° C	3100	32.0° C	30	0.60° C
ΔT (RTD)	40	-4.8° C	3960	14.8° C	120	0.60° C

3) Simple derivative filter, designed to trap short noise bursts by comparison of current value with previous value. If the difference exceeded a pre-set rate-of-change limit for that type of instrument, the datum was flagged "R." The rate-of-change limits are listed in Table 7.

4) Tower noise limit, designed to trap "high-frequency" noise, which looked similar to a sinusoidal oscillation superimposed on the sequence of instrument signals in a scan from a tower. For the data not otherwise flagged as bad, the sum of the absolute values of changes of each channel's output in one scan from that in the previous scan was accumulated, averaged, and compared with a preset limit for the tower. If the average difference exceeded the limit, all the data from that tower and scan were flagged "T."

The limits used in the rate-of-change filter, shown in Table 7, are acknowledged to be generally higher than could be reasonably expected in light of the mechanical and electronic response of the instruments to likely changes in the atmosphere, particularly for the steel-encapsulated platinum resistance temperature probes (RTDs), whose time constant probably exceeds five seconds. The limits are rather the result of trial and error with less lenient filters that removed excessive amounts of data because of continuous high-frequency "ripple" in the signals; in short, they are compromise values.

The filtering and flagging process produced a new 1-sec database of flagged values in counts, which has been retained in tape copies by ERT. The flags and their meanings follow:

" "	(blank)	good data
"O"		Over maximum range limit
"U"		Under minimum range limit
"L"		Lost (first affected channel in channel-skip)
"M"		Moved (reassigned from previous channel by skip-correction)
"T"		Tower noise limit exceeded
"S"		Several (more than one) flags from the above

Only the " " and "M" flags indicate good data.

Some noise remains in the 1-sec data even after the filtering procedure. In the Tower A data for Experiments 4 through 6, there is probably a ripple having an amplitude on the order of 0.1 VAC, which overpowers the variability in most of the instrument signals and degrades the usefulness of the turbulence data. The data from the other towers seem not to be so affected, perhaps because they were communicated to the central collector by radio rather than cable.

3.1.2 Correction of Signals

Corrections to the tower instrument signals have been made on the basis of the audit results and the cosine response characteristics of the fixed axis propeller (UVW) anemometers (Strimaitis et al., 1984). No corrections have been made to either the propeller or cup data on the basis of wind tunnel calibrations of these instruments since they appear to be within a few percent of the manufacturer's standard transfer functions used in the signal processing. Neither have corrections been made for tower wake effects, although these are certainly substantial, apparently amounting to up to 40 percent speed deficit for Tower A (See SHIS #1 QA Report). Instruments were mounted on the towers on booms extending in directions away from wakes when winds were blowing from the release area to the ridge so that the data would not be adversely affected during "modelable" hours. However, the lower levels (up to 5 m; sometimes higher) on Towers A and B often showed decoupled drainage winds in strongly stable periods even when the winds aloft were blowing towards the Hogback, and consequently these instruments were sometimes in wakes.

Table 8 lists changes made to instrument output during calculation of 5-min and 1-hr average values to improve their accuracy by correcting for electronic misalignment and audited errors in orientation to true north. Tower C propeller data were not corrected for orientation because audit results conflicted with visual observations. Both agreed that errors were less than 3 degrees in any case. The propeller anemometer data were corrected by iterative applications of the cosine response corrections at every 1-sec scan, provided both horizontal props showed good data. The iterations were terminated when the wind direction resolved from the corrected components changed less than one degree from one iteration to the next. The W-prop signal was corrected similarly after the horizontal wind was corrected to provide a basis for estimating angle of attack.

3.1.3 Calculation and Flagging of Averaged Measures

Five-minute and one-hour averaged values of 250 measures were calculated from the corrected and flagged 1-sec data. Only "good" data, flagged " " or "M," were used in these calculations, and all instrument inputs to each measure had to be "good" for a scan to be used in the measure's averaged value.

Measures were calculated according to the formulas given in the SHIS #2 Work Plan with one exception for wind direction variability. The standard deviation of wind direction from the F460 vanes was calculated in two ways. One method, denoted "sdx2," was a simple standard deviation of the voltage signal; the other, "sdx1," followed the procedure recommended by Yamartino (1984), a single-pass method which accounts for discontinuities in vane output and retains its precision when variability is high. The simple method was used only to provide data for comparison with Yamartino's method for periods when the vane's range was less than 180° and it didn't switch potentiometers. Standard deviation of wind direction from propeller anemometers, "sd," was calculated only by the Yamartino method.

TABLE 8. CORRECTIONS MADE TO INSTRUMENT OUTPUTS

Tower A	Level (m)	U-prop	V-prop	W-prop	Orientation	T or ΔT
	2	-.06 m/s	-.06 m/s	0.00 m/s	-2 deg	-.07° C
	5	-.09	-.08	-.03	1	0.00
	10	-.04	-.08	-.04	1	-.08
	20	-.07	-.04	-.01	0	-.05
	30	-.06	-.06	-.05	-1	-.05
	40	-.05	-.02	-.01	-2	-.04
	60	-.05	-.05	-.02	-6	-.05
	80	-.12	-.07	-.05	-6	-.04
	100	-.06	-.06	-.02	-5	-.04
	150	-.09	-.08	-.05	-3.5	-.08

Level (m)	Cups	Vane
20	-.02 m/s	1 deg
40	-.03	-1.5
60	-.02	3.5

Tower B	Level (m)	U-prop	V-prop	W-prop	Orientation	ΔT
	5	-.21 m/s	-.18 m/s	-.09 m/s	1 deg	-.16° C
	20	-.23	-.17	-.09	1	-.13
	30	-.19	-.18	-.10	1	-.13

Level (m)	Cups	Vane	T or ΔT
1	-.18 m/s	-1 deg	-.04° C
10	-.20	0	-.05
30	-.22	0	-.13

Tower C	Level (m)	U-prop	V-prop	W-prop	Orientation	T or ΔT
	2	-.15 m/s	-.14 m/s	-.04 m/s	0	-.03° C
	5	-.16	-.16	-.08	0	-.09
	10	-.18	-.17	-.09	0	-.03

Tower P	Level (m)	Cups	Vane	T or ΔT
	9	-	-	.09° C
	18	-.02 m/s	1.5 deg	-
	61	0.00	6	.06

Flags were assigned to the averaged data values on the basis of the number of "good" data points in the values. For 5-min data, there are a possible 300 points; for 1-hr data, 3600. A value was flagged "E" (Excellent) if it incorporated at least 97 percent of the possible 1-sec values; " " (blank or good) if between 75 and 97 percent; "S" (Suspect) if between 50 and 75 percent; and "B" (Bad) if less than 50 percent.

3.1.4 Comparison of Measures from Collocated Systems

Plots of measures from collocated systems are useful for comparison of instrument performance in terms of low-speed response, relative precision, and in the case of HBR, the effects of noise on the output values. Plots of this sort are shown in this section, and inferences are made in regard to data quality. Only 5-min averaged data flagged "blank" or "E" are used in these comparisons.

Figure 7 is a time series plot of σ_w both from the sonic and from the propeller anemometer sets at 40 m on Tower A during Experiment 6. The propeller anemometer trace shows no particular correlation with the sonic, which it quite generally exceeds by about 0.2 m/s. This increase in variance corresponds to roughly 0.07 VAC RMS or 0.1 VAC amplitude, the "AC ripple" noted by field personnel at the time. Figure 8 is a similar plot of data from Experiment 12, which was conducted after the completion of the noise suppression work. Here the two traces correspond much more closely. ERT's field people at the time reported an AC ripple of about 3 mV amplitude, which corresponds to only about .01 m/s in σ_w. The noise remaining in the prop output from all sources no longer overpowers the atmospheric component, and the trace follows the sonic trace quite well. One may infer from these plots that the turbulence data from the Tower A props are of no practical use in Experiments 4 through 6 but provide a reasonable basis for estimation of atmospheric turbulence thereafter.

Figures 9 and 10 correspond to 7 and 8 but are traces of the σ_w's from 5 m on Tower A rather than 40 m. For the earlier experiment (Figure 9) the large up and down movements in the prop traces at 5 m track those at 40 m (Figure 7) very well, as would be expected if the bursts of noise are consistent on Tower A. Figure 10 shows that the fraction of the vertical turbulence measured by the props is smaller at the lower level. This effect is probably due to the suppression of low frequency eddies by the closeness of the ground; a larger percent of the spectral energy is in high frequency motions to which the propeller systems don't respond.

These plots imply that the quality of the turbulence data from the propeller anemometers could be improved substantially by application of corrections to bring them into better agreement with the sonic data. Such corrections have not been applied to the values submitted in the data base so that individual users may make adjustments at their own discretion. A correction factor of 1.5 or so would seem to get the data within about 20 percent of the sonic values almost all the time, at least for this experiment. A somewhat smaller correction would be appropriate at 40 m.

Figure 11 is a plot of the σ_v data at 40 m during Experiment 12 and corresponds therefore to the σ_w plot in Figure 8. The fraction of crosswind turbulence captured by the props is shown to be

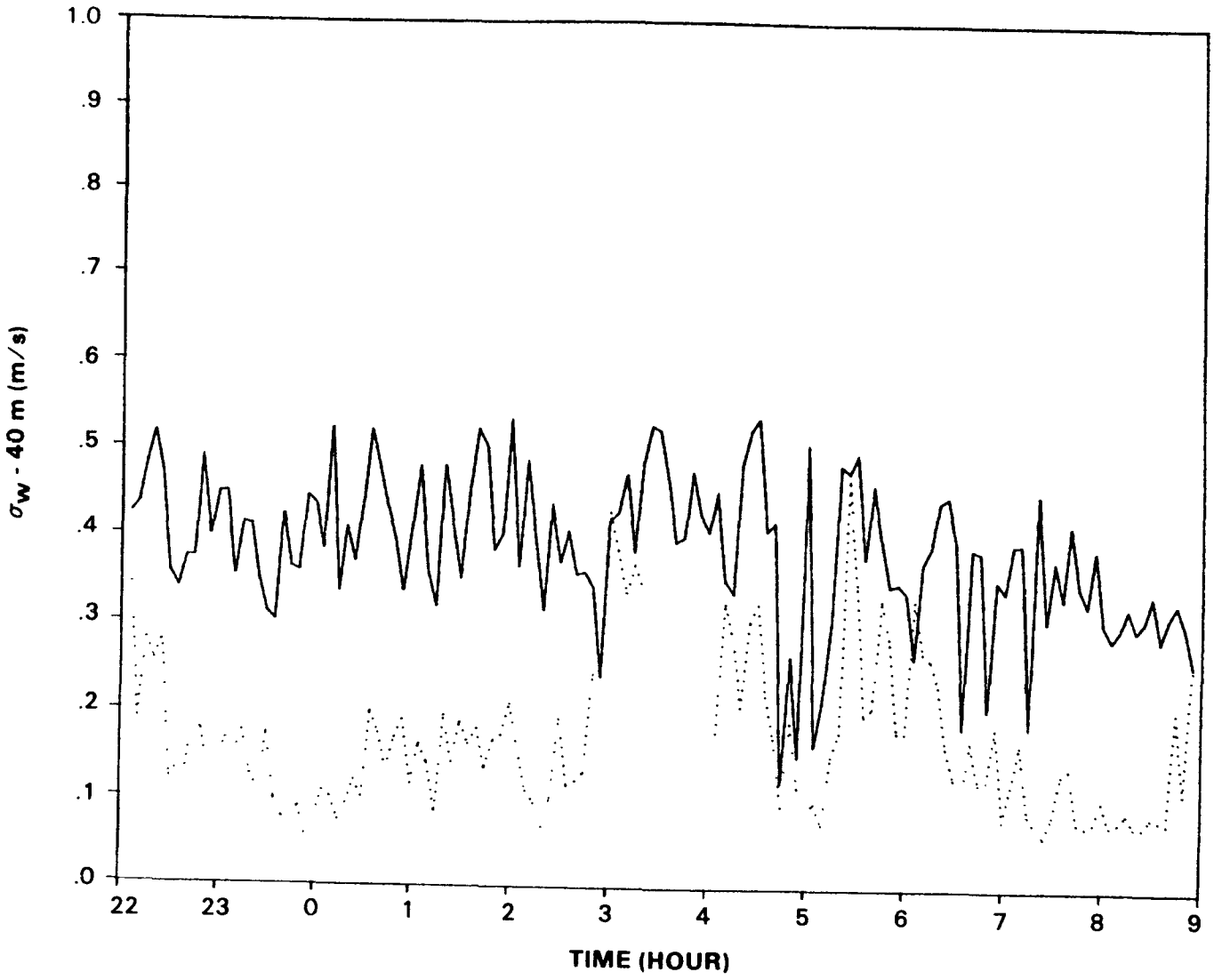

Figure 7. Time series of sonic (....) and propeller (____) σ_w data from 40 m Tower A during Experiment 6.

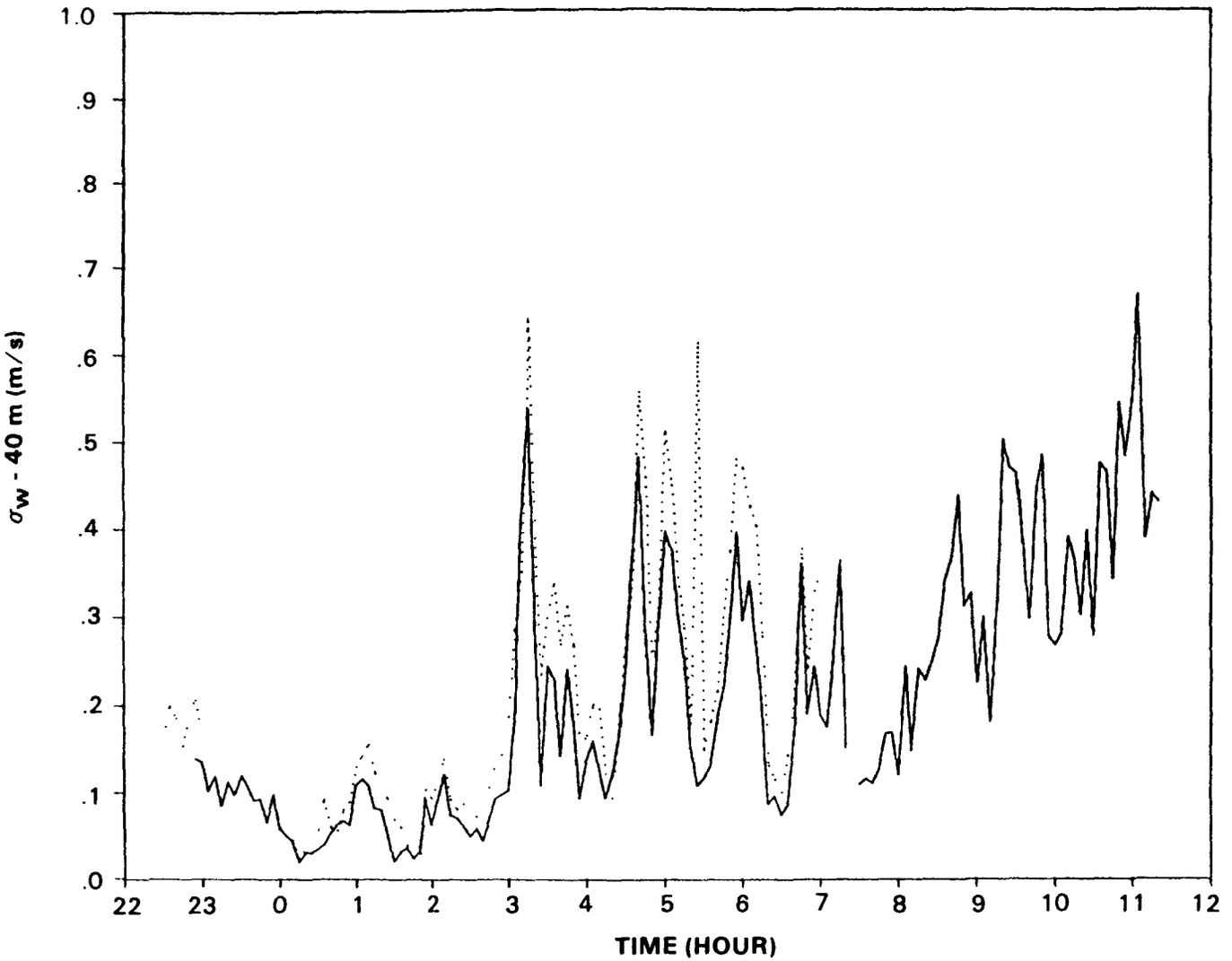

Figure 8. Time series of sonic (....) and propeller (_____) σ_w data from 40 m, Tower A during Experiment 12.

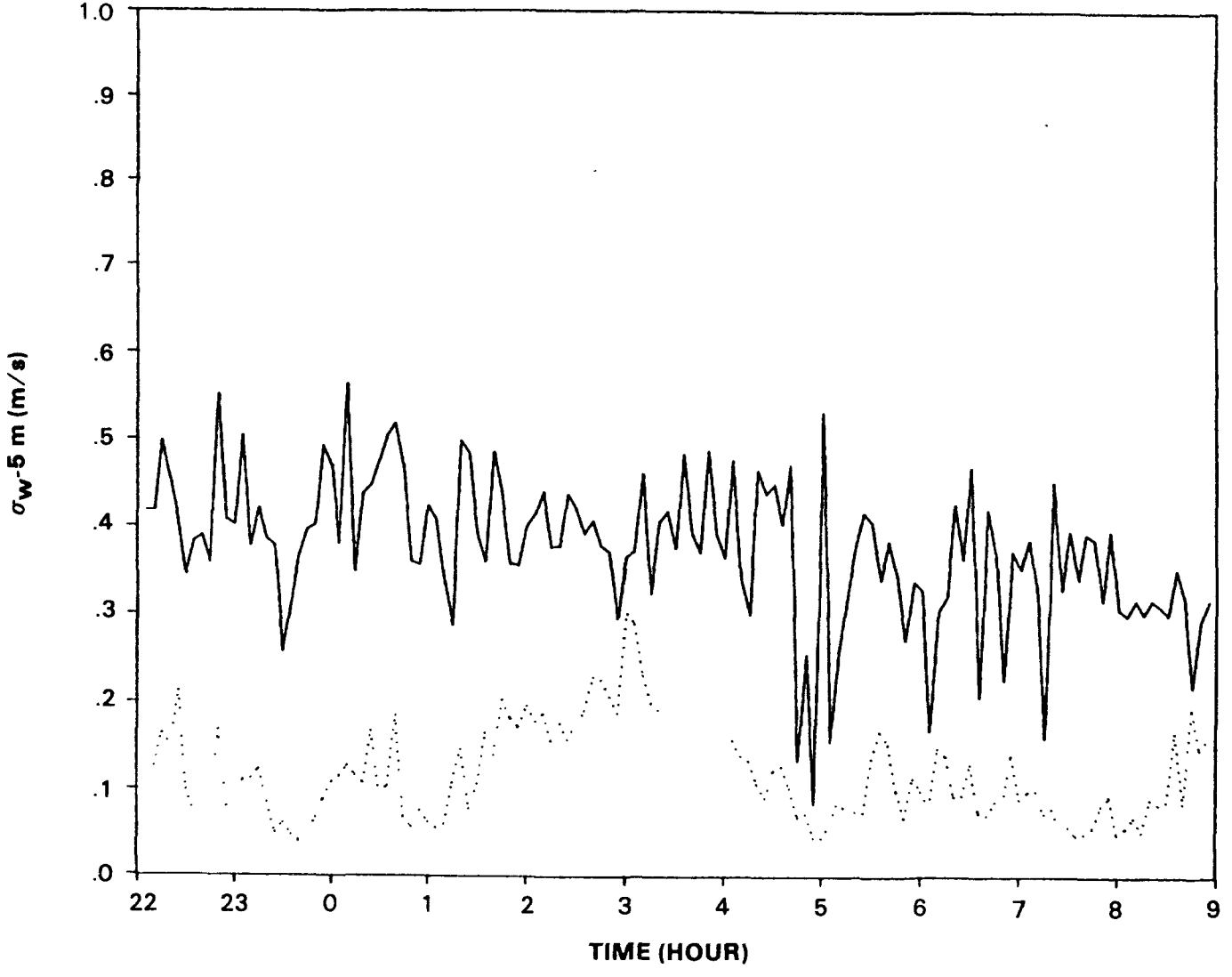

Figure 9. Time series of sonic (....) and propeller (____) σ_w data from 5 m, Tower A during Experiment 6.

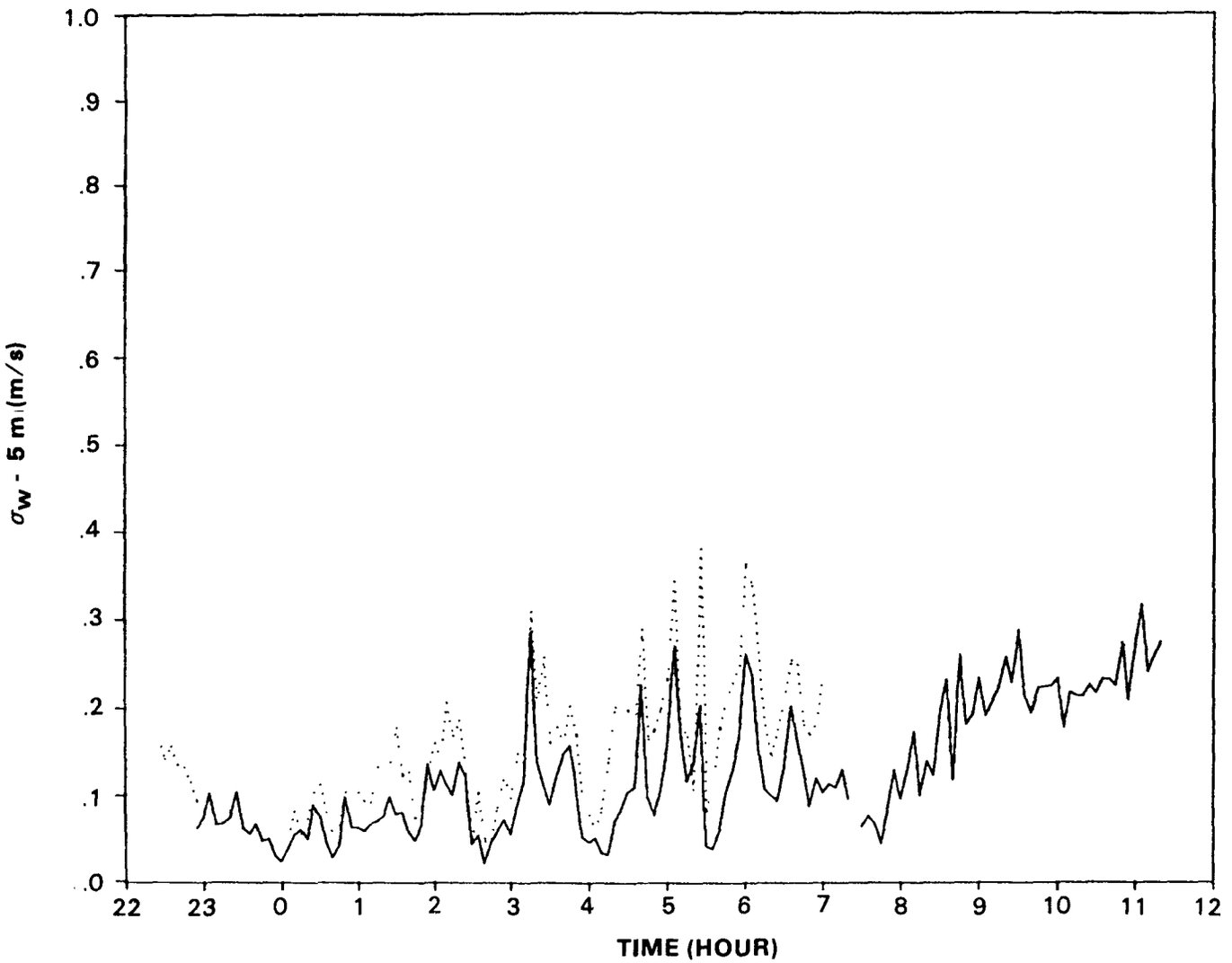

Figure 10. Time series of sonic (....) and propeller (____) σ_w data from 5 m, Tower A during Experiment 12.

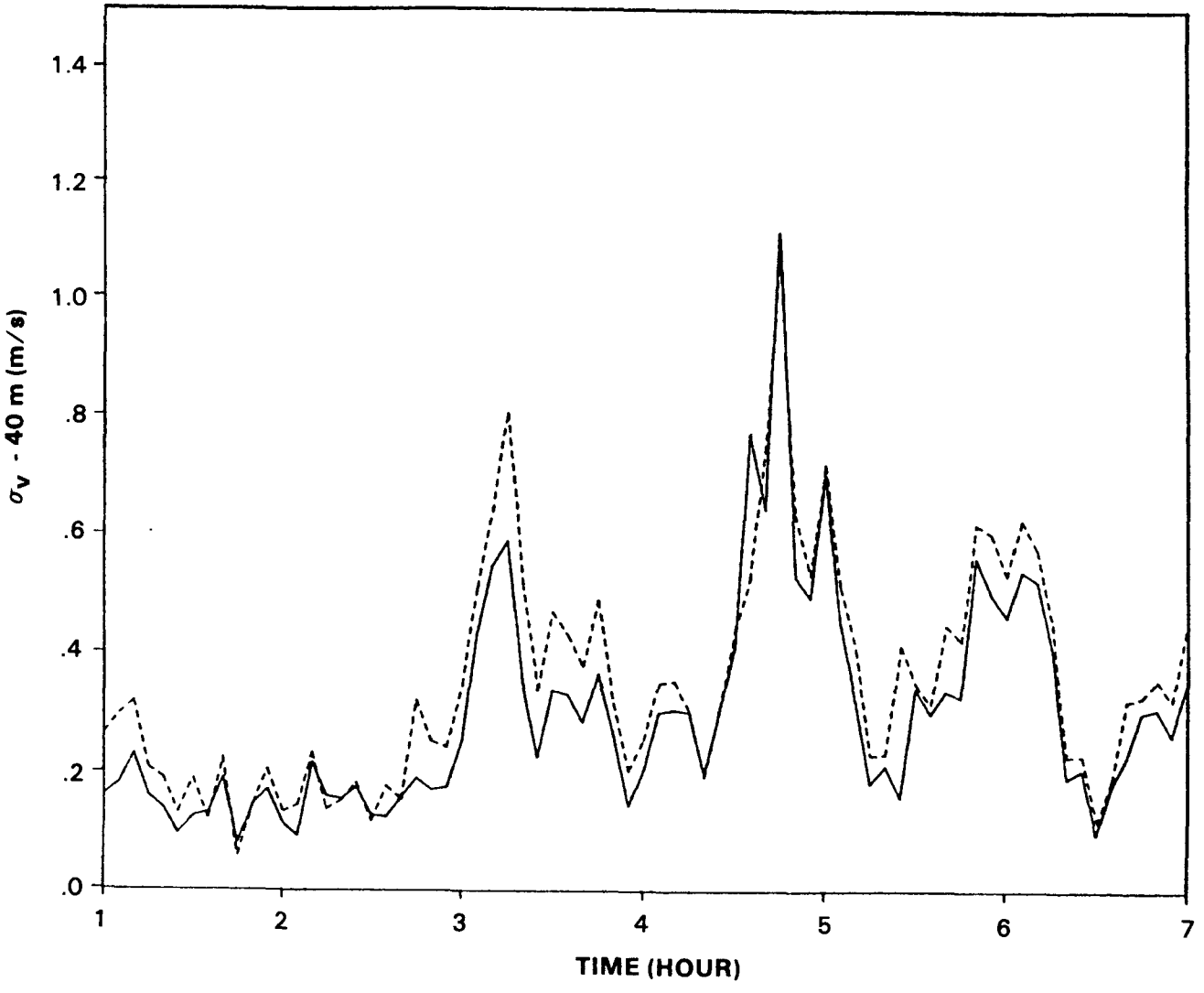

Figure 11. Time series of sonic (----) and propeller (____) σ_v data from 40 m, Tower A during Experiment 12.

a little higher than the fraction of vertical turbulence. Note that the spike in the vertical sonic trace (Figure 8) at 0520 hrs that is not tracked by the prop occurred at a time when both the σ_v traces are fairly quiescent, whereas the other peaks in the sonic σ_w correspond to peaks in the prop σ_w and in both prop and sonic σ_v traces. This observation suggests that perhaps the peak in the sonic σ_w is due to some effect of noise.

The noise in the early experiments also degraded mean values. Mounted at 40 m on Tower A were one of WPL's sonic anemometer systems, an F460 cup and vane system, and a triaxial propeller anemometer set. This configuration allows intercomparison of the mean wind speeds and directions determined from the three systems. In principle, the sonic system is close to an absolute standard because of its rapid response and insensitivity to calibration errors provided the output is properly zeroed and the A-to-D conversion is accurate. The HBR systems were not entirely free of noise, however. The comparisons that follow are based on vector resultant mean speeds and directions produced both by the sonic anemometers and the mechanical systems.

Figure 12 is a plot of the differences between 5-min average prop-derived wind direction D and sonic-derived wind direction DS as a function of DS; data are from 40 m on Tower A during Experiments 4 through 6. The plot symbols indicate three wind speed categories according to the sonic output. For the few 5-min periods with wind speeds in excess of 3.0 m/s (triangles plotted near 60 deg and 300 deg), the prop direction is within 15 deg of the sonic. The lighter winds show more scatter. Figure 13 is a corresponding plot of the differences between vane and sonic directions showing very much less scatter in the lighter winds. The differences between vane and prop directions for these experiments, plotted in Figure 14, show somewhat less scatter than the sonic and prop differences in Figure 12. The smaller number of points in Figure 14 with speed less than 1 m/s results from the fact that the cup speeds generally exceed the sonic speeds, particularly in light winds.

Figures 15 through 17 display the differences between sonic (SS), prop (S), and cup (SX) vector resultant speeds for Experiments 4 through 6. These plots indicate that the cups generally yielded speeds greater than either the prop or the sonic system, particularly in light winds. For higher speeds, all three plots have about the same scatter, with the props tending to agree less well than the cups with the sonic data.

Experiments 7 and 8 were performed during an intermediate period when certain grounding and other wiring improvements had been made to the central data collection system, but the noise suppression efforts were not completed. The prop data from Tower A were particularly noisy in Experiment 9, there are no sonic data from Experiment 7, and the 40-m V-prop transmitter appears to have suffered a partial failure in Experiment 15. These various anomalies affect what data are most appropriately included in comparisons for the later experiments.

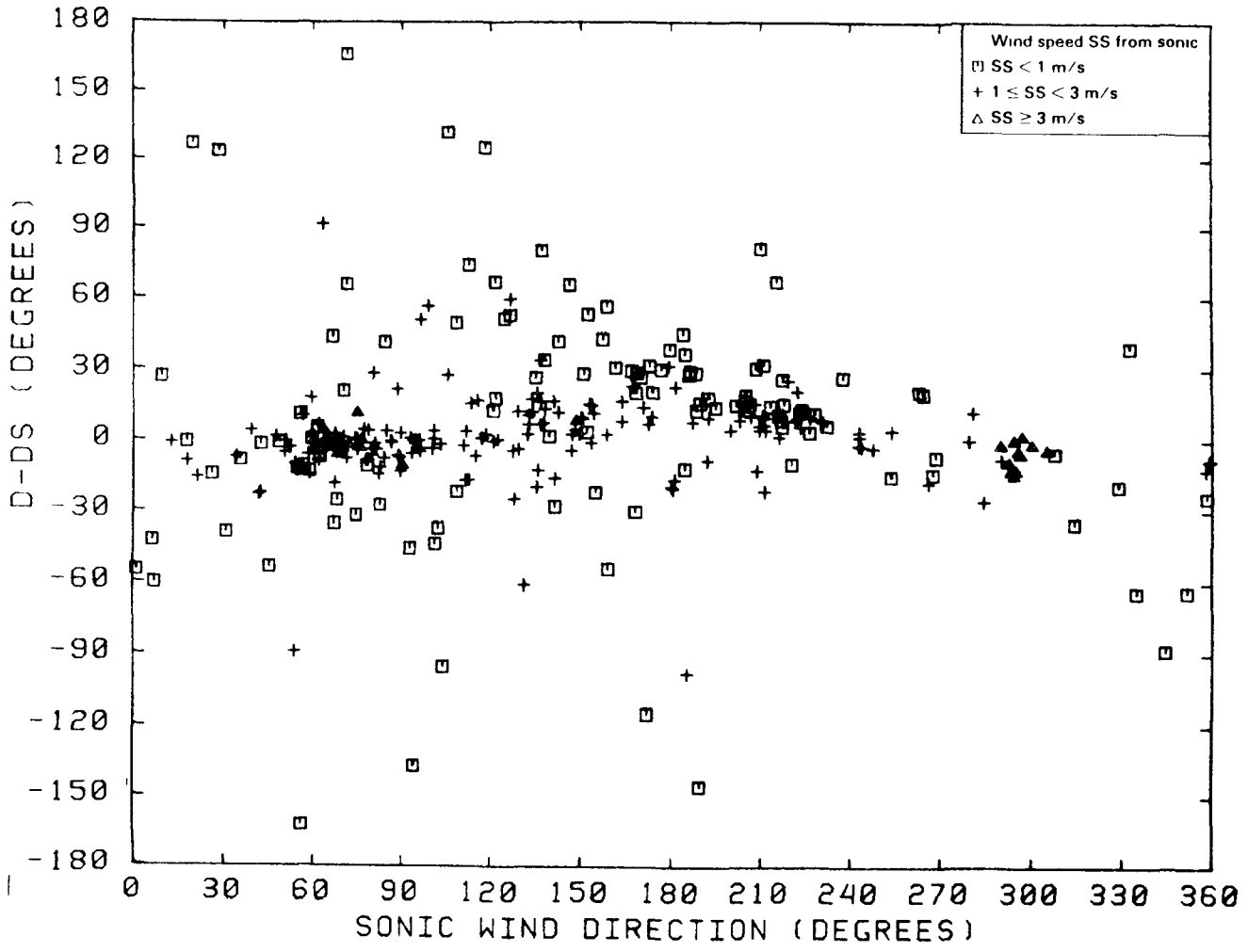

Figure 12. Differences between prop-derived wind direction D and sonic-derived wind direction DS vs. DS for Experiments 4 to 6 from 40 m, Tower A

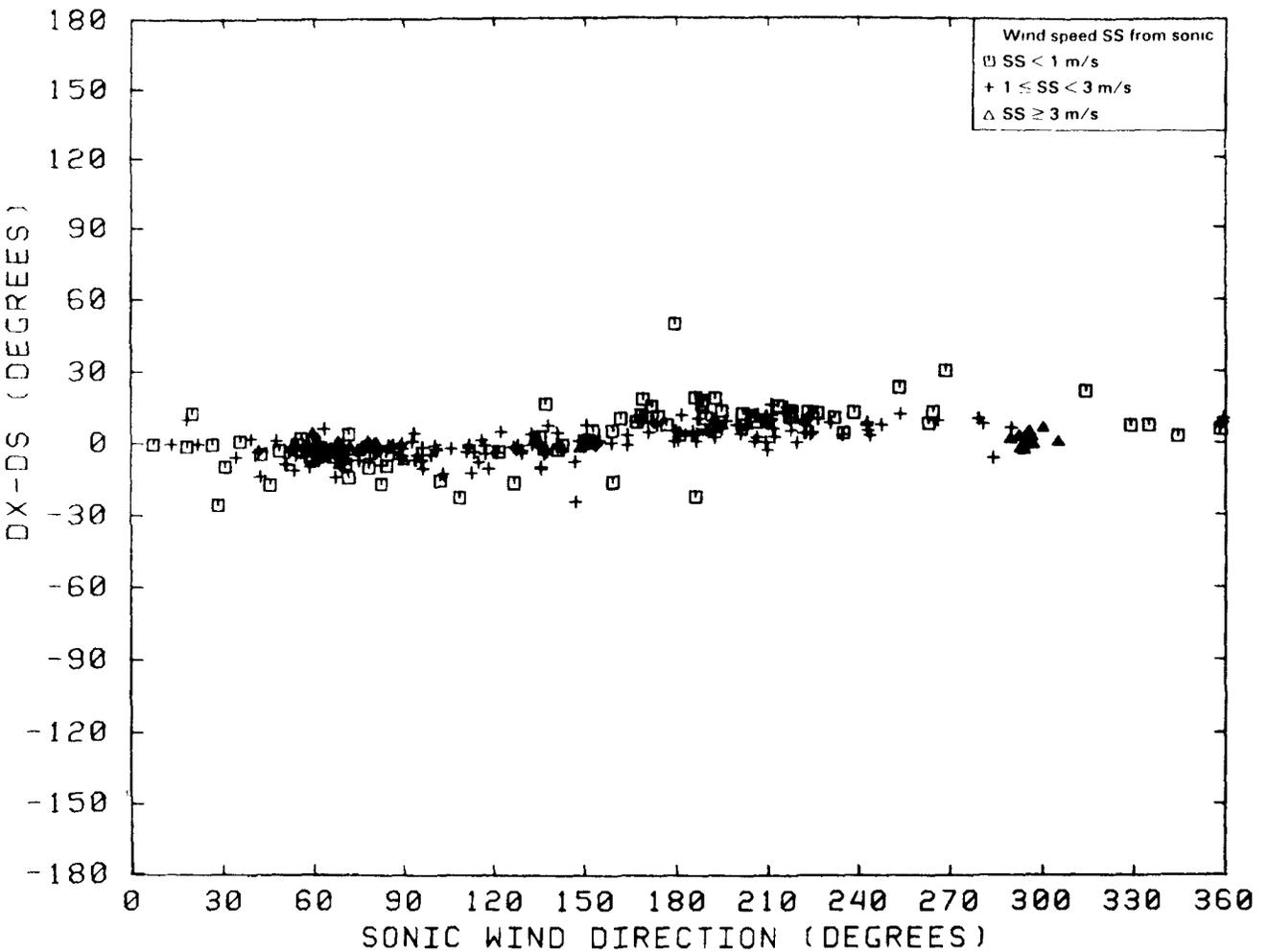

Figure 13. Differences between vane (DX) and sonic (DS) wind direction vs. DS for Experiments 4 to 6 from 40 m, Tower A.

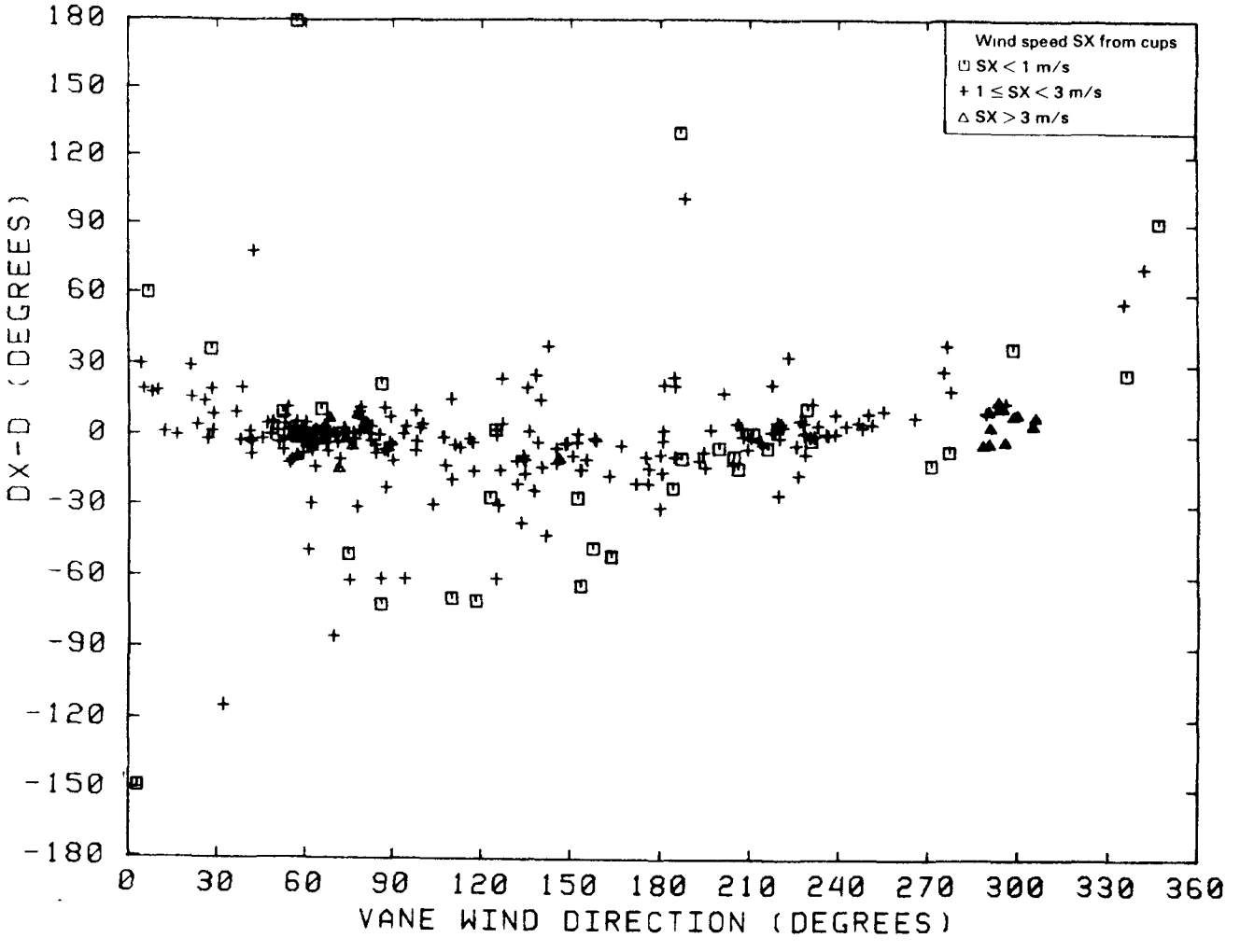

Figure 14. Differences between vane (DX) and prop (D) wind direction for Experiments 4 to 6 from 40 m, Tower A.

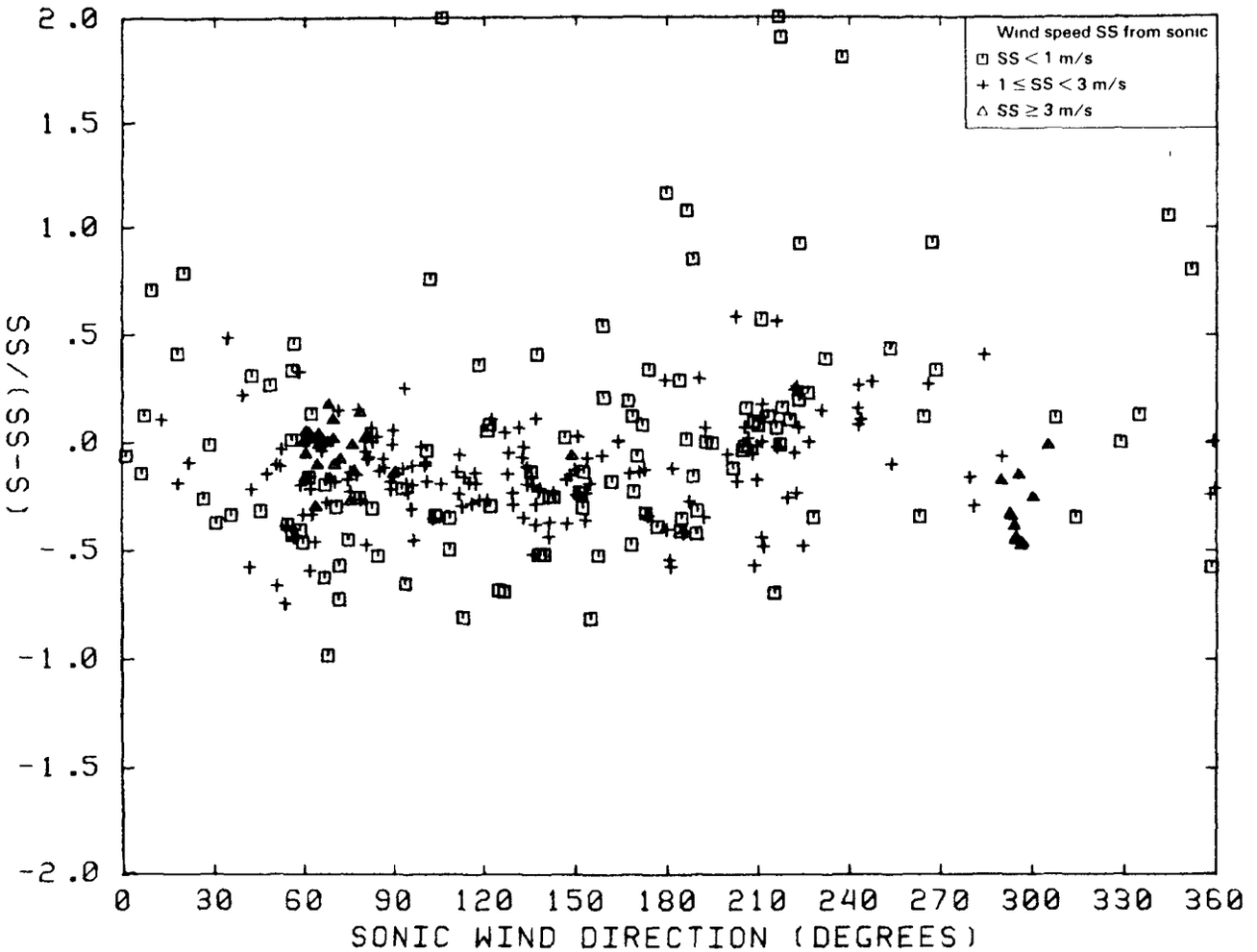

Figure 15. Differences between prop speeds (S) and sonic speeds (SS) as fraction of SS vs. sonic direction for Experiments 4 to 6 from 40 m, Tower A.

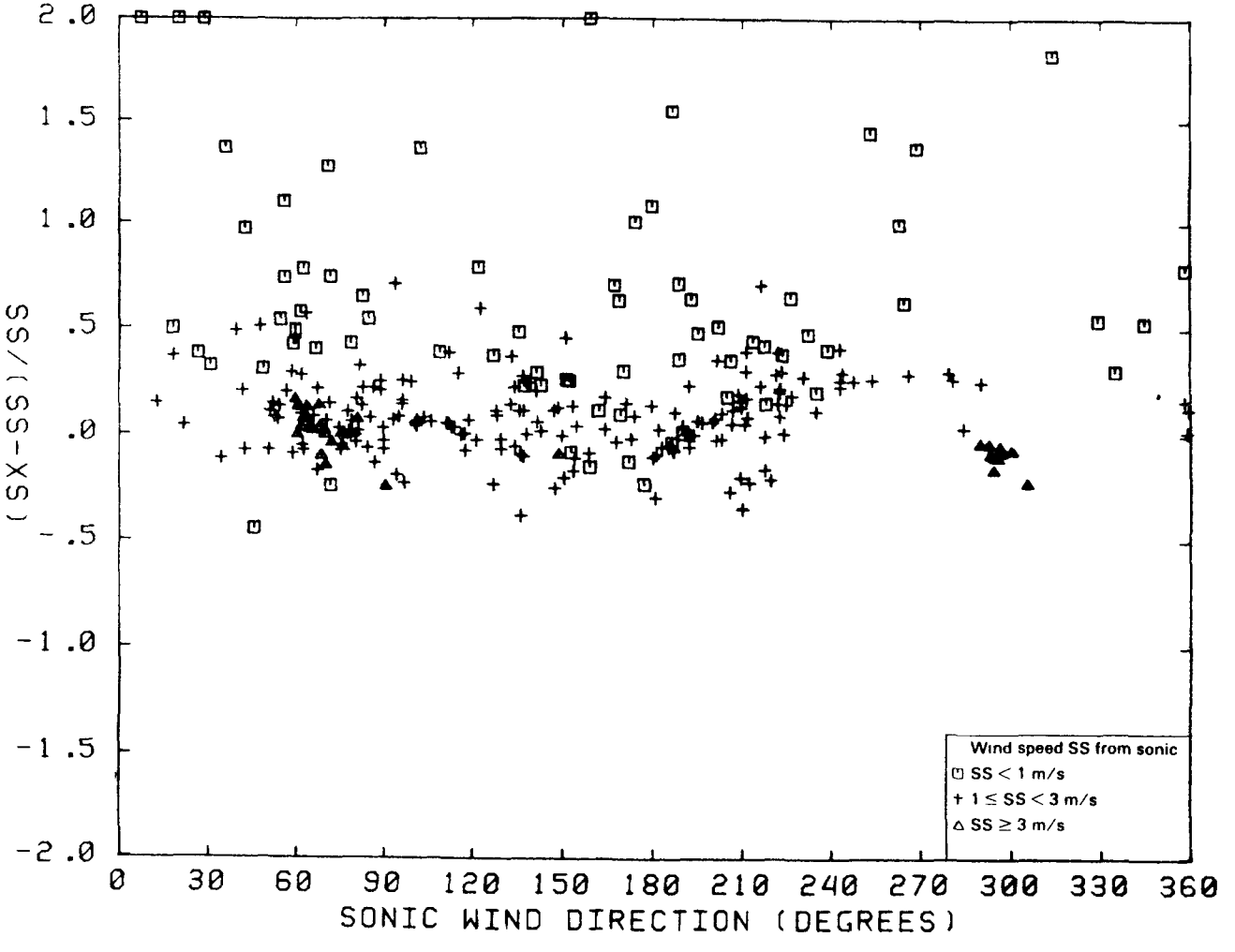

Figure 16. Differences between cup speeds (SX) and sonic speeds (SS) as fraction of SS vs. sonic direction for Experiments 4 to 6 from 40 m, Tower A.

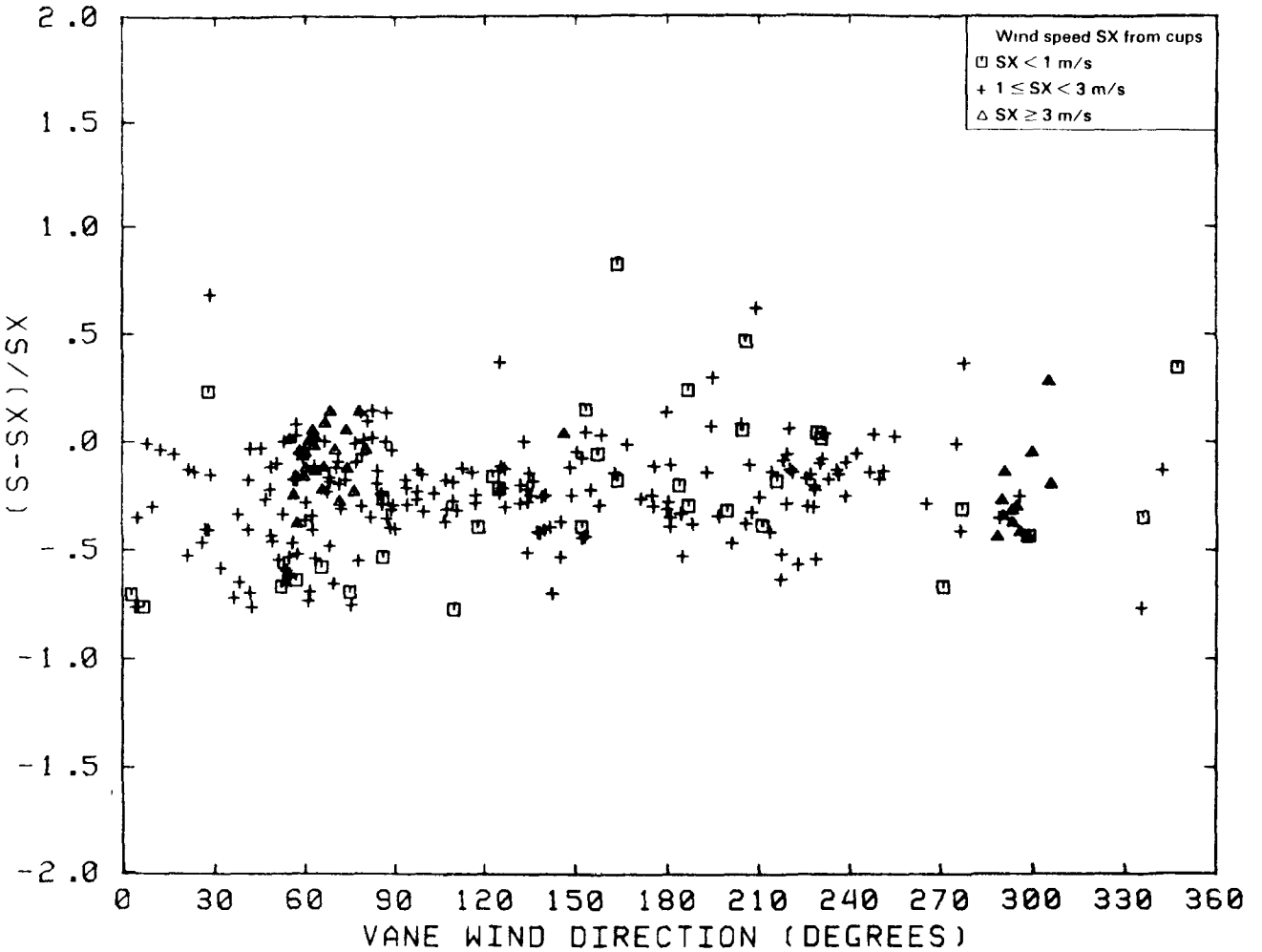

Figure 17. Differences between prop speeds (S) and cup speeds (SX) as fraction of SX vs. vane direction for Experiments 4 to 6 from 40 m, Tower A.

Differences between vane and sonic directions and between cup and sonic speeds at 40 m are plotted in Figures 18 and 19 respectively for Experiment 8. Prop and sonic comparisons are similar for this experiment. These plots show a larger degree of scatter than those for the earlier experiments in spite of the reduction of high frequency noise in the central data system evidenced in the σ_T and σ_w values. The prop and cup-and-vane data agree with each other quite well for this experiment, so the problem might be in the sonic data.

The success of the noise reduction efforts in improving the quality of the mean tower measurements is clear in the plots of data from the later experiments (10 through 14). Figures 20 through 22 correspond to the earlier plots in Figures 12 through 14. With a few exceptions, even the data for speeds less than 1 m/s agree within about 10 deg for all three systems. There is an apparent relative bias of about 3 to 5 deg between the sonic and cup-and-vane systems, with the sonic system yielding the larger wind direction. With this bias removed, the great majority of the points for speeds above 1 m/s and for "modelable" periods (winds from 60 to 150 deg) indicate a relative uncertainty of about 5 deg or less.

Wind speed comparisons for the later experiments are plotted in Figures 23 through 25. In very light winds, the cups' speeds were up to 80 percent higher than the sonics' speeds (Figure 23). As the speed increases, the agreement between the two systems improves as expected, until the relative uncertainty is reduced to about 5 percent in the "modelable" directions. The differences between the prop and sonic speeds are similarly scattered (Figure 24). The props yield a smaller fraction of the sonic speed as the speed decreases. At higher speeds, the prop data tend to be about 5 to 10 percent lower than the sonic. The comparison of cup and prop speeds in Figure 25 shows that the cup speeds are almost universally higher than the props. In very light winds, the cup speeds may be as much as twice as high as the props. At higher speeds and in "modelable" directions, the difference reduces to about 10 percent, as it does in the comparison of sonic and prop speeds.

If it is assumed that the sonic data are generally the most accurate of the outputs from the three collocated systems because the sonic sensors are the most responsive (and may have suffered least from noise), then it would appear that the propeller data are up to 10 percent low at speeds of about 3 m/s or more. The cups, on the other hand, are generally more accurate at the highest range of speeds. Part of the overestimate by the cups at low speeds is due to the zero offset of 0.22 m/s in the cup transfer function; it is likely that the winds at the Hogback were frequently lighter than this, at least for some times during a 5-min averaging period. In fact, in the data presented here, some of the 5-min vector averages from the sonic anemometers are below 0.1 m/s. Nonetheless, the cups' offset alone doesn't account for their averaged responses being consistently higher than the props', nor do the calibrations used. This discrepancy between cup and prop speeds corroborates the inference drawn from comparison of sonic and prop speed; that is, prop speeds may be low.

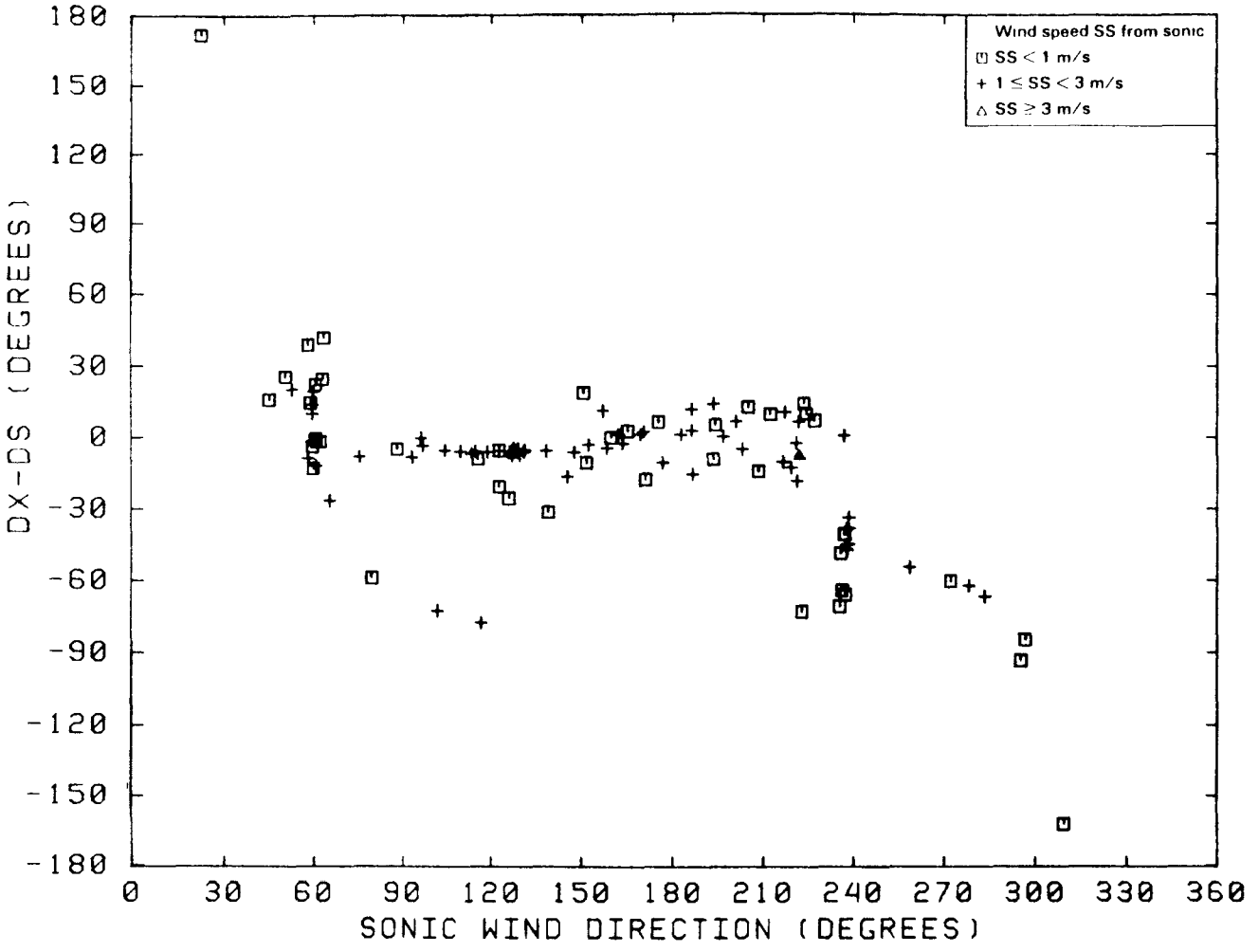

Figure 18. Differences between vane (DX) and sonic (DS) wind direction vs. DS for Experiment 8 from 40 m, Tower A.

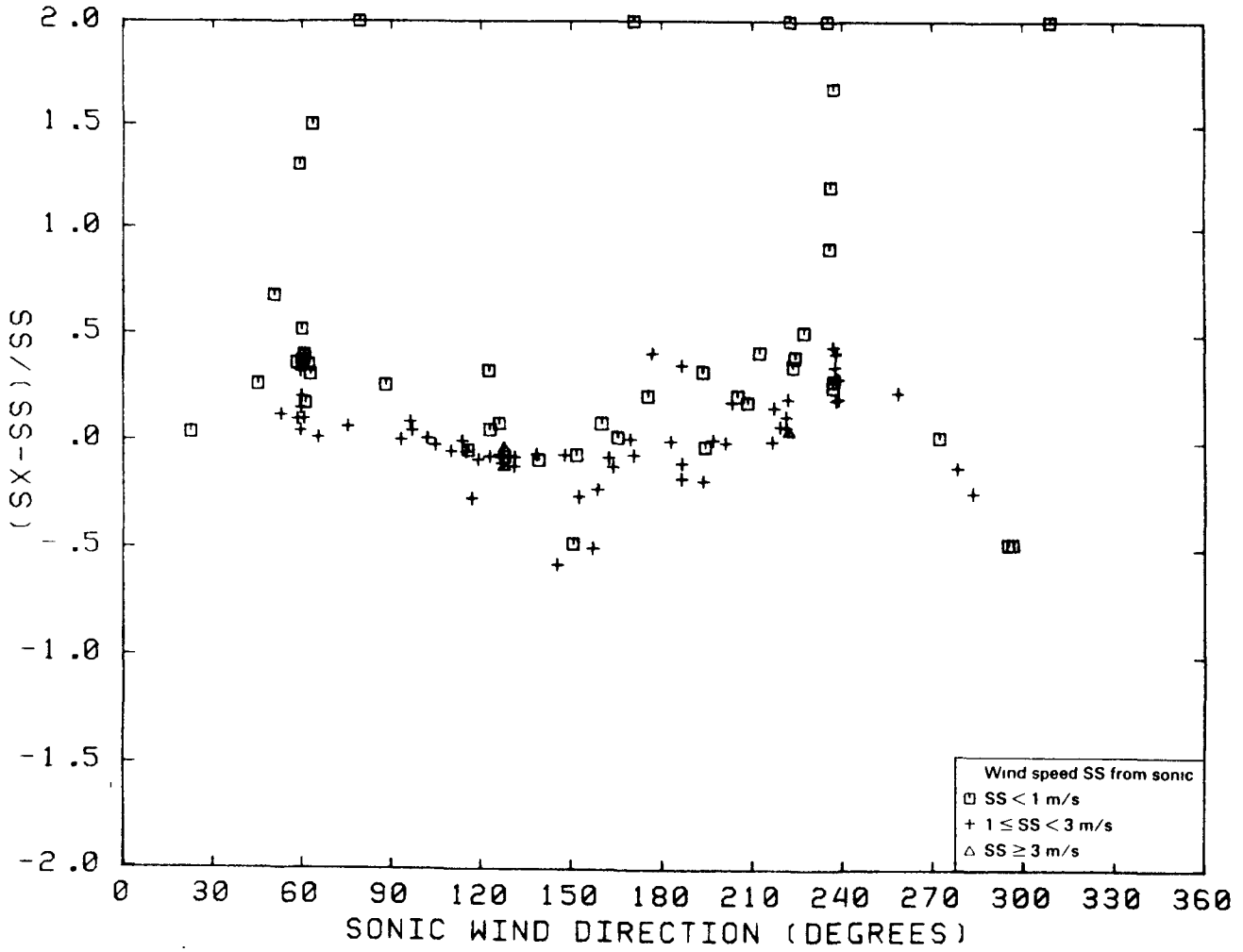

Figure 19. Differences between cup speeds (SX) and sonic speeds (SS) as fraction of SS vs. sonic wind direction for Experiment 8 from 40 m, Tower A.

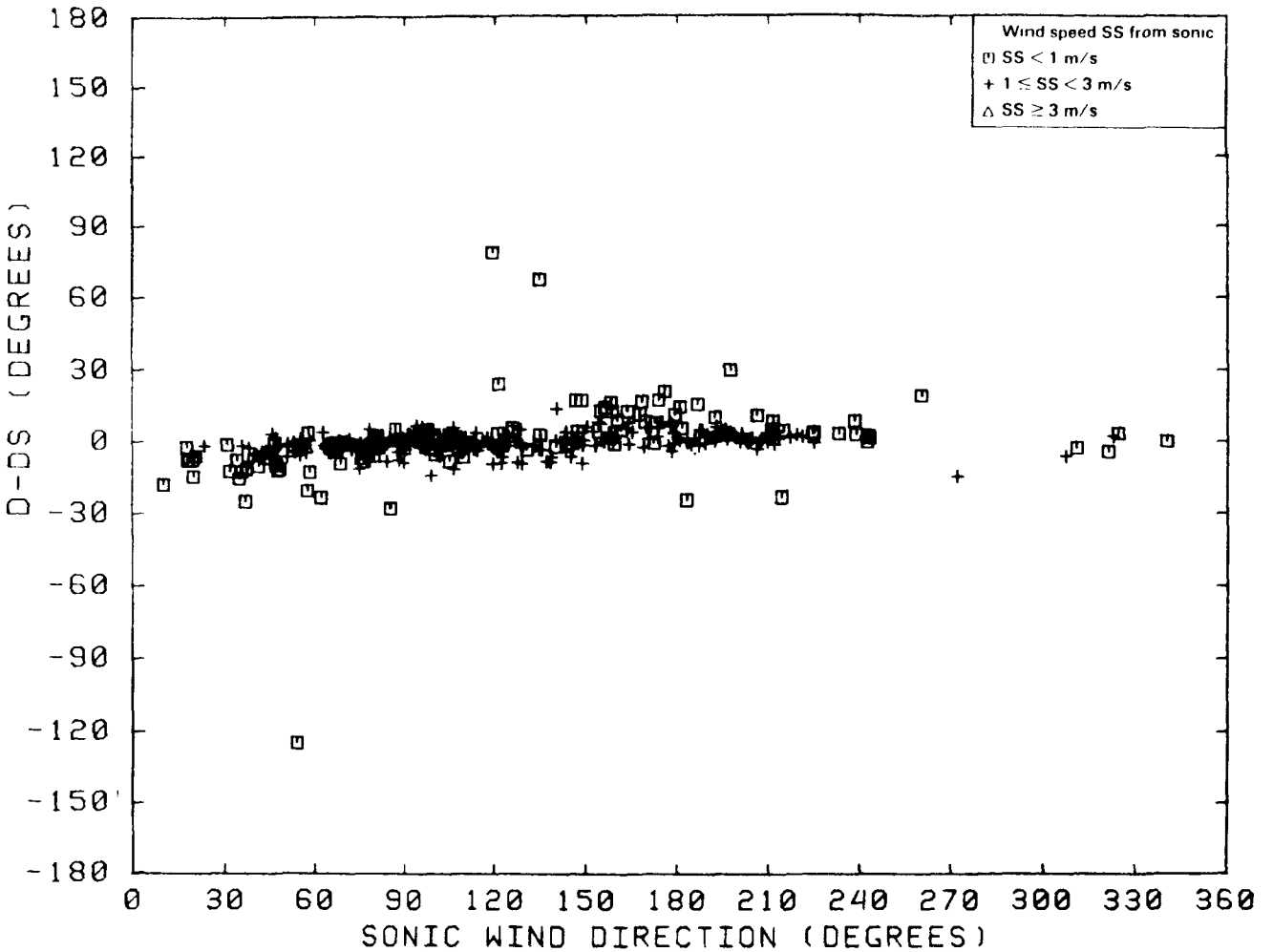

Figure 20. Differences between prop direction (D) and sonic direction (DS) vs. DS for Experiments 10 to 14 from 40 m, Tower A.

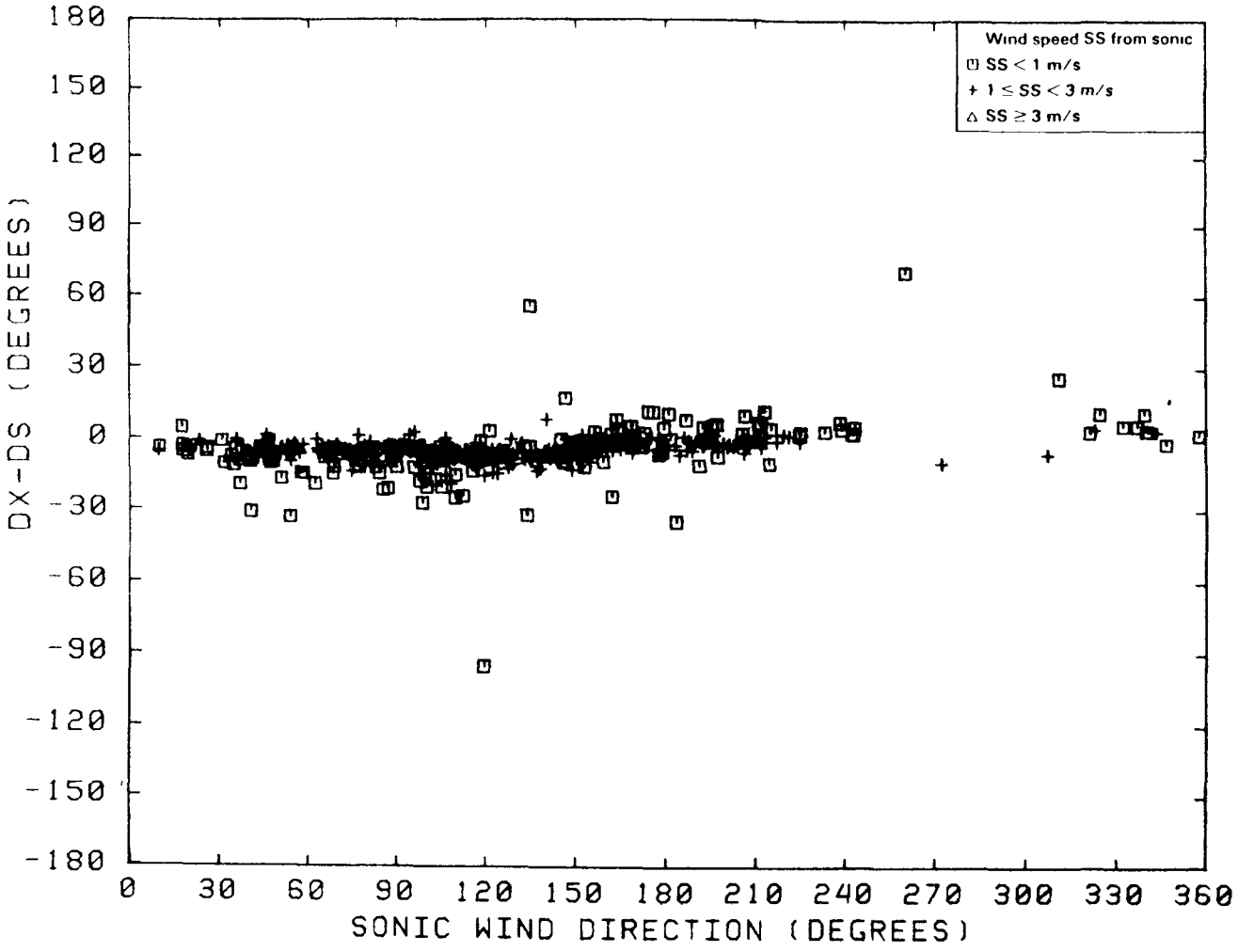

Figure 21. Differences between vane direction (DX) and sonic direction (DS) vs. DS for Experiments 10 to 15 from 40 m, Tower A.

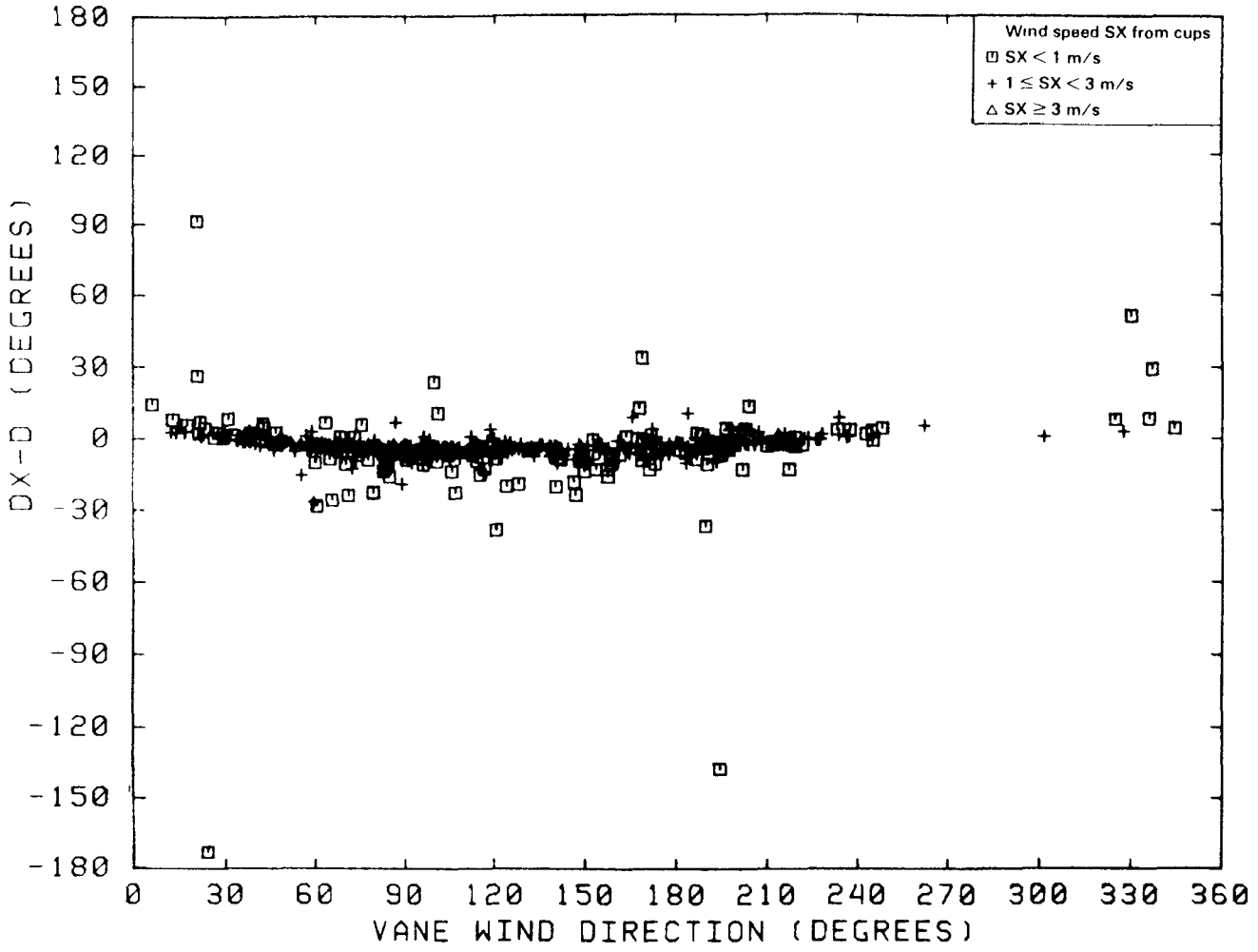

Figure 22. Differences between vane direction (DX) and prop direction (D) vs. DX for Experiments 7 to 14 from 40 m, Tower A.

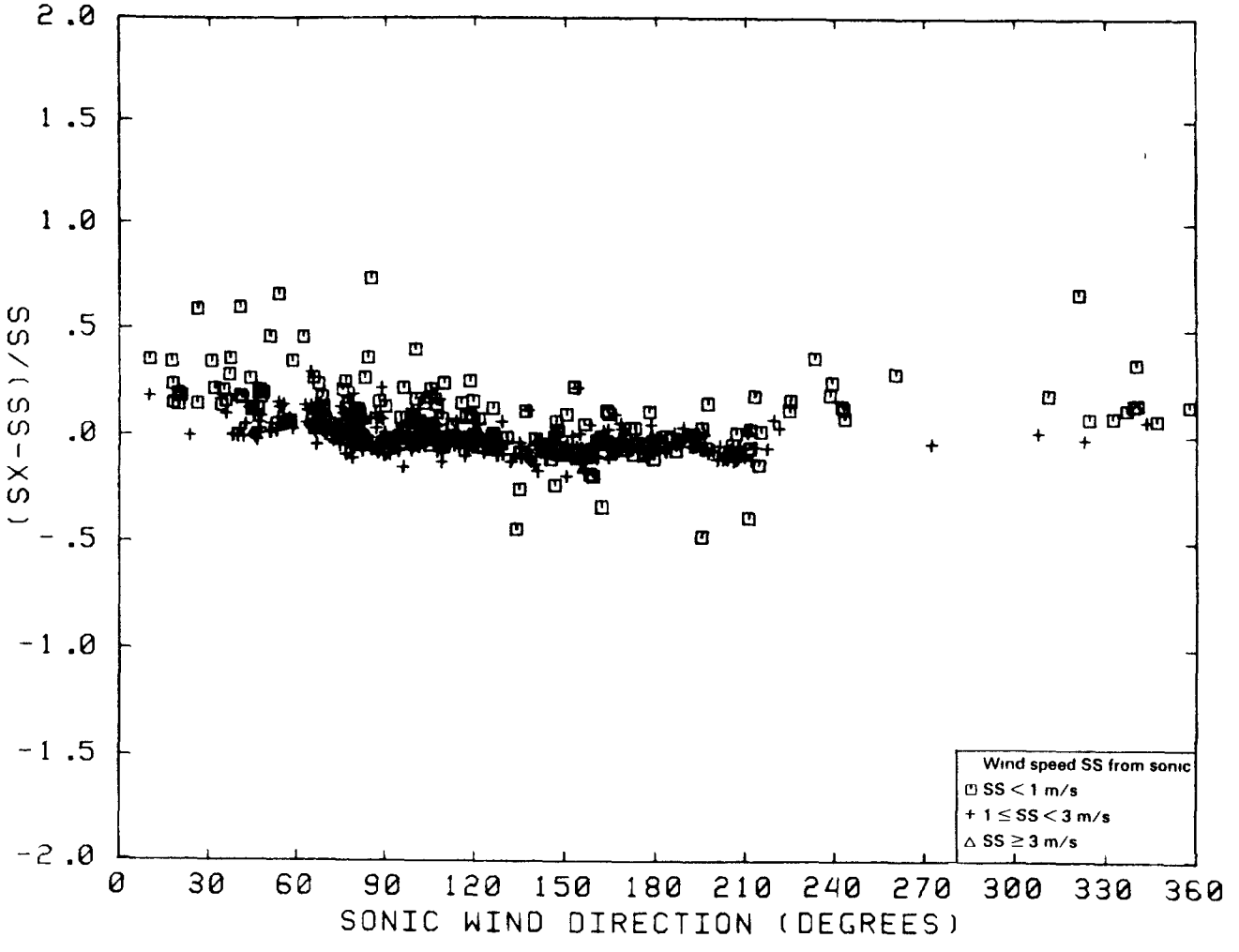

Figure 23. Differences between cup (SX) and sonic (SS) wind speeds as a fraction of SS vs. sonic direction for Experiments 10 to 15 from 40 m, Tower A.

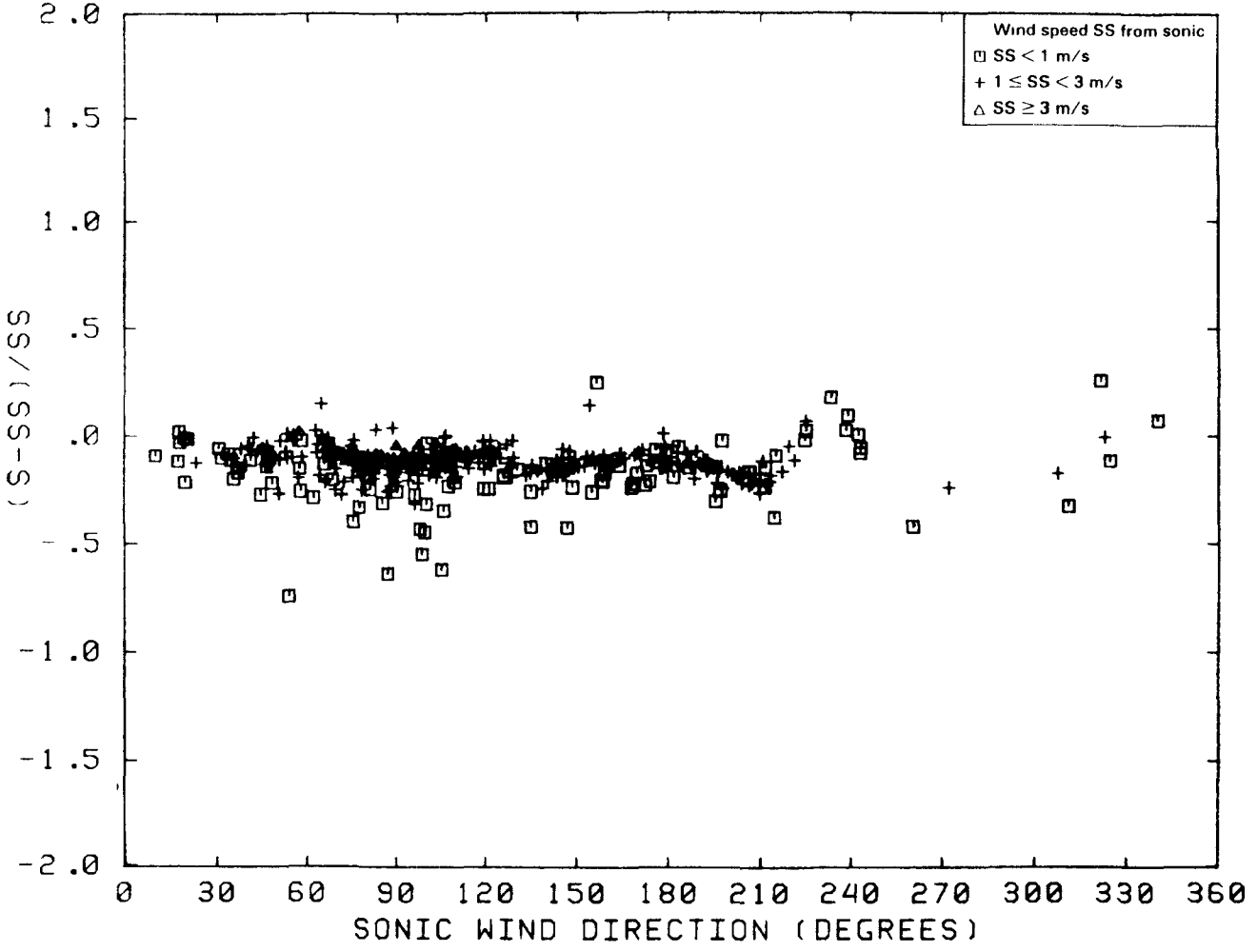

Figure 24. Differences between prop (S) and sonic (SS) wind speeds as fraction of SS vs. sonic direction for Experiments 10 to 14 from 40 m, Tower A.

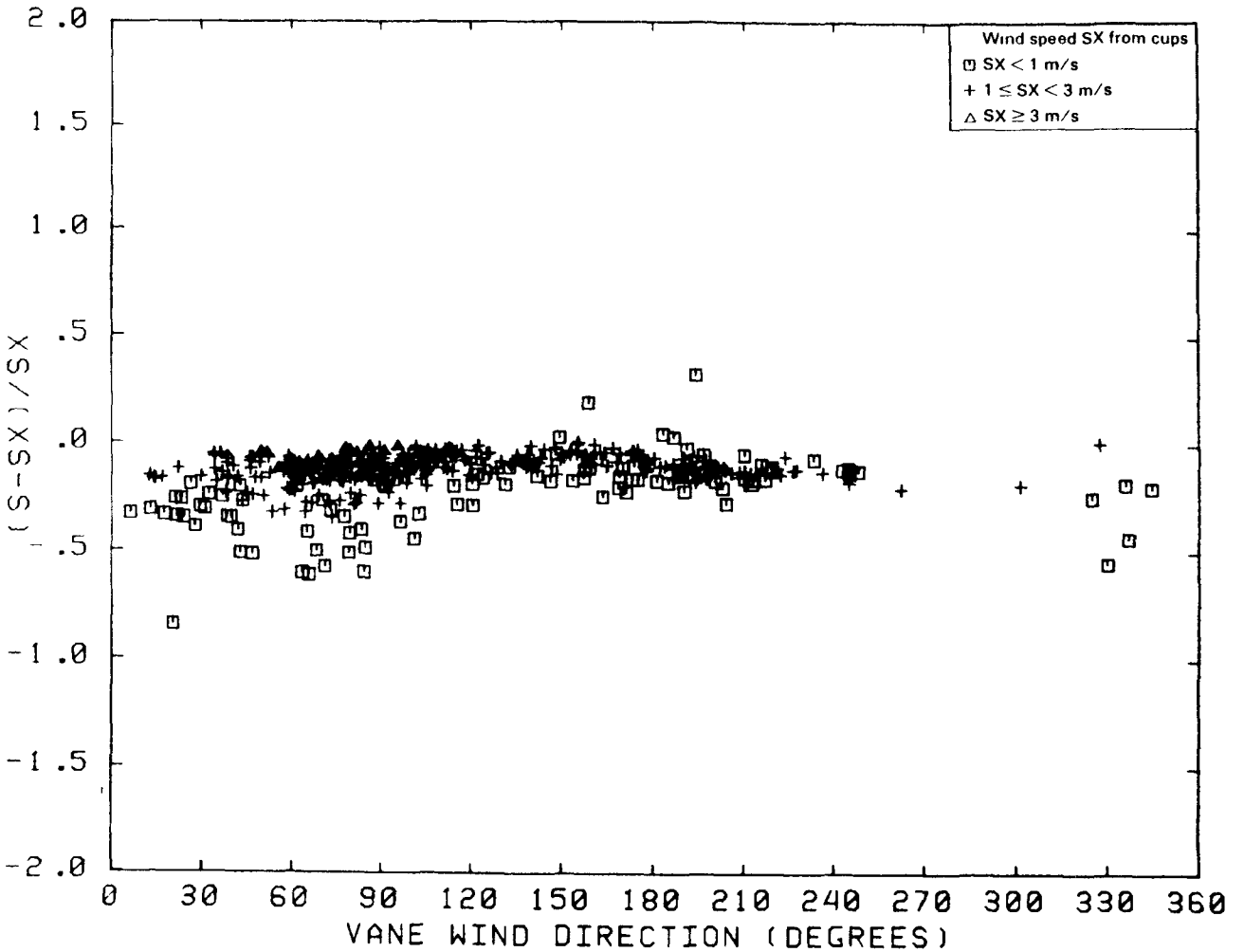

Figure 25. Differences between prop (S) and cup (SX) wind speeds as fraction of SX vs. vane direction for Experiments 10 to 14 from 40 m, Tower A.

The reader should note that the comparisons and inferences in the preceding discussion really relate only to data from the 40-m level of Tower A. Data from other instruments, however, were processed in the same way and the results are comparable.

The improvement in consistency between collocated measurements in the refined data over the preliminary data is demonstrated in Figures 26 and 27, in which the differences between vane and prop wind directions are plotted as a function of vane direction for the instruments at 40 m on Tower A during Experiments 9 through 15. The distinct trends in direction differences in the preliminary data evident in Figure 26 have been removed in Figure 27. The improved consistency in the refined data results from the use of the wind tunnel calibrations and cosine-response corrections for the props and probably only to a minor extent from the data-filtering described above; the raw data were also subjected to substantial filtering in the production of the preliminary database.

An overall assessment of the quality of the HBR meteorological (and tracer gas) data base can be found in the Quality Assurance Project Report (Greene, 1985). It presents estimates of the precision and accuracy of all the measurements. The bottom line of this assessment is that the data from Experiments 9 through 15 are completely useful for modeling purposes. The data from the other experiments are still somewhat noisy, especially the turbulence data from Experiments 4, 5, and 6.

3.1.5 Remaining Problems in the Tower Data

Certain propeller anemometers showed intermittent lack of response at HBR as they had at CCB, in spite of the installation of new bearings. A systematic appraisal that will identify all such faulty prop data has not yet been completed. When this has been done, 5-min and 1-hr averaged measures calculated from the affected propellers will be flagged "F" (for Faulty, Failure, Friction, or Frozen). Some periods of suspect temperature outputs have also been identified; these too will be flagged.

3.2 HBR Streamline Analysis

In modeling the maximum ground-level concentration of material from an elevated plume released upwind of a hill, one important aspect of the flow that must be considered is the vertical deflection of the plume relative to the surface of the terrain. When the flow is stably stratified, air nearer the surface possesses a greater potential density than that at greater elevations. Using a "parcel" argument, Sheppard (1956) suggested that this air may pass over the top of a hill only if there is sufficient kinetic energy. Because the denser air near the surface often possesses insufficient kinetic energy, only air above a "critical" dividing-streamline height, H_c, is able to pass over the hill. The flow below H_c must pass around the sides of the hill, or it may be "blocked" if the hill is an infinite ridge. Streamlines above H_c will therefore pass closer to the surface of the hill so that a plume in this flow will travel nearer the surface

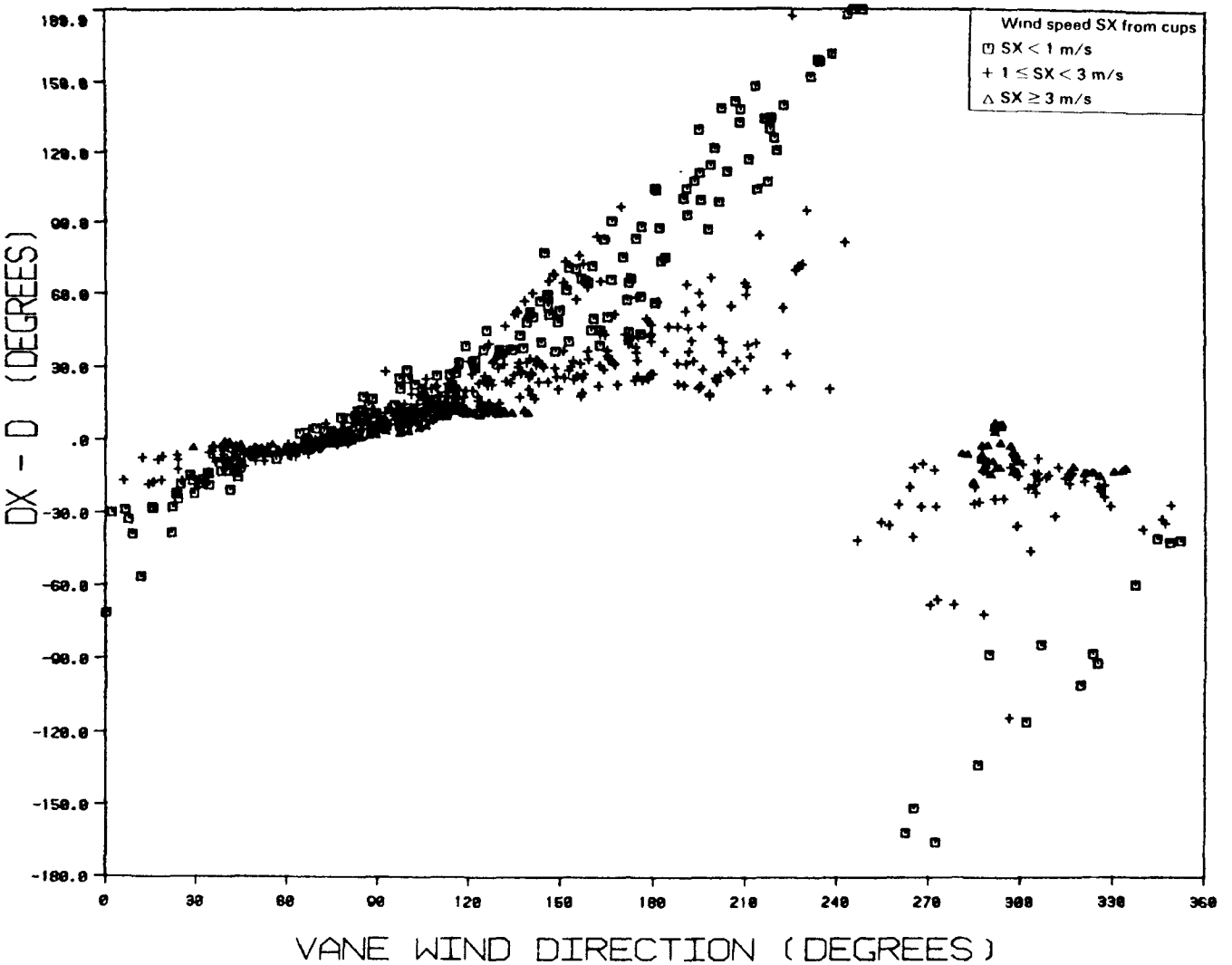

Figure 26. Differences between vane direction (DX) and prop direction (D) vs. DX for Experiments 9 to 15 from 40 m, Tower A, preliminary data base.

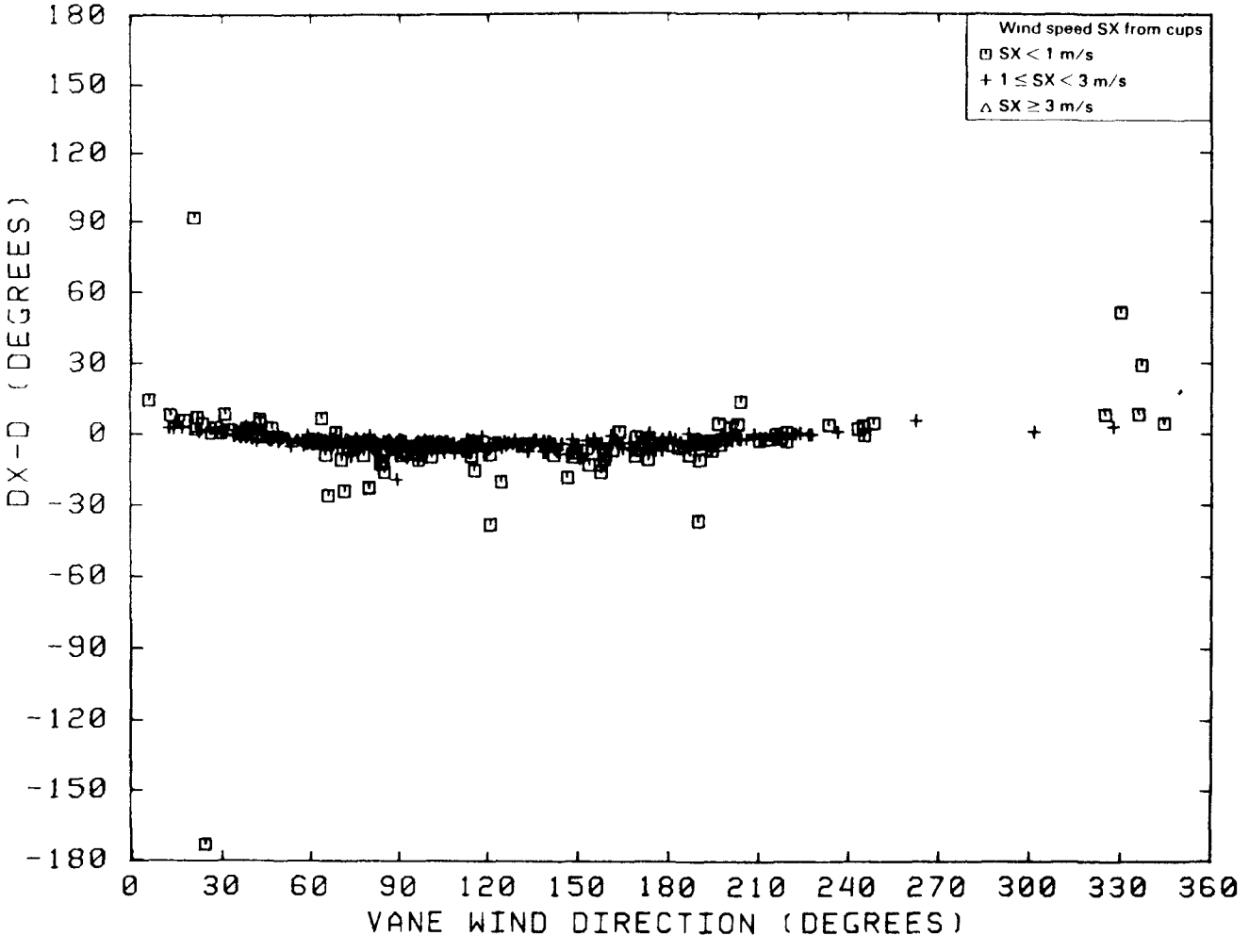

Figure 27. Differences between vane direction (DX) and prop direction (D) vs. DX for Experiments 9 to 15 from 40 m, Tower A, refined data base.

of the hill and will produce greater ground-level concentrations. Diffusion models that explicitly account for this two-layer flow structure are said to incorporate the "cut-off" hill approach to simulating the flow above H_c. In this section of the report the vertical deflection of a streamline in the flow above H_c as it passes over the crest of HBR is discussed. These deflections are known to depend on the initial height of the streamline above H_c, on the shape of the hill above H_c, on the stratification of the flow, and on the wind speed profile.

In the first subsection, the height and shape dependencies are considered through potential flow theory. The second subsection extends the analyses through a perturbation analysis using a linearized form of the Navier-Stokes equations. Here stratification and wind speed shear are considered. In both subsections, model calculations of stand-off distance are compared to lidar measurements of the height of the oil-fog plume centerline above the crest of HBR.

3.2.1 Representativeness of Potential Flow above H_c

Lidar data received from WPL have been used to compare estimated streamline heights upwind and over the crest of HBR to calculations from potential flow theory. Heights of the centerline of oil-fog plumes have been assumed to represent streamlines. This information has been used to examine the extent to which the field data collected at HBR support the "cut-off" hill approach to calculating the flow above the dividing streamline height. In this modeling approach, the layer of air below H_c is presumed to remain below the hill top and the flow above H_c is presumed to behave as potential flow (a surrogate for weakly stratified flow) over a hill of reduced height.

This analysis makes use of the lidar data obtained at the section nearest the release point (but after the plume had reached its approximate equilibrium height), and at the section nearest the crest of HBR. The centroid of the distribution of backscatter intensity in each section is assumed to mark the same streamline during each five-minute period. Meteorological data associated with each of the streamlines are the five-minute average data for the standard five-minute interval containing both centroid observations. Furthermore, of all the periods for which lidar data were available, only those periods were selected in which the transport wind direction was fairly steady, and in which the lidar section nearest the crest lay on the windward side of HBR. This subset of the database is best suited to study the relationship between the elevation of the plume above the surface and the incident flow.

The relationship between the initial (H) and final (η) height of the streamline, the dividing-streamline height (H_c), the hill height (A), and half the hill breadth at A/2 (L) is presented in Figure 28. The estimated height of the streamline above H_c measured at a distance x_c from the center of the ridge is denoted z_c. Lidar measurements close to the source are used to estimate z_c.

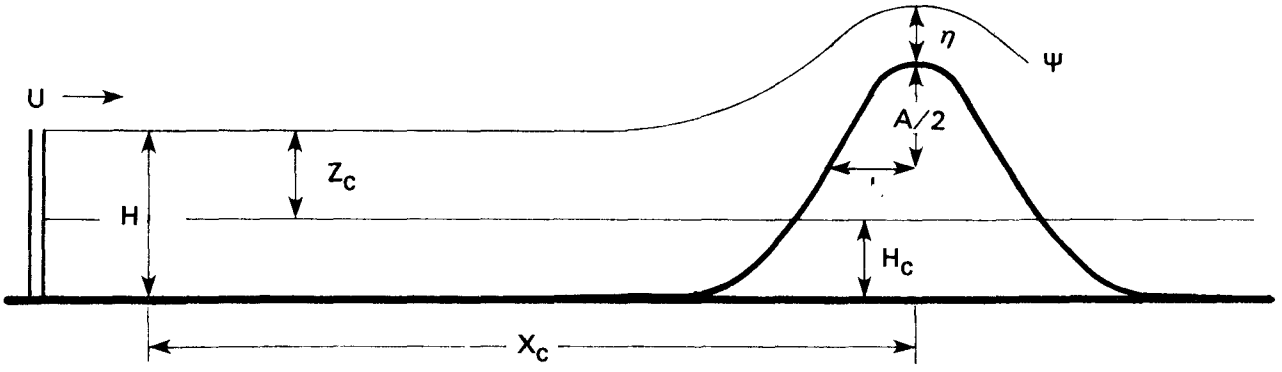

Figure 28. The relationship between the initial (H) and the final (η) height of the streamline, the dividing-streamline height (H_c), half the hill height (A/2), and half the hill breadth at A/2 (L). H is measured a distance x_c from the center of the hill.

The oil-fog plume centerline height H is used to approximate the streamline height at $x = \infty$. Calculations of potential flow over an elliptical cylinder were used to estimate $H(x = \infty)$ for each of the lidar measurement periods and the results were quite similar to $H(x = x_c)$. For example, during Experiment 10 at 0801, H is measured to be 86 m at x_c equal to 517 m from the center of the ridge with H_c calculated at 42 m. $H(x = \infty)$ is calculated to be 85.1 m, a negligible difference of only 0.9 m. Larger differences occur if the lidar measurement of H is made over the edge of the ridge. For example, during Experiment 7 at 0351, H is 56 m at x_c equal to 245 m from the center of the ridge with H_c calculated at 28 m. $H(x = \infty)$ is calculated to be 48 m. The lidar measurement is over the leading edge of the ridge where an ellipse is not a good approximation.

Three different types of cylinders (circular, 2-D Rankine, and elliptical) are used for the potential flow calculations. The flow over a circular cylinder,

$$\Psi = - uH \left(1 - \frac{A^2}{x^2 + H^2}\right) \tag{1}$$

is the simplest potential flow solution, but its results may be unrealistic because it does not account for the aspect ratio of HBR. The along-wind (at 117 degrees) breadth (190 m) of HBR at half its maximum elevation (45 m) is used to calculate the aspect ratio (4.2, i.e., 190/45). A hill with an aspect ratio of 4.2 is likely to cause a greater degree of deflection of streamlines over its crest than a semicircular hill with an aspect ratio of 1.0 because the semicircular hill has a steeper slope. (See the discussion in Section 2 of the Second Milestone Report.) Thus, an aspect ratio of 4.2 is used to solve the potential flow solutions for a 2-D Rankine cylinder,

$$\Psi = - uH \; - m \tan^{-1} \left(\frac{2a'H}{x^2 + H^2 - a'^2}\right) \tag{2}$$

where $m \equiv \frac{1}{2} u a' \left(\frac{\ell^2}{a'^2} - 1\right)$

ℓ = 190 m = along-wind breadth of the hill at A/2

a' = 347 m = half the distance between the source/sink pair

and an elliptical cylinder,

$$\Psi = - uA(1+\lambda) \sinh (\mu-\mu_o) \sin \nu \tag{3}$$

where μ and ν are elliptical coordinates, λ is the aspect ratio, and

$$\mu_o \equiv \ell n \left[\frac{1+\lambda}{1-\lambda}\right]^{0.5} \quad (4)$$

The heights of observed 5-minute plume centroids (η) above the crest of HBR for various effective plume heights H (lidar measured oil-fog plume centerline heights at $x = x_c$) are presented in Figure 29a. The values are scaled by A, the height of HBR. The figure includes computed curves of η/A versus H/A derived from potential flow over a circular cylinder, an elliptical cylinder, and a 2-D Rankine cylinder. A majority of the points lie well below the circular cylinder curve, i.e., the measured plumes pass much closer to the ridge than is expected on the basis of potential flow estimates that ignore H_c.

The variation of the height of the observed plume centroid (η) above the crest of HBR for various effective plume heights in excess of H_c ($H-H_c$) is presented in Figure 29b. H_c is included because it is expected that the layer of air below H_c does not pass over HBR. The values are scaled by the effective hill height ($H_* = A-H_c$). The data now better fit the curves that represent potential flow over a cylinder. This result supports the "cut-off" hill modeling approach in conjunction with the assumption that the flow above H_c is essentially neutral. The majority of the data lie above the circular cylinder curve, suggesting that a measure of the ridge, shape, e.g., the along-wind aspect ratio, should be included. The fact that the majority of points lie between the elliptical and circular curves suggests that streamlines are typically deflected to a larger extent than would be modeled by potential flow over an elliptical cylinder with an aspect of 4.2. Although in principle some other terrain shape may better fit the data, it is likely that a measure of density stratification or wind speed shear or both needs to be taken into account in specifying the flow above H_c.

3.2.2 Effects of Stratification and Shear on Streamline Deflections

<u>An Empirical, Neutral Flow Base Case</u>

The results of the previous subsection indicate that for releases above H_c, a substantial portion of the streamline deflection can be understood in terms of neutral potential flow of the air above H_c over an appropriate hill shape. In fact, a least squares minimization of the predicted versus observed centerline standoff distance, η, modeled as

$$\eta = m \cdot (H-H_c) \quad , \quad (5)$$

yields a slope, m(=0.68), that represents a hill shape somewhere between the circular and elliptical cylinders. This fact and the

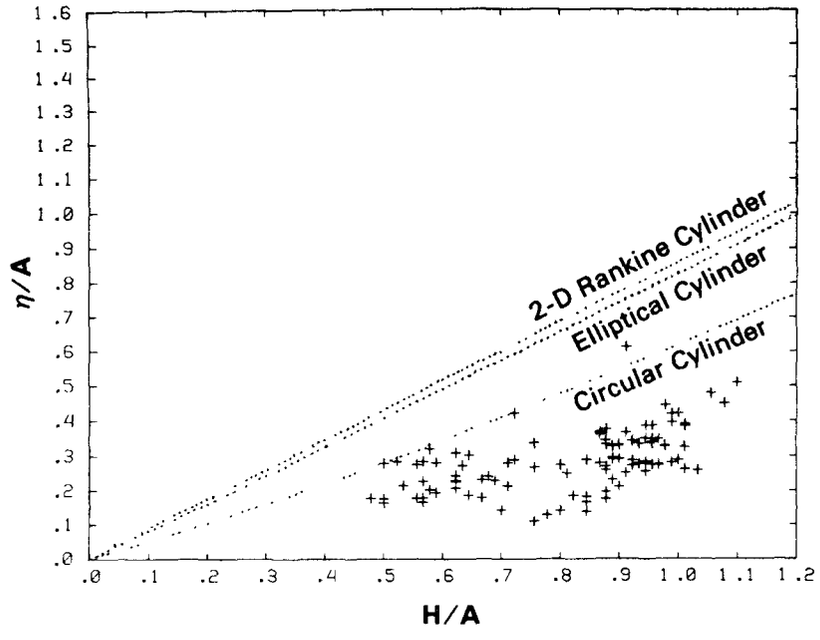

Figure 29a. Height of the source streamline (η) above the crest of HBR for various source heights (H). Values are scaled by the height of HBR (A).

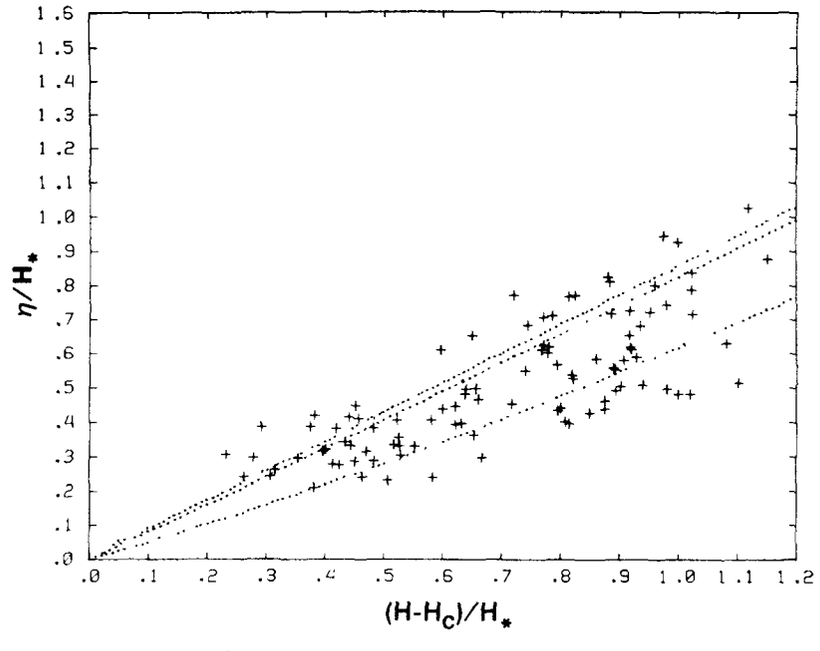

Figure 29b. Height of the source streamline (η) above the crest of HBR for various effective source heights ($H - H_c$). Values are scaled by the effective hill height (H_*).

associated statistical performance measures presented in Table 9 are important in that they provide a "base case" for judging the improvements gained through inclusion of stratification and shear. It is interesting that Equation 5 provides a significantly better fit to the lidar centerline data than a comparable model that ignores H_c (i.e., $H_c = 0$ yielding an $m = 0.34$) and is slightly better in mean square error (MSE) than RTDM, which uses a somewhat different formula for those cases (i.e., 20 of the total 94) where H exceeds the hill height, h. A scatterplot of predicted versus observed η values for this potential flow base case is shown in Figure 30.

Streamline Deflection Theory

A number of researchers, e.g., Scorer (1949), Long (1953), Wurtele (1957) have used perturbation analysis to reduce the Navier-Stokes equations of motion to (1) a single equation of the displacement, $\delta(x,y,z)$, that a fluid particle at point x,y,z has experienced; or (2) as an equation in the vertical velocity perturbation Δw. In two dimensions (i.e., infinite in y direction) these equations are:

$$\nabla^2\delta + 2\alpha\frac{\partial\delta}{\partial z} + (N/u)^2\delta = 0 \qquad (6)$$

and

$$[\nabla^2 + (N/u)^2 - \beta]\Delta w = 0 \qquad (7)$$

respectively, where $\alpha \equiv \frac{1}{u}\frac{du}{dz}$, $\beta \equiv \frac{1}{u}\frac{d^2u}{dz^2}$, and $\nabla^2 = \frac{\partial^2}{\partial x^2} + \frac{\partial^2}{\partial z^2}$.

Since the w velocity can be computed from δ as

$$\Delta w = u\frac{\partial\delta}{\partial x} \quad , \qquad (8)$$

Equations 6 and 7 should yield identical results, but this is only obvious when shear is negligible (i.e., $\alpha = \beta = 0$).

Models Incorporating Stratification Only

In the case where shear is negligible Equation 6 may be solved by first taking the Fourier transform of the equation with respect to x. Defining

$$\{\delta\} = \frac{1}{2\pi}\int_{-\infty}^{\infty} dx\ \delta(x,z)e^{-ikx} \quad , \qquad (9)$$

Equation 6 reduces to the ordinary differential equation

$$\{\delta\}'' + (\ell^2 - k^2)\{\delta\} = 0 \qquad (10)$$

TABLE 9. HBR STREAMLINE STANDOFF AT CREST MODELING

Equation	$\bar{\eta}_{TH}$ †	MSE*	% MSE As Bias	% MSE Stochastic	Corr. Coeff. (r)
Empirical					
$\eta = m \cdot (H-H_c)$ $m = 0.68$	24.2	38.5	2.0	97.7	0.707
$\eta = m \cdot H$ $m = 0.34$	24.9	45.3	0.8	82.9	0.530
RTDM	24.2	40.2	2.1	96.6	0.712
Stratification Only					
Queney See Eq. 18	24.6	35.7	0.7	98.5	0.733
Hunt Eq. 20	23.4	37.8	8.3	91.4	0.732
Stratification and Shear					
Eq. 27 and $\beta = \alpha^2$	23.9	34.8	4.3	95.6	0.736
Eq. 29	25.0	38.7	0.04	97.5	0.729

† $\bar{\eta}_{TH}$ is the average value of the streamline height above crest (in meters) for the 94 cases considered. The average observed streamline height (η_{OBS}) is 25.1 m.

*MSE is mean square error in m^2.

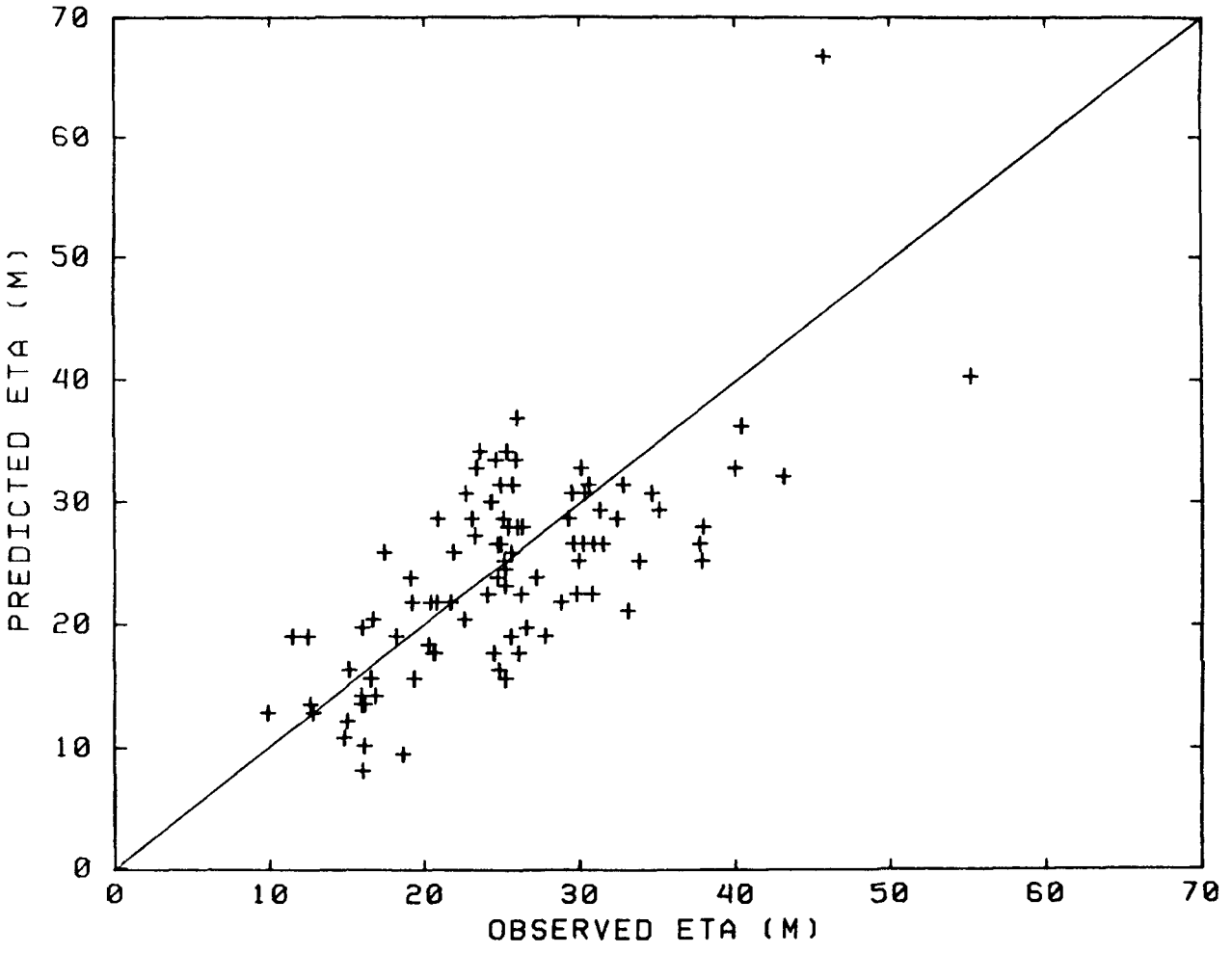

Figure 30. Predicted versus observed plume centerline standoff distance (eta) at the crest of HBR using the empirical equation (5).

where $\ell = N/u$ and the prime denotes differentiation with respect to z. Equation 10 has the solution

$$\{\delta\} = e^{+imz} \{\delta(0)\} \quad , \tag{11}$$

where the + sign ensures outgoing waves (i.e., the radiation condition) and where

$$m = (\ell^2 - k^2)^{1/2} \tag{12}$$

is the solution of the algebraic equation that results when Equation 11 is inserted into 10. Determination of the solution $\delta(x,z)$ also involves satisfying the lower boundary condition

$$\delta(x,h(x)) = h(x) \quad , \tag{13}$$

which constrains the streamline at the surface to follow the surface. This non-linear condition is usually linearized as

$$\delta(x,0) = h(x) \tag{14}$$

so that the final solution can be written as

$$\delta(x,z) = \int_{-\infty}^{\infty} dk \{h\} e^{imz} e^{ikx} \tag{15}$$

where $\{h\}$ is the transform of the terrain function h(x). If however we rewrite the exp(imz) term in Equation 15 as exp(imz'), where $z' = z - h(x)$, the resulting expression satisfies the non-linear condition (13), although Lilly and Klemp (1979) caution that such a simplistic adjustment will disturb the radiation condition at $z = +\infty$. Irrespective of this point, the main difficulty in evaluating Equation 15 is the "branch cut" singularity created by m.

Queney (1947) obtained a solution to Equation 15 in the hydrostatic limit (i.e., $k^2 << \ell^2$, so that $m \simeq \ell$) for the case of the inverse polynomial hill function,

$$h(x) = h/(1+ (x/L)^2) \quad , \tag{16}$$

chosen because of its simple transform,

$$\{h\} = \frac{1}{2}hLe^{-|k|L} \quad . \tag{17}$$

Inserting Equation 17, along with the simplification $m = \ell$, into Equation 15 yields the solution

$$\delta(x,z) = h[\varepsilon \cos \ell z' - (x/L) \sin \ell z']/[\varepsilon^2 + (x/L)^2] \quad , \qquad (18)$$

where $\varepsilon = 1$ in Queney's work but is set to $\varepsilon = 1 + z'/L$ here in order to recover the exact solution in the neutral limit where $\ell = 0$ and $imz = -kz$. Perhaps the only drawback of Equation 18 is that for a known source height H, one must solve Equation 18 iteratively to find $\eta \equiv z'$, subject to the constraint

$$h(x) + z' - \delta(x,z') = H \qquad (19)$$

It should also be noted that for the case of a cutoff hill, $H_* = h - H_c$, the hill length is approximated as $L_c = (H_*/h)L$ and the effective source height becomes $H - H_c$. Results of applying these Equations 18 and 19 at the crest (i.e., $x = 0$) of the cutoff HBR are presented in Table 9. What is striking is that for this parameter-free model, both MSE and r are superior to an empirical model; thus indicating the value of a model that explicitly includes the influence of the stratification, $\ell = N/u^+$, in the layer between H_c and H.

Since a goal of this project is to include effects predicted by successful theories of stratified flow over terrain into pollutant dispersion models, a model component developed by Hunt and co-workers for the "outer flow" region was also tested. For flow over a 2-d ridge, the standoff height η at the crest may be approximated from mass conservation as

$$\eta = (H - H_c)/(1 + \Delta u) \qquad (20)$$

where Δu is the dimensionless speed perturbation given as

$$\Delta u \simeq (H_*/L_c)(1 + 0.5\ s \log(s)) \qquad (21)$$

for small s, for the inverse polynomial, cutoff hill, and $s = NL_c/u$. Despite the fact that Hunt et al. (1981) indicate that the long "skirted" inverse polynomial hill is an inappropriate shape for the cutoff hill problem and that the upper level solution, Equation 21, should be accompanied by a properly matched inner boundary layer (and possibly a shear dominated middle layer), the results presented in Table 9 indicate that this simple, upper layer approximation performs nearly as well as the more complex, iterative

[+] Both N and speed u were evaluated at $z = H$. Results obtained using the wind component perpendicular to the ridge were poorer for all models considered.

model of outer layer flow previously described. The scatterplot of predicted versus observed lidar standoff heights is shown in Figure 31.

Before considering the added effect of wind speed shear, several features of the "stratification only" results are worth considering.

- For centerline standoff measurements made at the crest (i.e., x = 0), the Equation 18 with $\epsilon = 1$ solution is independent of the hill width L and, in fact, is completely independent of the hill shape function assumed. Addition of the neutral limit case inserts the $\epsilon = 1 + z'/L$ dependence, but this is a small correction for the small standoff (i.e., $z'/L << 1$) cases of principal interest. In comparison, the Hunt relations appear more sensitive to hill shape and hill length, though an exhaustive study has not been performed.
- The 94 cases considered here span an $s(= NL_c/u)$ range of 0 to $\simeq 2.5$; thus, one is reasonably sensitive to the explicit s dependence in Equation 21, although it should be noted that Equation 21 was derived for small values of s. An alternative expression suggested by Hunt et al. (1981) reduces to $\Delta u = (H_c/L_c)/(1 + s^2)$ at the crest of the inverse polynomial hill and yields a 40% higher MSE than Equation 21. An accompanying drop in r to 0.60 suggests that this alternative expression induces $s >> 1$ asymptotic behavior too quickly.
- Consideration of "stratification only" yields a mean streamline height that is just 0.5 m (1.75 m for Equation 20) below the observed mean standoff height and r.m.s. errors of about ± 6 m. With event dependent lidar resolutions of order few meters, greatly improved model performance cannot be expected to result from using more sophisticated approaches (e.g., multiple layers) or adding additional dependencies (e.g., shear).

Inclusion of Wind Shear

Based on various measures of the first (α) and second (β) derivatives of the wind speed profiles for the HBR events being considered, the effects of shear might be expected to dominate stratification effects characterized by $\ell = N/u$; however, the previous subsection has indicated that models without shear appear to adequately model streamline standoff distances measured at the crest. To understand the influences of shear, it is convenient to return to Equation 6, take the Fourier transform with respect to x, and hypothesize a solution of the form

$$\{\delta(z)\} = e^{-p(z)}\{\delta_o(z)\} \quad , \tag{22}$$

where $\{\delta_o(z)\}$ becomes the new unknown function with the governing equation

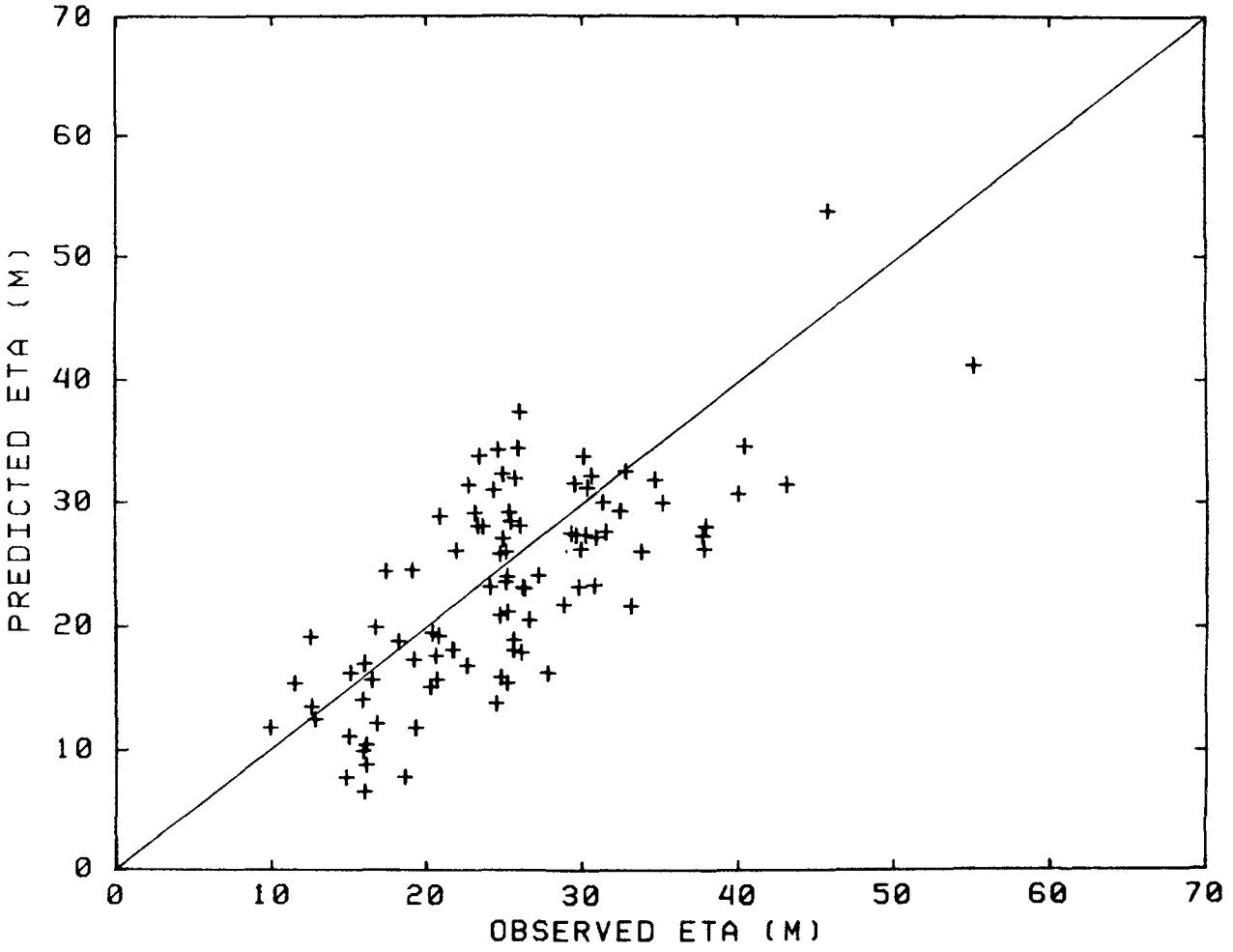

Figure 31. Predicted versus observed plume centerline standoff distance at the crest of HBR using the "outer-layer" solution (Eq. 20) of Hunt et al. (1980), that includes stratification but neglects shear.

$$\{\delta_o\}'' + 2(\alpha - p')\{\delta_o\}' + (p'^2 - p'' - 2\alpha p' + \ell^2 - k^2)\{\delta_o\} \quad . \qquad (23)$$

Since a simple wave equation results if we eliminate the $\{\delta_o\}'$ term, it is reasonable to choose $p' = \alpha$. The real decision comes in deciding what p and p" should be. Two cases will be considered:

1) Define α as a layer average constant, $\alpha = \frac{1}{u}\frac{\Delta u}{\Delta z}$, so that $p = \alpha z$ and $p'' = 0$. In this case we obtain the familiar Scorer equation,

$$\{\delta_o\}'' + (\ell^2 - k^2 - \alpha^2)\{\delta_o\} = 0 \quad , \qquad (24)$$

that leads to solutions of the form

$$\{\delta\} \propto \exp(-\alpha z \pm z(\alpha^2 - \ell^2 + k^2)^{1/2}) \quad ; \text{ or} \qquad (25)$$

2) Define α as the function, $\alpha = \frac{1}{u(z)}\frac{du}{dz}$, so that $p'' = \beta - \alpha^2$, β is the observed second derivative, $\beta = \frac{1}{u}\frac{d^2u}{dz^2}$, and $p = \text{Log } u(z)$. In this case we obtain the equation

$$\{\delta_o\}'' + (\ell^2 - k^2 - \beta)\{\delta_o\} = 0 \quad , \qquad (26)$$

that corresponds to Equation 7 for Δw, and yields solutions of the form

$$\{\delta\} \propto \exp\,[-\log u(z) \pm z\,(\beta - \ell^2 + k^2)^{1/2}] \qquad (27)$$

Interestingly, Equations 25 and 27 are identical for an exponential wind profile $u(z) \propto \exp(\alpha z)$--a not very realistic profile.

In experimenting with Equations 25 and 27, it became clear that the choice of the minus sign forced the streamlines much too close to the hill compared to observations, so the plus sign was selected. The plus sign, on the other hand, suggests the curious result in Equation 25 that the influence of shear disappears in the limit of very large shears (i.e., $\alpha >> \ell$). The very lowest MSE result was obtained by using the $\alpha^2 = \beta$ constraint from the exponential wind profile and a locally parabolic determination of α from the approach flow data. This avoided use of potentially "noisy," spline-determined second derivatives but does create some conceptual inconsistency. The scatterplot of predicted versus observed values is shown in Figure 32 and the performance measures presented in Table 9. Despite the fact that addition of shear has forced the mean streamline position down an

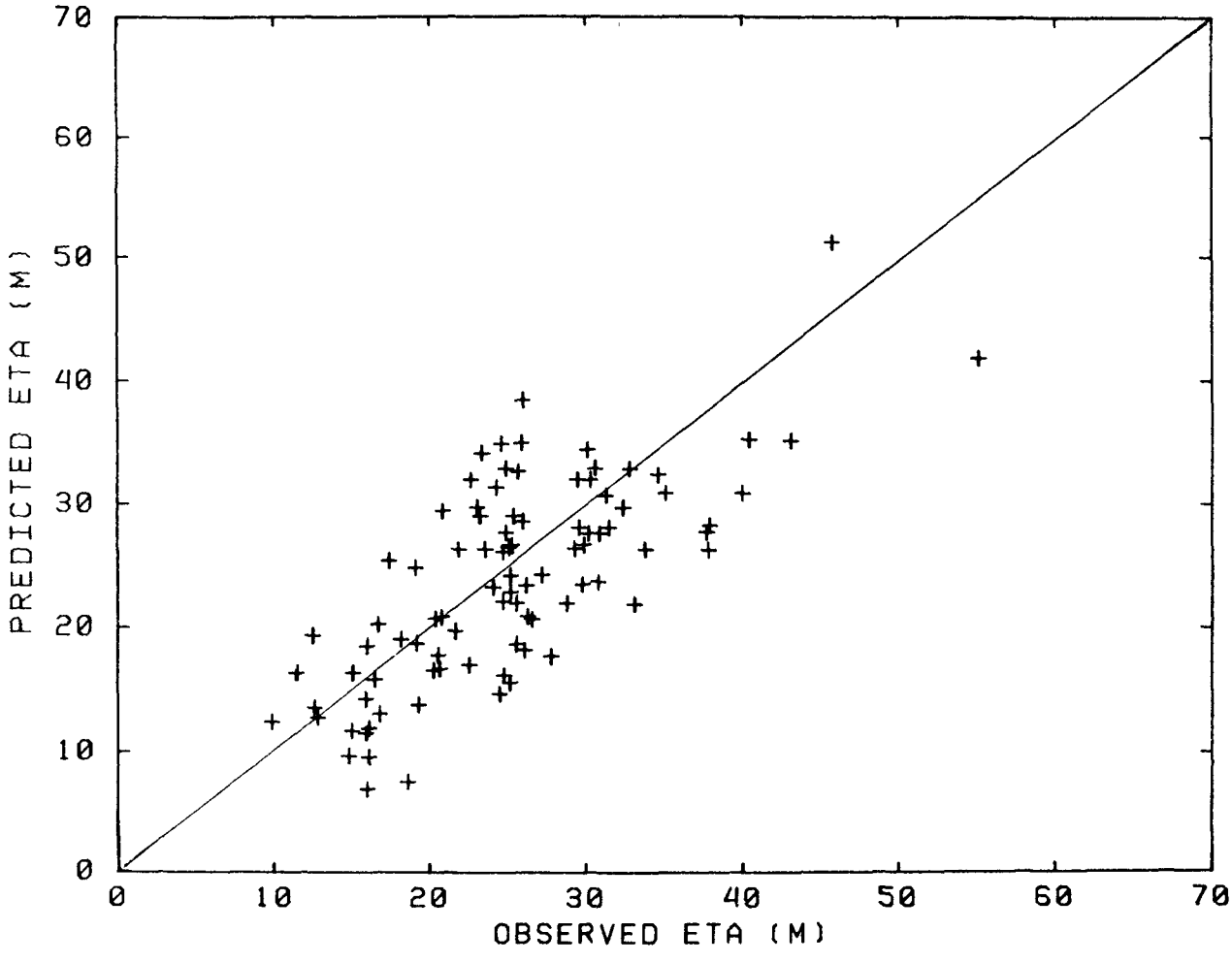

Figure 32. Predicted versus observed plume centerline standoff distance at the crest of HBR using equation (7) that includes both stratification and shear. The shear was computed using spline interpolated values of $u(H_c)$ and $u(H)$, the assumption of $\beta=\alpha^2$, and a local parabolic determination of α.

additional 0.75 m below the Queney solution without shear, the increase mean bias is offset by a reduced MSE and increased r. All other attempts to include shear led to a poorer result (i.e., higher MSE) than the stratification only results.

One of the more interesting of these attempts involved assumption of a linear incident wind profile, $u(z) = u(H) + \alpha(z-H)$, in Equation 27. If the incident profile is assumed to follow the terrain and the perturbation to the wind field is included, so that

$$u_T(z') = u(z') \left[1 - \frac{\partial \delta_Q}{\partial z'}\right] \quad , \tag{28}$$

then the streamline deflection can be written as,

$$\delta(x,z) = \frac{u(H)}{u_T(z')} \delta_Q(x,z') \quad , \tag{29}$$

where δ_Q is the "stratification only" deflection from Equation 18. With appropriate adjustment to u(z') to ensure that the lower boundary condition is still satisfied, the results in Table 9 indicate that the mean streamline height is in nearly perfect agreement with observations, although the MSE is somewhat higher than that obtained with the "stratification only" counterpart.

3.3 Representativeness of Stable Boundary Layer Similarity Theory

Much of what is known about the structure of the stably stratified atmospheric boundary layer over uniform terrain applies to a layer with depth of order L next to the ground, where L is the Monin-Obukhov length scale. It is in this layer that the surface shear stress is important in determining the properties of heat and momentum exchange to the extent that "universal" flux-profile relationships can be prescribed in terms of the dimensionless height above the surface, z/L (e.g., see Businger 1973). At elevations much greater than L, the surface shear stress is unimportant in determining the structure of the flow, and it is often assumed that vertical turbulence approaches zero above the surface layer and the upper flow is decoupled from the surface layer. Whatever turbulence is found at these heights is intermittent and is ascribed to internal processes such as wave-breaking or instabilities associated with internal shear layers. In complex terrain, however, turbulence is advected from nearby terrain or is generated by shear produced by the terrain.

The dispersion of a plume released above the surface in a stably stratified atmosphere would therefore seem to be quite dependent on its dimensionless elevation. When the plume height is of order L or less, the diffusion of plume material may be expected to be similar to the turbulent exchange of sensible heat ($K_z \sim K_h$). At greater elevations, one possible assumption for modeling buoyant plumes is that the ambient turbulence is nearly zero, and that the dilution of the plume is primarily determined by the degree of entrainment of ambient air experienced during buoyant plume rise. Note, however, that the depth of such a plume in the vertical could collapse to some

extent as it traveled away from the source. The growth of a plume due to buoyancy is typically modeled (Pasquill, 1976) as

$$\sigma_{zb} = \frac{\Delta z}{\sqrt{10}} \tag{30}$$

where Δz is the plume rise. The plume will collapse if σ_{zb} is less than σ_w/N. In this case this "bubble" of plume material will not only seek its equilibrium height in the stratified atmosphere, it will also spread out at this level to reduce the potential energy of the initial configuration.

For plume heights less than or equal to L, it may be possible to infer the meteorology (wind and temperature structure as well as the turbulence) at plume elevation from near-surface measurements. This has obvious implications for the type of meteorological data needed for dispersion modeling. In applying a model, one would need to know when data obtained below the elevation of the plume are likely to be representative of the flow at plume elevation and above.

This section of the report addresses this issue and describes an analysis of data from CCB and HBR performed to see to what extent surface boundary layer similarity theory can be used to characterize the data measured at these two complex terrain sites.

CCB Meteorological Data

The scaling length L was not determined at CCB by measuring the momentum flux and heat flux near the surface. Rather, it was estimated from wind speed and temperature measurements near the ground. With wind speed measured at 10 m, and temperature measured at 2 m and 10 m, the bulk Richardson number might be computed as

$$Ri_b = \frac{g}{\theta_2} \frac{(\theta_{10} - \theta_2)/(8\ m)}{(u_{10}/z_g)^2} \tag{31}$$

where g is the acceleration due to gravity, θ is the potential temperature, and z_g is the geometric mean height of the layer between 2 m and 10 m. When the non-dimensional temperature gradient (ϕ_h) is set equal to the non-dimensional wind shear (ϕ_m), a reasonable assumption in the stable atmospheric boundary layer (Panofsky and Dutton 1984), L is related to the gradient Richardson number (Ri) by

$$\frac{z}{L} = \frac{Ri}{1 - \beta Ri} \tag{32}$$

where β is approximately 5. Ri is defined

$$Ri = \frac{g}{\theta} \frac{d\theta/dz}{(du/dz)^2} \tag{33}$$

Upon writing the temperature difference and the wind speed profile in terms of $\phi_m = 1 + \beta z/L$, Ri_b can be related directly to L, and a quadratic equation is obtained for L.

The condition that L be positive for stable stratification places the following restriction on Ri_b for the 2- and 10-m heights used at CCB:

$$Ri_b \leq (z_g/10)^2/\beta \tag{34}$$

This is equivalent to the condition

$$Ri \leq 1/\beta \simeq 0.2 \tag{35}$$

From Equation 32, we see that the similarity profiles require that $z >> L$ as $Ri \rightarrow 0.2$. In essence, the production of turbulence by shear is found to expire when the Richardson number is greater than approximately 0.2. For the CCB database, the bulk Richardson number from 2 m to 10 m exceeds the critical value for sustaining turbulence in approximately half of the hours. Presumably, the value of L in these cases is less than 2 m.

Data at 2 m and 10 m were used to obtain estimates of L and u_*, the friction velocity. For those cases in which L could be obtained, the applicability of the flux-profile relations was evaluated by estimating the wind speed at 40 m (the next measurement height on the tower) and the temperature difference between 10 m and 40 m. The results are presented in Figures 33 and 34. The upper portion of Figure 33 shows the predicted wind speed versus the observed wind speed, and the lower portion shows the corresponding ratio of the two versus z/L. The predicted speeds lie quite close to those observed when z is less than or approximately equal to L. At greater non-dimensional heights, the speeds are overestimated by 50% or more. The predicted and observed temperature differences between 10 m and 40 m shown in Figure 34 also show that better predictions are obtained when z/L is less than or approximately equal to 1. Similar results have been reported by others (Webb (1970), Skibin and Businger (1985)).

The behavior of the wind speed and temperature residuals for z greater than L suggests that neither the speed nor temperature increases with height as fast as $\phi_m = (1+\beta z/L)$ would indicate. This too has been reported by others. Webb (1970) suggests that a reasonable median profile is obtained if $\phi_m = 1+\beta$ for z/L greater than 1. This assumed profile allows the gradient Richardson number to increase with height, and Webb suggests that this profile should be most representative for Ri less than 1.0. Figures 35 and 36 show the results obtained when the "Webb extension" is applied to the data in Figures 33 and 34. The extension improves the predicted profiles considerably, and reasonable correspondence is now obtained at heights in excess of 10L.

Another method of extending the profiles of wind speed and temperature above z = L has been discussed by van Ulden and Holtslag

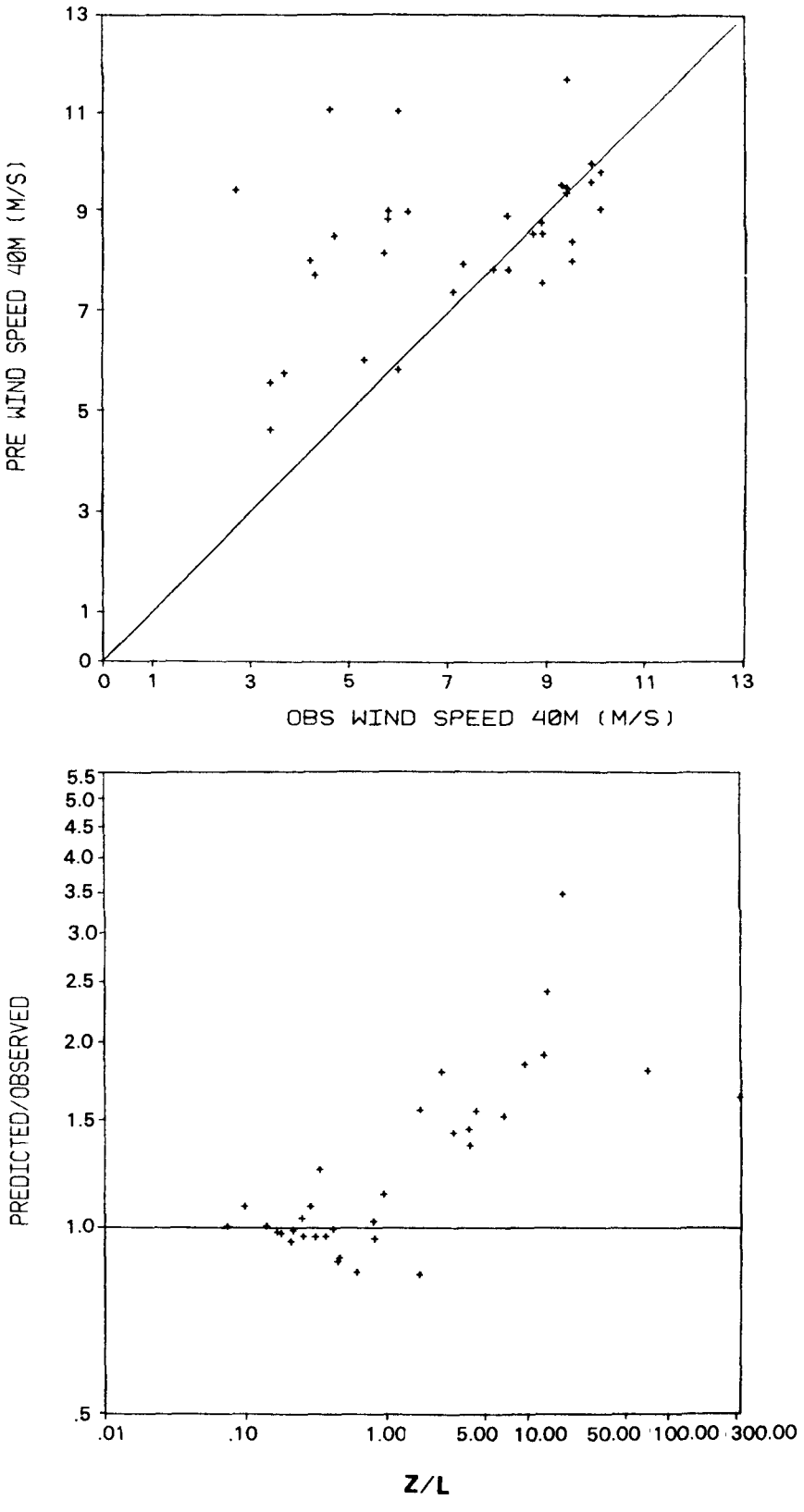

Figure 33. Comparison of the observed wind speed at 40 m with that estimated from surface-layer similarity theory and Ri_b (10 m) at CCB.

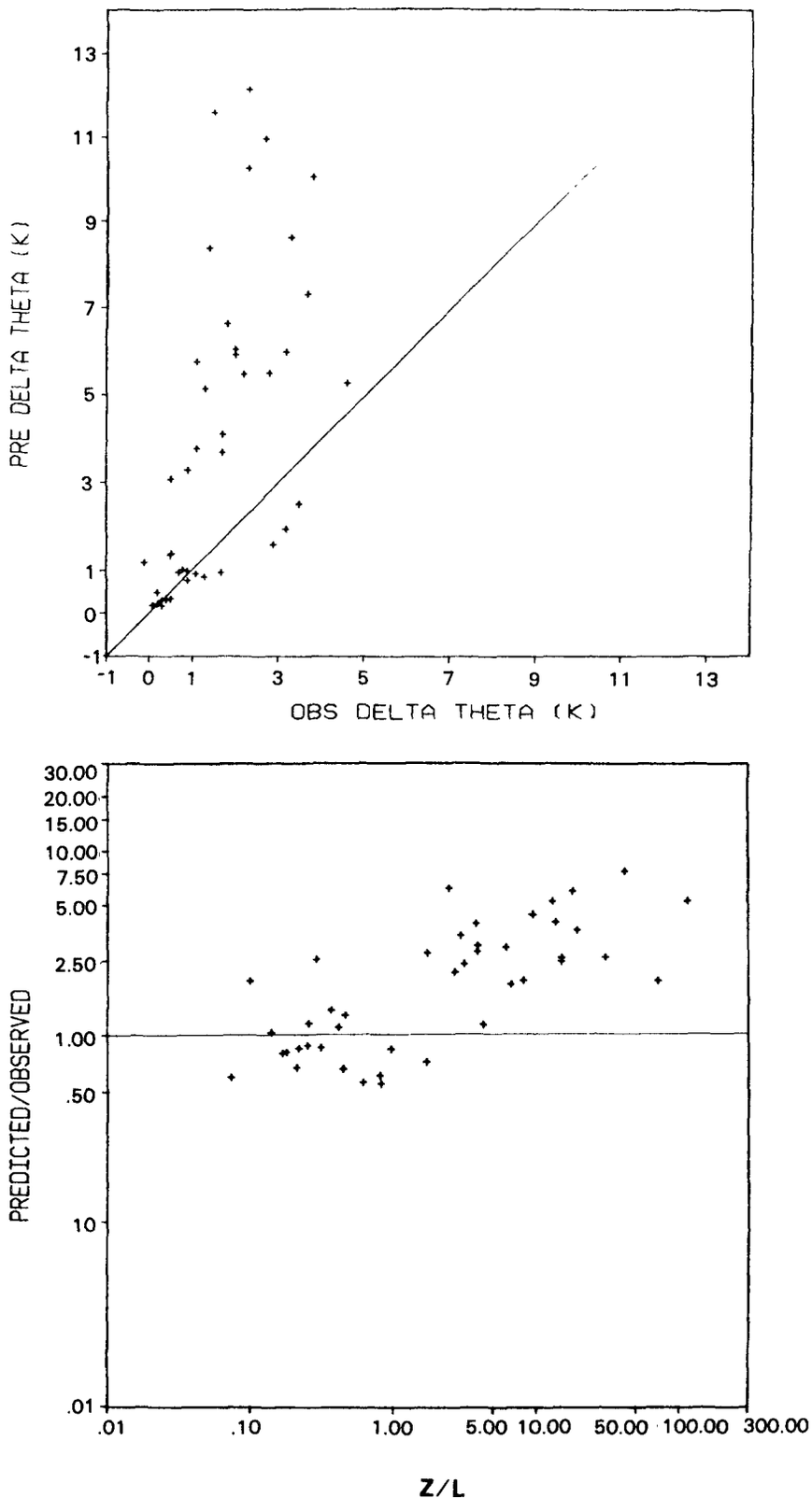

Figure 34. Comparison of the observed potential temperature difference between 10 m and 40 m with that estimated from surface-layer similarity theory and Ri_b (10 m) at CCB.

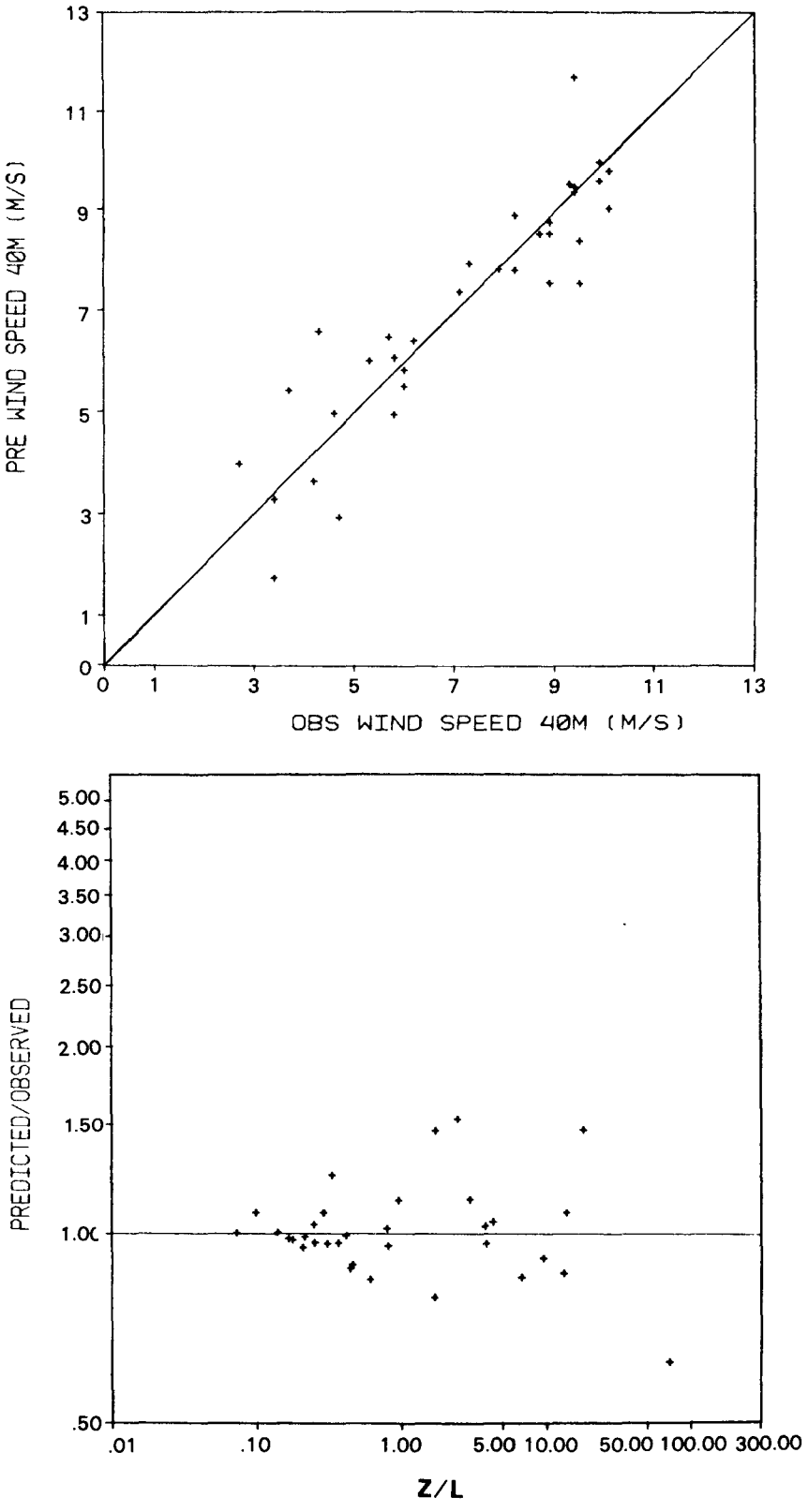

Figure 35. Comparison of the observed wind speed at 40 m with that estimated from the Webb extension to the surface-layer similarity theory and Ri_b (10 m) at CCB.

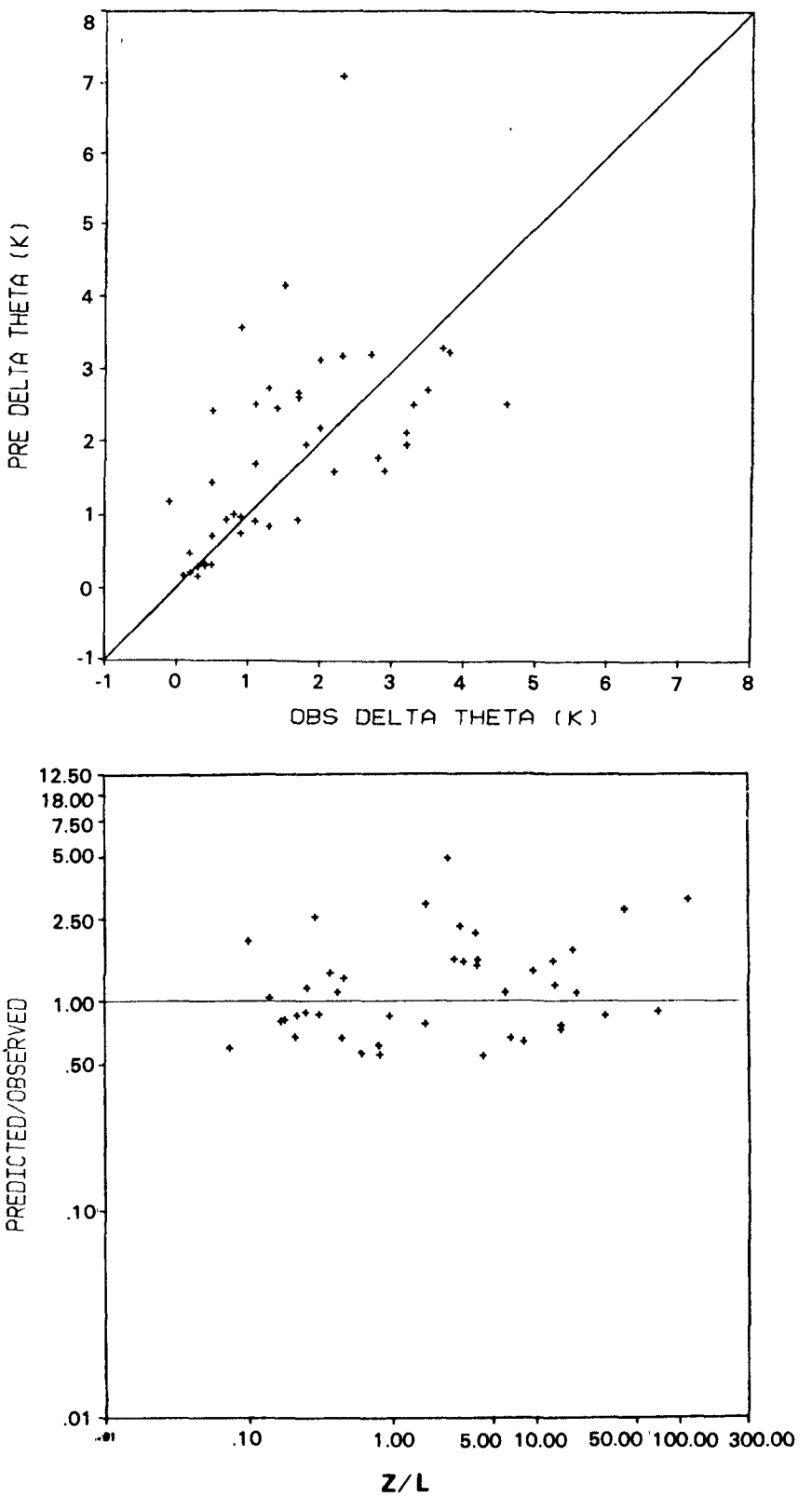

Figure 36. Comparison of the observed potential temperature difference between 10 m and 40 m with that estimated from the Webb extension to the surface-layer similarity theory and Ri_b (10 m) at CCB.

(1985). They suggest that the dimensionless wind shear should have the form

$$\phi_m = 1 + (4.93\ z/L)\ \exp\ (-.29\ z/L) \qquad (36)$$

This profile mimics the traditional ϕ_m for z less than L, but allows ϕ_m to approach a constant value at greater heights. If we assume that ϕ_h should have the same form, then we obtain a temperature profile similar to that reported by Stull (1983) and Yamada (1979), provided that we assume that the height at which the temperature gradient reaches 2% of the total gradient through the depth of the ground-based inversion is between 3 and 4 times L. With this choice of the dimensionless wind speed shear and temperature gradient profiles, the bulk Richardson number provides a transcendental equation for L. The results of using this expression with the data presented in Figures 33 and 34 are presented in Figures 37 and 38. The performance is nearly the same as that obtained with the Webb extension, but the computed values of L are not as small for Richardson numbers approaching 0.2.

The relationship between Ri_b and L obtained by assuming Equation 36 is valid for all z does not require that the Richardson number be less than some critical value. Consequently, an estimate for L can be obtained for all stable hours in the CCB modeling database (i.e., all Ri_b). Figures 39 and 40 contain the results of comparing observed with predicted values of wind speed and temperature difference at 40 m for all stable hours.

All of the points in Figures 39 and 40 that were not included in Figures 37 and 38 appear at z/L greater than approximately 20. Because z is taken to be 40 m in these plots, z/L = 20 is equivalent to L = 2 m, which is the lower height for the data used to calculate Ri_b. The ability of these extended profiles to match the observed profiles beyond z = 10L deteriorates as z/L increases. This is especially true for the temperature profile. In fact, the behavior of the residuals seen in Figure 40 suggests that there is a systematic problem with the assumed temperature profile.

The expression for the temperature difference is

$$\theta_2-\theta_1 = \frac{u_1^2\ \theta_1}{gL}\ \frac{\ln\ (z_2/z_1) + 17\ [\exp\ (-.29\ z_1/L) - \exp\ (-.29\ z_2/L)]}{\{\ \ln\ (z_1/z_o) + 17\ [1- \exp\ (-.29\ z_1/L)]\}^2} \qquad (37)$$

The subscript 1 denotes data at 10 m, and the subscript 2 denotes data at 40 m. If the 10-m wind speed is held constant, $\theta_2-\theta_1$ begins to drop sharply at $z_2/L = 20$, and does not recover again until z_2/L is greater than approximately 400. Its minimum value is approximately one tenth its value for $z/L \simeq 400$, and this apparently accounts for the factor of 10 underestimation seen in Figure 40. No alternate temperature profile assumptions have been tested as yet, but it seems that the observed wind speed and temperature well above L for very small L are the best indicators of speeds and temperatures at even greater heights, and the "correct" form of the profiles as scaled

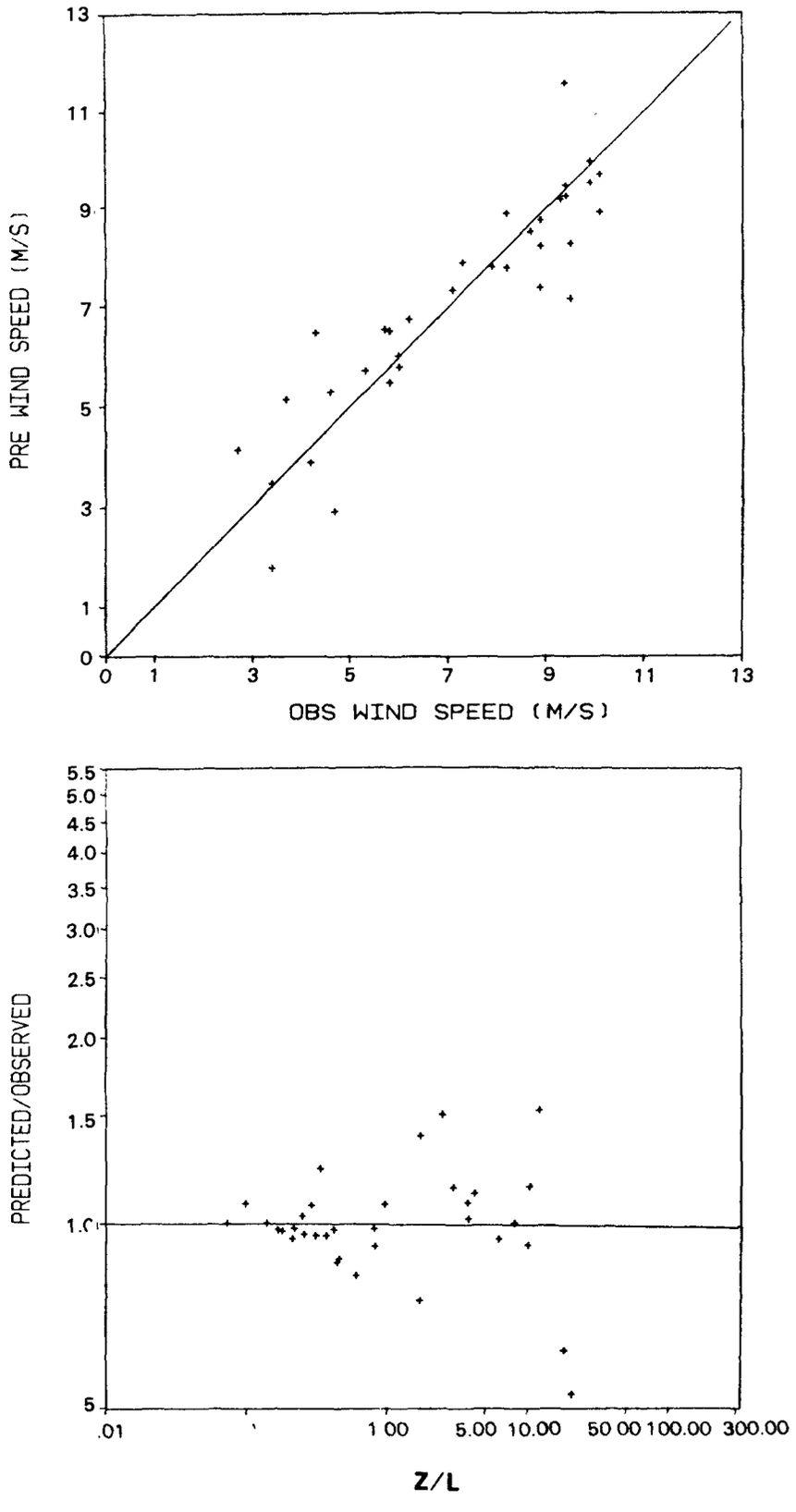

Figure 37. Comparison of the observed wind speed at 40 m with that estimated from the van Ulden/Holtslag extension to the surface-layer similarity theory and Ri_b (10 m) for those data contained in Figure 33.

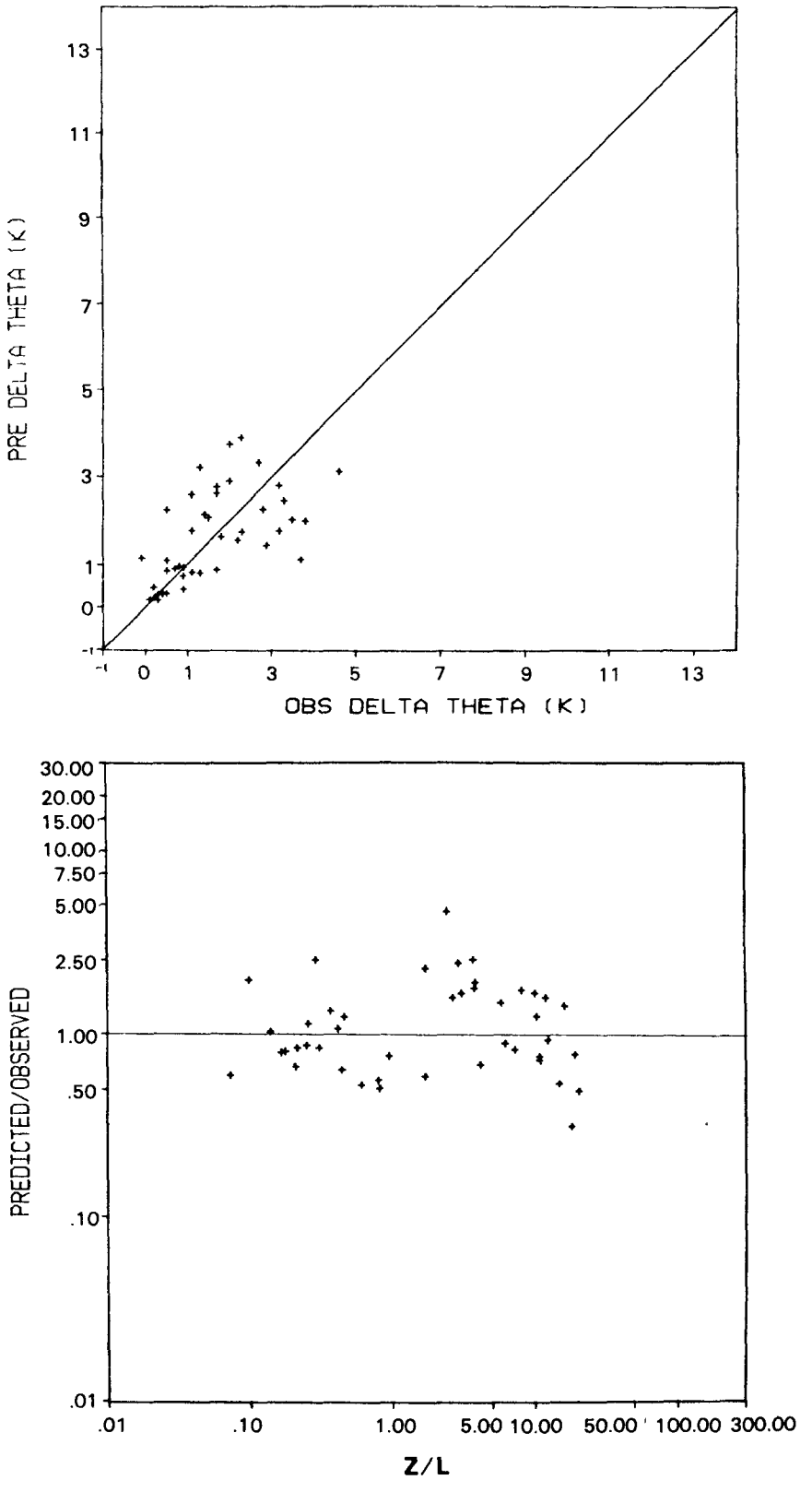

Figure 38. Comparison of observed potential temperature difference between 10 m and 40 m with that estimated from the van Ulden/Holtslag extension to the surface-layer similarity theory and Ri_b (10 m) for those data contained in Figure 34.

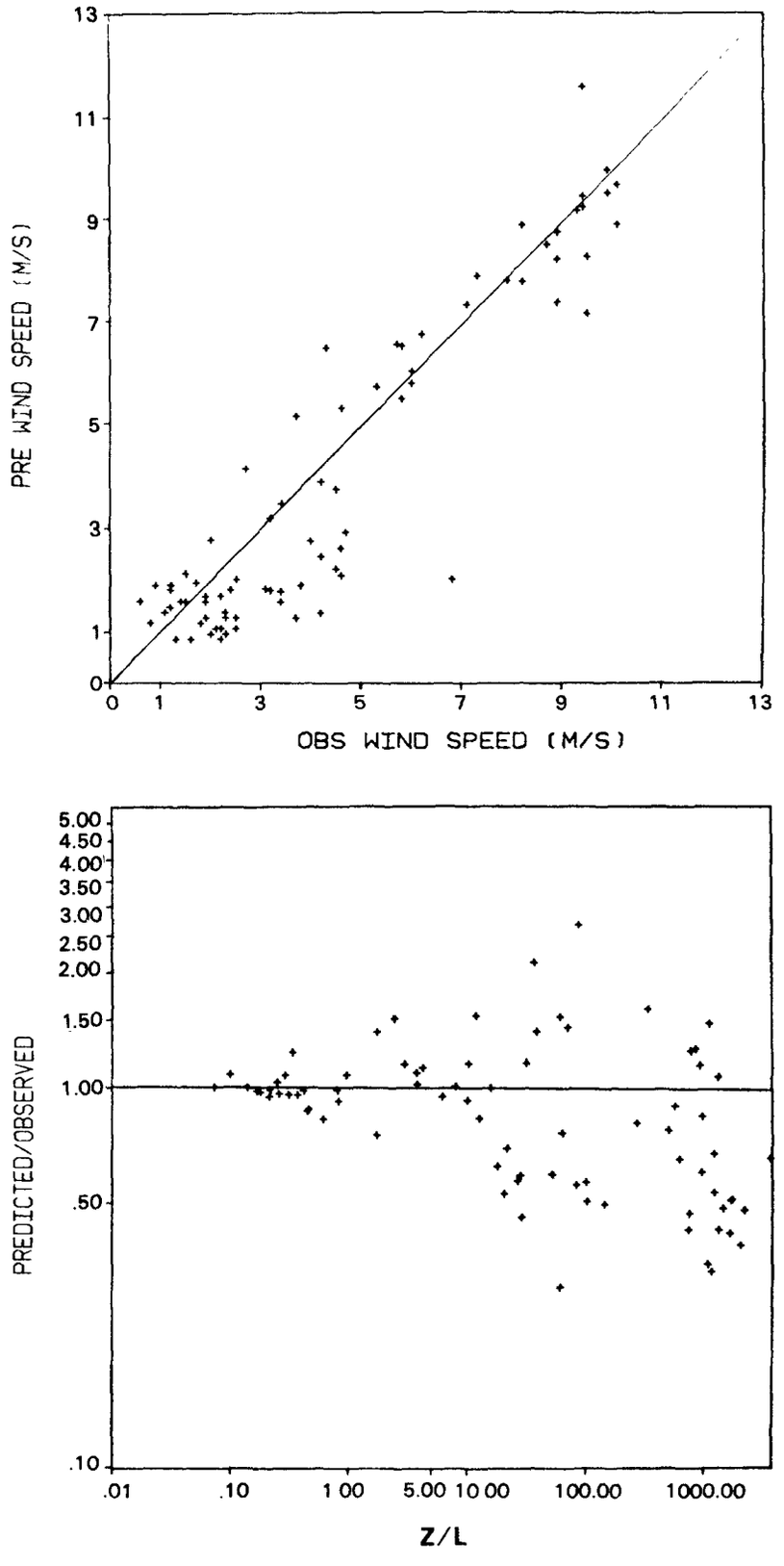

Figure 39. Comparison of the observed wind speed at 40 m with that estimated from the van Ulden/Holtslag extension to the surface-layer similarity theory and Ri_b (10 m) for all stable hours at CCB.

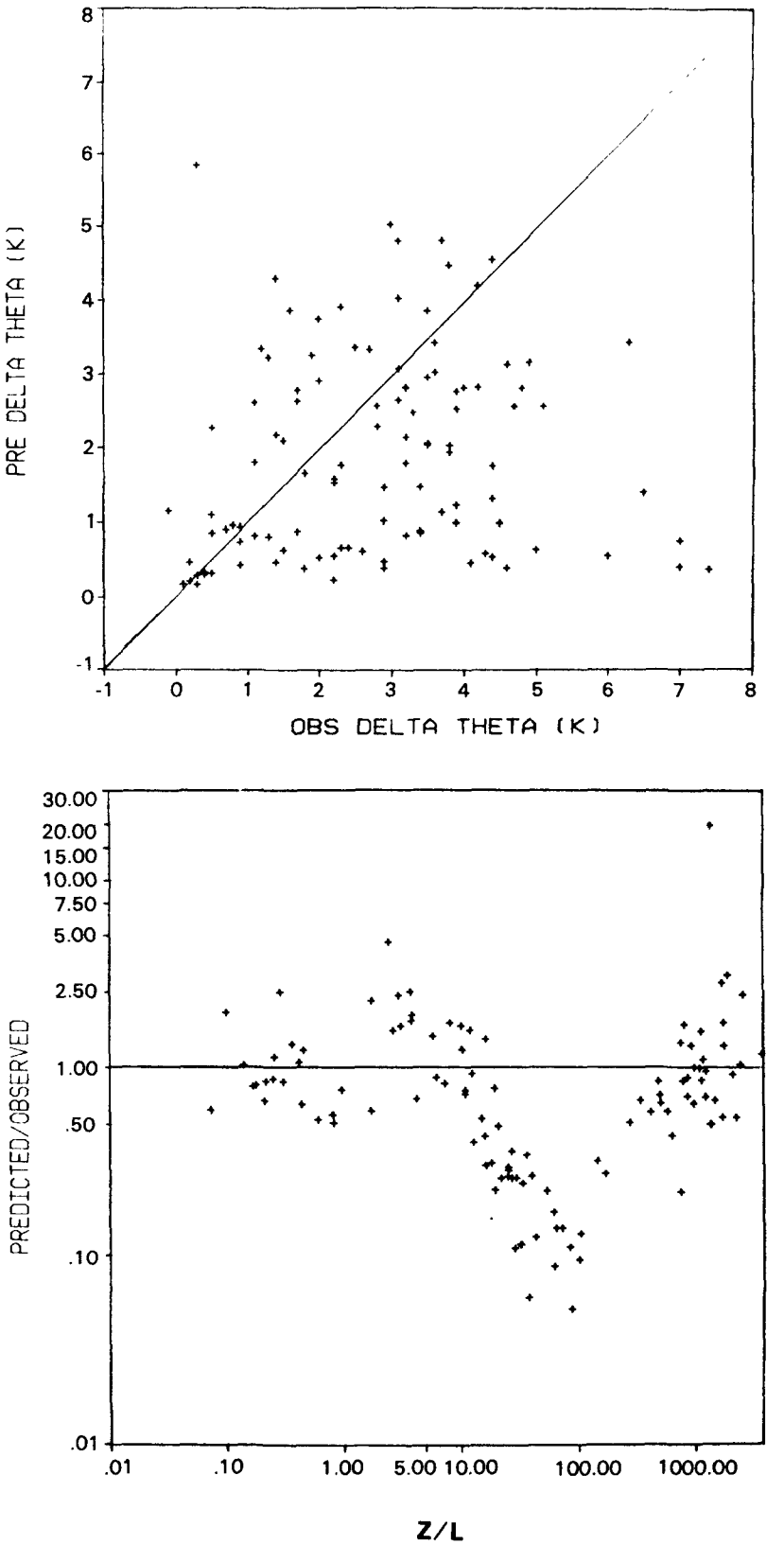

Figure 40. Comparison of the observed potential temperature difference between 10 m and 40 m with that estimated from the van Ulden/Holtslag extension to the surface-layer similarity theory and Ri_b (10 m) for all stable hours at CCB.

by surface properties (L, u_*, θ_*) are relatively unimportant beyond z/L values of about 10. Profiles in this region should not be estimated from surface properties.

These results at 40 m are reproduced at greater heights as well. Figures 41 and 42 illustrate the performance of the profiles in estimating wind speed and temperature at 150 m from data measured at 2 m and 10 m. The wind speed estimate for z/L less than 10 shows somewhat greater scatter, but the real difference in performance is seen at greater values of z/L. There is a strong tendency to underestimate wind speed with increasing z/L. Perhaps this is because the structure of the nocturnal jet is not accounted for.

For $z/L < 1$, the temperature is estimated less well at 150 m than it is at 40 m, there being a tendency to underestimate the observed temperature difference. However, the behavior of the residuals at greater z/L is reproduced. Note that the region of greatest underestimation has shifted toward somewhat greater z/L. Note also that the scatter about this systematic trend is nearly the same in both datasets, which suggests that a different extrapolation method for the temperature profile stands a chance of performing better.

With these encouraging results for the applicability of the extended similarity profiles for wind speed and temperature up to heights of order $z = 10L$, what should we expect of the vertical turbulence velocity (σ_w)?

Within the lower part of the surface layer, σ_w is typically constant with height (i.e., this is the constant flux layer) and proportional to the surface friction velocity (u_*);

$$\sigma_w = a u_* \tag{38}$$

where a is typically 1.2 to 1.3. However, in the outer part of the surface layer, one would expect the turbulence to decrease with height once the Richardson number exceeds 0.2.

Figure 43 shows the behavior of σ_w/u_* as z/L increases. The σ_w data are taken at the oil-fog plume elevation so that photographs and lidar sampling of the plume could serve as a check on the measured values of σ_w. The quotient σ_w/u_* is approximately constant for $z/L < 1$, but increases steadily with z/L beyond 2. Because much of the increase in z/L is associated with a decrease in L, u_* typically decreases on this figure. Therefore, although σ_w may not be growing with z/L, it certainly is not decreasing more rapidly than u_*! This behavior is probably the result of inherently including in measured σ_w vertical velocity fluctuations associated with wave motion and advected turbulence. More will be said about this in subsection 3.4.

HBR Meteorological Data

At HBR, meteorological data were obtained at heights of 2, 5, and 10 m on the 150-m tower. Consequently, bulk Richardson numbers could

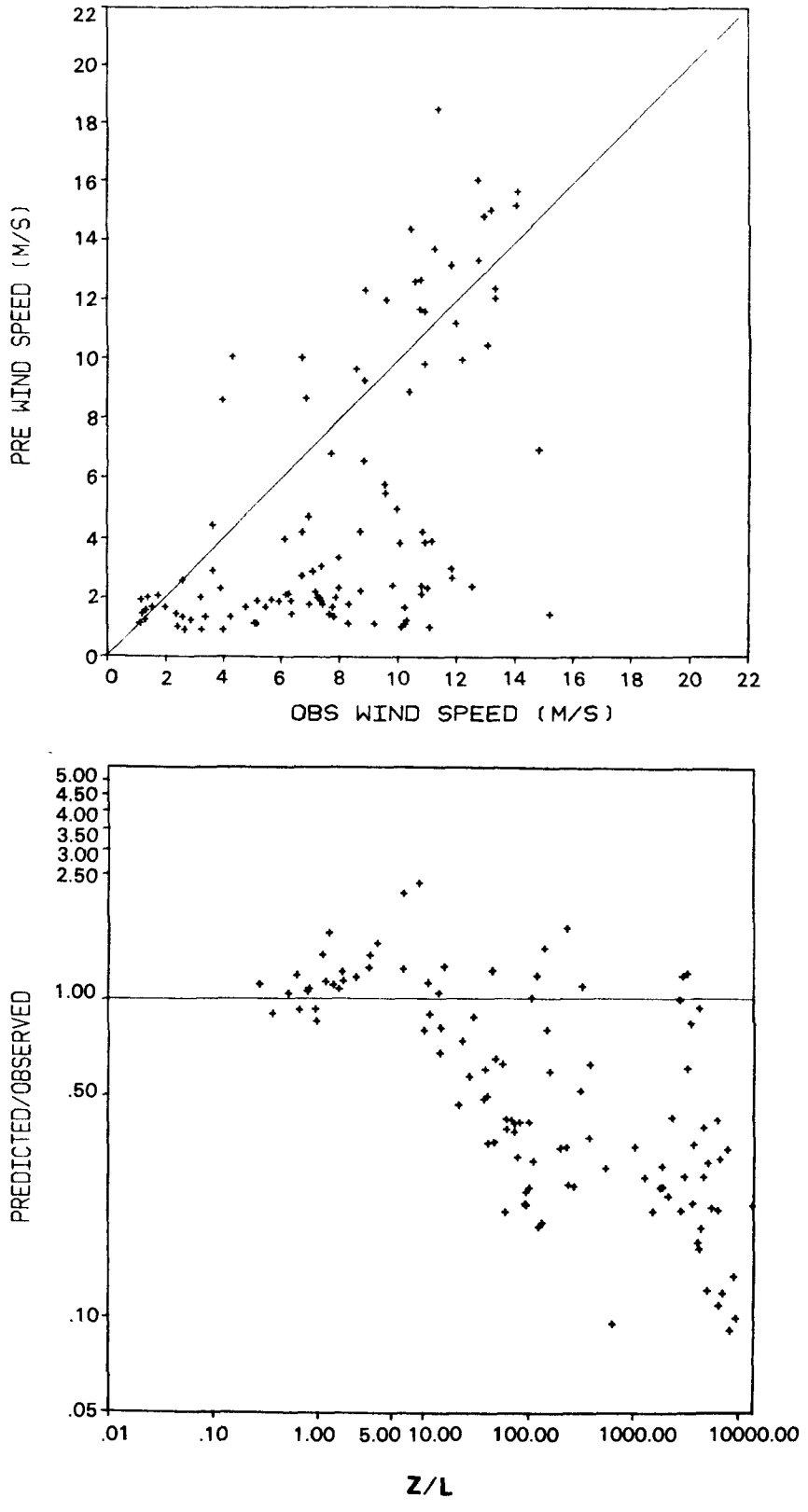

Figure 41. Comparison of the observed wind speed at 150 m with that estimated from the van Ulden/Holtslag extension to the surface-layer similarity theory and Ri_b (10 m) for all stable hours at CCB.

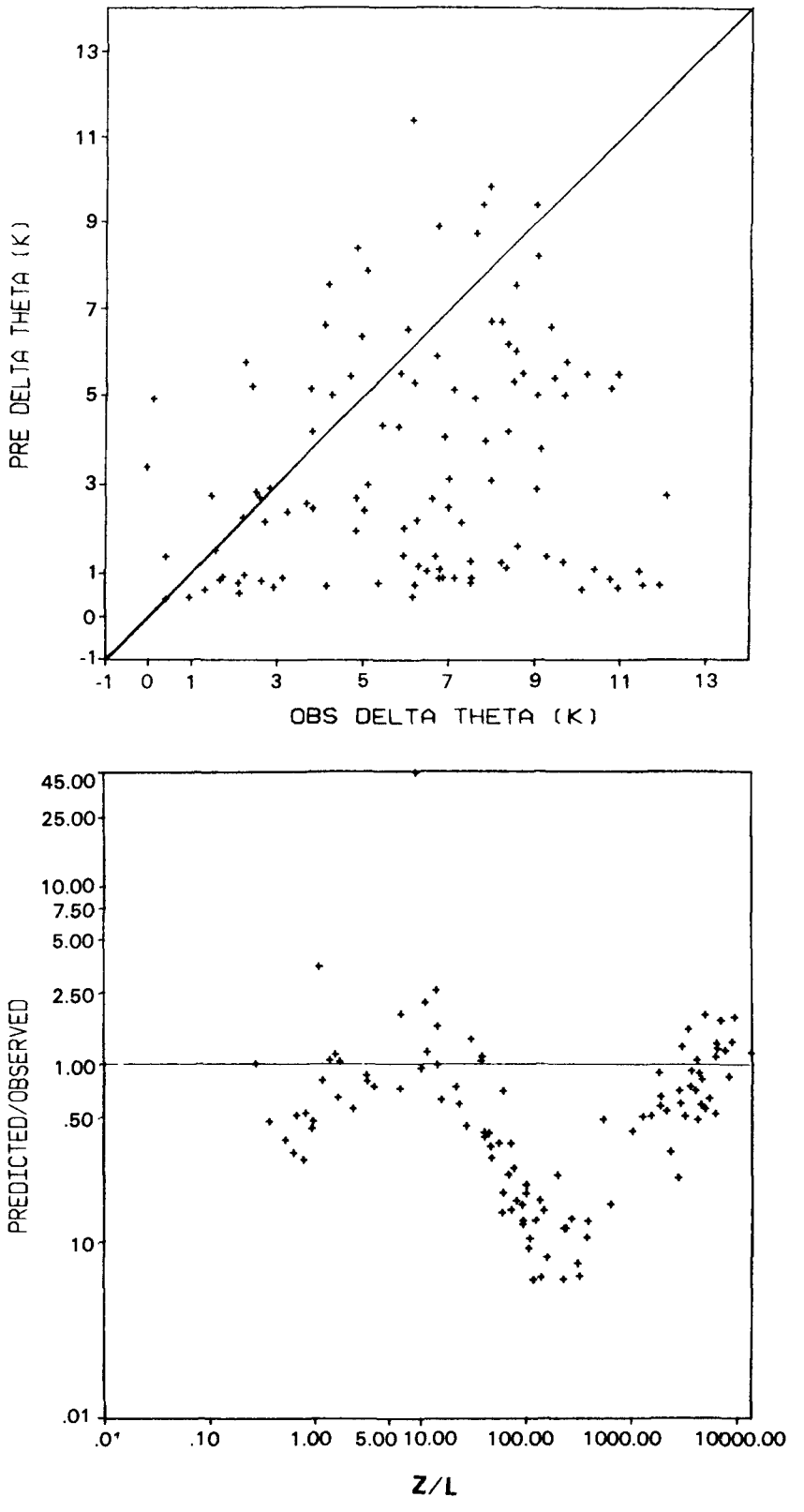

Figure 42. Comparison of the observed potential temperature difference between 10 m and 150 m with that estimated from the van Ulden/Holtslag extension to the surface-layer similarity theory and Ri_b (10 m) for all stable hours at CCB.

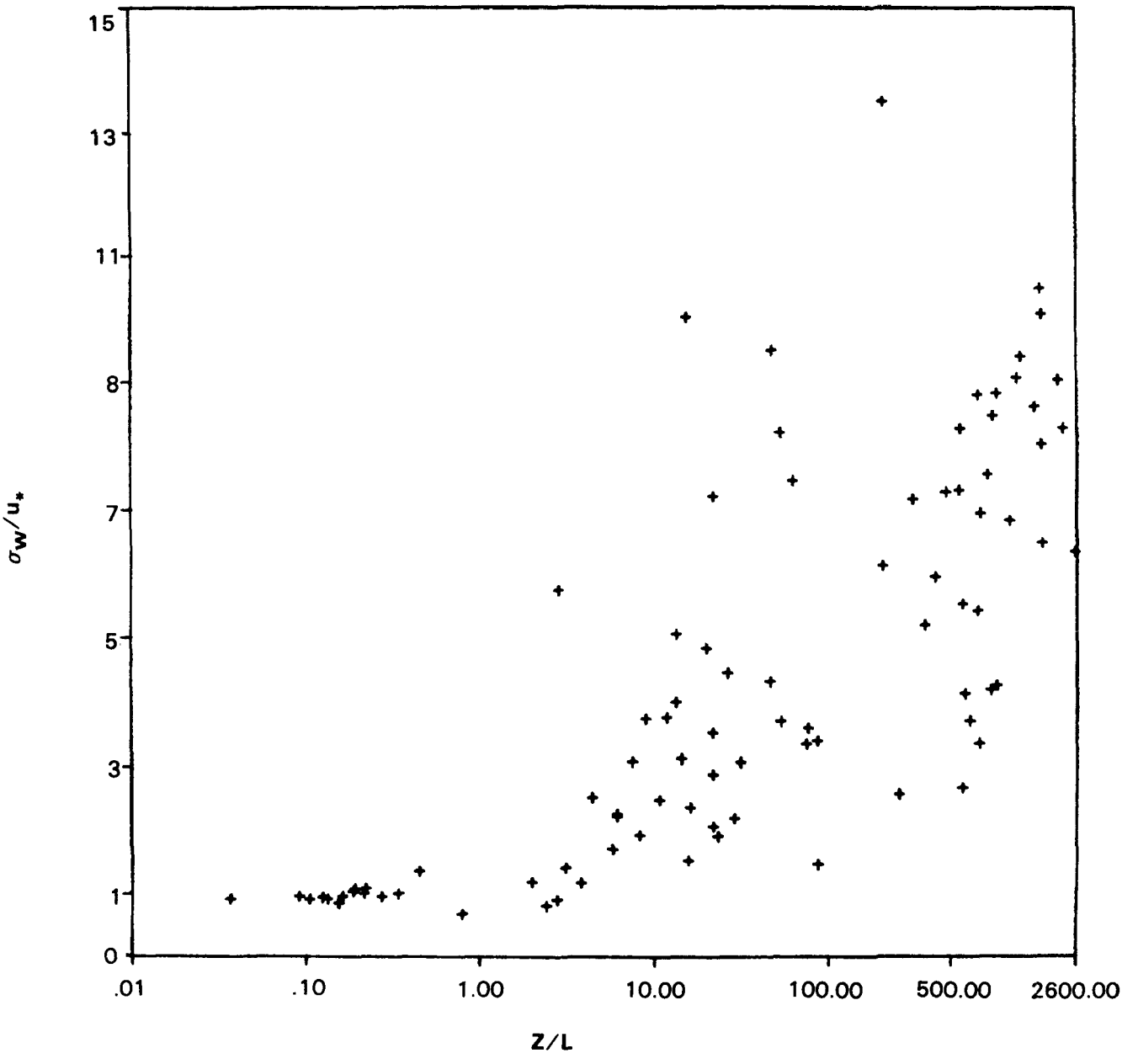

Figure 43. Variation of σ_w/u_* with non-dimensional height z/L at CCB. Data are obtained at or interpolated to the release elevation of the oil-fog plume.

be obtained for the layer between 2 m and 5 m as well as for the layer between 2 m and 10 m.

Wind speeds measured on the 150-m tower at HBR were generally smaller than those measured at CCB. Given the limitation that Ri_b must be less than about 0.2 (see Equation 34), the HBR data base produces 16 values of L for Ri_b (2-10 m), and 26 hours for Ri_b (2-5 m) out of a total of 127 hours.

Figure 44 shows a comparison of those values of L obtained from Ri_b (2-5 m) and Ri_b (2-10 m). There is a definite bias towards larger values when Ri_b (2-5 m) is used to obtain L, and with the exception of four data points well to the right of the 1:1 line, the greatest relative difference between the two estimates of L occurs for small values of L (say, 5 m or less). Of the four "outliers," three points are from hours in which the flow at all levels of the main tower was coming from the "backside" of HBR; that is, the tower was in the lee of HBR.

Residual plots of the wind speed and temperature predicted for 40 m are presented in Figure 45. They show the result of using the profile of Equation 36 (assuming $\phi_h = \phi_m$) to estimate L and thereby the meteorology at the 40-m elevation from the 10-m data. Better estimates of the wind speed are generally obtained for z/L less than 10, as was found at CCB (Figure 39). But notice that the scatter is considerably greater at HBR. Beyond z/L = 10, Figure 45 also displays the trend toward underestimating the speed with increasing z/L.

The temperature residuals also tend to follow the pattern observed in the CCB data, but the scatter is very great.

In general, the utility of attempting to extend the surface similarity profiles to heights in the neighborhood of z/L = 100 and greater is dubious.

One reason for the poorer comparison of the profile estimates at HBR is the presence of the low-level flow away from or parallel to HBR that was frequently observed during the experiments. In effect, the surface similarity scaling parameters are calculated for a locally-generated flow that would be expected to exert very little influence on the flow at greater heights. As at CCB, it is probably better to consider the structure of the elevated flow separately from that at the surface when L is very small. Indeed, this is what the surface similarity theory would advocate. The overall results of these analyses of the CCB and HBR observations indicate that the similarity relationships reproduce the observations fairly well (to within a factor of 2.0) to elevations less than about 10 L. Above 10 L the predictions have little reliability.

3.4 Analysis of $\sigma_z(t)$ Observed During FSPS

One of the most critical quantities for an air quality model to predict accurately in a stably-stratified atmosphere is the growth of

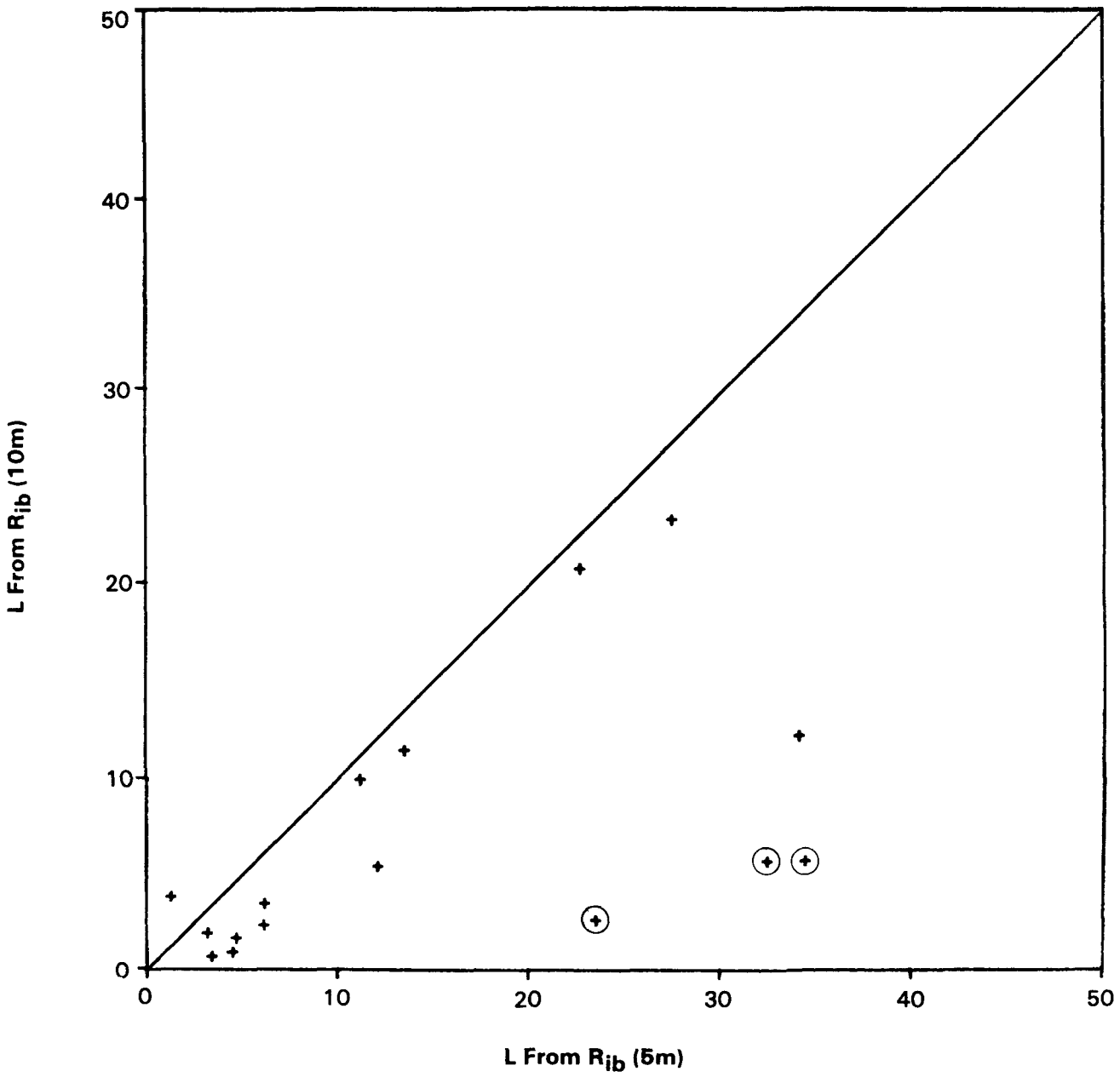

Figure 44. Comparison of values of Monin-Obukhov length L obtained for HBR using the bulk Richardson number method and gradients obtained between 2 m and 5 m, and 2 m and 10 m. The three circled data points are from hours in which the meteorological tower was in the lee of HBR.

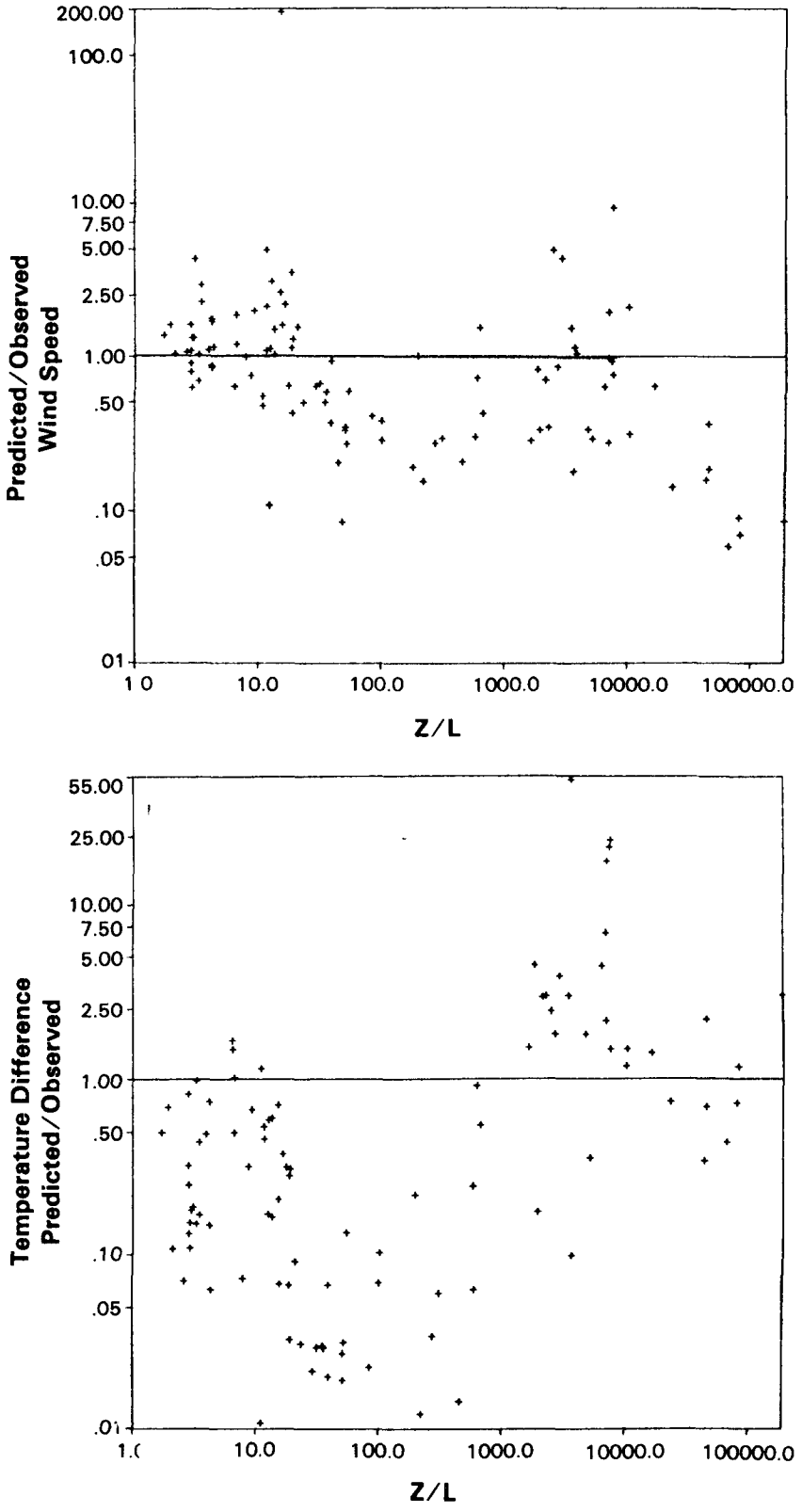

Figure 45. Comparison of observed wind speed (top) at 40 m and potential temperature difference (bottom) between 10 m and 40 m with that estimated from the van Ulden/Holtslag extension to the surface-layer similarity theory and Ri_b (10 m) for all stable hours at HBR.

a plume in the vertical (σ_z). A considerable effort went into analyzing σ_z data that were estimated from CCB photographs and lidar data in order to evaluate the σ_w data obtained from the w-props, and to evaluate the algorithm for σ_z contained in CTDM. Satisfactory results were obtained (see Venkatram et al., 1984).

A similar analysis of the growth of σ_z with time is currently underway using the FSPS data, but at Tracy the ranges of height and distance of the observations are considerably greater. The Tracy plume was generally seen to rise to elevations above 150 m, whereas the plumes released at CCB were generally at elevations below 50 m (they were at 30 m to 40 m most frequently). In other words, under very stable conditions, the Tracy plume marked the dispersive conditions at heights (z/L) some 3 to 5 times greater than those at CCB. Furthermore, the Tracy plume could be observed over a much greater distance downwind--generally 4 to 6 km compared to 1 to 2 km at CCB. This data set therefore allows a better evaluation of the evolution of σ_z with time under very stable conditions and is more representative of real air pollutant sources.

From the discussion contained in Section 3.3, we would expect z/L to be much greater than 10 for most of these hours, and so it may be important to distinguish between "turbulence" and "wave motions" measured as σ_w. Just as important, however, is the question of how applicable the σ_z equation obtained from the surface similarity theory is at elevations well in excess of L. Does the plume growth scale with the measured σ_w? Does the plume continue to grow at all after long times of travel? Does the vertical scale of the plume decrease once final plume rise is reached? A preliminary analysis of lidar data obtained during 14 hours from the FSPS has been performed to investigate these questions. More extensive analyses are underway.

3.4.1 Derivation of $\sigma_z(t)$ from the Flux-Profile Relationships

The equation for σ_z contained in CTDM is from Venkatram et al. (1984). Its derivation is based on the empirical flux-profile relationships of surface similarity theory, but the form of the equation in the limits of neutral and stably-stratified density profiles are obtained separately, and then "patched" together. In particular, the length scale for dispersion in the vertical has a neutral form (ℓ_n) and a stable form (ℓ_s) given by

$$\frac{1}{\ell_n} = \frac{1}{\Gamma z} \qquad \frac{1}{\ell_s} = \frac{N}{\gamma^2 \sigma_w} \tag{39}$$

where $\Gamma = k/(a\alpha)$ and $1/\gamma^2 = \sqrt{B}\, a^2$. Note that k is the von Karman constant, a is the constant of proportionality between σ_w and u_* assumed applicable to the stable boundary layer, and α and B are the constants in the expression for the dimensionless temperature gradient

$$\phi_h = \alpha + \beta\ z/L \tag{40}$$

Venkatram et al. (1984) suggested that the length scale for diffusion in the vertical could be constructed as

$$\frac{1}{\ell} = \frac{1}{\ell_n} + \frac{1}{\ell_s} \tag{41}$$

This assertion is not necessary. Virtually the same result is obtained directly from the flux-profile relationships. Assume that passive material diffuses in the same way as heat in a turbulent flow so that $K_z = K_H$ and

$$K_z = \frac{u_* kz}{\phi_h} \simeq \frac{\sigma_w kz}{a\ \phi_h} \tag{42}$$

Therefore the length scale is defined as

$$\ell = \frac{K_z}{\sigma_w} = \frac{kz}{a\phi_h} = \frac{kz}{a(\alpha + \beta z/L)} \quad . \tag{43}$$

z/L is related to the gradient Richardson number and hence to N/σ_w by assuming that $\sigma_w = au_*$:

$$\frac{z}{L} = \frac{\phi_m^{\ 2}}{\phi_h} Ri = \left(\frac{Nkaz}{\sigma_w}\right)^2 / \phi_h \tag{44}$$

By replacing ϕ_h with $(\alpha + \beta\ z/L)$ and solving for z/L,

$$\frac{z}{L} = \frac{1}{2}\ \frac{\alpha}{\beta}\ \left((1 + \beta\ (2Nkaz/\alpha\sigma_w)^2)^{0.5} - 1\right) \tag{45}$$

Let $1/\gamma^2 = \sqrt{\beta}\ a^2$ and $\Gamma = k/(a\alpha)$ as before, then

$$\frac{1}{\ell} = \frac{1}{2\Gamma z} + \sqrt{\left(\frac{1}{2\Gamma z}\right)^2 + \left(\frac{N}{\gamma^2 \sigma_w}\right)^2} \tag{46}$$

This expression has the limiting form of $\ell = \ell_s$ when z is very large (for non-zero N), and $\ell = \ell_n$ when N is nearly zero (for finite z).

This derivation relies only on the appropriateness of the flux-profile relations for the surface layer and on the assumption that σ_w is proportional to u_*. Beyond the surface layer, the length scale for turbulent mixing still should scale with σ_w/N when stratification is important, and Venkatram et al. (1984) assume that the factor γ^2 obtained from surface layer data is a property of turbulent mixing in a stably stratified atmosphere, and is therefore applicable at any height above the surface. However, the scale $\gamma^2\sigma_w/N$ is only appropriate if σ_w is due solely to turbulence. Boundary layer theory (e.g., Van Ulden and Holtslag 1985) suggests that turbulence decays to nearly zero at the top of the surface layer (of order 3 or 4 L?), so that the measured σ_w at greater elevations is produced by waves, by advected turbulence from terrain features upwind, or by turbulence induced by internal shear layers. If Equation 46 is to be valid, the wave portion of the measured σ_w must be isolated and removed.

Csanady (1964) and Pearson et al. (1983) have discussed mixing and diffusion in the presence of waves. In this theory, measurement of the vertical temperature flux as well as the mean temperature gradient and σ_w are needed to estimate γ^2 (Hunt 1982, 1985). In essence, γ^2 is treated as a variable parameter which indicates how much of the measured σ_w is able to cause mixing as evidenced by the measured temperature flux. Consequently, γ^2 can become quite small in the presence of waves.

From a modeling viewpoint, we are interested in how rapidly σ_z changes with travel time after plume rise in a stably-stratified atmosphere. During the rise of a buoyant plume, the turbulence generated by the rising plume mixes the plume over a volume that is related to the amount of plume rise. This growth due to buoyancy is typically modeled (Pasquill, 1976) as Equation 30. Beyond this point, the rate of growth is dominated by the turbulence of the flow. If the ambient turbulence is small enough, then the rate of additional growth will be nearly imperceptible when compared to σ_{zb}.

3.4.2 Lidar Data on Plume Growth

The oil-fog plume from the Tracy stack was sampled by the WPL ground-based lidar. The plume was usually sampled in a cross-wind vertical plane at about five downwind azimuths out to distances of about 5 km when the plume traveled along the river valley toward the east. One sequence of scans along a trajectory of the plume could be completed in a period of 5 minutes. Consequently, the plume was sampled in each scanning plane about 12 times during each hour.

WPL processes these data and produces a distribution of oil-fog concentration for each scan. The centroid and moments of this distribution are then computed. An hourly-averaged plume cross-section is also produced for each scanning plane by superimposing the 12 concentration distributions from each individual scan during the hour. This enables the hourly average plume

statistics (e.g., centroid position and the moments σ_y and σ_z) to be obtained.

This analysis of plume growth focuses on the hourly-average lidar data and thereby avoids problems in trying to work out the relationship between instantaneous plume cross-sections obtained for times-of-travel varying from a few minutes to a half hour or more, and it also avoids the problem of identifying the meteorology that most influences each of the scans. Use of the average data also reduces the variability associated with the discrete sampling, and provides a measure of time-averaged plume spread that includes any vertical wave motions.

A total of 14 FSPS experiment-hours were selected from those hours processed by WPL and from the subset of the FSPS defined by the top one-third of the entire SF_6 concentration data set. These same hours were also used in the Tracy modeling analysis which is presented in subsection 5.4. They represent stable, plume impingement conditions when the plume was transported towards the Beacon Hill or Target Mountain areas.

The initial growth of the plume due to entrainment associated with the buoyant rise of the plume (σ_{zb}) was estimated from the hourly-averaged lidar scan made nearest the stack, once the plume had leveled off. Typically, σ_{zb} was estimated for a distance of 700 m from the stack. The lidar scans taken downwind of this distance were then used to evaluate the subsequent growth of σ_z.

WPL provided maps of the plume centroid position for each scanning plane during each hour. Those scans obtained when the plume was in the vicinity of Beacon Hill or Target Mountain for more than half of the hour were not included in this analysis because we wanted to evaluate the evolution of the plume before terrain effects became important. A total of 43 observations were used in this analysis--with the downwind distance of the plume centroid ranging from 293 to 4944 m from the stack.

3.4.3 Comparison of Model Predictions with Observations

Figure 46 shows a plot of $\sigma_z/\sigma_w T$ versus T/T_L, where the Lagrangian time-scale is

$$T_L = \frac{\ell}{\sigma_w} \; ; \quad \frac{1}{\ell} = \frac{1}{2\Gamma z_r} + \sqrt{\left(\frac{1}{2\Gamma z_r}\right)^2 + \left(\frac{N}{\gamma^2 \sigma_w}\right)^2} \tag{47}$$

where $\gamma = 0.52$, $\Gamma = 0.36$, and z_r is the effective height of the plume. Both σ_w and N are calculated from data collected at the 150-m level of Tower A. The time T is taken to be

$$T = t + t_v \tag{48}$$

where t_v is the virtual time-of-travel given by

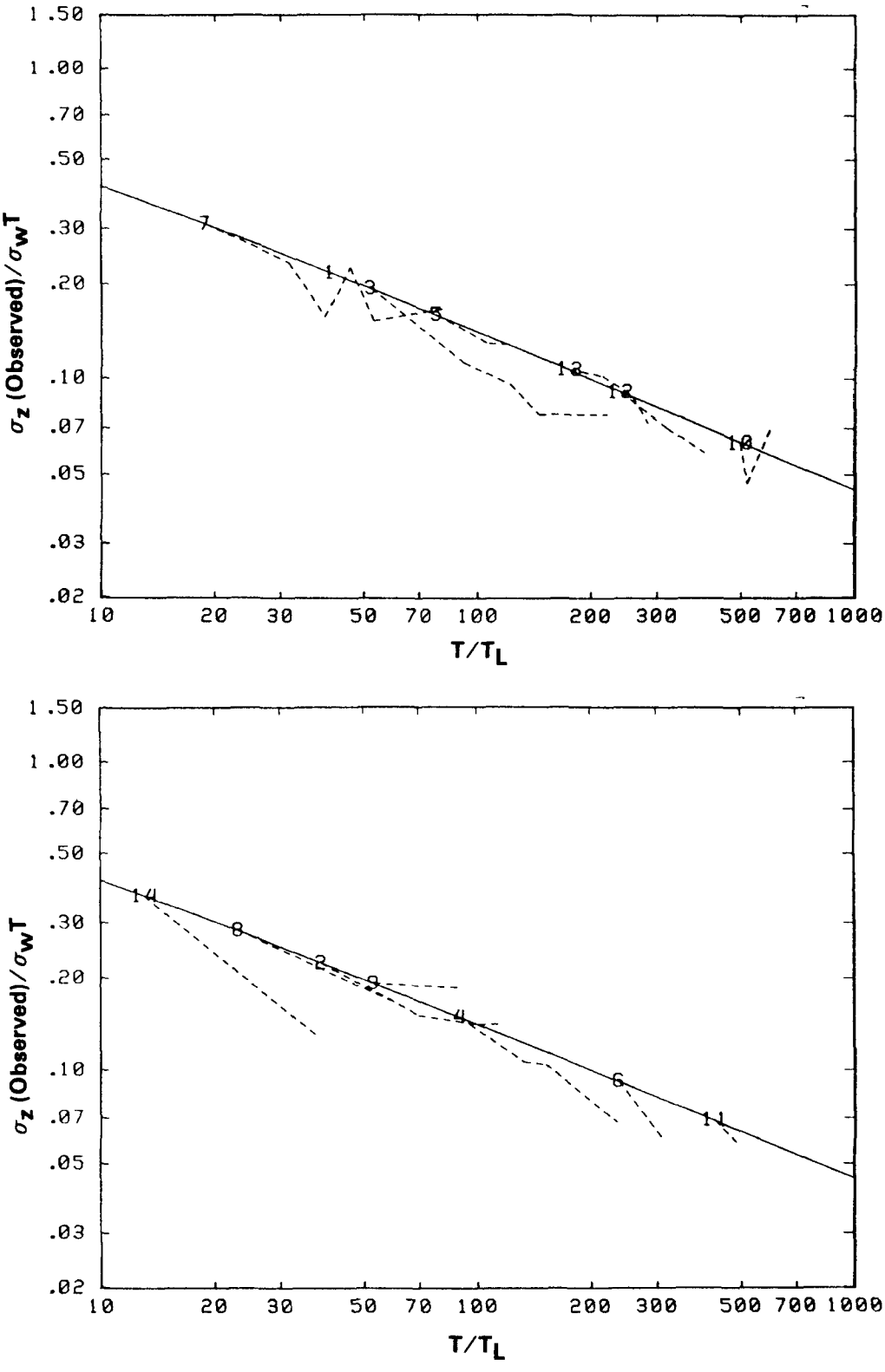

Figure 46. Variation of $\sigma_z/\sigma_w T$ with T/T_L using the CTDM formulation for σ_z.

$$t_v = \frac{1 + \sqrt{1 + 4\left(\frac{2T_L\sigma_w}{\sigma_{zb}}\right)^2}}{T_L\left(\frac{2\sigma_w}{\sigma_{zb}}\right)^2} - t_b \qquad (49)$$

where t_b is the travel time from the stack to the point at which σ_{zb} is measured. The travel time t is taken to be x/u_r where u_r is the wind speed at z_r, i.e., 150 m for the 14 hours.

The solid line in the figure is the relationship given by

$$\sigma_z = \frac{\sigma_w T}{\left(1 + \frac{T}{2T_L}\right)^{0.5}} \qquad (50)$$

which is the equation for σ_z used in CTDM. Each of the 14 hours is labeled by a number. The number for each hour corresponds to the σ_{zb} value estimated from the lidar data for that hour. It was set to fit the model for σ_z exactly. The subsequent values for each hour (represented by the dashed lines) compare the model estimates to the observed values. For the entire ensemble the model estimates of σ_z (and T_L) are roughly within 50 percent of the observed values. Note however that the observed data tend to fall below the model line. This indicates that the subsequent growth of σ_z beyond σ_{zb} is actually overestimated, in general, by the model.

This tendency of the observed plume growth to be overestimated by the model could result from modeling T_L incorrectly, not screening out the wave contribution to σ_w, or not accounting for a collapse of the plume in the vertical after plume rise. None of these possibilities has been investigated in detail as yet. Currently, a method for estimating γ^2 using vertical temperature flux and σ_w data is being tested in the CTDM σ_z-algorithm. This method, which is based on the theory of Pearson et al. (1983) does not depend on whether the σ_w measurements include waves.

Figure 47 presents the ratios σ_z (observed)/σ_z (predicted) versus time-of-travel. The triangles in this figure represent the σ_{zb} value estimated from the lidar data for that hour which correspond to the numbers in Figure 46. From this figure, the predicted values are generally seen to lie within a factor of 1.5 of the observed values. That is, the predictions lie in the range σ_z (observed)/1.5 to 1.5 σ_z (observed).

Several existing complex terrain dispersion models use the P-G curves to simulate plume growth. It is informative to ask how well do estimates of σ_z taken from the P-G curves match the observed data?

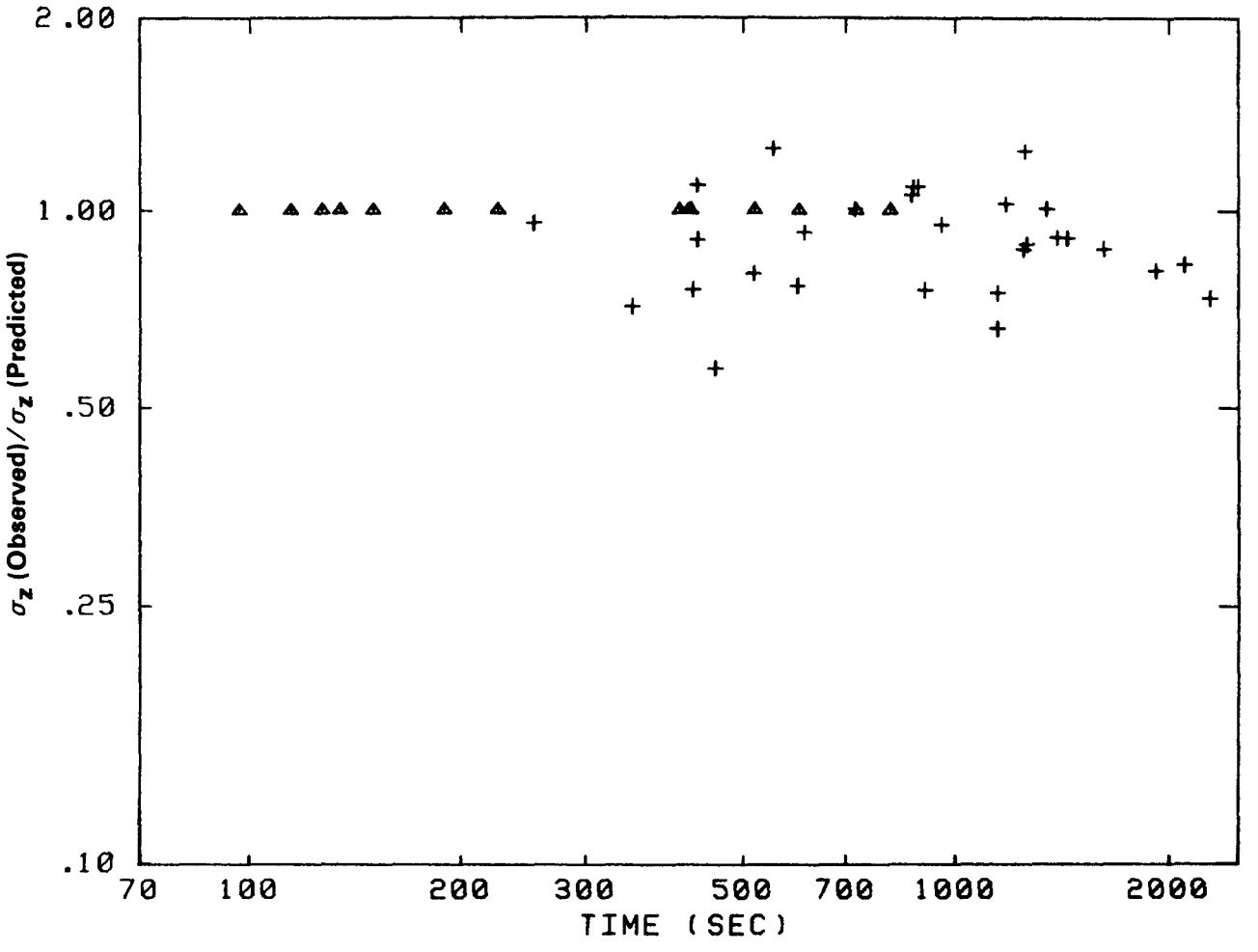

Figure 47. Variation of σ_z (observed)/σ_z (predicted) with travel-time using the CTDM formulation.

To find out, the oil-fog plume observations were compared with σ_z (P-G) where

$$\sigma_z^2 \text{ (P-G)} = \sigma_{zb}^2 + (0.362\ x^{0.55} - 2.7)^2 \qquad \text{for } x < 1000 \text{ m} \qquad (51)$$

$$\sigma_z^2 \text{ (P-G)} = \sigma_{zb}^2 + (33.6\ x^{0.14} - 75)^2 \qquad \text{for } x > 1000 \text{ m} \qquad (52)$$

This is the formulation that is used by COMPLEX I, which adds in quadrature the initial buoyancy-enhanced plume spread to the growth expected due to ambient turbulence for very stable (Class F) conditions. The results of the comparison are displayed in Figure 48 (top).

These results are quite similar to those of Figure 47. Apparently, the slow growth rate prescribed by the Class F P-G curves provides a reasonable (± 50%) estimate of the observed growth rate for this particular data set (14 hours). Note that the points for σ_{zb} (the triangles) do not lie along the perfect prediction line. This results from adding the buoyancy-induced spread to the ambient spread in quadrature. A more direct comparison can be made with Figure 47 if the virtual source method of including σ_{zb} is used. The results are contained in the lower portion of Figure 48. The similarity between these estimates of σ_z, relying on the observed σ_{zb} and the Class F P-G curves, and those obtained by the CTDM algorithm, relying on the observed σ_{zb}, N, σ_w, u, and the surface similarity flux-profile description of diffusion in the stable boundary layer, primarily reflects the dominance of the buoyancy-enhanced growth.

The P-G curves have been interpreted as a description of the growth of a plume with distance for a representative turbulence intensity, i.e., $\sigma_z = \sigma_w \times f(x)$ where x is the downwind distance, f(x) is a function of distance (e.g., the straight line in Figure 46), and σ_w is the representative turbulence intensity. The form of the distance function and the value of the turbulence intensity is specified for each stability class. RTDM has adopted this interpretation as a means for including measurements of turbulence intensity in calculating σ_y and σ_z. The distance function is retained, but the representative turbulence intensity is replaced by the measured value. Specifically, RTDM adopts the Briggs (1973) formulation of the distance functions (based in part on the P-G curves) so that the total estimate of σ_z for stability class F, including buoyancy-enhancement, is given by

$$\sigma_z^2 \text{ (RTDM)} = \sigma_{zb}^2 + (\sigma_w x/u)^2/(1 + .0003x)^2 \qquad (53)$$

The performance of this algorithm is illustrated in Figure 49. It is apparent that this algorithm substantially overestimates plume growth in the vertical for this data set.

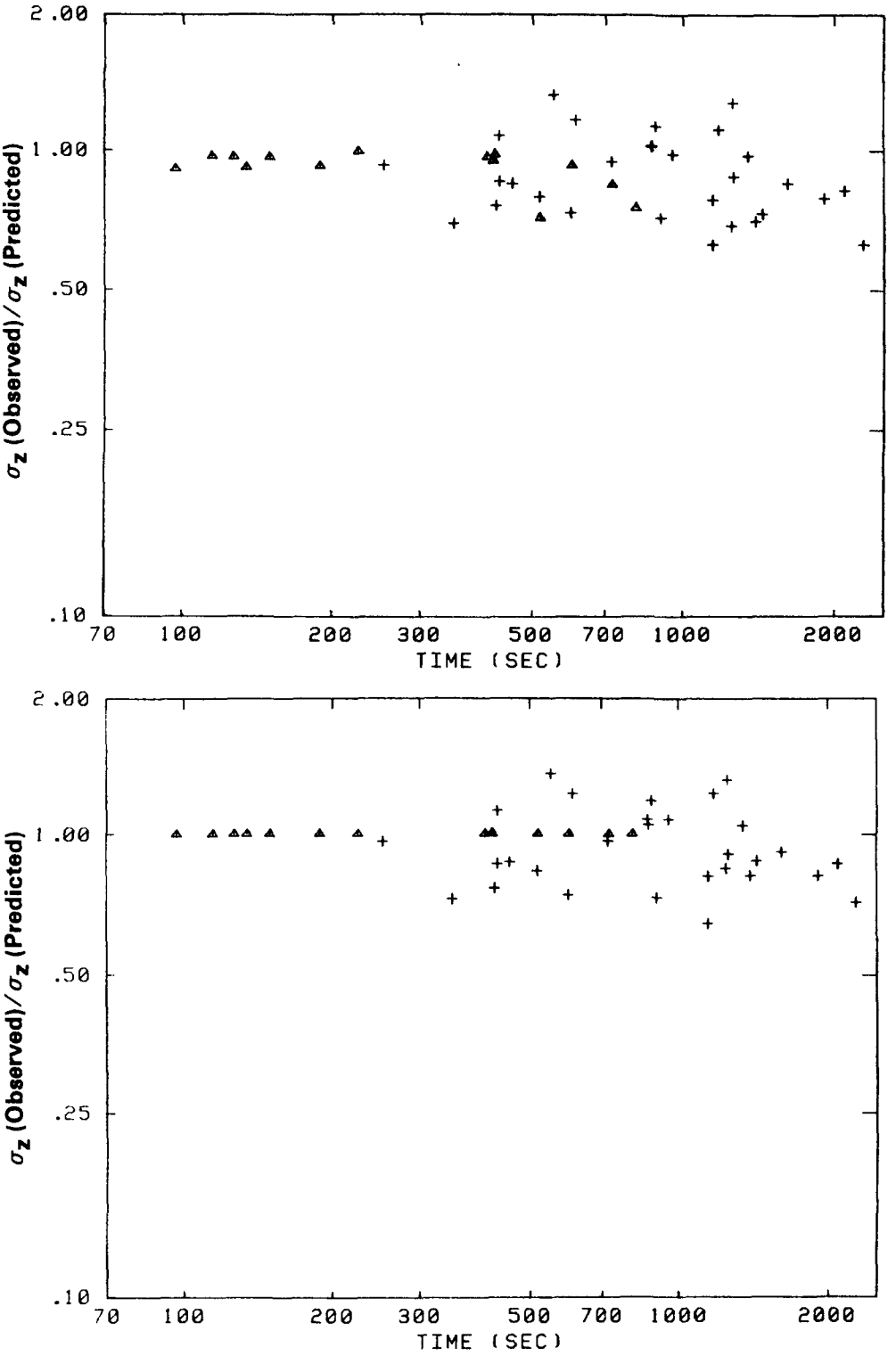

Figure 48. Variation of σ_z (observed)/σ_z (predicted) with travel-time using the PGT formulation. The upper plot corresponds to predicting σ_z by adding the buoyancy enhanced and the ambient turbulence σ_z portions in quadrature, while the lower plot uses the virtual source approach.

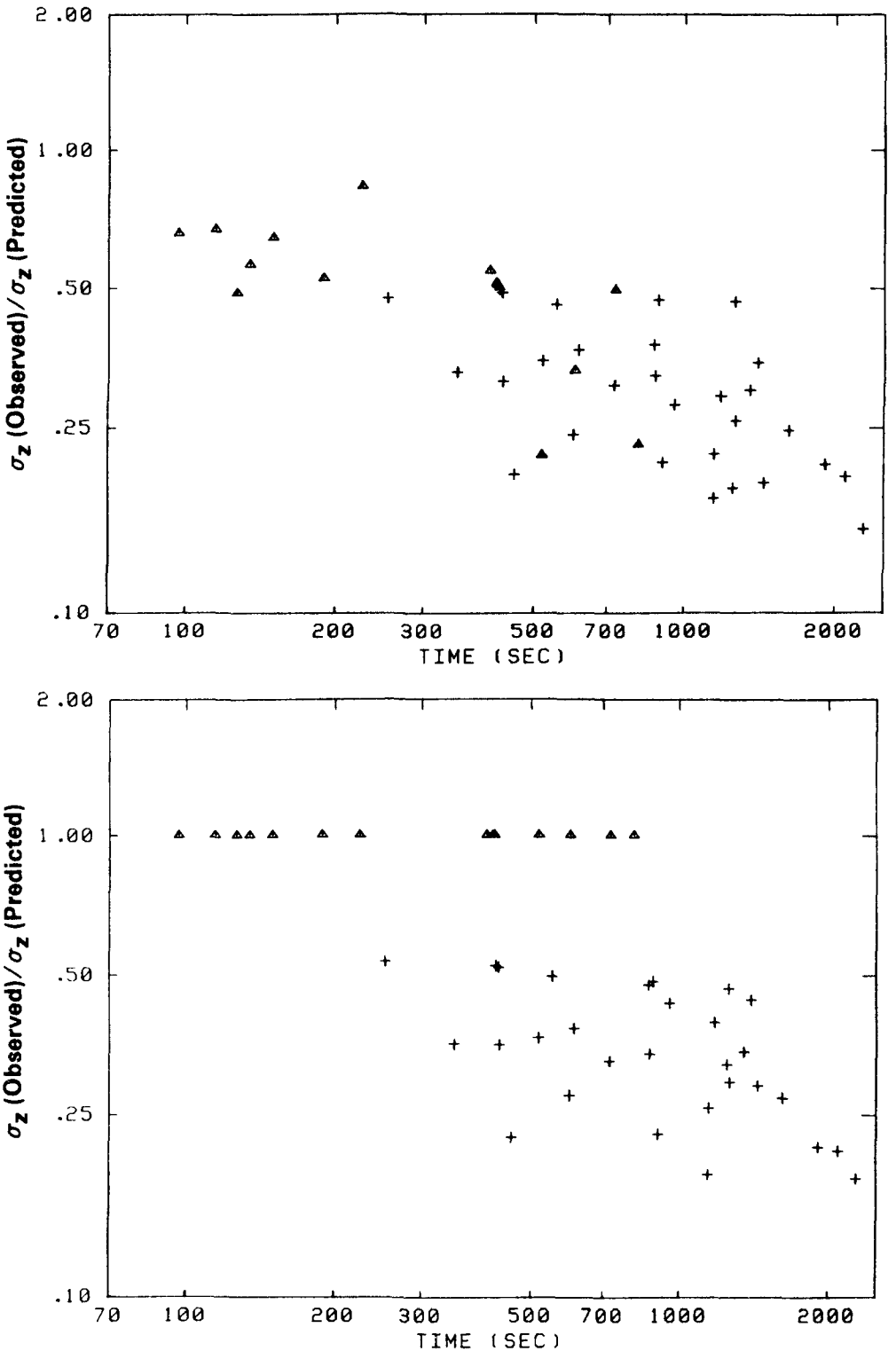

Figure 49. Variation of σ_z (observed)/σ_z (predicted) with travel-time using the RTDM formulation with measured turbulence. The upper plot corresponds to predicting σ_z by adding the buoyancy-enhanced and the ambient turbulence σ_z portions in quadrature, while the lower plot uses the virtual source approach.

If the measured σ_w data contain a significant wave component, and if this is thought inappropriate for the RTDM algorithm, then "default" values of the turbulence intensity might be substituted. The default turbulence intensity for Class F is 0.016 (i.e., the Briggs (1973) expression). The algorithm performs much better when the default turbulence values are used, as shown in Figure 50. This nearly matches the performance of the buoyancy-enhanced P-G algorithm.

This comparison suggests that the turbulence intensity that drives the plume growth should be very small in very stable conditions if the stability-class-dependent distance function is used. What happens if the turbulence intensity of 0.016 is used in the CTDM algorithm, and how does this compare with the assumption that plume growth in excess of σ_{zb} might be ignored? Figure 51 contains the results. The CTDM algorithm overestimates plume growth in only three scans, and the bias has certainly shifted toward underestimating plume growth. In fact, when i_z is set equal to 0.016, the resulting predictions of σ_z are nearly equal to σ_{zb} (i.e., no growth). This is reflected in the degree of similarity between the two plots in Figure 51. Apparently, the inclusion of a turbulence time-scale based upon measurements of N and σ_w is necessary in calculating σ_z if on-site measurements of σ_w are to be used. On the whole, some plume growth must be contained in the σ_z algorithm to match the observations.

The results of this initial analysis of σ_z data from the FSPS at Tracy suggest the following observations on modeling the vertical size of elevated plumes in very stably stratified flows:

- σ_{zb} can at times be a good estimate of plume size at moderate distances (these data go out to about 5 km).
- The slow growth rate of the P-G Class F σ_z curve increases σ_z very little beyond σ_{zb}.
- The growth rate function contained in RTDM (i.e., Briggs 1973) performs poorly in combination with buoyancy enhancement when measured σ_w values are used. The growth rate calculated is much too great.
- The σ_z algorithm of CTDM produces a slow growth in σ_z beyond σ_{zb} even though the measured σ_w undoubtedly contains wave motions. An adequate theory for T_L appears essential when on-site turbulence data are used (the RTDM algorithm contains only a representative value of T_L implicitly in its distance function, and this algorithm performs poorly with the measured turbulence data.)
- The CTDM algorithm tends to overestimate the rate of growth of σ_z, presumably because a portion of the measured σ_w is due to waves.

As a final remark on this analysis, it should be remembered that this subset of the database is biased toward those hours in which the rate of plume growth is relatively small. As such, it is not surprising that a slow growth rate assumption about σ_z (e.g., either the no-growth σ_z, the σ_z (P-G), or the default σ_z

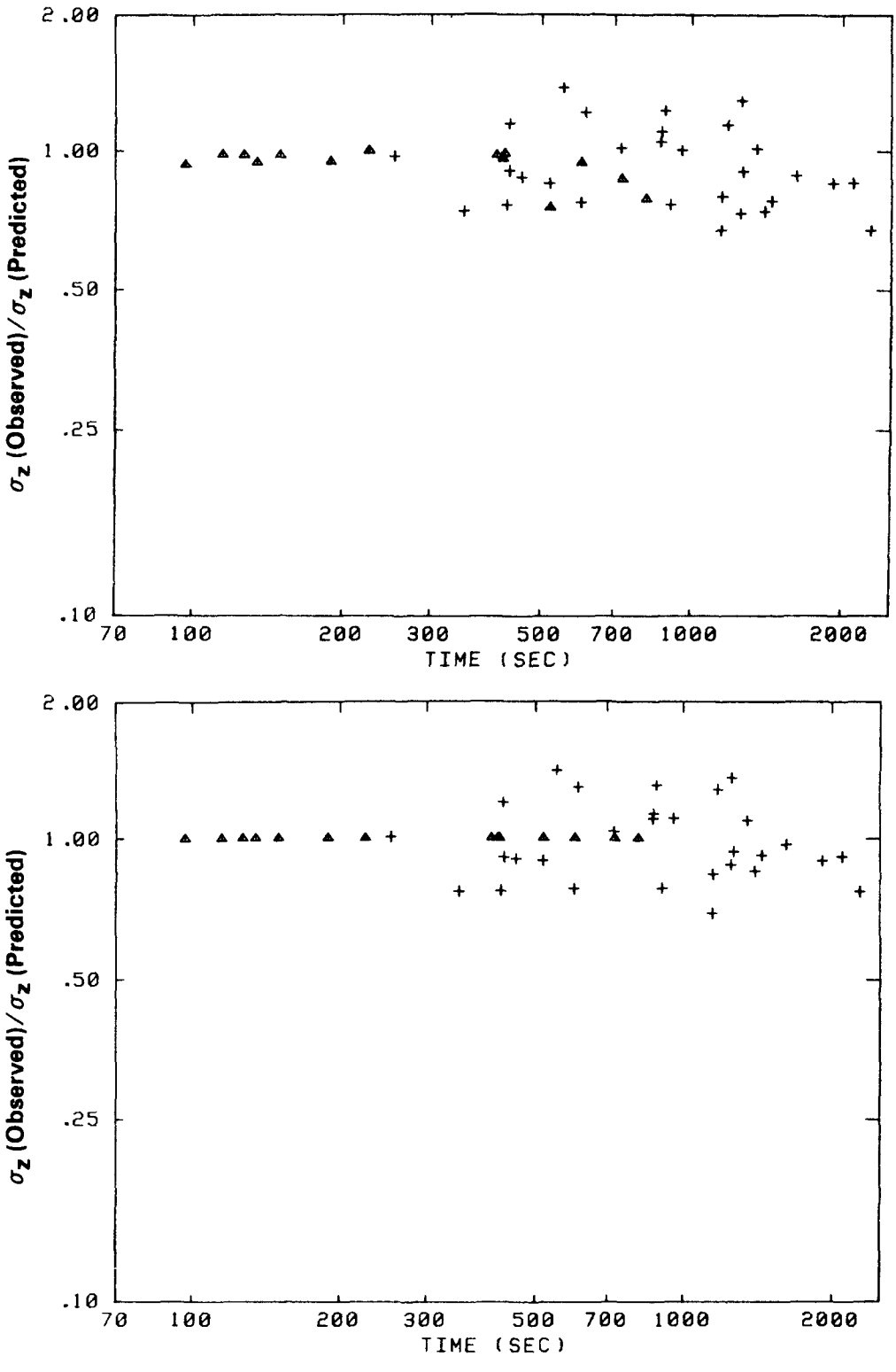

Figure 50. Variation of σ_z (observed)/σ_z (predicted) with travel-time using the RTDM formulation with Briggs rural (ASME, 1979) dispersion coefficients. The upper plot corresponds to predicting σ_z by adding the buoyancy-enhanced and the ambient turbulence σ_z in quadrature, while the lower plot uses the virtual source approach.

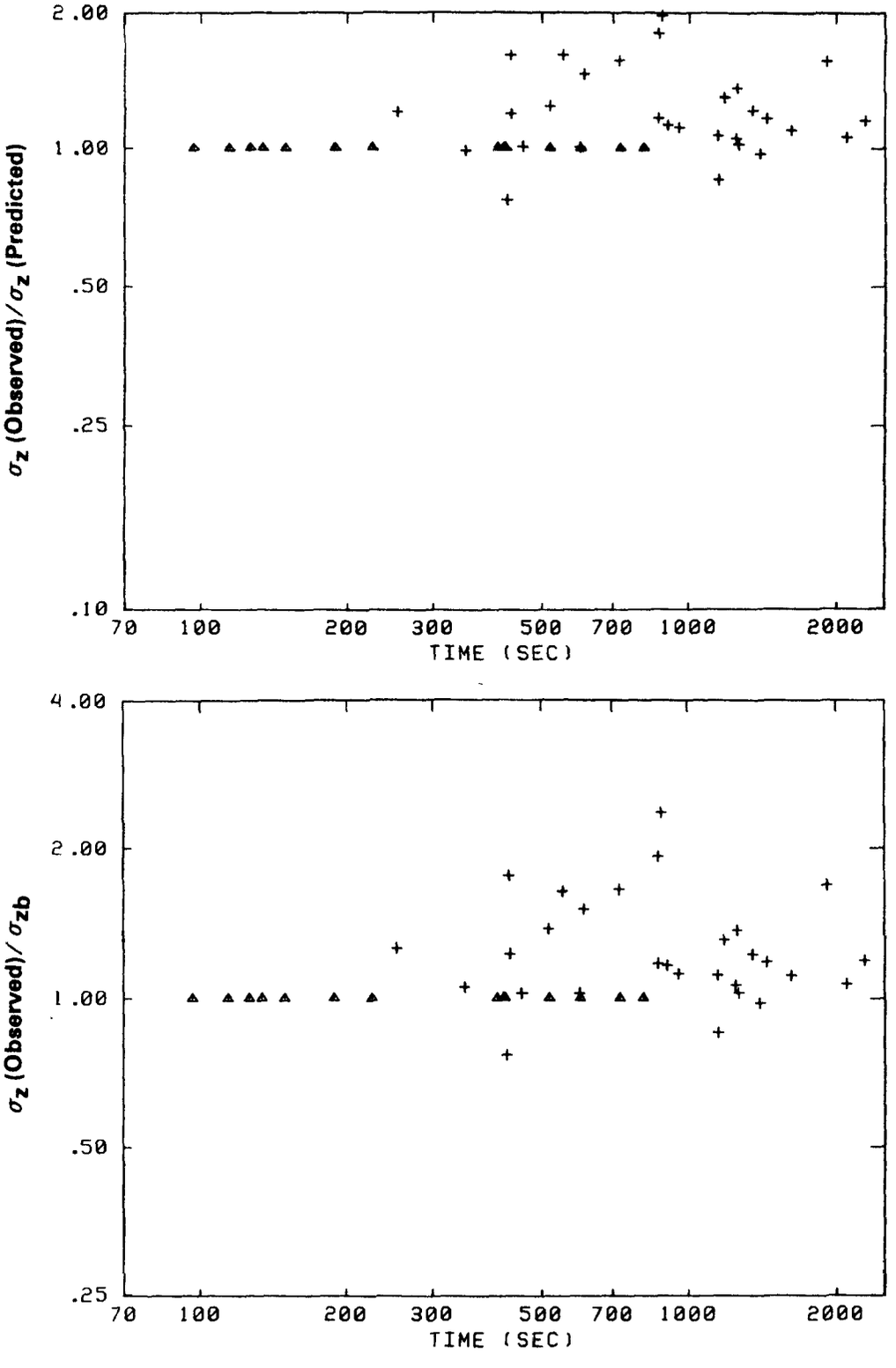

Figure 51. Variation of σ_z (observed)/σ_z (predicted) with travel-time using the CTDM formulation with i_z = 0.016 (upper plot), and variation of σ_z (observed)/σ_{zb} with travel time (lower plot).

(RTDM)) does as well as the σ_z model that uses meteorological data obtained near plume elevation. However, realistic simulations of sequences of hourly concentrations should rely upon observed meteorology rather than worst-case modeling assumptions. To this end, the performance of the CTDM algorithm for σ_z provides encouragement that observed meteorology can be effectively incorporated.

SECTION 4

ANALYSIS OF HIGHEST GROUND-LEVEL CONCENTRATIONS AT EACH SITE

The purpose of this section is to describe the meteorological conditions that produced the highest ground-level concentrations during each field experiment. In particular, the applicability of the dividing-streamline concept to describe stable flow in complex terrain is assessed. For each field experiment, the top ten SF_6 and CF_3Br concentrations are presented along with the meteorological conditions estimated for the release heights. Detailed analyses of four experiment hours are presented to illustrate plume behavior above, below, and near the dividing-streamline height. These four case studies represent the highest ground-level concentrations at each field site. Each case-study analysis includes a description of the observed concentration distribution and meteorological data. Also, a calculated centerline concentration is compared with the observed maximum concentration. Finally, a comparison of the concentration events observed at each of the three field sites is made.

The CCB tracer and flow visualization experiments are described in detail in the First Milestone Report (Lavery et al., 1982). The HBR studies are discussed in the Third Milestone Report (Lavery et al., 1983).

4.1 Cinder Cone Butte

The ten highest observed SF_6 concentrations scaled by the emission rate (shown as χ/Q in units of $\mu s/m^3$) measured at CCB are presented in Table 10a. The net release height (z_r), dividing-streamline height (H_c), and sampler elevation (z_{max}); wind speed (u), sigma-v (σ_v), sigma-w (σ_w), and Brunt-Vaisala frequency (N), all estimated at z_r; and the downwind distance of the sampler (d) are also listed. All heights are referenced to the base elevation of the hill coordinate system. Of the ten highest concentrations, five occurred when $z_r \sim H_c$. Throughout the entire experiment, there were about 20 hours when the SF_6 was released near H_c. During the 15 hours not listed in the table, relatively high concentrations were produced; but the observed wind direction at the emission height was not quite oriented along the stagnation streamline. This resulted in the plume being directed toward a side of the butte. In general at CCB tracer gas plumes released well below H_c tended to remain roughly horizontal and travel around the sides of the hill, producing relatively low

TABLE 10a. TEN HIGHEST χ/Q OBSERVED SF_6 CONCENTRATIONS AT CCB[+]

Exp No.	Hour End	χ/Q ($\mu s/m^3$)	z_r (m)	H_c (m)	z_{max} (m)	$u(z_r)$ (m/s)	$\sigma_v(z_r)$ (m/s)	$\sigma_w(z_r)$ (m/s)	N (1/s)	d (m)
206	08	164.0	30	33	25.3	1.8	.196	.155	.0372	300
214	09	120.0	22	7	30.0	2.7	.533	.278	.0266	353
206	06	115.0	30	33	25.3	1.8	.209	.134	.0347	300
214	05	103.0	15	39	-3.5	1.6	.691	.206	.0653	556
211	05	98.3	11	21	30.0	2.3	.408	.163	.0738	973
206	07	90.3	30	27	31.2	2.4	.208	.142	.0362	437
217	04	85.7	23	0	77.0	5.1	.230	.104	.0289	1089
203	08	83.8	43	36	-2.4	3.4	.449	.181	.0452	160
203	06	83.3	20	40	-2.4	1.0	.230	.091	.0631	394
214	08	73.8	22	18	30.0	2.2	.271	.164	.0470	243

[+]Elevations referenced to base of CCB.

TABLE 10b. TEN HIGHEST χ/Q OBSERVED CF_3Br CONCENTRATIONS AT CCB[+]

Exp No.	Hour End	χ/Q ($\mu s/m^3$)	z_r (m)	H_c (m)	z_{max} (m)	$u(z_r)$ (m/s)	$\sigma_v(z_r)$ (m/s)	$\sigma_w(z_r)$ (m/s)	N (1/s)	d (m)
210	07	75.3	22	11	50.0	5.1	.594	.361	.0388	1060
217	07	64.6	8	0	11.8	4.6	.262	.286	.0200	869
217	08	55.2	8	0	11.8	4.4	.262	.234	.0171	869
210	06	47.5	22	5	50.0	5.5	.225	.155	.0348	944
216	02	36.1	43	7	32.9*	3.6	.441	.123	.0191	1289
214	04	34.4	38	27	99.0	2.8	.338	.145	.0281	709
210	03	32.7	23	22	46.9	3.9	.356	.104	.0591	1003
213	06	30.4	51	45	90.9	3.1	.254	.142	.0456	1099
217	09	25.4	8	0	30.0	5.2	.447	.239	.0256	1270
217	10	24.6	8	0	22.1	5.1	.502	.400	.0087	945

[+]Elevations referenced to base of CCB.
*Concentration measured on lee side of CCB.

ground-level concentrations. Only 2 of the 29 releases below H_c produced concentrations listed in the top ten. Plumes above H_c tended to flow up and over the hill and produced concentrations near the top or on the lee side of CCB. Only 3 of the 60 releases above H_c produced χ/Q values listed in the table.

Table 10b lists the ten highest normalized observed CF_3Br concentrations measured at CCB along with the appropriate release and meteorological information. At CCB, approximately 88% of the CF_3Br releases were made at heights above H_c, about 10% near H_c, and 2% below. Most of the time CF_3Br was released at a height higher than the SF_6 release height. As expected, the highest CF_3Br concentrations occurred when the release height was above the calculated dividing-streamline height, typically at elevations higher than the release height. Four of the highest ten concentrations were observed during the neutral Experiment 217 (H_c=0). Evidently, as shown by the relatively large values of σ_w, there was enough mixing to bring the CF_3Br plume to the hill surface on the windward side.

Of the ten highest observed concentrations, there is only one release (Experiment 210 Hour 3) near H_c. The results of this case are similar to CF_3Br releases above H_c in that the highest concentrations occurred at an elevation higher than the release height.

4.1.1 Experiment 206, Experiment-Hour 8 (0700-0800 MST)

The SF_6 tracer gas and oil-fog were released southeast of the hill at a release height 35 m above the ground. Local terrain elevations near the release point are estimated to be 5.5 m below the base elevation of the hill coordinate system, so the net release height corresponds to the 29.5-m height level on the hill. Although the SF_6 release terminated early at 0753, there was nearly a full hour of tracer impact on the hill because the travel time from the source to the hill center at 1.8 m/s was about 5 minutes.

Wind and temperature data measured at Tower A during this hour were used to characterize the flow in terms of H_c. Because the v-component of the 40-m wind set was missing, wind speeds at this height were estimated before H_c was calculated. The data from the 80-m wind set and the good u-component measured at 40 m were used to infer the 40-m wind speeds.

Time series plots of the calculated 5-minute H_c and bulk hill Froude numbers above H_c ($Fr(H_c)$) for this experiment-hour are presented in Figure 52. The dashed line represents the SF_6 tracer gas release height. At the beginning of the hour H_c is 27 m but quickly rises to above 40 m. H_c falls steadily to below 30 m during the latter half of the hour. $Fr(H_c)$ during the same period exhibits a similar pattern, rising as high as 3.6. The hourly averaged H_c value is 33 m; thus, this hour represents transport along streamlines very near H_c.

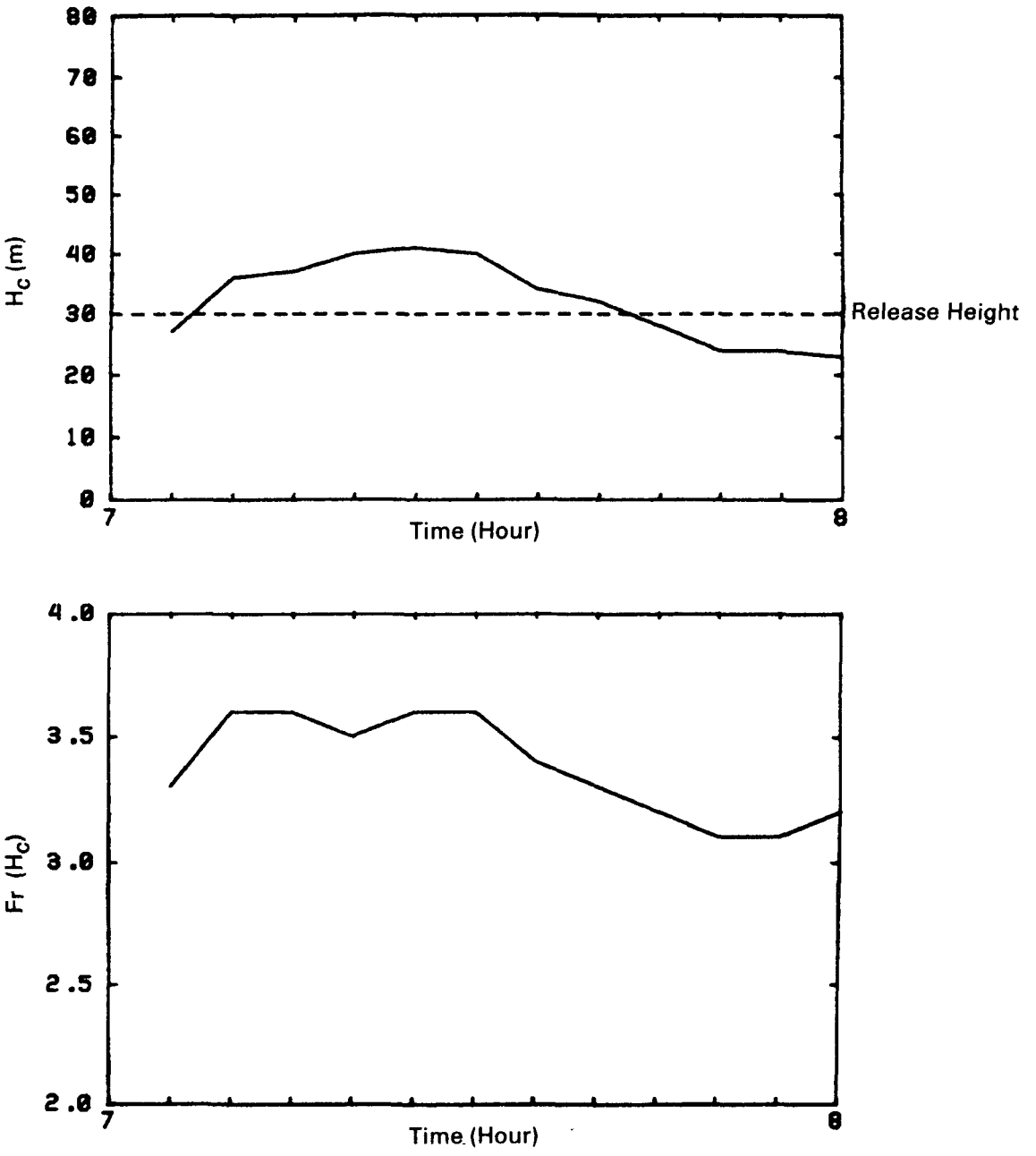

Figure 52. Time series of 5-minute calculated dividing-streamline heights (H_c) and bulk hill Froude numbers above H_c ($Fr(H_c)$). (CCB, Experiment 206, 10/24/80, 0700-0800 MST).

Time series plots of the 5-minute propeller anemometer data measured at Tower A are presented in Figure 53. The Tower A data along with the reconstructed 40-m winds are "splined under tension" to the tracer gas release height and these release height values are represented by the solid line.

The 10-m winds were light and variable during this hour, whereas the winds at 80 m were quite steady. The plume at 35 m was observed to be flowing toward the hill so that the direction shear must have occurred below this height. The 40-m wind speeds decreased significantly during the first half-hour causing the rise of H_c.

The relatively large vertical turbulence intensities are corroborated by observations that strong eddies appeared to bring the plume down to the ground. The eddies gave the plume a rotating appearance as one observer looked back at the source along the plume axis.

An hourly average of the 5-minute temperature and propeller wind data measured during this hour at Tower A were used to construct vertical profiles. A "spline under tension" method was used to interpolate the meteorological variables for every 5 m between instrument levels. The vertical profiles of hourly averaged wind direction, wind speed, and temperature are presented in Figure 54. The large directional wind shear below the release height is clearly evident. The wind speeds were also quite light below the release height.

The distribution of the observed hourly averaged normalized SF_6 concentrations (χ/Q in $\mu s/m^3$) is shown in Figure 55. Hill height contours in 10-m intervals starting at 5 m are also shown. The 5-minute average wind flow vectors estimated at the tracer gas release height are drawn at the release position. The length of each flow vector is proportional to the 5-minute wind speed. The 1-hour average flow vector, derived from a vector average of the 12 5-minute wind vectors, is depicted by the long dotted line emanating from the release position.

Observations indicate that the plume mixed down to the hill surface near the base of the draw on the southeast side of CCB producing the maximum observed SF_6 concentration (164 $\mu s/m^3$) at an elevation (25.3 m) less than H_c. This is the highest observed normalized concentration found at the CCB field experiment. Concentrations are also found on the northeast and north sides of the butte. Plume material was mixed to the surface of the hill and then advected directly over and around the hill.

A centerline concentration was calculated by means of the one-hour average meteorology estimated at the tracer gas release height. A comparison of the highest observed concentration with the estimated centerline concentration provides information on plume dilution and the reasonableness of the σ_z and σ_y formulations. The

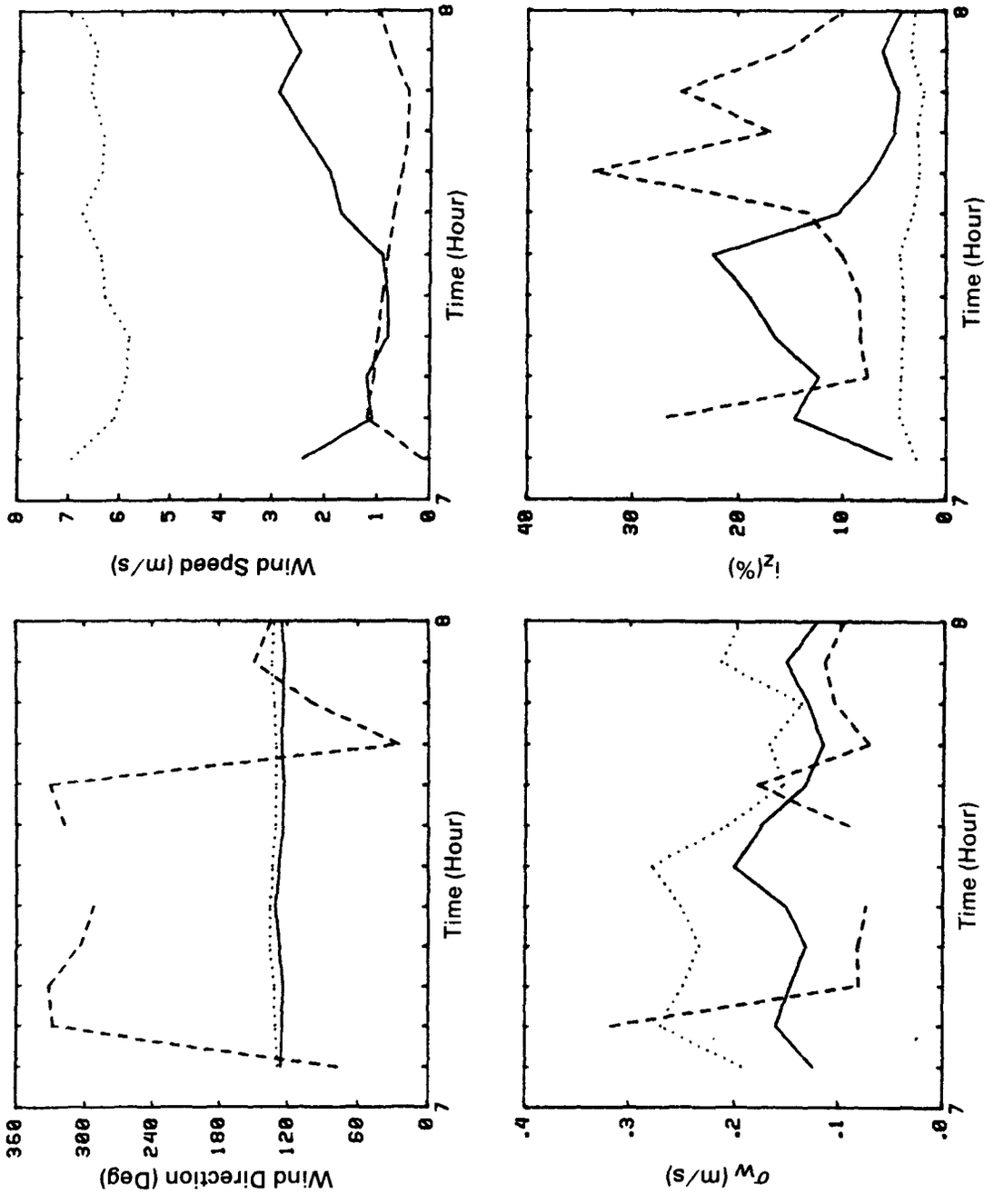

Figure 53. Time series of 5-minute propeller anemometer data from Tower A (CCB, Experiment 206, 10/24/80, 0700-0800 MST). Values at SF_6 release height (____), 80 m (....), and 10 m (----).

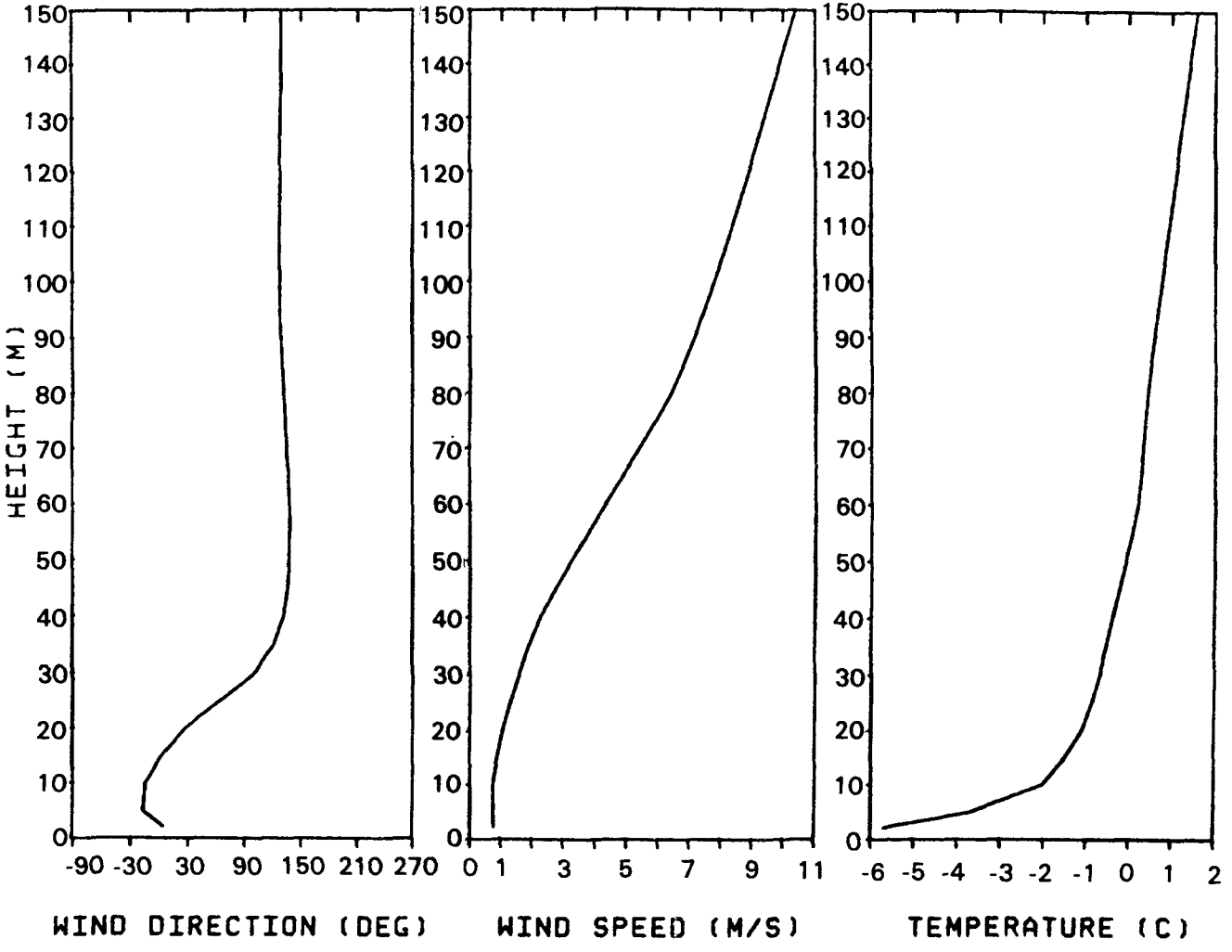

Figure 54. Vertical profiles of hourly meteorological data from Tower A (CCB, Experiment 206, 10/24/80, 0700-0800 MST).

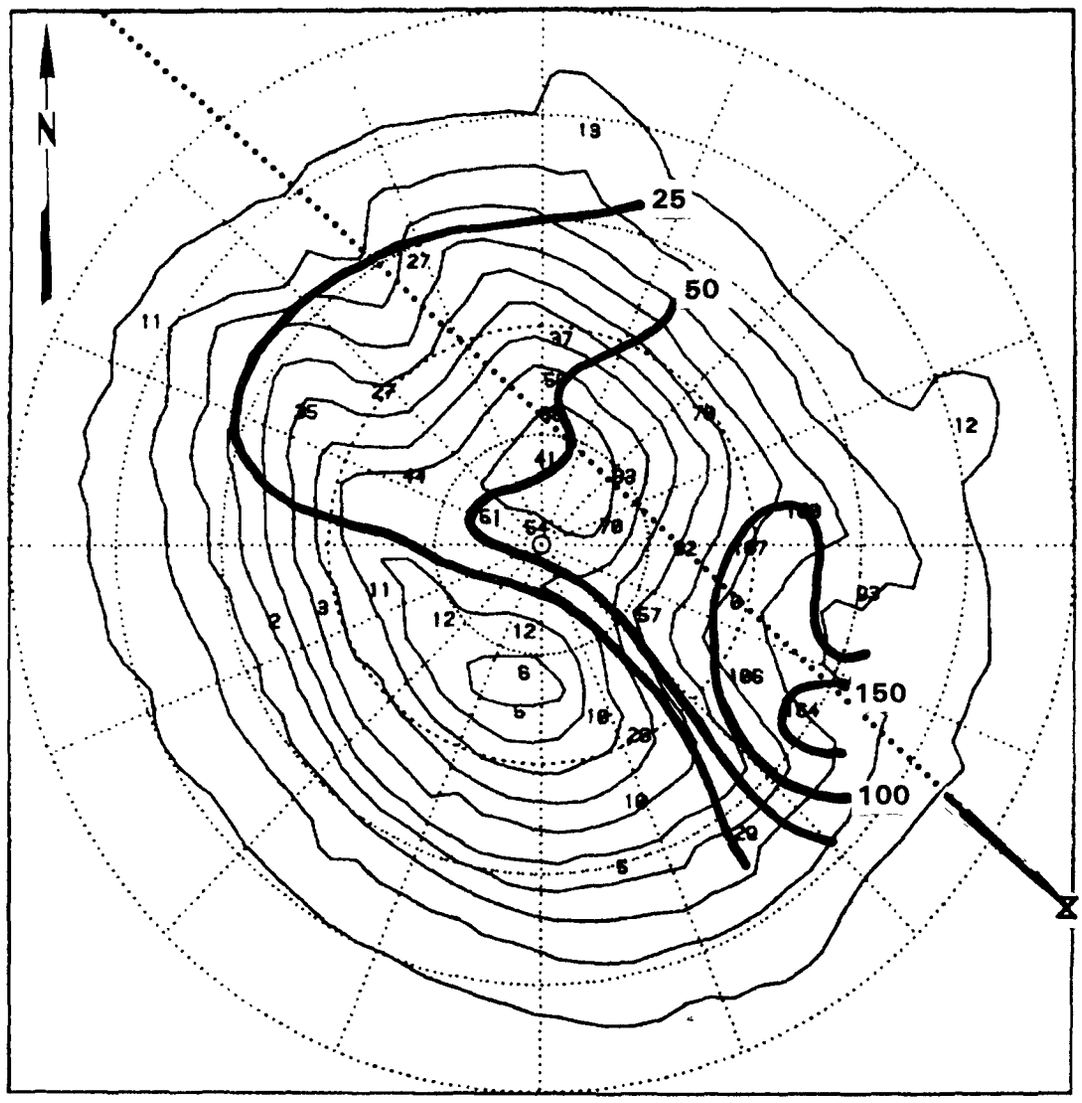

OBSERVED
Exp: 206-8
Z_r = 35 m
Q = .062 g/s
σ_v = .196 m/s
N = .0372 s^{-1}

Gas: SF_6 ($\mu s/m^3$)
Hour: 800
Base = -5.5 m
H_c = 33 m

σ_w = .155 m/s

Figure 55. One-hour averaged observed SF_6 concentrations scaled by emission rate ($\mu s/m^3$) (CCB, Experiment 206, 10/24/80, 0700-0800 MST).

method used to calculate σ_z (Venkatram et al. 1984) at $d + x_v$ is as follows:

$$\sigma_z = \frac{\sigma_w (d + x_v)}{u \left[1 + \frac{(d + x_v)}{2T_L u}\right]^{1/2}} \tag{54}$$

where x_v is a virtual source distance defined as

$$x_v = \frac{1}{2} AB + \sqrt{\left(\frac{1}{2} AB\right)^2 + B} \tag{55}$$

$$A = \frac{i_z}{2} \left(\frac{1}{2\Gamma z_r} + \sqrt{\left(\frac{1}{2\Gamma z_r}\right)^2 + \left(\frac{N}{q^2 \sigma_w}\right)^2}\right) \tag{56}$$

$$B = \left(\frac{\sigma_{zo}}{i_z}\right)^2 \tag{57}$$

and the initial spread of the plume (σ_{zo}) is estimated to be 0.5 m, $\gamma = 0.52$, and $\Gamma = 0.36$.

The dispersion time scale is given by

$$T_L = \ell/\sigma_w \; ; \quad \frac{1}{\ell} = \frac{1}{2\Gamma z_r} + \sqrt{\left(\frac{1}{2\Gamma z_r}\right)^2 + \left(\frac{N}{\gamma^2 \sigma_w}\right)^2} \tag{58}$$

where ℓ is the mixing length scale.

For this case-study hour, $x_v = 6.5$ m, $T_L = 7.0$ sec, and $\sigma_z(d + x_v) = 7.3$ m. A simple growth formula ($\sigma_y = i_y d$) is used to calculate σ_y as 32.7 m.

Finally, the centerline concentration scaled by the emission rate,

$$\chi/Q = \frac{1}{2\pi \sigma_y \sigma_z u} \tag{59}$$

is calculated to be 372 $\mu s/m^3$. The maximum observed normalized concentration is 164 $\mu s/m^3$. As mentioned previously, photographs and observations suggested strong vertical eddying of the plume as it approached the slope of CCB. These vertical motions forced the plume to be brought down to the surface on the upwind face of the hill. The measured ground-level concentration illustrates the dilution (about a factor of 2.0) of the relatively stable elevated plume as it is advected to the hill slope. To simulate this event the σ_z formula in the CTDM (see Sections 5.1 and 5.2) model would have to be modified to produce larger values of σ_z. We have not yet analyzed the

physical causes of the eddies; nor have we analyzed the meteorological data to predict their occurrence.

4.2 Hogback Ridge

The ten highest normalized SF_6 concentrations measured at HBR are presented in Table 11a. H_c and the meteorological parameters were estimated from Tower A data. The highest concentrations generally occurred when $z_r > H_c$. At HBR the SF_6 was released coincidentally with the oil-fog through the nozzle of the jet fogger. Except for two hours, the CF_3Br was never released at a greater height than the SF_6. Because of the very light winds that were typical below the crest of the ridge and the thermal buoyancy of the oil-fog release, the coincidental SF_6 and oil-fog plumes frequently rose well above H_c. As observed at CCB, plumes above H_c flowed up and over the ridge, producing the highest concentrations at $z_{max} > z_r$, typically near the top or on the lee side of the ridge.

Table 11b lists the ten highest normalized observed CF_3Br concentrations measured at HBR along with the appropriate release and meteorological information. In this table the meteorological parameters and H_c were estimated from Tower B data. For CF_3Br, the highest concentrations occurred when $z_r < H_c$. Releases below H_c tended to stagnate, producing high concentrations on the windward side of the ridge at typically $H_c > z_{max} > z_r$. Occasionally plume material was slowly transported up and over the ridge after impingement on its windward side. However, if the winds near the release had a substantial component parallel to the ridge, then most of the plume material stayed below the crest.

The CF_3Br emissions released well below H_c produced the highest concentrations observed during the three field experiments. The results at HBR are quite different from those experienced at CCB. At HBR the flow below H_c was impeded by the ridge and the tracer gas pooled against the ridge and subsequently was either lifted over the top or was transported parallel to the ridge line to the south. At CCB the flow well below H_c traveled around the sides of the hill, and consequently tracers released well below H_c produced relatively low concentrations.

4.2.1 Experiment 6, Experiment-Hour 9 (0700-0800 MDT)

The CF_3Br tracer gas was released 100 m from the base of the ridge at a release height 20 m above the ground. The release base elevation was 17.4 m above the zero elevation of the hill coordinate system, so the net release height corresponds to the 37.4 m height level on the ridge.

The 5-minute H_c and $Fr(H_c)$ time-series plots are presented in Figure 56. The 5-minute temperature and propeller anemometer wind data measured at Tower B (1, 5, 10, 20, 30 m) near the base of the ridge were used in conjunction with Tower A (80, 100, 150 m) data to characterize the flow in terms of H_c. If the wind direction was not within a defined sector of HBR (117° $\pm$ 45°), the projected

TABLE 11a. TEN HIGHEST χ/Q OBSERVED SF_6 CONCENTRATIONS AT HBR[++]

Exp No.	Hour End	χ/Q ($\mu s/m^3$)	z_r** (m)	H_c (m)	z_{max} (m)	$u(z_r)$ (m/s)	$\sigma_v(z_r)$ (m/s)	$\sigma_w(z_r)$ (m/s)	N (1/s)	d (m)
07	07	91.4	64	41	74.9*	2.5	.439	.160	.0275	646
05	06	81.1	70	71	97.4	1.2	-+	-+	.0293	366
07	05	78.6	60	40	97.4	2.5	.392	.165	.0307	366
15	03	55.9	42	46	79.1	1.7	.492	.091	.0514	781
04	03	51.6	62	42	79.5	1.7	-+	-+	.0220	441
15	11	47.9	70	5	85.8	4.6	.576	.442	.0000	956
07	04	44.9	70	39	76.1*	2.3	.435	.209	.0208	610
11	09	42.2	49	30	72.4*	2.3	.463	.205	.0269	1024
10	02	41.9	73	46	76.1*	1.2	.365	.170	.0150	610
09	06	40.1	57	-	83.7*	-	-	-	-	595

[++]Elevations referenced to 1600 m MSL.
*Concentrations measured in lee of HBR.
**Release height plus plume rise estimated from lidar.
+The turbulence data collected in Experiment 4 through 6 are considered invalid.

TABLE 11b. TEN HIGHEST χ/Q OBSERVED CF_3Br CONCENTRATIONS AT HBR[++]

Exp No.	Hour End	χ/Q ($\mu s/m^3$)	z_r (m)	H_c (m)	z_{max} (m)	$u(z_r)$ (m/s)	$\sigma_v(z_r)$ (m/s)	$\sigma_w(z_r)$ (m/s)	N (1/s)	d (m)
06	08	444.7	37	56	30.4	0.5	.358	.131	.0464	235
07	07	429.5	27	43	21.6	0.5	.282	.081	.0065	259
04	07	404.7	32	61	31.9	0.8	.231	.099	.0389	271
05	06	392.6	32	56	30.1	0.8	.406	.124	.0584	141
08	04	328.7	43	63	21.6	1.1	.267	.150	.0238	270
07	03	282.2	37	56	79.4	0.5	.330	.152	.0121	369
07	08	235.9	22	51	30.4	0.6	.376	.074	.0000	235
07	06	200.2	27	51	21.6	0.7	.213	.086	.0014	259
11	03	166.0	37	56	52.9	0.4	.141	.119	.0339	350
06	07	144.1	42	53	57.5	0.7	.677	.165	.0130	225

[++]Elevations referenced to 1600 m MSL.

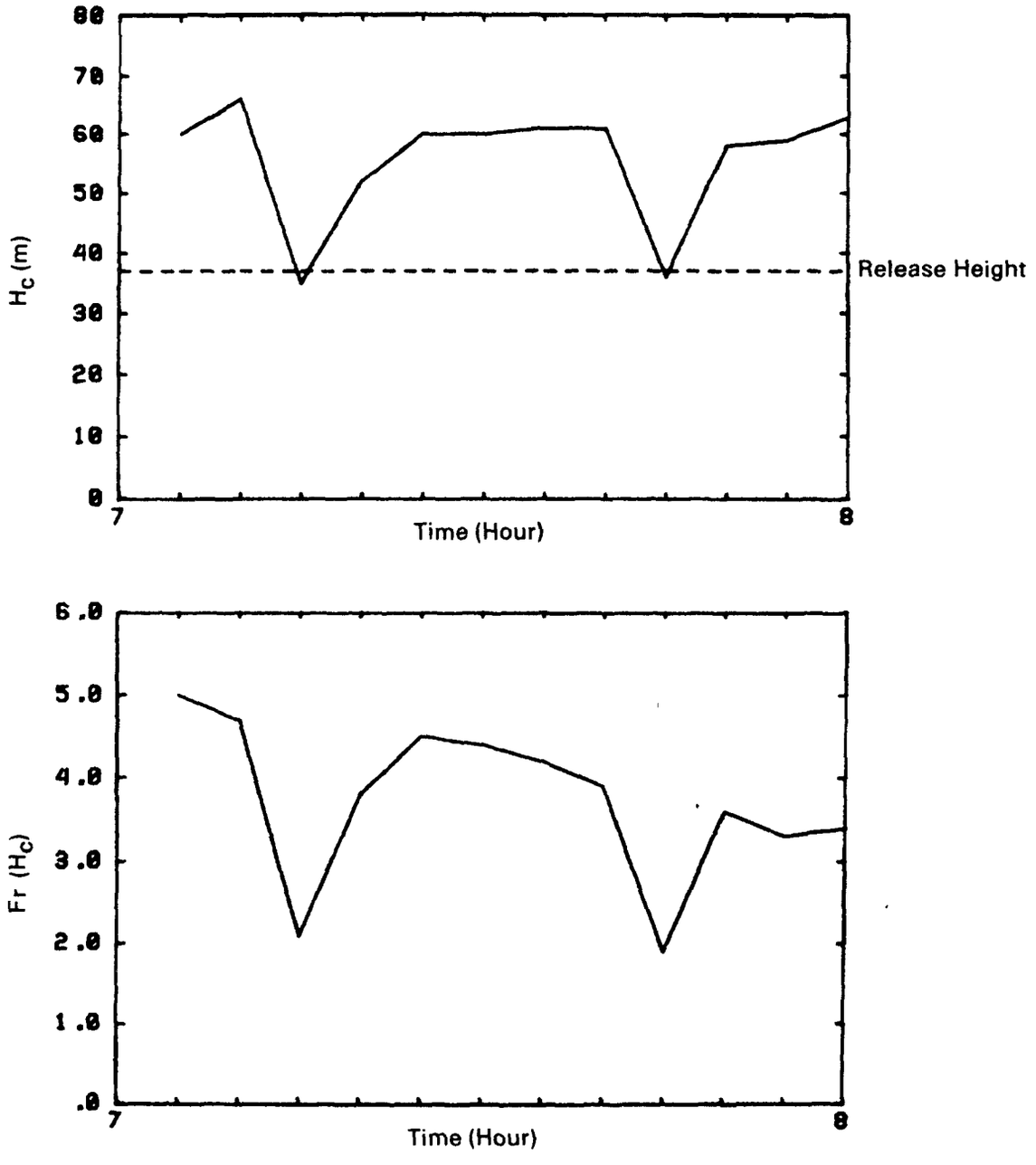

Figure 56. Times series of 5-minute calculated dividing-streamline heights (H_c) and bulk hill Froude number above H_c (Fr(H_c)) (HBR, Experiment 6, 10/13/82, 0700-0800 MDT).

(Equation 60) wind speed was used. If the projected wind speed was less than zero, then the wind speed was set to zero for that particular level. The effective height of HBR was taken to be 85 m. The 5-minute values of H_c are all greater than the release height, except for two periods when H_c drops to z_r. The sudden decreases in H_c correspond to decreases in the Tower A temperatures measured at 80 to 150 m. The average of the 5-minute H_c values over the hour is 56 m; thus, this hour is representative of flow below H_c. $Fr(H_c)$ slowly decreases during the hour, with the exception of the two sharp decreases.

The propeller anemometer data from Tower B, the 30-m tower near the base of HBR, are used to represent the flow at the release height. The trend in wind speeds and directions at 5, 20, and 30 m is shown in Figure 57. The local release height corresponds with the 20-m level on Tower B. The winds at the release height are less than 1 m/s, and there is a gradual shift in direction from 10° at the beginning of the hour to 240° by the end of the hour. Tethersonde measurements of wind direction at the release height also show a shift in wind direction through the hour.

The trends in i_z and σ_w values during the hour are also shown in Figure 57. The values of i_z and σ_w estimated at the release height vary from 18 to 32% and 0.10 to 0.16 m/s respectively. The one-hour value for σ_w estimated at the release height is 0.131 m/s (i_z = 26%).

The vertical profiles of the 150-m Tower A temperature and propeller anemometer wind data measured during this hour are presented in Figure 58. A large amount of directional wind shear is found near the vicinity of the tracer release height (34-m level on Tower A). This is corroborated by sonic anemometer measurements also made at Tower A which indicate more than 90 degrees of wind direction shear between 5 and 40 m.

A terrain elevation profile of HBR with the locations of the three meteorological towers (A, B, and C) and the appropriate instrument levels are shown in Figure 59. The numbers shown at each instrument level are the component of the wind perpendicular to the ridge (m/s), the parallel component (m/s), and the potential temperature (°C). The components of the wind are defined as

$$u = \perp \text{ component} = S \cos (117-\theta) \quad (60)$$

$$v = /\!/ \text{ component} = S \sin (117-\theta) \quad (61)$$

where S is the wind speed and θ is the wind direction. A positive u represents flow from the east or towards the ridge and a positive v represents flow from the north or parallel to the ridge. The height used to calculate the potential temperature is referenced to the base of Tower A. The dashed line represents the one-hour average value of H_c. The solid lines with arrows represent isentropes or lines of constant potential temperature (θ). The flow above H_c travels up and over the ridge; whereas the flow below H_c is blocked. The wind

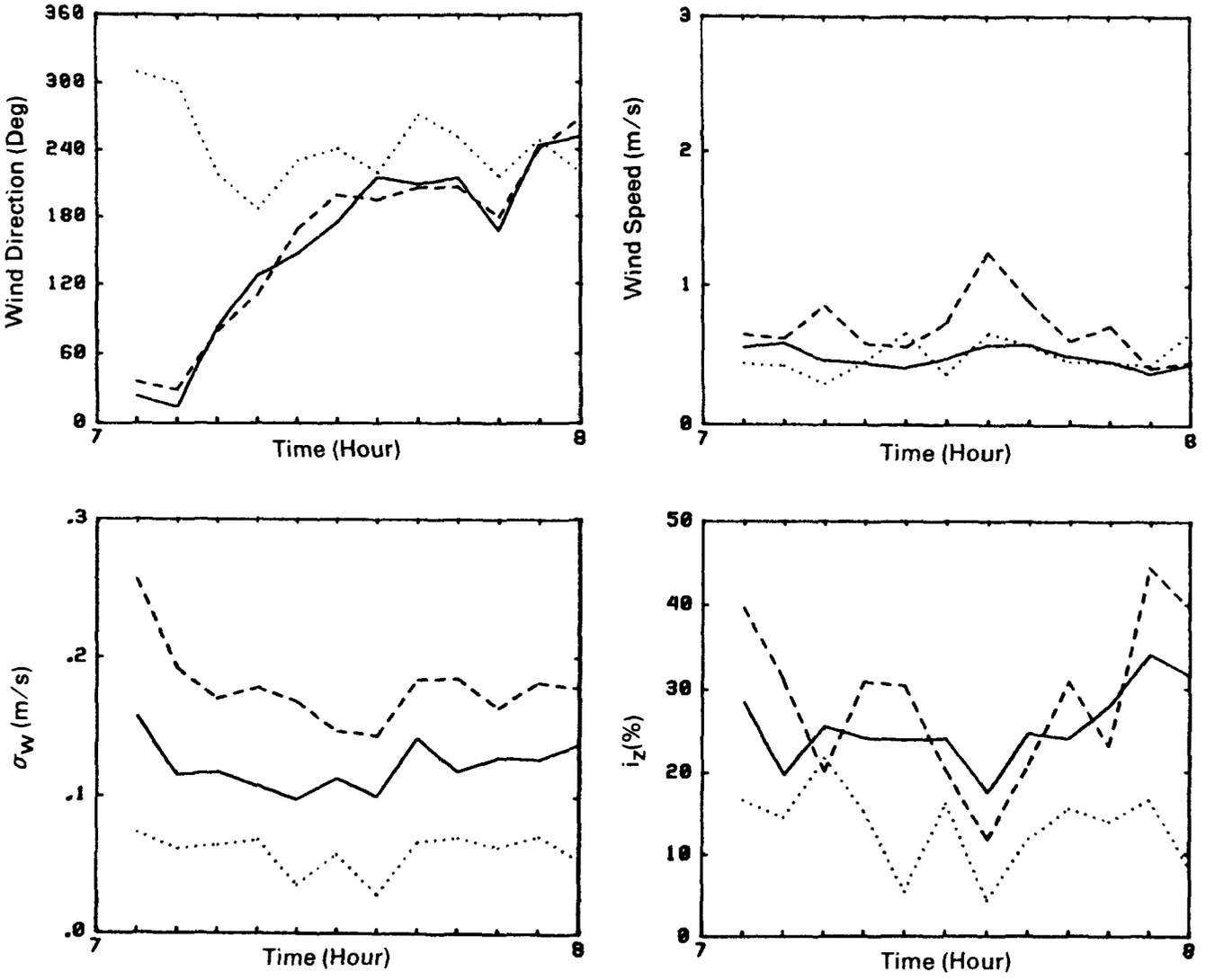

Figure 57. Time series of 5-minute propeller anemometer data from Tower B (HBR, Experiment 6, 10/13/82, 0700-0800 MDT). Values at CF_3Br release height (____), 5 m (.....), and 30 m (_ _ _).

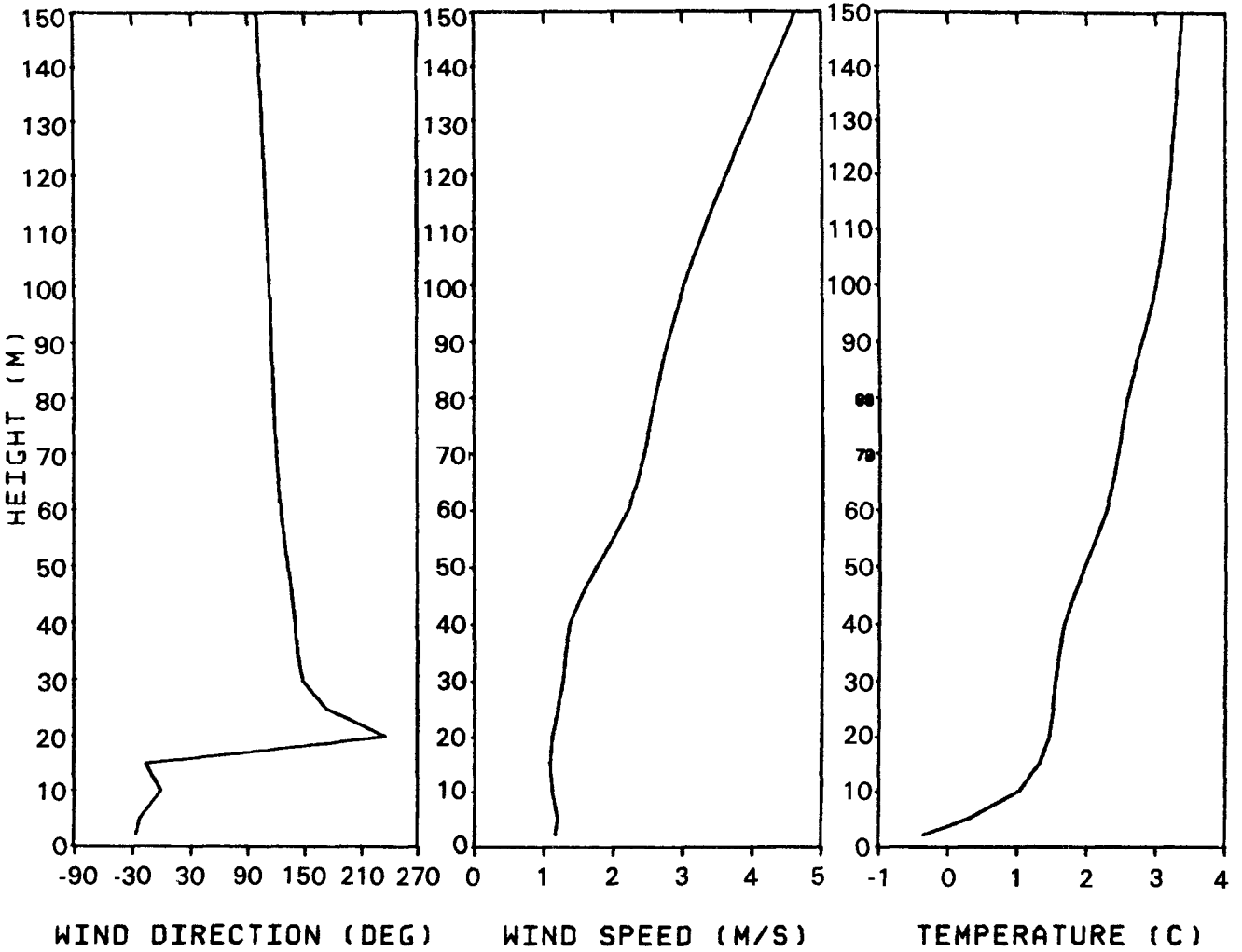

Figure 58. Vertical profiles of hourly meteorological data from Tower A (HBR, Experiment 6, 10/13/82, 0700-0800 MDT).

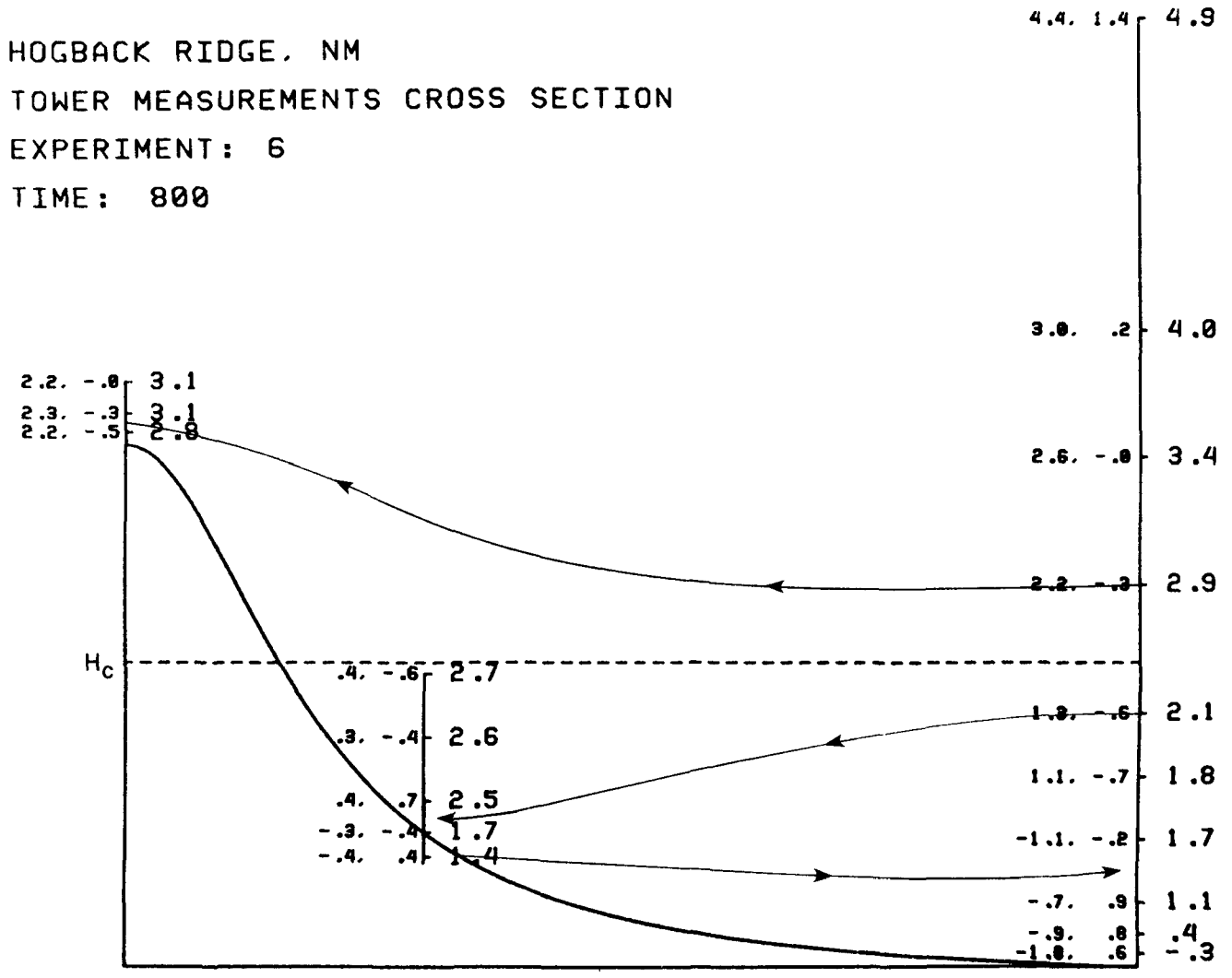

Figure 59. Potential temperature and wind measurements cross section at HBR. The values at each instrument level are (left to right) the perpendicular component of the wind to the ridge (m/s), the parallel component (m/s), and the potential temperature (°C). The solid lines with arrows are isentropes and the dashed line represents the dividing-streamline height. (HBR, Experiment 6, 10/13/82, 0700-0800 MDT).

components indicate that at the lowest levels of Tower A (2-10 m) the flow is from the northwest, and at the lowest levels of Tower B (1-5 m) the flow is from the northwest to southwest or down the slope of HBR. Above this layer, the flow is predominantly from the southeast or up the slope of HBR.

This cross section corroborates previous analyses which suggested that releases below H_c tended to stagnate with the tracer gas impinging against the ridge. These meteorological conditions and release height produced the highest concentrations that were observed on the windward side of HBR.

The distribution of the observed hourly averaged normalized CF_3Br concentrations over the surface of the ridge is shown in Figure 60. The largest concentrations are found near the bottom half of the sampler array at an elevation that is less than H_c. The maximum observed concentration (445 $\mu s/m^3$) is found 7 m below the net release height at an elevation of 30.4 m. This is the largest observed normalized concentration found in the CTMD modeling data set. This maximum concentration is confirmed by a collocated sampler which measured 425 $\mu s/m^3$ for the same period. A sharp decrease of observed tracer concentrations is found above the mean H_c surface (1656 MSL) although some CF_3Br was transported above H_c to the crest of the ridge.

Using the method presented in subsection 4.1.1, σ_y is calculated to be 168.3 m and σ_z is calculated to be 9.4 m with the initial size of the plume set to zero. From this, a centerline concentration is calculated to be 202 $\mu s/m^3$. Because the propeller anemometer winds estimated at the tracer release height are so light and variable during the hour, there is a great deal of uncertainty in calculating a one-hour average centerline concentration. If the hourly averaged sonic anemometer data are used to estimate σ_y, σ_z, and u (see the Fourth Milestone Report for a discussion of this experiment-hour using the sonic data), then a centerline concentration is calculated to be 278 $\mu s/m^3$.

4.2.2 Experiment 7, Experiment-Hour 6 (0600-0700 MDT)

The SF_6 tracer gas was released 100 m from the base of the ridge at a release height 15 m above the ground. Figure 61, a photo taken at 0655 MDT from the 150-m tower, shows the smoke plume traveling from the release crane over the ridge. The oil-fog generator produced enough heat flux to cause a thermally-induced rise in the oil fog and collocated SF_6 plumes. Lidar measurements taken near the source, meteorological profiles, and photographs were used to estimate a 32-m plume rise. Thus, the effective plume elevation after plume rise is 47 m above the ground. Local terrain elevations near the release point are estimated to be 17.4 m above the base elevation, so the net release height corresponds to the 64.4-m level on the ridge.

Time series plots of the 5-minute H_c and $Fr(H_c)$ values are presented in Figure 62. The 5-minute temperature and propeller wind data measured at the 150-m tower were used to characterize the flow in

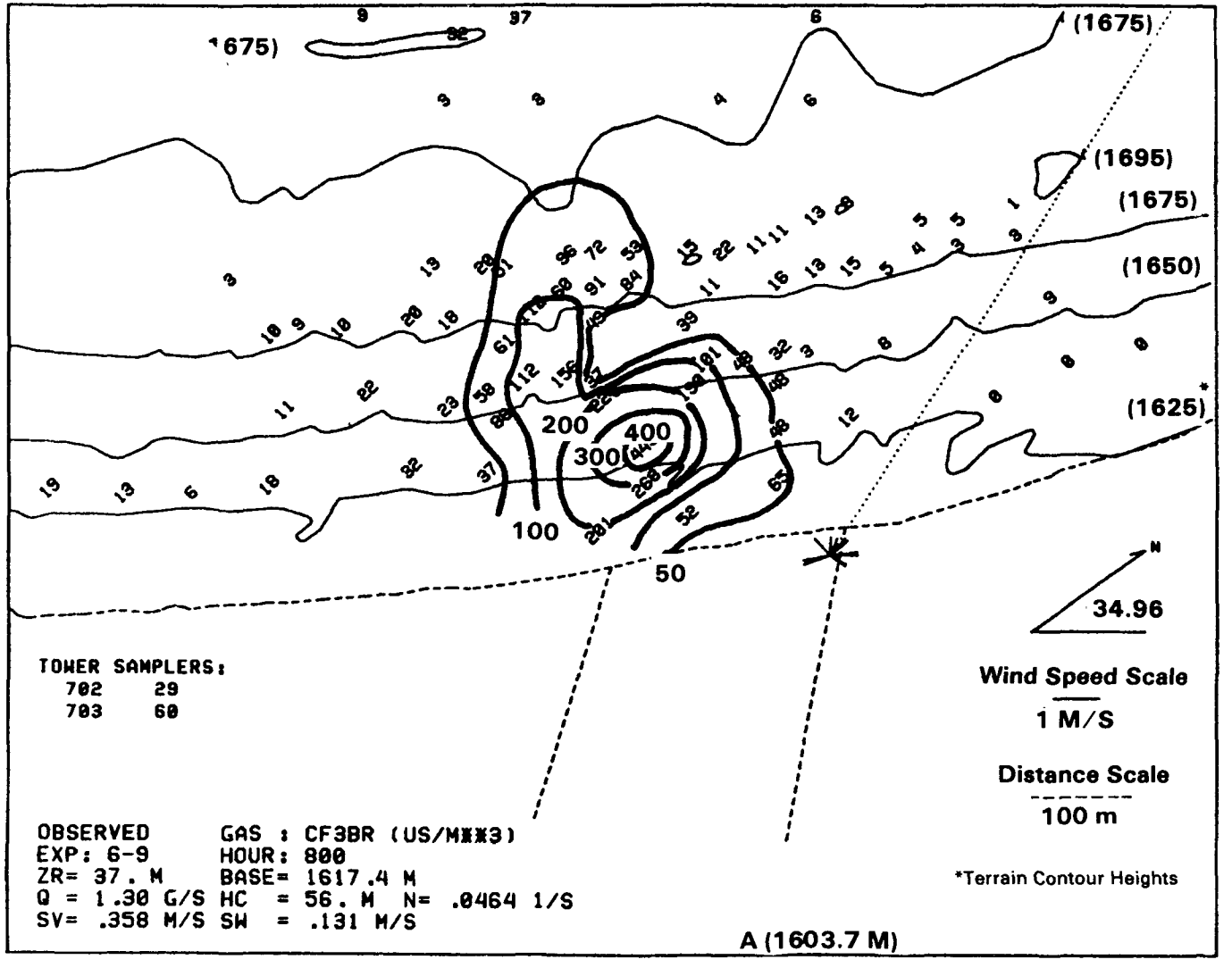

Figure 60. One-hour averaged observed CF_3 Br concentrations scaled by emission rate ($\mu s/m^3$) (HBR, Experiment 6, 10/13/82, 0700-0800 MDT).

Figure 61. Instantaneous photo from Tower A of release position with plume traveling over the ridge (HBR, Experiment 7, 10/14/82, 0655 MDT).

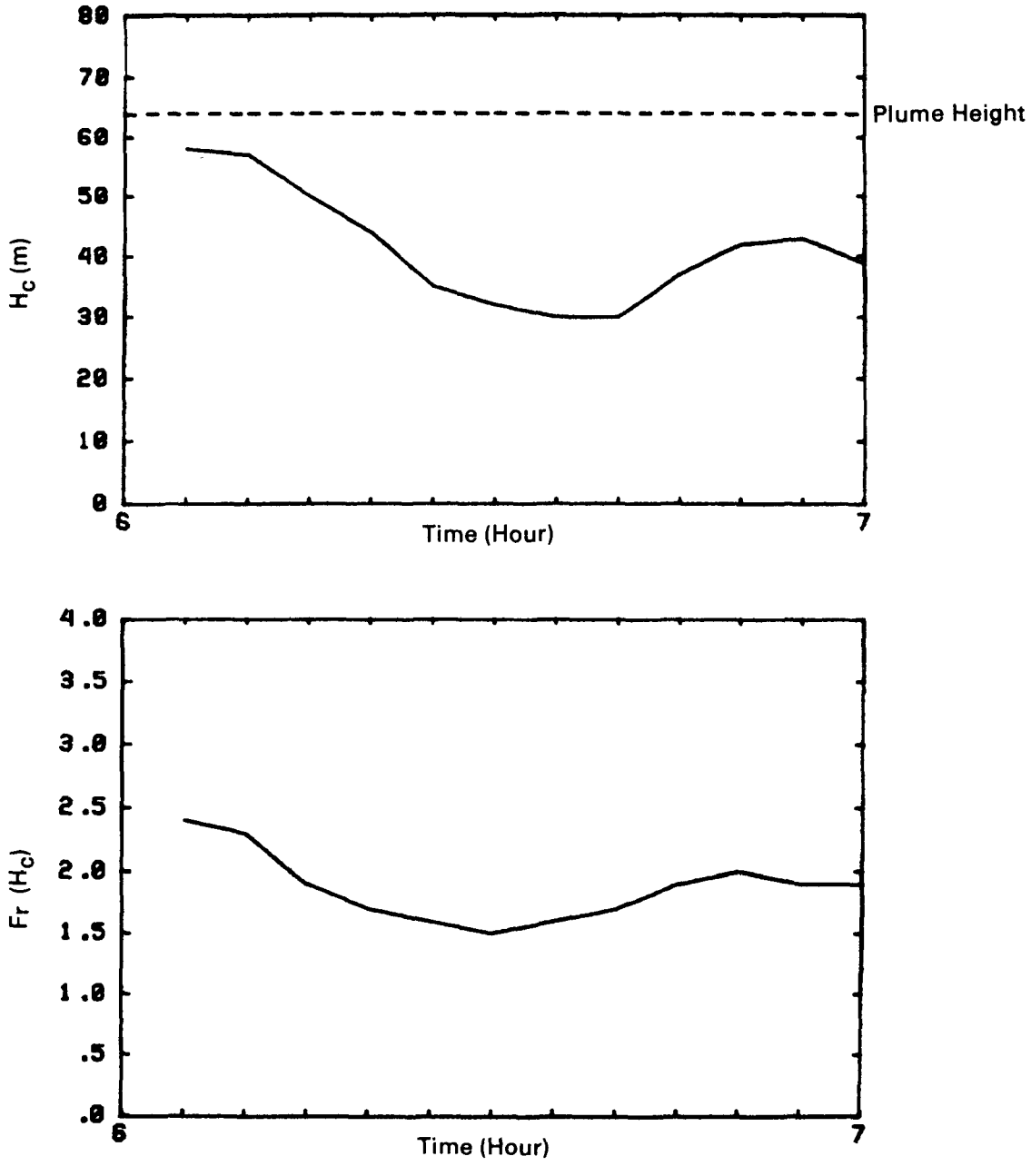

Figure 62. Time series of 5-minute calculated dividing-streamline heights (H_c) and bulk hill Froude numbers above H_c ($Fr(H_c)$) (HBR, Experiment 7, 10/14/82, 0600-0700 MDT).

terms of H_c. For the first forty minutes of the hour, H_c decreases from 59 m to 30 m before slowly rising. The average of the 5-minute H_c values over the hour is 41 m; thus, this hour represents flow above H_c. The trend in $Fr(H_c)$ values correlates with the trend of H_c. $Fr(H_c)$ starts off at 2.4, decreasing to 1.5 before slowly rising.

Time series plots of the 5-minute propeller anemometer data from Tower A are presented in Figure 63. The data at 80 m (dotted lines) and 40 m (dashed lines) are presented along with the data "splined under tension" to the tracer gas release height (solid lines). The splined values are close in value to the measured 60-m values which are not presented in this figure. The wind directions at all three levels are quite steady. Tethersonde measurements of the wind direction at the release height indicate winds ranging from 70° to 130°. The wind speeds at the release height slowly increase from 1 m/s to more than 3 m/s during the first forty minutes, before slowly decreasing. This coincides with the trend in 5-minute H_c values mentioned above.

The profile of HBR with the locations of the three meteorological towers and the appropriate instrument levels are shown in Figure 64. The numbers shown at each instrument level are the propeller derived σ_u, σ_v, and σ_w values in units of m/s. On Tower A, the values of σ_w begin to decrease above the 80-m level. The turbulence found at the top of the ridge at Tower C is much lower than that at the equivalent level of Tower A.

The one-hour average profiles of the 5-minute temperature and propeller wind data measured at Tower A are presented in Figure 65. There is more than 90° of wind direction shear below 40 m. Above this level, the wind directions are fairly uniform with height. There is also a marked increase in wind speed above the 40-m level.

The isentropic cross section for this hour is presented in Figure 66. The isentropes represented by the solid lines with arrows show that the flow above H_c travels up and over the ridge; whereas the flow below H_c is blocked, forming a recirculating flow. It is expected that the highest concentrations will occur at an elevation greater than the release height near the top or on the lee side of the ridge. The wind components indicate that at the lowest levels of Towers A and B the flow is from the northwest to southwest, or downslope. Above this layer, the flow is from the northeast to southeast, or upslope.

The distribution of the observed hourly averaged normalized SF_6 concentrations is shown in Figure 67. As expected, the maximum observed concentration (91 $\mu s/m^3$) is found in the lee of HBR. The concentrations are much lower below the mean H_c level (1658 MSL), indicating that the bulk of the plume material was transported above H_c up and over the ridge. Figures 68 and 69 are instantaneous photos taken at 0710 MST from atop the ridge. The plume is surmounting the ridge as shown in Figure 68 and ground-level impact occurs in the lee of the ridge as shown in Figure 69.

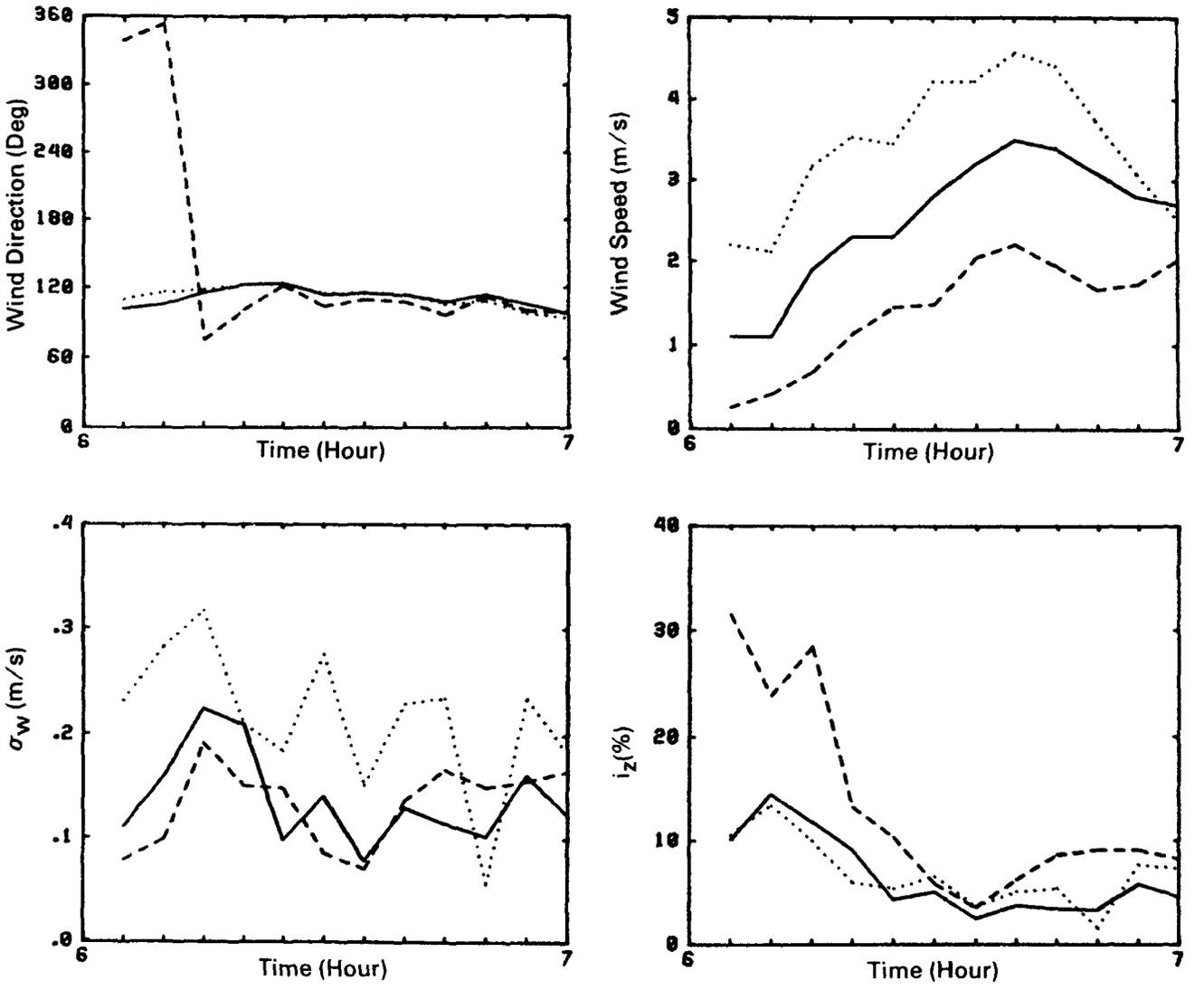

Figure 63. Time series of 5-minute propeller anemometer data from Tower A. (HBR, Experiment 7, 10/14/82, 0600-0700 MDT). Values at SF_6 release height (____), 40 m (_ _ _), and 80 m (.....).

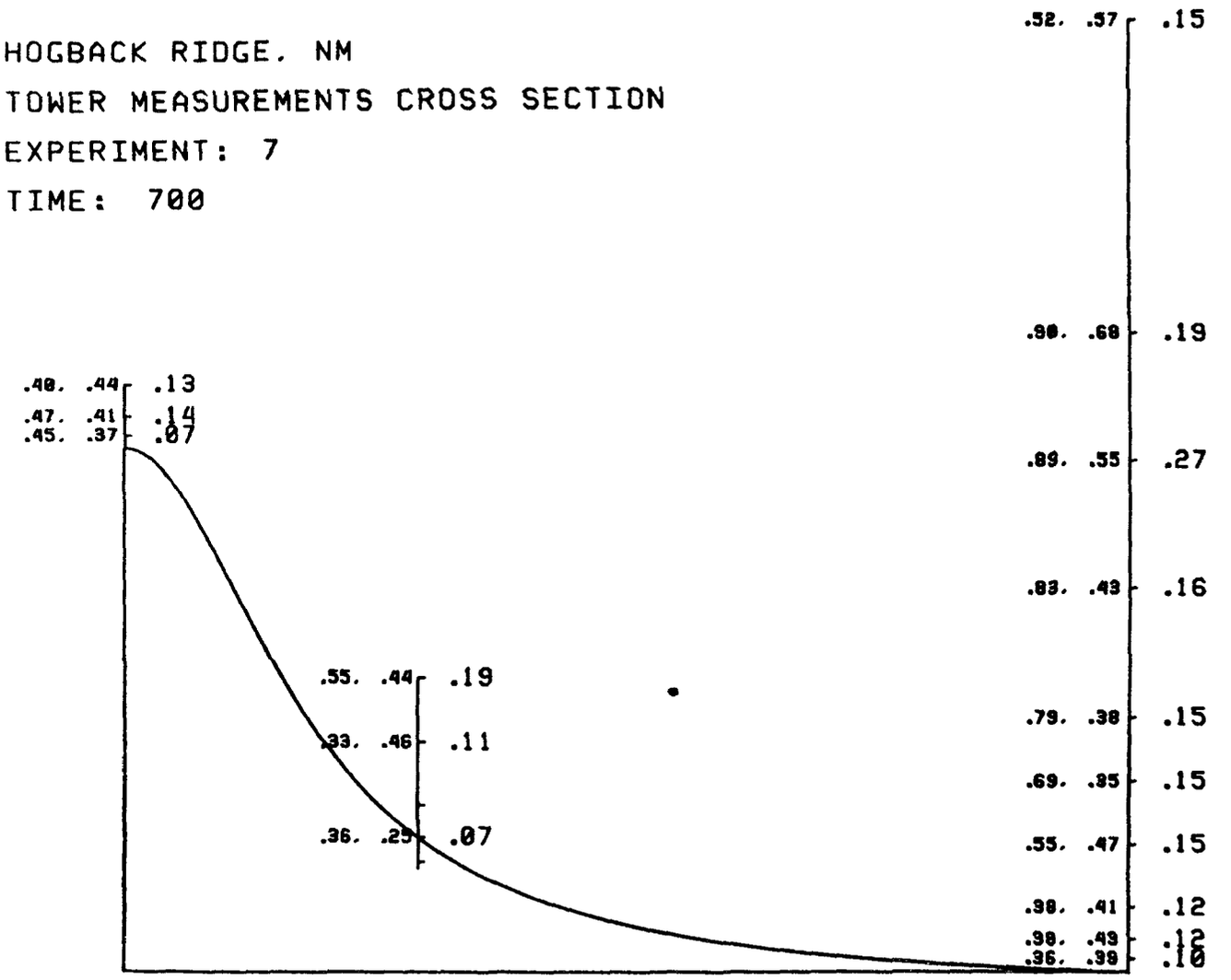

Figure 64. Turbulence measurements cross section at HBR. The values at each instrument level are σ_u, σ_v, and σ_w (m/s). (HBR, Experiment 7, 10/14/82, 0600-0700 MDT).

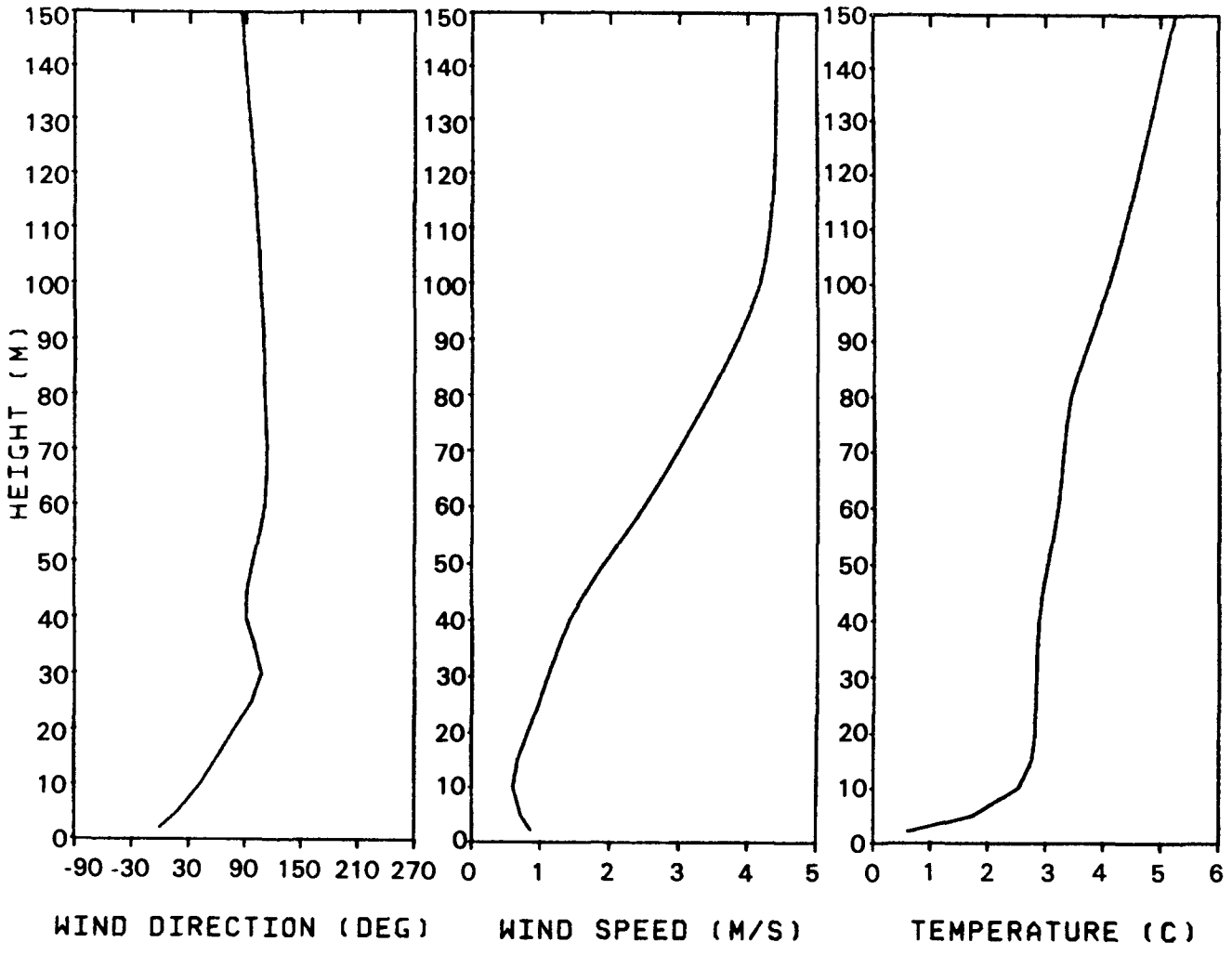

Figure 65. Vertical profile of hourly meteorological data from Tower A (HBR, Experiment 7, 10/14/82, 0600-0700 MDT).

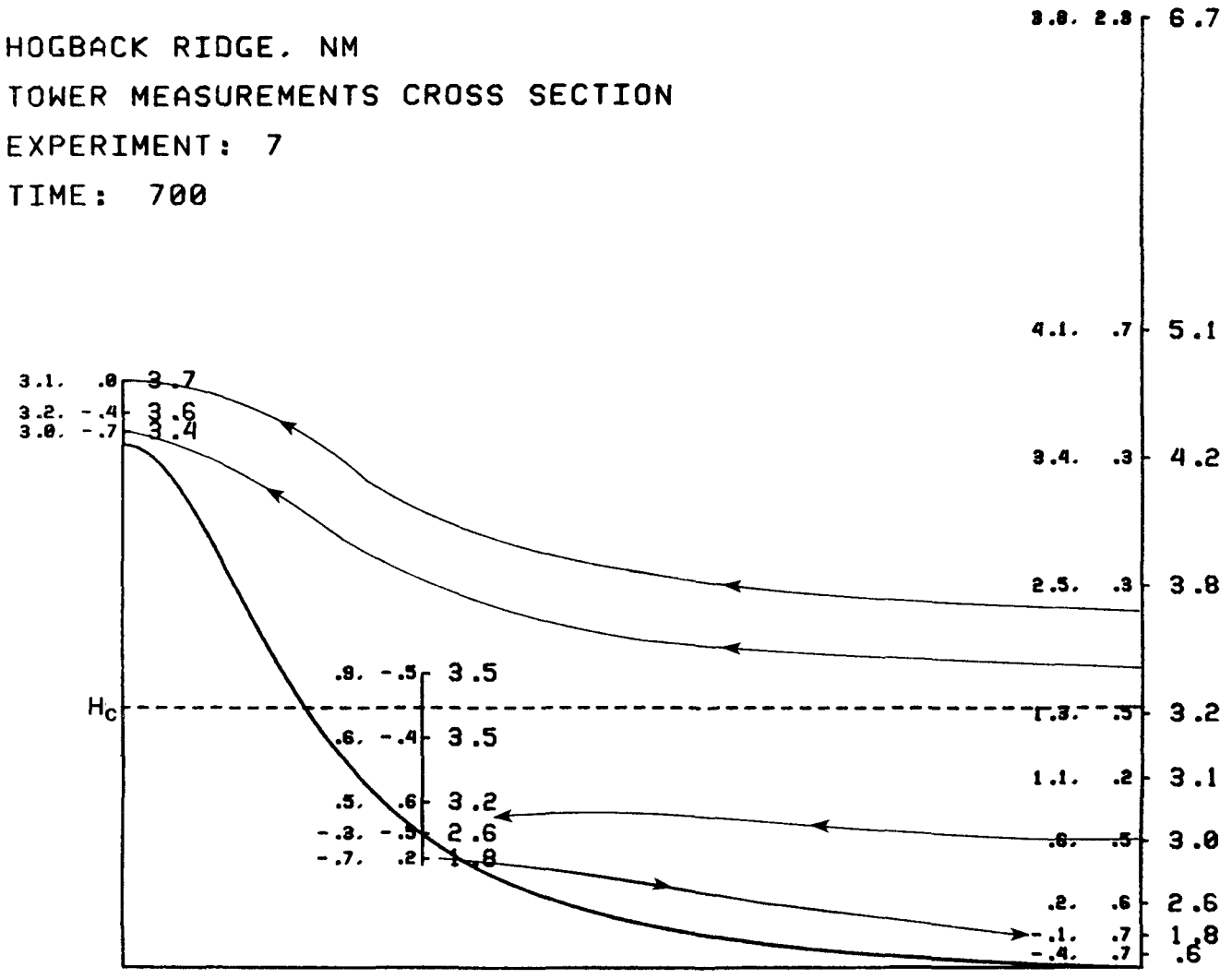

Figure 66. Potential temperature and wind measurements cross section at HBR. The values at each instrument level are the perpendicular component of the wind to the ridge (m/s), the parallel component (m/s), and the potential temperature (°C). The solid lines with arrows are isentropes and the dashed line represents the dividing-streamline height. (HBR, Experiment 7, 10/14/82, 0600-0700 MDT).

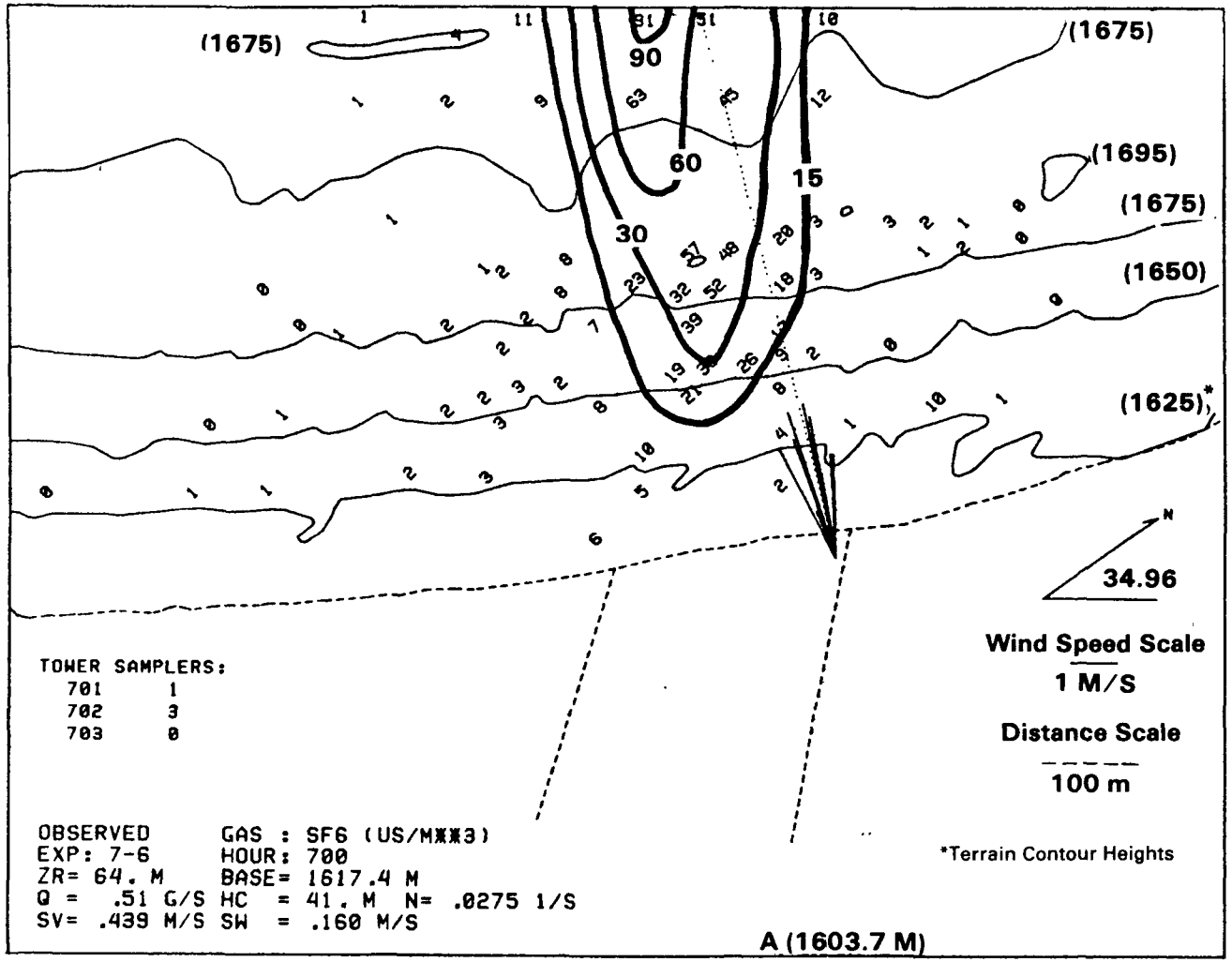

Figure 67. One-hour averaged observed SF_6 concentrations scaled by emission rate ($\mu s/m^3$) (HBR, Experiment 7, 10/14/82, 0600-0700 MDT).

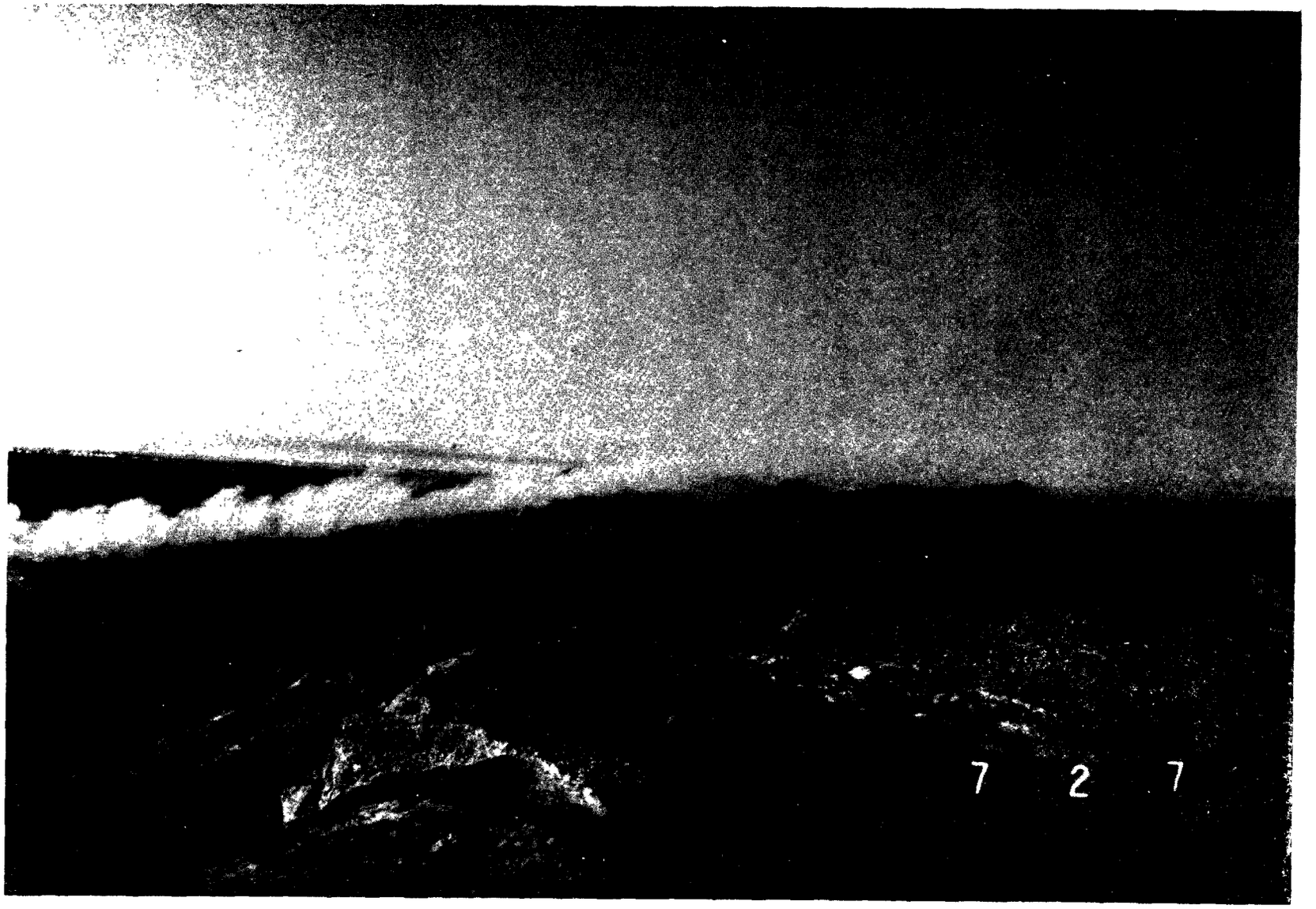

Figure 68. Instantaneous photo from the crest of HBR showing the plume as it surmounts the hill (HBR, Experiment 7, 10/14/82, 0710 MDT).

Figure 69. Instantaneous photo from the crest of HBR looking towards the lee where the plume is impacting (HBR, Experiment 7, 10/14/82, 0710 MDT).

The hourly averaged lidar scans made at an along-plume distance of 60 m from the source yield an estimate of initial plume size (σ_{zo}) of 12.9 m. By the method discussed in subsection 4.1.1, the virtual source distance is calculated to be 904.3 m and $\sigma_z(d+x_v)$ is 16.7 m. The lidar-measured value of σ_y at a distance of 60 m from the source is 32.6 m, and at a distance of 127 m from the source σ_y is estimated as 35.3 m. Continuing this rate of growth, σ_y is estimated to be 56.5 m at the distance d = 646 m from the source. By means of Equation 59, the normalized centerline concentration is calculated to be 67 $\mu s/m^3$. The maximum observed normalized concentration of 91 $\mu s/m^3$ is found above H_c in the lee of the HBR. If the plume does not grow vertically ($\sigma_z = \sigma_{zo}$), then a centerline concentration is calculated to be 87 $\mu s/m^3$. An estimate of the ground-level, centerline concentration can be made using the equation:

$$\chi = \frac{1}{2\pi\ \sigma_y \sigma_z u}\ e^{-\frac{1}{2}\left(\frac{\Delta z}{\sigma_z}\right)^2} \qquad (62)$$

where Δz is the height of the plume above H_c. For this case-hour the lidar measurements suggest Δz is 6 m, and χ/Q is calculated to be 78 $\mu s/m^3$ which compares reasonably with the maximum observed concentration.

4.3 FSPS

The ten highest normalized observed SF_6 concentrations measured at the FSPS are presented in Table 12a. The SF_6 tracer gas and the oil-fog smoke were released simultaneously from the 91.4 m stack. Because the lidar data are still in the processing stage, plume rise estimates are available for only five of the top ten hours. For four of those hours when the final plume height can be determined from the lidar data, the highest concentrations occur when $z_r \simeq H_c$ and on average, $z_{max} < z_r$.

Table 12b lists the ten highest observed normalized CF_3Br concentrations measured at the FSPS along with the appropriate release and meteorological data. The H_c values listed in the table are preliminary estimates that were calculated in real-time during the FSPS; they were not developed specifically for this report. The CF_3Br tracer gas was released from the 150-m instrument tower located about 1.2 km east of the Tracy stack. The highest concentrations mainly occur when $z_r < H_c$ and $z_{max} < H_c$.

4.3.1 Experiment 13, Experiment-Hour 9 (0800-0900 PDT)

The SF_6 tracer gas and oil-fog were released simultaneously from the 91.4 m stack. The one-hour averaged plume rise is estimated from hourly-averaged lidar data to be 120 m; hence an effective stack height is 211 m.

TABLE 12a. TEN HIGHEST χ/Q OBSERVED SF_6 CONCENTRATIONS AT FSPS[+]

Exp No.	Hour End	χ/Q (μs/m³)	z_r (m)	H_c (m)	z_{max} (m)	$u(z_r)$ (m/s)	$\sigma_v(z_r)$ (m/s)	$\sigma_w(z_r)$ (m/s)	N (1/s)	d (m)
05	22	10.2	91.4*	0.	212.9	5.4	1.005	.500	.0057	6922
13	09	8.3	211.0	225	172.8	1.6	.429	.148	.0239	4086
05	05	8.2	91.4*	276	170.2	0.7	.340	.137	.0249	3191
02	05	8.0	134.0	177	75.5	3.2	.323	.210	.0280	3835
12	10	7.9	91.4*	202	19.8	2.2	.670	.310	.0239	1645
11	06	7.5	198.0	243	115.4	1.5	.512	.168	.0273	4522
13	08	6.7	206.0	246	172.8	1.3	.734	.125	.0250	4086
05	06	6.5	91.4*	280	170.2	0.7	.290	-	.0292	3191
10	05	6.4	91.4*	386	130.1	1.7	.404	.130	.0256	3191
07	07	5.5	163.0	143	180.9	2.7	.350	.230	.0239	5877

[+]Elevations referenced to base of Tracy Stack.
*Stack height; estimates of final plume height not yet available.

TABLE 12b. TEN HIGHEST χ/Q OBSERVED CF_3Br CONCENTRATIONS AT FSPS[+]

Exp No.	Hour End	χ/Q (μs/m³)	z_r (m)	H_c (m)	z_{max} (m)	$u(z_r)$ (m/s)	$\sigma_v(z_r)$ (m/s)	$\sigma_w(z_r)$ (m/s)	N (1/s)	d (m)
12	09	35.1	100	393	164.3	0.5	.278	.066	.0333	4595
02	07	19.5	100	282	106.5	1.4	.077	.115	.0200	2391
04	02	13.4	100	92	2.7	1.8	1.167	.272	.0075	1532
13	03	12.8	100	234	199.6	2.5	.315	.121	.0313	5000
11	09	11.0	100	170	25.9	1.7	.460	.277	.0378	2923
13	09	11.0	100	225	43.5	1.3	.258	.094	.0273	2334
10	09	10.8	100	224	53.9	1.2	.275	.099	.0267	4101
10	08	10.6	100	214	43.5	0.5	.122	.085	.0200	2334
09	08	10.3	100	187	170.2	2.7	.718	.250	-	2028
10	06	9.8	100	676	170.6	0.7	.660	.076	.0233	1957

[+]Elevations referenced to base of Tracy Stack.

A plot of the hourly averaged lidar scan closest to the source, which was used to estimate plume rise, is presented in Figure 70. This is a two-dimensional display of the plume cross-section along the path of the lidar scan. The darkest and largest symbols indicate where the signal from the plume is strongest. The x-axis represents the horizontal distance in meters from the lidar, and the y-axis represents the vertical height in meters relative to the lidar. The profile drawn from the y-axis is a vertical profile of the plume signal in the scan plane, which is found by integrating the array horizontally. The profile drawn from the x-axis is a horizontal profile of the plume signal in the scan plane, which is found by integrating the array vertically. From these analyses, it can be seen that the average plume is reasonably well-defined and coherent; hence, the lidar-derived height of the plume is a good estimate of the plume rise.

The 5-minute H_c and plume height time series plots are presented in Figure 71. Because the travel time to the receptor of maximum concentration is approximately one hour, the meteorology from the previous hour is used to calculate H_c. H_c is first calculated from

$$H_c = H - (u/N) \tag{63}$$

where H is the effective height of the terrain towards which the plume is directed. If H_c is calculated to be less than 150 m, then H_c is recalculated by means of the integral formula presented in the CTMD First Milestone Report (Equation 4). The 5-minute temperature data measured at six levels of Tower A (10, 50, 75, 100, 125, 150 m) and the 5-minute cup-and-vane wind data measured at four levels of Tower A (10, 75, 100, 150 m) are used to characterize the flow in terms of H_c. The cup-and-vane data are used in this analysis because the cosine response corrections have not yet been applied to the propeller anemometer data. If the vane wind direction is not towards Beacon Hill or Target Mountain (197 to 307°), the wind speed is set to zero for that particular level. The average of the 5-minute H_c values over the hour is 225 m and the hourly average height of the plume is 211 m; thus, this hour is representative of transport along streamlines near H_c.

In Figure 72, the top two plots are two-hour time series of cup-and-vane wind data measured at 150 m, 100 m, and 75 m. Because the wind speeds are less than 2 m/s, the travel time to the receptor of maximum concentration is approximately one hour; thus, the meteorology from 0700 to 0800 is believed to be more representative. During this time period, there is more than 60° of wind direction shear between the winds at the release height (estimated from the 150-m level) and at 100 m.

The bottom two plots in Figure 72 are two-hour time series of propeller anemometer vertical turbulence intensities and σ_w values measured at 150 m, 125 m, and 100 m. The one-hour averaged value of σ_w (with the Horst correction for response errors in the props)

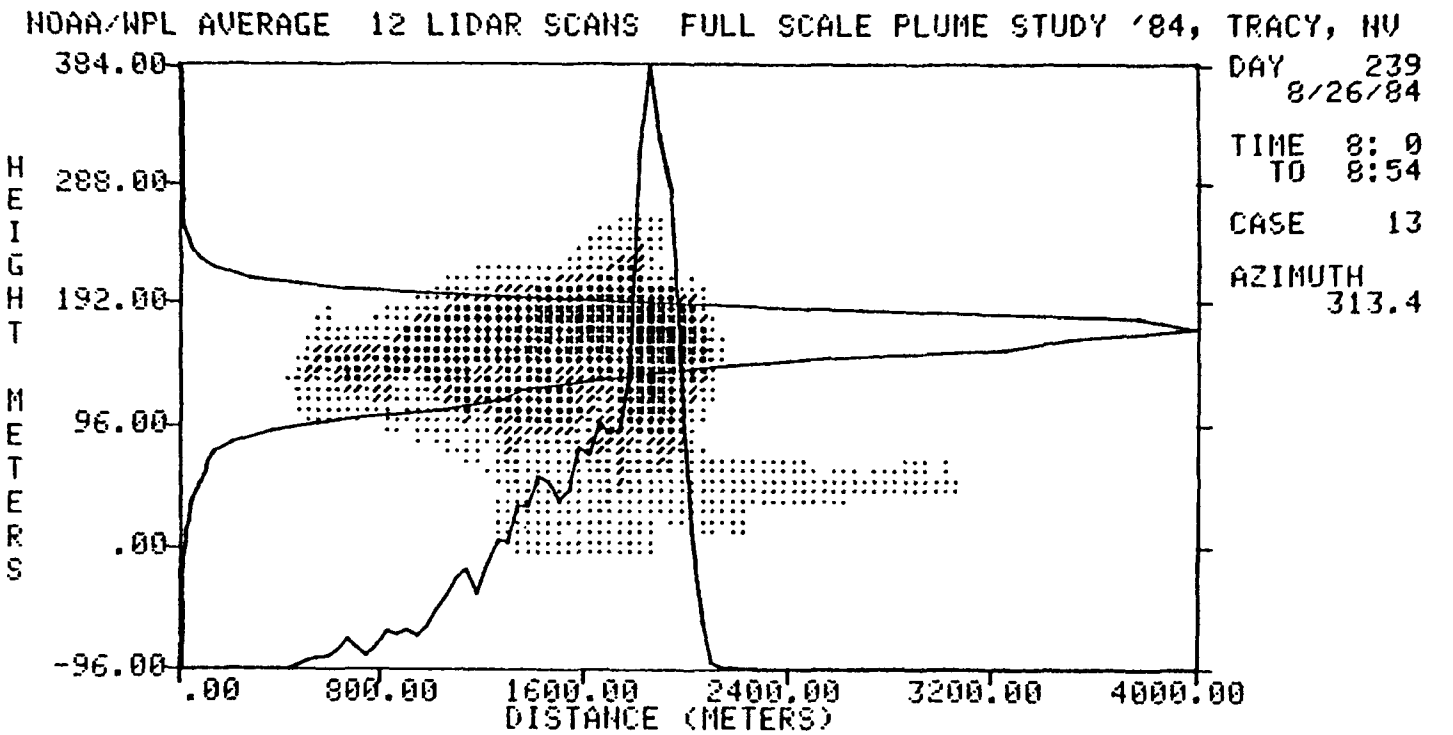

Figure 70. Two-dimensional display of the plume cross section along the path of the lidar scan (FSPS, 08/26/84, 0800-0900 PDT).

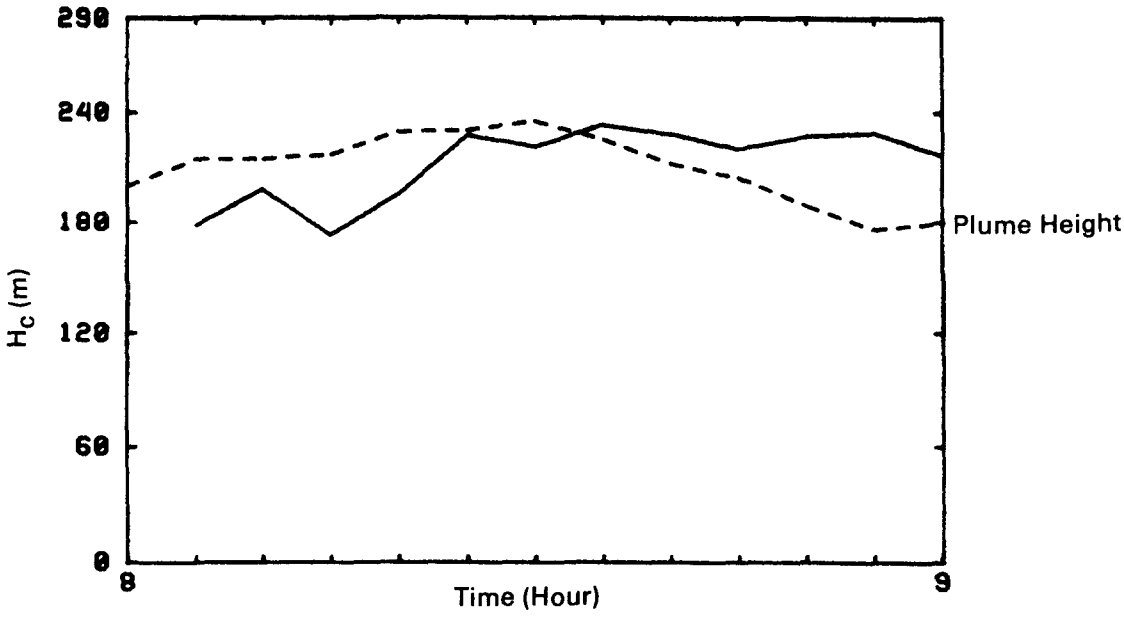

Figure 71. Time series of 5-minute calculated dividing-streamline heights (H_c) (FSPS, Experiment 13, 08/26/84, 0800-0900 PDT).

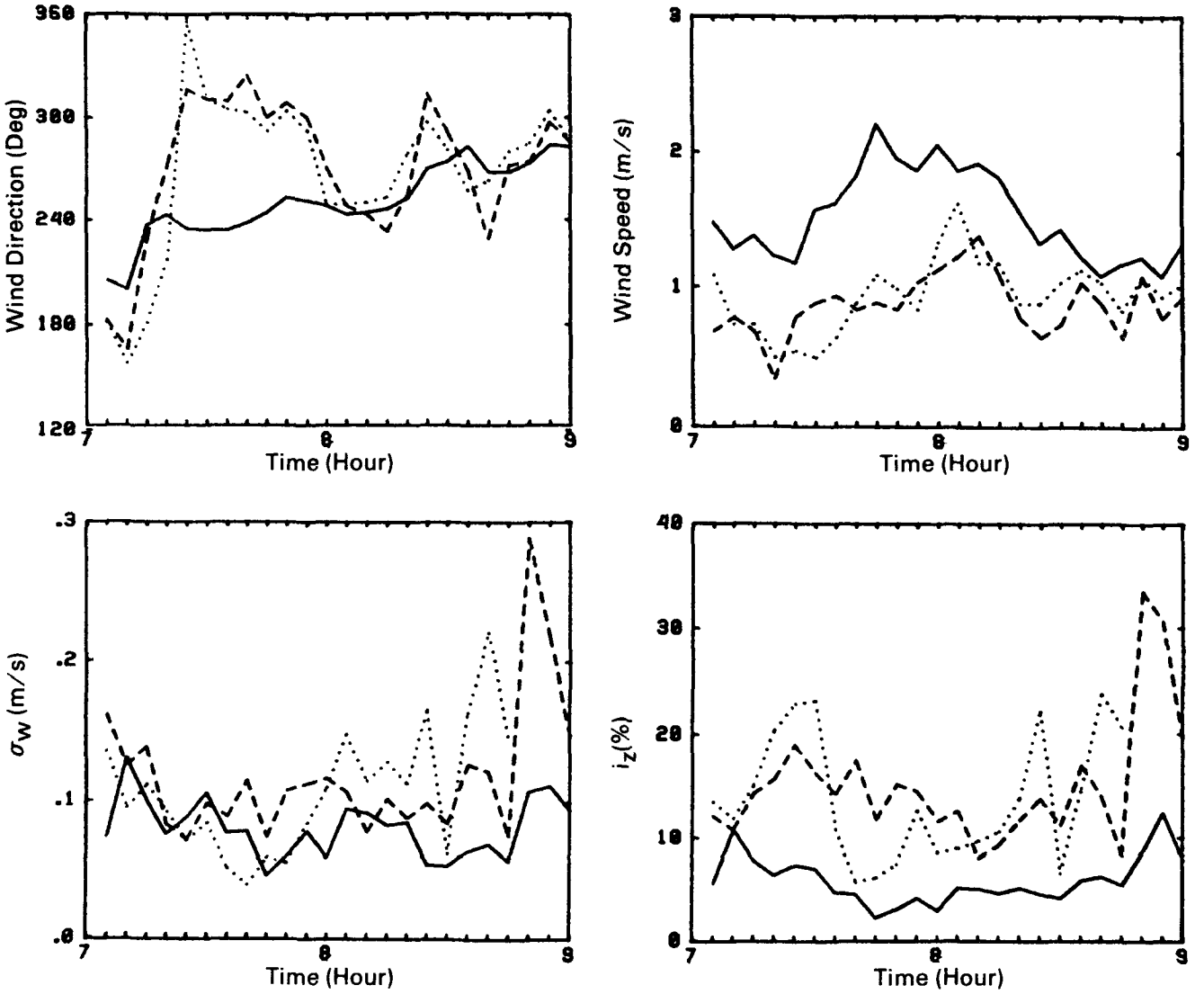

Figure 72. Top: Time series of cup and vane wind data at 150 m (____), 100 m (....), and 75 m (____). Bottom: Time series of propeller anemometer turbulence at 150 m (____), 125 m (____), and 100 m (....). (FSPS, Experiment 13, 08/26/84, 0700-0900 PDT).

estimated at the release height from the 150-m level is .148 m/s (i_z = 9%). The vertical profiles of the one-hour average of Tower A temperature and cup-and-vane wind data measured during hour ending 0800 are presented in Figure 73.

The hourly-averaged observed normalized SF_6 concentration ($\mu s/m^3$) distribution is presented in Figure 74. The wind flow vectors drawn at the release position are from the cup-and-vane data measured during the preceding hour. Observations and photographs indicate that as the plume approached "Beacon Hill," it split and traveled around the sides of the hill to the north and south. There was impingement on the southeast flank of Beacon Hill where the maximum observed concentration (8.3 $\mu s/m^3$) was measured. The plume also impinged to the north of Beacon Hill where the second highest concentration (8.0 $\mu s/m^3$) for the hour was observed. Figure 75 is an instantaneous photo taken with a polarizing filter at 0805 from a location west of the plant. As seen in this photo, filaments of plume material traveled up toward the summit of Beacon Hill. The plume can be seen to split as it approaches Beacon Hill and travels around the sides of the hill. Half-way through the hour, the plume shifted so that the main segment passed over the southern portion of Beacon Hill and the valley. Figure 76 was taken at 0845 from the camera position at Clark Mountain and shows the plume now traveling over the river valley. Notice the downward wisp of turbulent plume material in the vicinity of the Tracy stack.

The lidar measured plume centroid positions for approximately every five minutes during the hour are presented in Figures 77 through 79. It should be noted that the lidar cannot sample oil-fog on the north side of Beacon Hill; hence, the centroid positions are based only on "seen" plume material. Lidar measurements and observer comments (including those from the scientists who operated the lidar) indicate that during the first half of the hour, the plume is traveling northeast with considerable horizontal dispersion. Observations suggest some of the oil fog is lingering against the north side of the river basin west of Beacon Hill, and some of the plume is splitting off and passing to the north of the hill. The lidar does measure a considerable amount of plume material as it impacts the south shoulder of Beacon Hill. As the plume exits the Beacon Hill area, the plume appears to be drawn down the river cut. As the hour progresses, the plume trajectory shifts clockwise, and by 0845, there is little or no plume material against the north basin slope.

A time series plot of the plume direction measured in degrees from north is shown in Figure 80. As the hour progresses, the plume shifts clockwise (from Beacon Hill towards the river valley) at all five measuring azimuths of the lidar. A time series plot of the vertical displacement of the plume centroid above the stack is presented in Figure 81. As the plume approaches Beacon Hill during the first half of the hour, the plume centroid increases in elevation. However, during the last half of the hour, as the plume travels clockwise toward the river valley, the plume centroid decreases by more than 50 m in elevation.

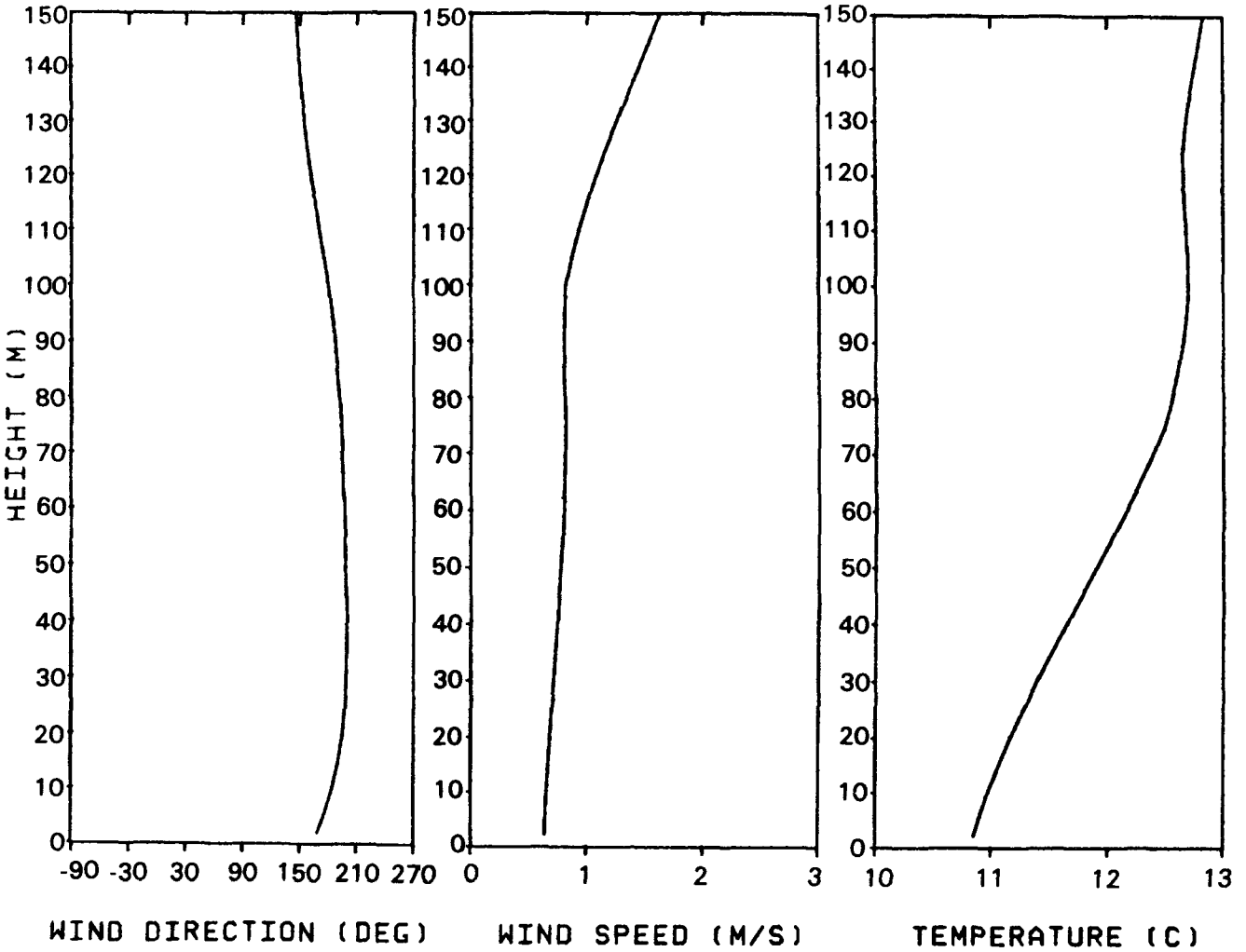

Figure 73. Vertical profiles of hourly meteorological data from Tower A (FSPS, Experiment 13, 08/26/84, 0700-0800 PDT).

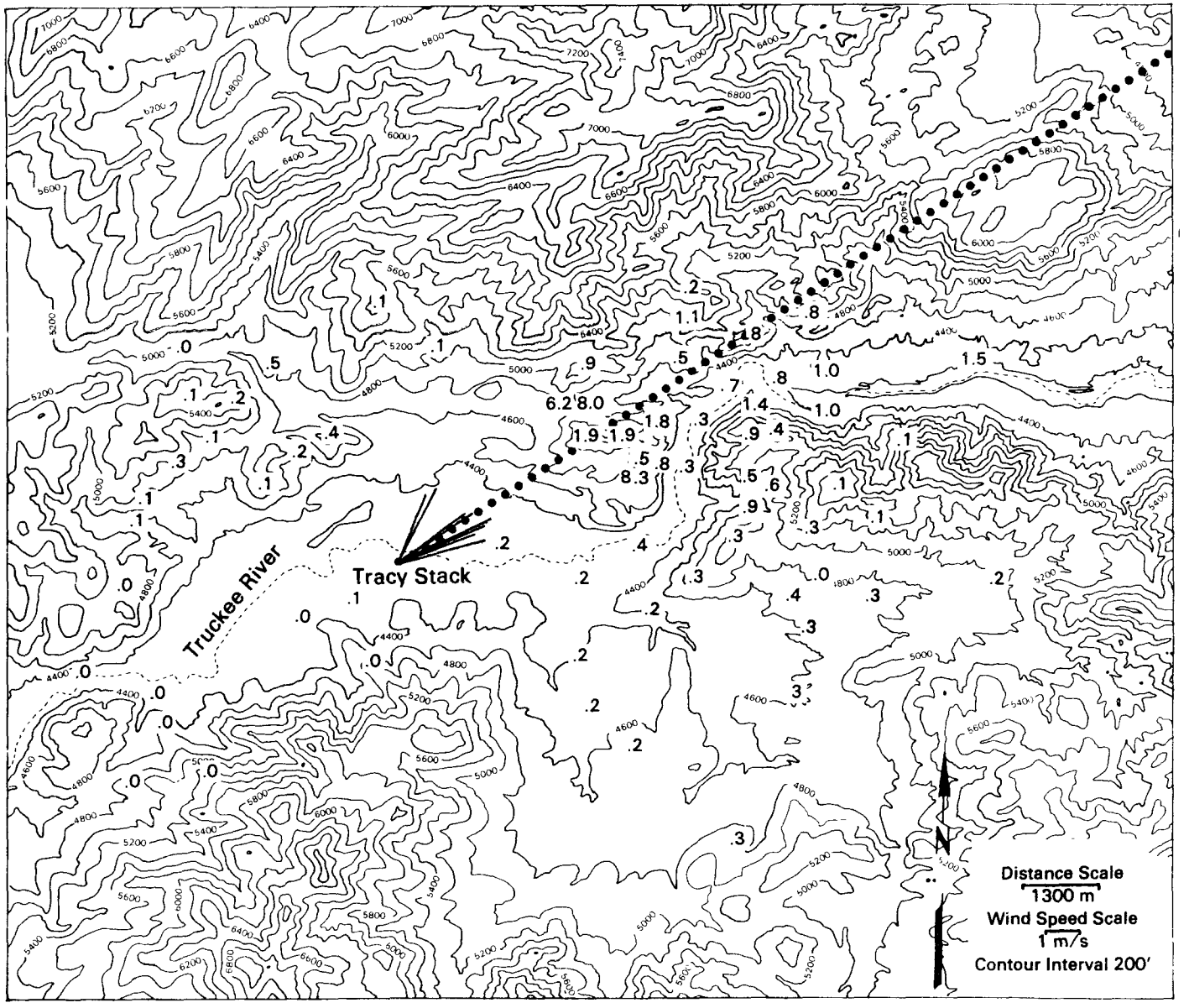

Figure 74. One-hour averaged observed SF_6 concentrations scaled by emission rate ($\mu s/m^3$) (FSPS, Experiment 13, 08/26/84, 0800-0900 PDT).

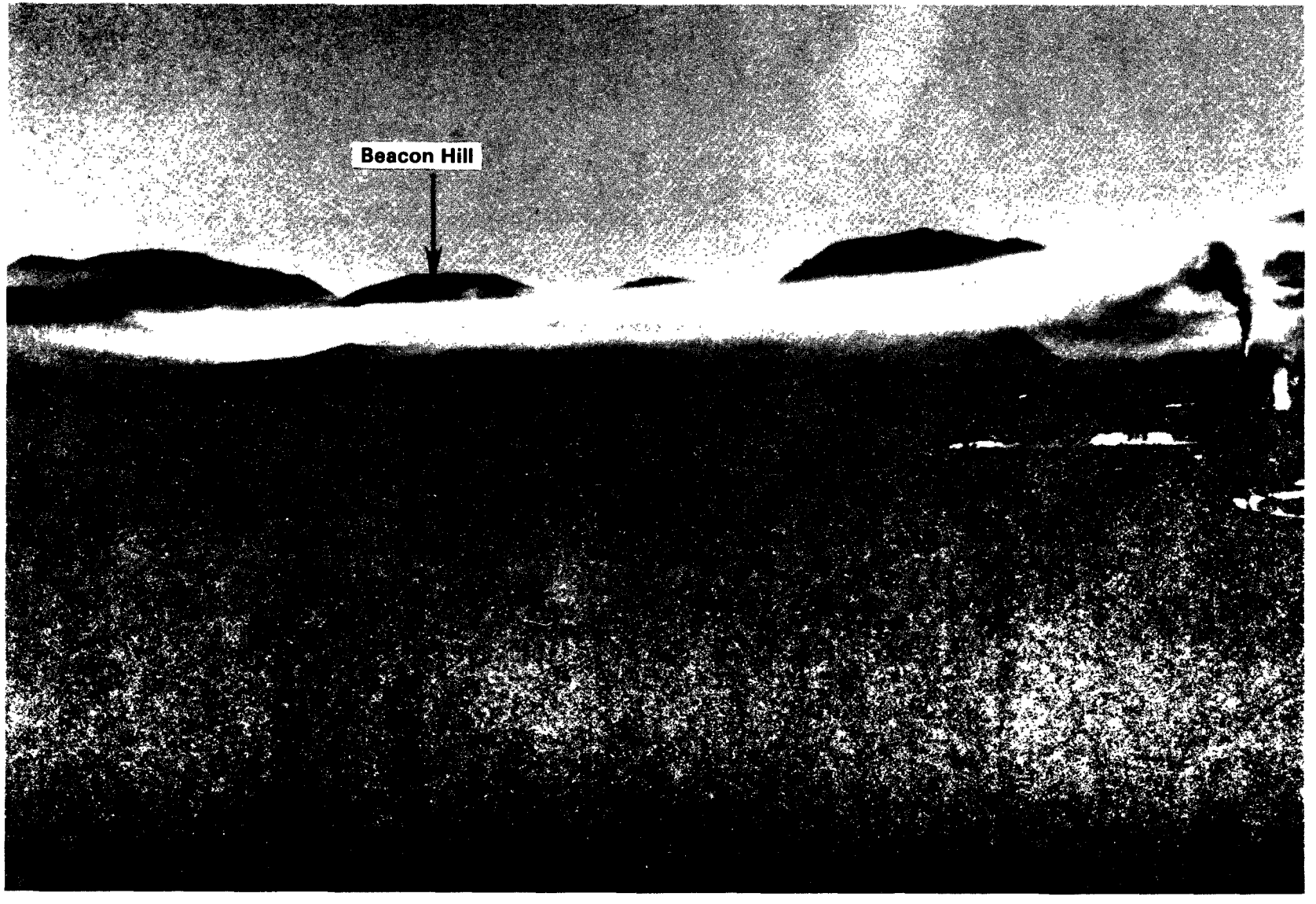

Figure 75. Instantaneous exposure with a polarizing filter taken from Old Lonesome of the plume as it interacts with Beacon Hill (*FSPS*, Experiment 13, *08/26/84, 0805 PDT*).

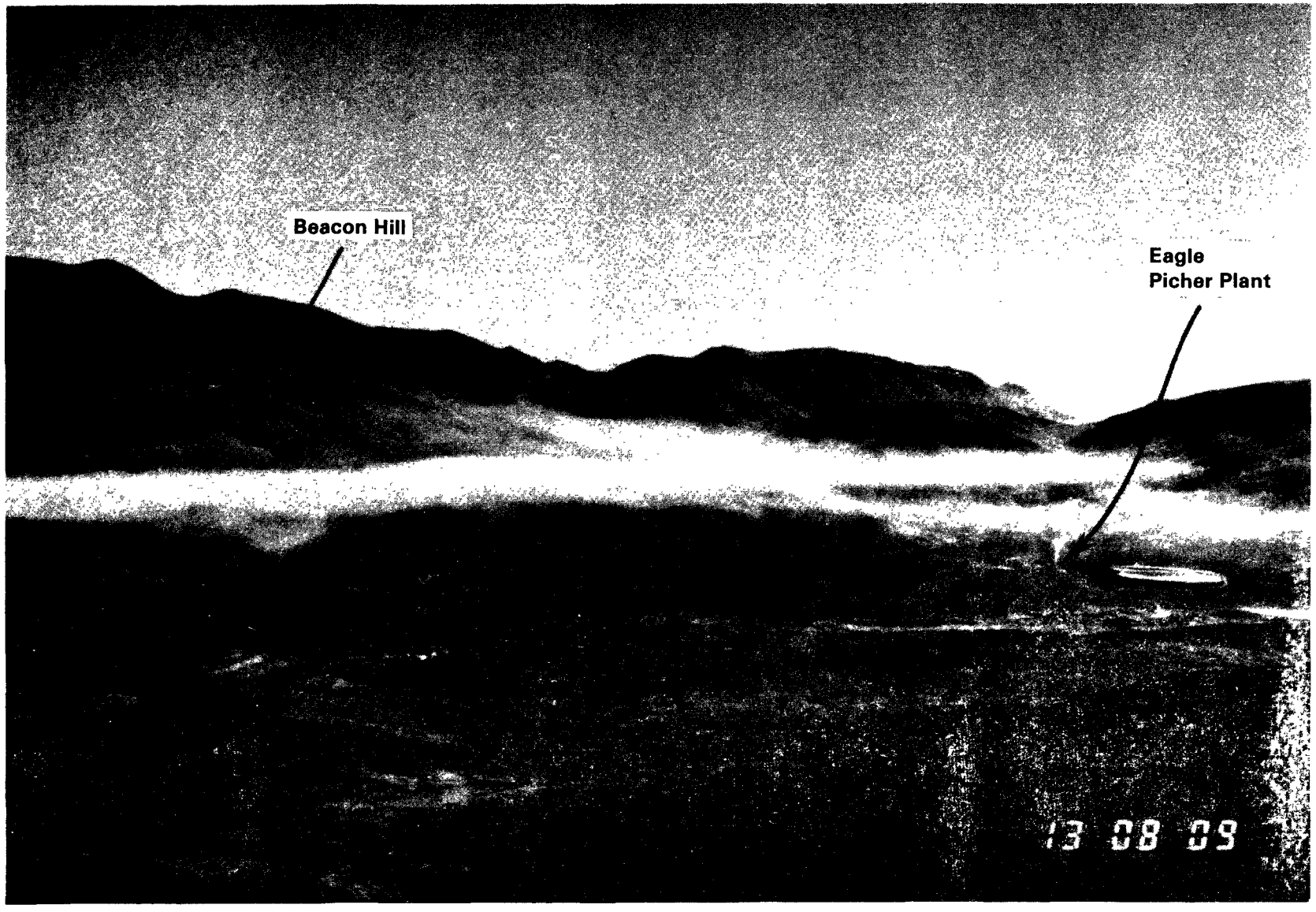

Figure 76. Instantaneous exposure taken from Clark Mountain of the plume traveling over the river valley (FSPS, Experiment 13, 08/26/84, 0845 PDT).

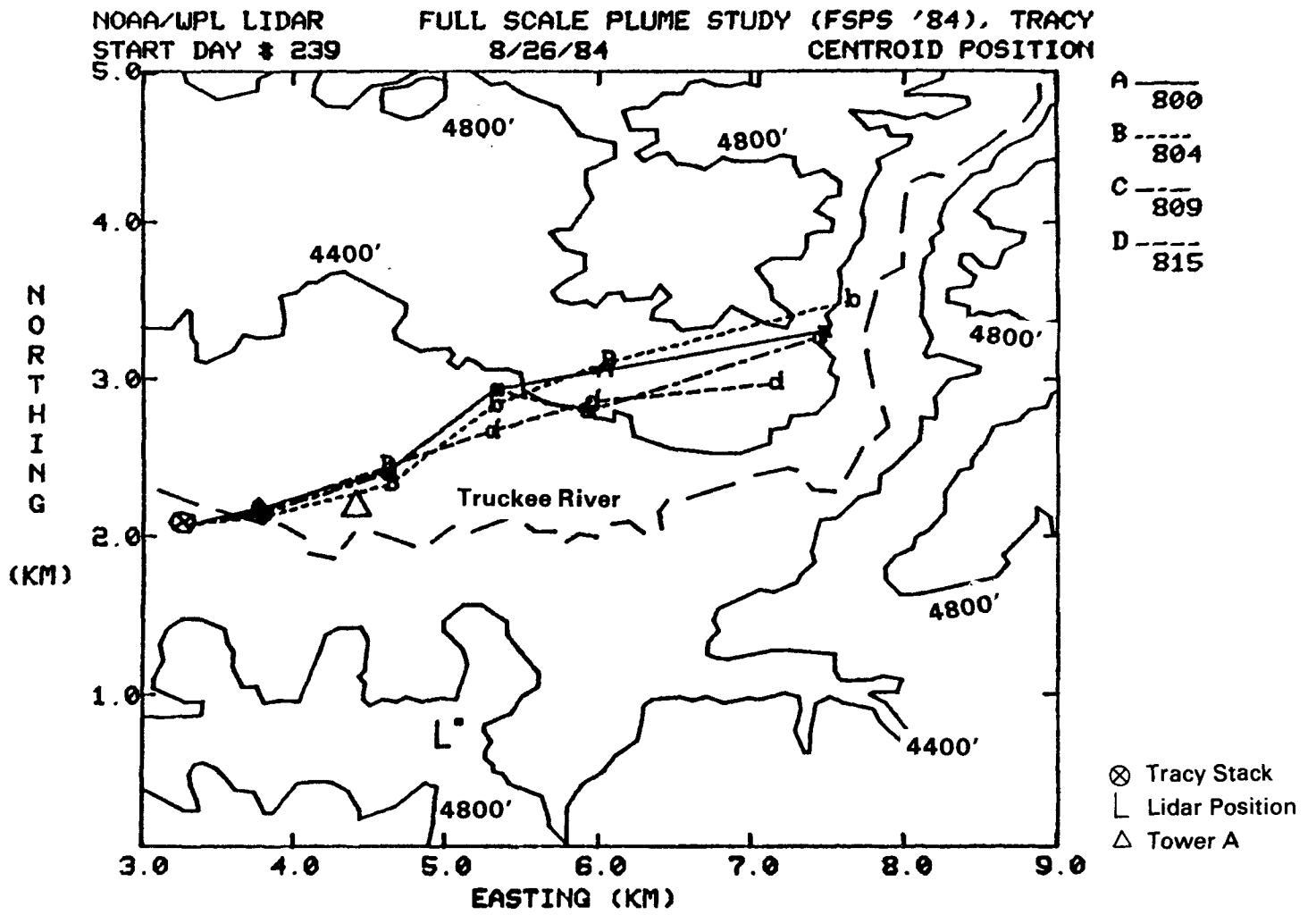

Figure 77. The lidar measured plume centroid positions (FSPS, Experiment 13, 08/26/84, 0800-0815 PDT). The plotting symbol, line type, and time of each lidar scan are presented in the upper right corner.

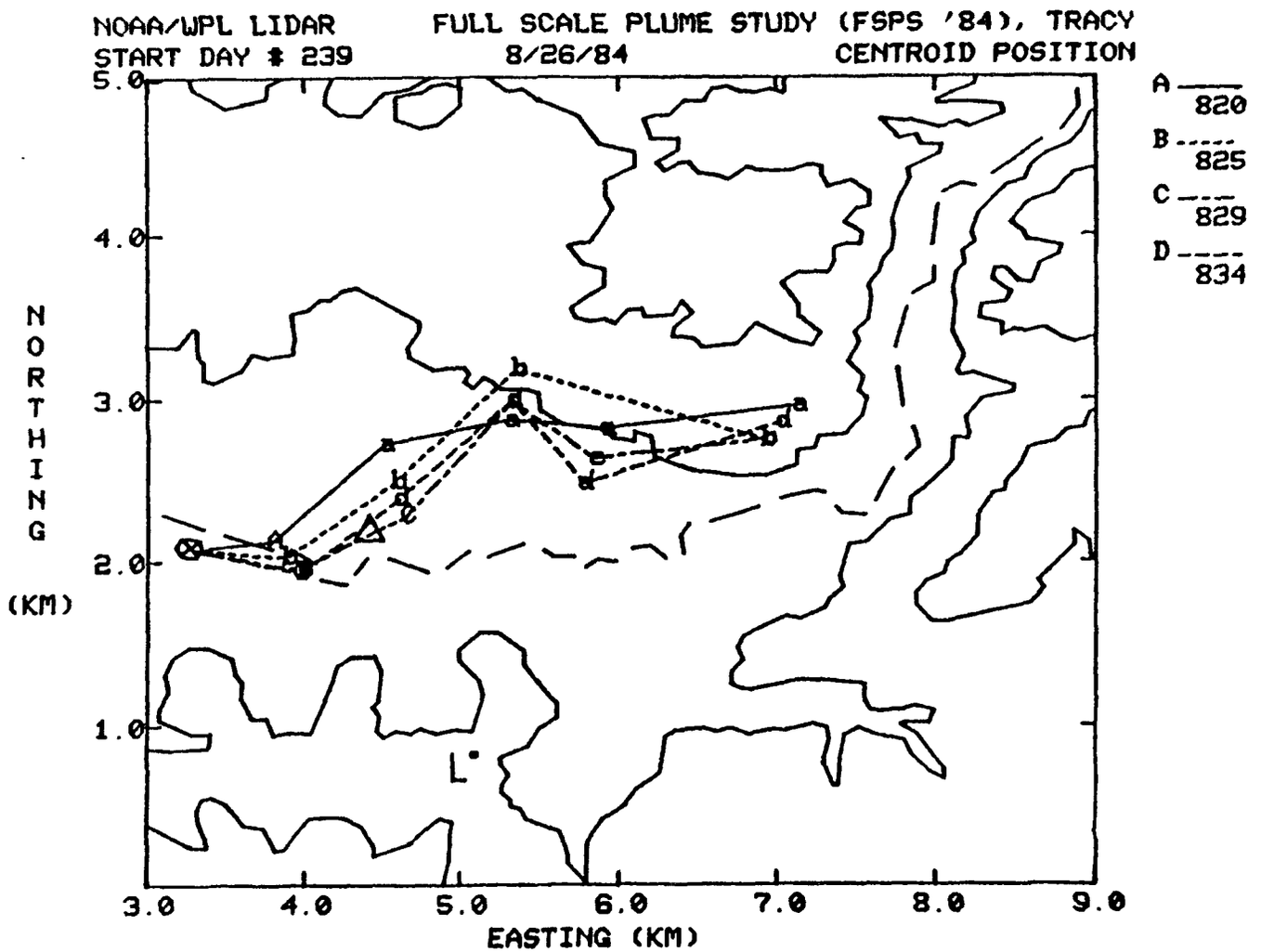

Figure 78. The lidar measured plume centroid positions (FSPS, Experiment 13, 08/26/84, 0820-0834 PDT). The plotting symbol, line type, and time of each lidar scan are presented in the upper right corner.

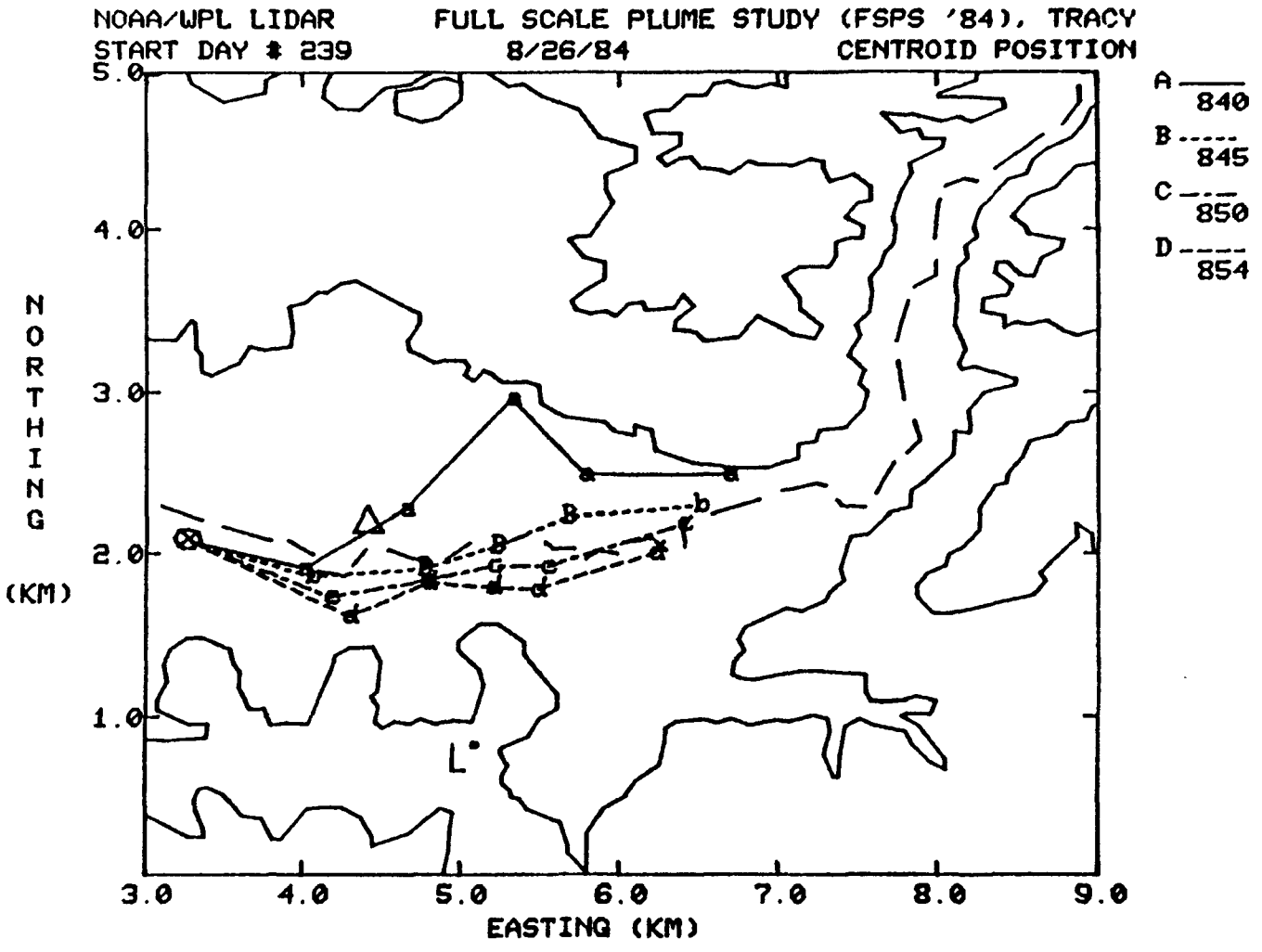

Figure 79. The lidar measured plume centroid positions (FSPS, Experiment 13, 08/26/84, 0840-0854 PDT). The plotting symbol, line type, and time of each lidar scan are presented in the upper right corner.

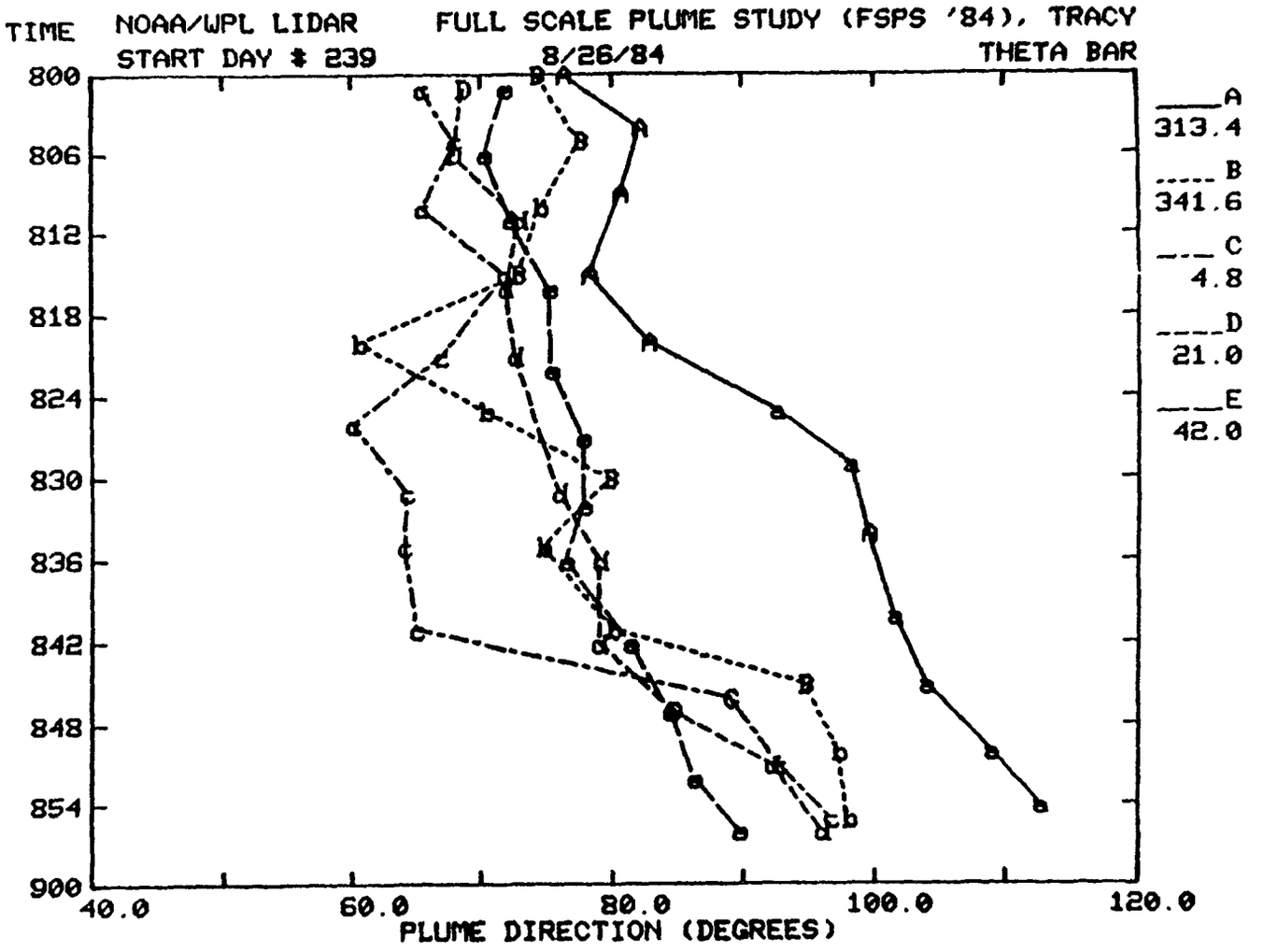

Figure 80. Time series of 5-minute lidar derived plume direction measured in degrees from north (FSPS, Experiment 13, 08/26/84, 0800-0900 PDT). The plotting symbol, line type, and lidar azimuth are presented in the upper right corner.

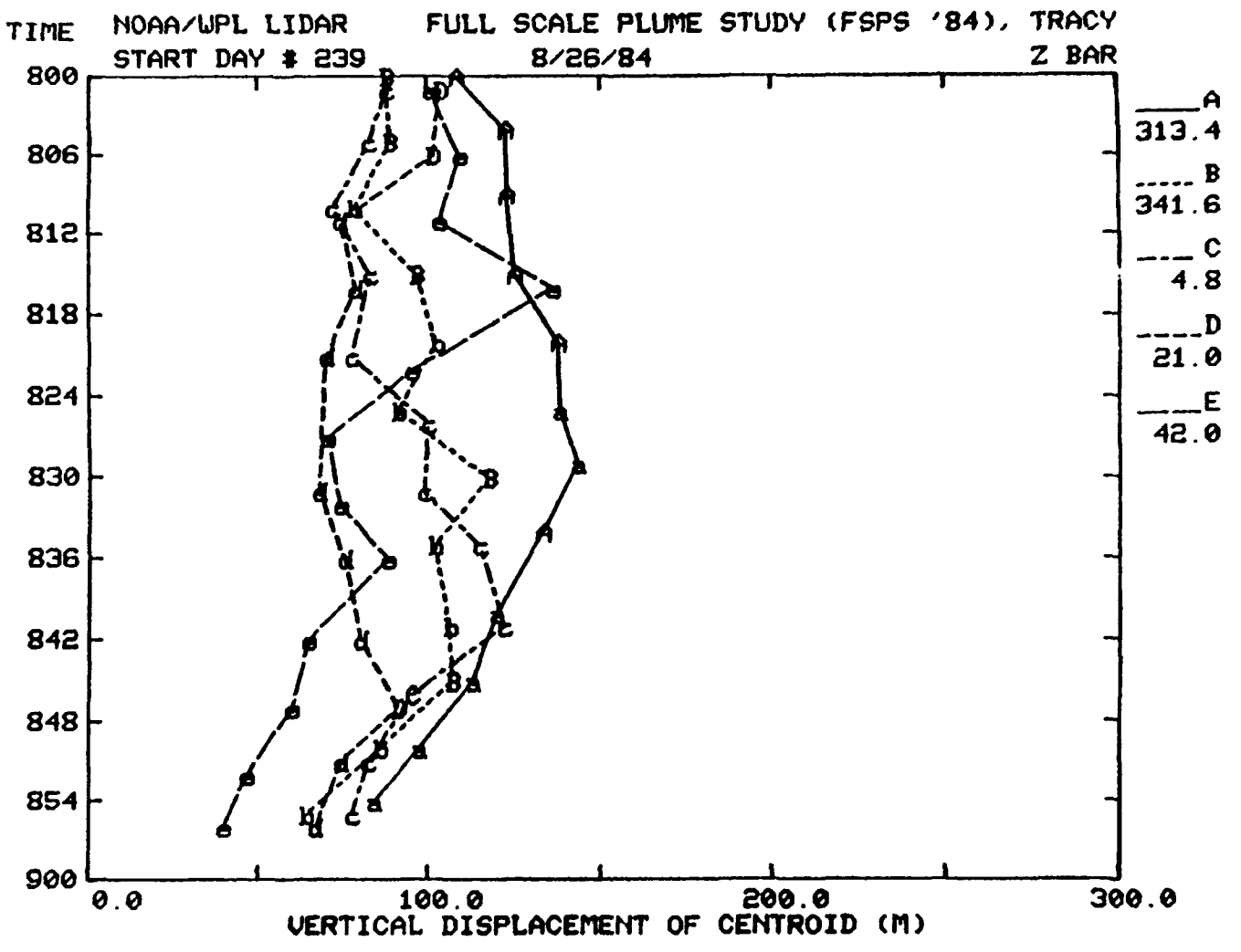

Figure 81. Time series of 5-minute lidar derived vertical displacement of the plume centroid above the stack (FSPS, Experiment 13, 08/26/84, 0800-0900 PDT). The plotting symbol, line type, and lidar azimuth are presented in the upper right corner.

The hourly averaged lidar scans made at a distance of 1384 m from the Tracy stack are used to estimate a vertical plume size (σ_z) of 36 m and a horizontal plume size (σ_y) of 515 m. Using Equation 59, the normalized centerline concentration is calculated to be 5.4 $\mu s/m^3$, which is comparable with the maximum observed normalized concentration of 8.3 $\mu s/m^3$.

4.4 Comparison of Field Sites

The distributions of the tracer concentrations and the lidar and photographic data collected at the three CTMD field sites support the concept of a dividing streamline that separates stable air flow into two layers. At CCB the highest concentrations were observed most often when the tracer gas was emitted at an elevation near the calculated dividing-streamline height. These highest concentrations were sampled typically at hill elevations lower than the release height. High concentrations also occurred with releases above and below H_c.

At the Hogback the highest concentrations were observed when the tracer gas was released below H_c. Evidently, at a long ridge setting like HBR, the flow below H_c is constrained or blocked by the ridge, thereby giving the tracer gas a prolonged opportunity to impinge on its windward side. These situations were also associated with very light winds at source height which contribute to the high χ/Q values. At the isolated, three-dimensional CCB site the air flow below H_c is not constrained, but "escapes" by flowing around the sides of the hill, effectively dispersing the tracer gas. At both sites tracers released above H_c tended to flow over the terrain and the higher concentrations were produced near the top or on the lee side.

Initial examination of the Tracy data base suggests the full-scale site exhibits dispersion characteristics of both small scale sites. The concentrations listed in Table 12a show that eight of the ten highest normalized SF_6 concentrations occurred when the tracer gas was released below H_c. We have not yet analyzed the meteorological data to ascertain if the low-level flow was blocked or constrained, if at all. For the hours with the ten highest SF_6 concentrations, five currently have lidar-based estimates of plume height. All five plume heights (or effective release heights) are near the calculated height of the dividing streamline.

SECTION 5

MODEL DEVELOPMENT AND APPLICATIONS TO CTMD EXPERIMENTAL DATA

5.1 Description of the Current Version (12185) of CTDM

This section describes changes that have been made to CTDM since preparation of the Fourth Milestone Report (Strimaitis et al. 1984). CTDM (12185) is the first version that can be readily applied to the three experiment sites. It has been run using "impingement" subsets of the three data bases and some of the results are reported here.

5.1.1 Terrain Description

To simplify the structure of the code, previous versions of CTDM had modeled the terain obstacle as either an isolated axisymmetric hill or an isolated two-dimensional ridge section. This required two separate terrain treatments in the model to handle both CCB and HBR. For general application, CTDM needs to be able to accommodate hill shapes intermediate between these two idealizations.

CTDM now simulates all isolated hills or hill segments as if they were ellipses in horizontal cross-section. At any height between the base of the hill and the crest, the hill shape is characterized by the lengths of its major and minor axes. However, the vertical cross-section of the hill is not assumed to be elliptical.

A height profile, h, along each "axis" of the hill is presumed to have the form:

$$h = \frac{H}{1+(x/L)^p} + h_o \qquad (64)$$

where H is the height of the crest of the hill above a zero-plane (i.e., H is the relief height of the hill), x is the distance from the crest along the axis, L is the horizontal scale of the hill that equals the value of x at the point on the hillside where h = 0.5 H, p is an exponent whose value is chosen to give an adequate representation of the hill shape in profile, and h_o is the height of the zero-plane above the elevation defined as zero in the coordinate system being used. For a particular hill, L and p may have values that differ from the major axis to the minor axis. For example, CCB is represented by the choices

H = 105 m		h_o = -10 m	
L(major) = 280 m		L(minor) = 225 m	
p(major) = 3.3		p(minor) = 4.0	

Also needed in this terrain specification is the orientation of the major axis relative to north. For CCB, it is 127° clockwise (CW) from north.

This method for describing the terrain features to the model allows the model to treat CCB and HBR with the same algorithms. The terrain parameters for HBR are:

orientation = 27° CW from north			
H = 90 m		h_o = 1599 m	
L (major) = 10,000 m		L(minor) = 150 m	
p (major) = 10.0		p(minor) = 1.8	

Note that the test-section of HBR is essentially a two-dimensional ridge, so that the major axis is specified by a very large length scale. Also, heights at HBR are referenced to sea level, whereas heights at CCB are referenced to 945 m MSL; hence h_o differs markedly between the two locations.

5.1.2 WRAP

Characteristics of Two-Dimensional Flow Around an Ellipse

A particle in a steady two-dimensional flow around an ellipse will experience both accelerations and decelerations as it passes by the ellipse. The magnitude of these changes in speed depends upon how close the particle is to the stagnation streamline of the flow. Maximum changes occur for particles on the stagnation streamline. Furthermore, the spacing between adjacent streamlines varies in inverse proportion to these changes in the speed along streamlines.

Figure 82 is a representation of a typical streamline pattern for flow around an ellipse when the incident flow is at an angle to the axes of the ellipse. The speed along a particular streamline reaches a minimum near the stagnation zone along the upwind face. It then increases to a maximum at some point near the apex of the boundary, beyond which the speed slows once again to a minimum before resuming the speed of the incident flow.

A plume in this steady flow (with some small-scale turbulence) will follow the streamline patterns, spreading slowly across adjacent streamlines. However, as streamlines spread apart (or contract) the plume size in the horizontal will expand (or shrink) to the same extent. In the absence of diffusion, these kinematic changes in the horizontal size of the plume will not alter the concentration of material within the plume. Changes to the horizontal scale of the plume are balanced by changes in the flow speed so that the flux of material is unchanged. With the addition of small-scale diffusion, the rate of plume growth in the horizontal can be altered by changes in streamline spacing (Hunt and Mulhearn, 1973). However, based on

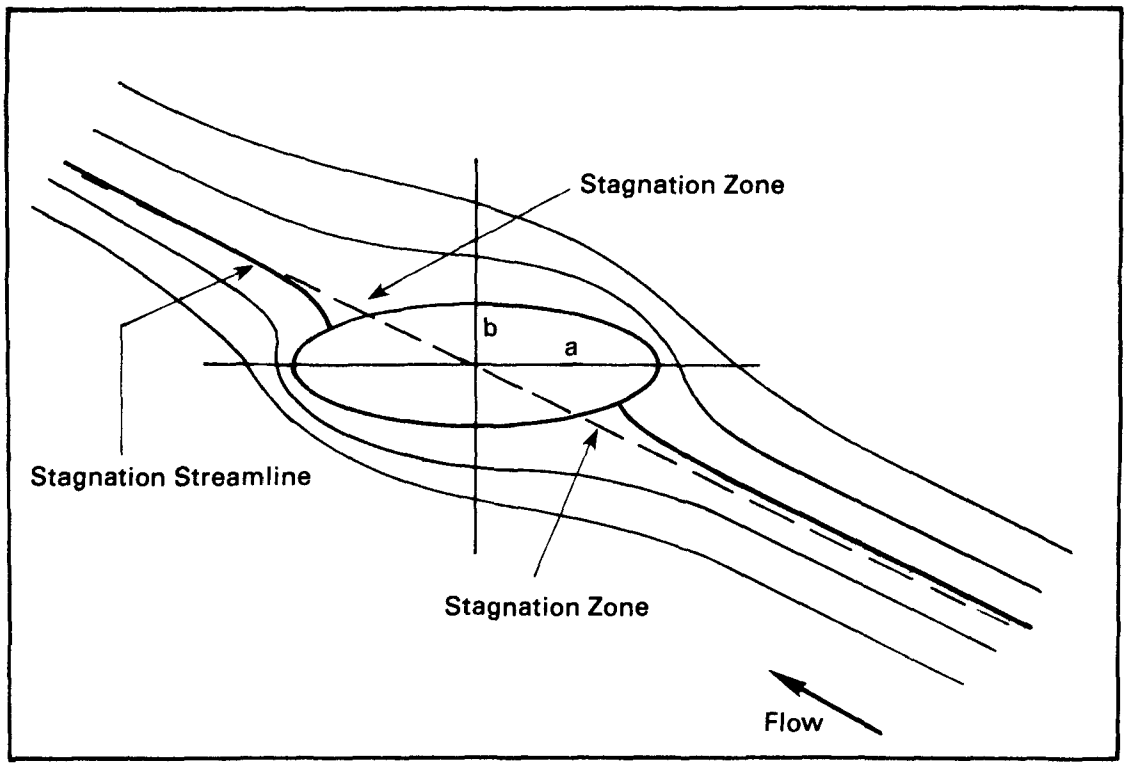

Figure 82. Typical streamline patterns in two-dimensional flow around an elliptical cylinder.

the observations at CCB and Tracy we choose to ignore the effects of small-scale diffusion on concentrations in the WRAP component of CTDM. The observations suggest that kinematic effects dominate short averaging times and that low frequency turbulence -- meanders -- control crosswind plume growth over hourly averaging times.

Plume growth in the vertical increases to the extent that the time-of-travel to a particular receptor increases compared to that in the absence of the hill. In principle, if plume material is traveling toward the hill along the stagnation streamline, it will take an infinite amount of time for that material to reach the hill (the speed along the stagnation streamline goes to zero at the stagnation point). This of course also gives diffusion an infinite amount of time to act on this material and remove it from the stagnation streamline. This idealization, of course, doesn't occur; but recent fluid modeling studies (Hunt, 1985), have shown the importance of the effect of travel-time on the vertical growth of plumes.

WRAP Reformulation

To simulate ground-level concentrations due to dispersion of releases below H_c in complex terrain settings, CTDM must approximate the key features of steady two-dimensional flow around an ellipse that were described above. Two key approximations in the WRAP component are (1) lateral diffusion is insensitive to accelerations in the flow (i.e., the kinematic deformation of the plume has no effect on the diffusion rate), and (2) vertical diffusion increases with increases in travel-time caused by terrain-induced alterations in the flow speed. Furthermore, the mean flow for the averaging period (one hour) is considered steady, while all of the variability in the flow over the period, including that due to meandering, is considered "turbulence."

This approach differs from that previously adopted in WRAP, in which some allowance had been made for alterations in lateral diffusion caused by the kinematic deformations in the flow while no allowance had been made for travel-time effects in the rate of vertical growth of the plume. Furthermore, a distinction had been made between fluctuations in the direction of the wind on the time-scale of the vertical turbulence and fluctuations on the time-scale of meanders in the flow so that concentrations on the surface of the hill depended upon the dilution of material in the "filament" plume, and the frequency (over the averaging period) that the wind came from a direction very near to the stagnation wind direction. Note that the effects of flow distortion on lateral diffusion only altered the rate of spread of the narrow "filament" plume and had no effect on the meander of the "filament" plume.

The change in WRAP has been motivated in part by the scale of the FSPS compared to that of SHIS #1 or SHIS #2. With the very light transport speeds typically associated with flows with impingement potential, transport times from the source to terrain frequently exceeded an hour at the FSPS site. Consequently, the travel-time could readily exceed the meander time-scale. When this occurs, the

path taken by a puff or plume segment is not straight, and plume material can be advected toward a hill along a number of potential stagnation streamlines rather than the single one for a flow that is steady over the travel time to the hill. This situation would appear to be better approximated by a wide plume in a steady flow.

A second reason for the change in the WRAP model was the observed tendency toward overestimating impingement concentrations at CCB (SHIS #1). Photographs of the plume during several primary impingement episodes showed a rather striking rate of plume growth in the vertical near the hill. In other words, the travel-time factor is important and should be included in the model.

With these approximations and assumptions in mind, the "filament" plume equation (Equation 33) presented by Strimaitis et al. (1984) for receptors beyond the impingement point was modified to include the total lateral turbulence measured during the averaging period, neglecting distortion effects. The Equation (33) now becomes

$$C = \frac{Q}{4\pi u_\infty \sigma_y \sigma_z} \mathrm{Exp}(-0.5(d/\sigma_y)^2)\ (1 + \mathrm{sign}(y_r)\mathrm{Erf}\ \frac{d\ \sigma_y^*}{\sqrt{2}\sigma_{yo}\sigma_y}) \cdot (B_1 \mathrm{Exp}(-0.5(\frac{z_r - z_R}{\sigma_z})^2) + B_2 \mathrm{Exp}(-0.5(\frac{z_r + z_R}{\sigma_z})^2)) \quad (65)$$

where

$$B_2 = \mathrm{Erf}(\frac{b_1 - b_2 + b_3}{b_o}) + \mathrm{Erf}(\frac{b_1 + b_2 - b_3}{b_o})$$

$$B_1 = \mathrm{Erf}(\frac{b_1 - b_2 - b_3}{b_o}) + \mathrm{Erf}(\frac{b_1 + b_2 + b_3}{b_o}) \quad (66)$$

and

$$b_o = \sqrt{2}\sigma_z \sigma_{zo} \sigma_z^*$$

$$b_1 = H_c \sigma_z^2$$

$$b_2 = z_R \sigma_{zo}^2$$

$$b_3 = z_r \sigma_z^{*2}$$

The subscript R denotes the receptor location, and the subscript r denotes the source location (see Figure 83). The distance from the stagnation streamline associated with the mean wind direction to the centerline of the plume is denoted as d, the total sigma-y (for horizontal spread of the mean plume) as σ_y, and the total sigma-z

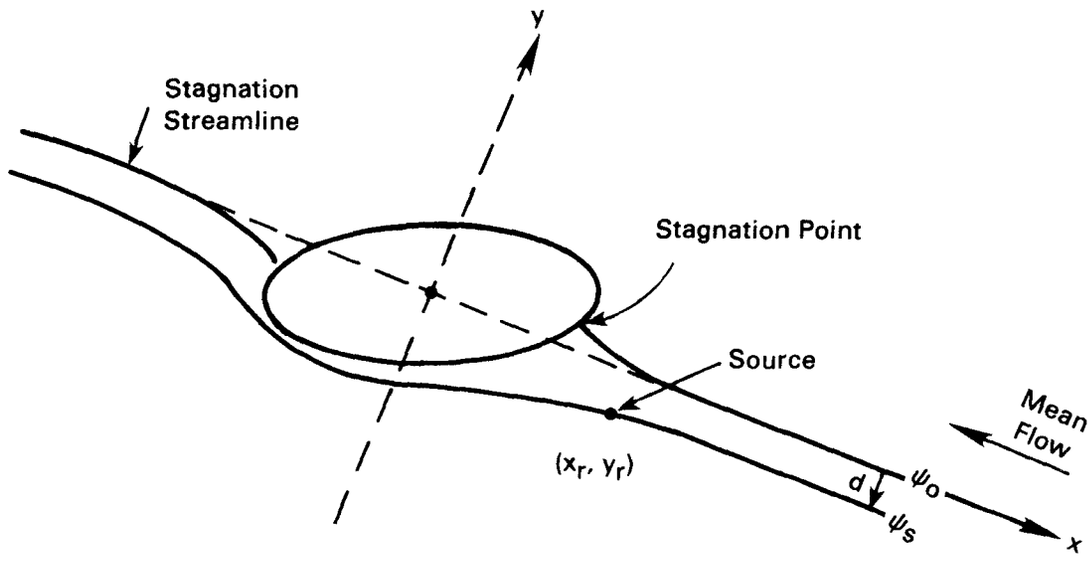

Figure 83. Sketch of the flow around an ideal cylinder of elliptical cross-section. The section shown is taken either at the elevation of the centerline of the plume (z_r), or at H_c, depending on which is smaller, and it indicates the relationship between the streamline through the source (ψ_s), the stagnation streamline (ψ_o=0), and the coordinate system with x-axis aligned with the mean wind direction.

(for the vertical spread) as σ_z. The amount of plume spread experienced over the distance to the stagnation point is denoted as σ_{zo} and σ_{yo}, and the rate of plume growth beyond the stagnation point to the receptor is denoted as σ_z^* and σ_y^*, where

$$\sigma_z^{*2} = \sigma_z^2 - \sigma_{zo}^2$$

$$\sigma_y^{*2} = \sigma_y^2 - \sigma_{yo}^2 \qquad (67)$$

The size of the ellipse that is used to estimate the flow below H_c is taken from the horizontal cross-section of the hill at the minimum of the following two elevations: either the elevation of the centerline of the plume, or the elevation of H_c. In this way the shape of the hill selected is associated with the peak concentration of plume material found within the layer of fluid below H_c. As a consequence, the position of the impingement point (or the stagnation point) is also associated with the peak concentration of plume material below H_c.

Concentrations at receptors located on the hillside upwind of the stagnation point (see Figure 83) are estimated as if the receptor sits on a pole of height equal to the receptor elevation above the base of the stack. Furthermore, the lateral distance between the plume centerline and the receptor is set equal to d, so that concentrations at all of these receptors are controlled by the amount of material on the stagnation streamline. In this way plume material below H_c and below plume centerline height follows streamlines around the hill, and only material which diffuses onto the stagnation streamline impinges on the hill. The equation for estimating these concentrations is:

$$C = \frac{Q}{2\pi u_\infty \sigma_y \sigma_z} \mathrm{Exp}(-0.5(d/\sigma_y)^2)\{\mathrm{Exp}(-0.5(\frac{z_R - z_r}{\sigma_z})^2) + \mathrm{Exp}(-0.5(\frac{z_R + z_r}{\sigma_z})^2)\} \qquad (68)$$

Equations 68 and 65 provide estimates of ground-level concentrations of plume material before and after plume material above H_c is "removed", respectively. That is, the upper and lower portions of the flow do not become distinct in CTDM until the impingement or stagnation point is reached. In these equations, the primary effects of the hill on ground-level concentrations are (1) the steering of the plume to the side of the hill, modeled through the lateral offset distance (d), and (2) the increase in the time-of-travel experienced by plume material near the stagnation streamline of the flow, modeled through increasing the size of the plume in the vertical (σ_z). Both the lateral offset of the plume streamline from the stagnation streamline and the time-of-travel are estimated from the theory of potential flow around an elliptical cylinder. They are obtained in the following way:

Incident Flow: The wind speed and direction measured at a tower near a hill may be influenced by the presence of the hill, so that the observed mean speed and direction must be estimated at infinity to determine the incident flow. This is calculated from the theory of two-dimensional potential flow around an ellipse. Denote this speed and direction by S_∞ and $-\alpha_w$, where the direction is measured counter-clockwise from the major axis of the ellipse (Figure 84).

Source Streamline: Once the size and shape of the ellipse and the incident flow angle relative to the major axis of the ellipse are known, the source position can be converted to the elliptical coordinates (μ_s, ν_s) and the stream function through the source (ψ_s) can be calculated from

$$\psi_s = -S_\infty (a + b) \sinh(\tilde{\mu}_s) \sin(\nu_s + \alpha_w) \tag{69}$$

where a is the semi-major axis of the ellipse, and b is the semi-minor axis (Batchelor, 1967). Note that $\tilde{\mu}$ equals $\mu - \mu_o$ in Batchelor's notation so that $\tilde{\mu} = 0$ on the surface of the ellipse. For an ellipse whose major axis lies along the x-axis, the relationship between (μ, ν) and (x,y) is given by

$$\begin{aligned} x^2 &= (a^2 - b^2) \cosh^2(\mu + \mu_o) \cos^2(\nu) \\ y^2 &= (a^2 - b^2) \sinh^2(\mu + \mu_o) \sin^2(\nu) \end{aligned} \tag{70}$$

Rotated Coordinate System: Distance is tracked along the x_β-axis, which is parallel to the stagnation streamline at the stagnation point. This coordinate system is needed to provide a convenient Cartesian coordinate system that allows the streamline through the source to be a single-valued function of x for all α_w. The rotation angle, ß, is given by

$$\tan \beta = -\frac{a}{b} \tan(\alpha_w) \tag{71}$$

Source Streamline Offset (d): The distance between the streamline through the source (ψ_s) and the stagnation streamline $(\psi_o = 0)$ far from the hill is related to the value of ψ_s and the wind speed at infinity, S_∞. Because the speed of the flow equals the gradient of the stream function far from the hill, we find

$$d = \psi_s / S_\infty \tag{72}$$

However, because σ_v may be measured closer to the hill, the speed at the source is substituted to estimate d near the source.

Time-of-Travel: Denote the component of the speed along ψ_s that lies along the x_β-axis as S_β. Then the time that it takes to travel from the source to the neighborhood of the impingement point, a distance $x_{o\beta} - x_{s\beta}$, is given by the integral of $1/S_\beta$ over that

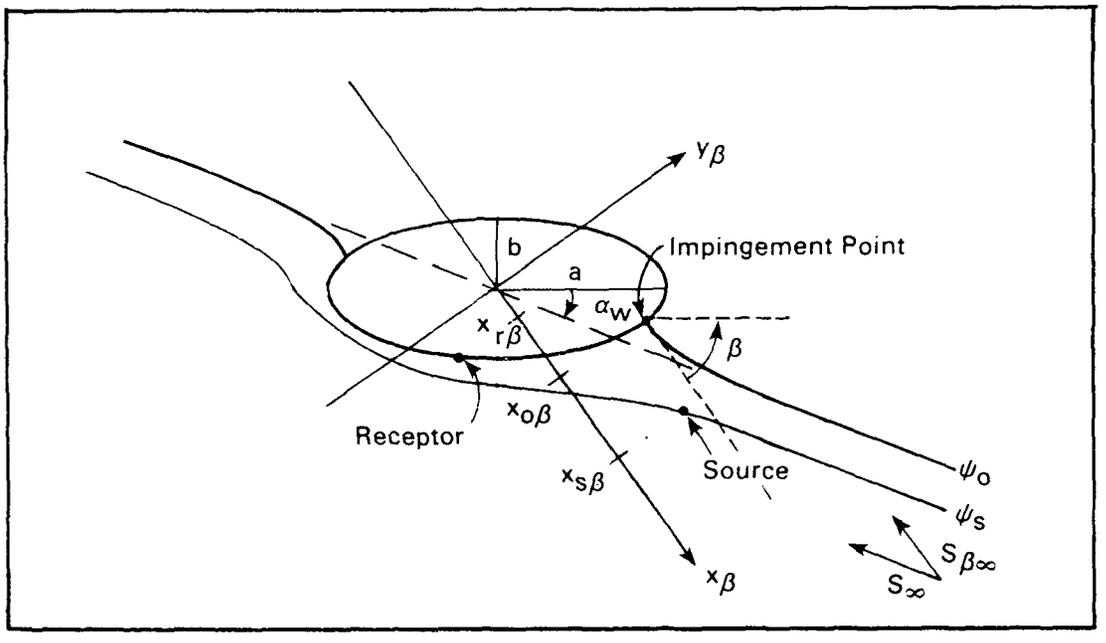

Figure 84. Definition of modeling variables, illustrating in particular the coordinate system in which the x_β-axis is aligned with the tangent to the stagnation streamline at the impingement point (the ß-coordinate system). The coordinates along the x_β-axis of the source are denoted by $x_{s\beta}$, $x_{o\beta}$, and $x_{r\beta}$, respectively.

interval. Furthermore the ratio of the time-of-travel in the presence of the hill to that in the absence of the hill, a time-of-travel factor, is given by the average of $S_{\beta\infty}/S_\beta$ over the interval. The quantity $S_{\beta\infty}/S_\beta$ is given by

$$\frac{S_{\beta\infty}}{S_\beta} = \frac{((r^2-1)\sin^2\nu + (r\sinh\tilde{\mu} + \cosh\tilde{\mu})^2)(1 + r\tan^2\alpha_w)}{r(r+1)((\sin\nu + \cos\nu\tan\alpha_w)^2 + \sinh^2\tilde{\mu}(1+\tan^2\alpha_w) + \sinh\tilde{\mu}\cosh\tilde{\mu}(1+r^2\tan^2\alpha_w\nu/r))} \tag{73}$$

where r = a/b. In practice, a time-of-travel factor is obtained by numerically integrating Equation 73 over the interval to find its average value.

Sigma-z: Changes to the flow speed along the plume centerline and the horizontal size of the plume due to kinematic effects do not alter the concentration of material in the modeled plume. Therefore, the total σ_y appearing in Equation 65 (or 68) is expressed in terms of the travel time given by $(x_{r\beta} - x_{s\beta})/S_{\beta\infty}$ where $x_{r\beta}$ is the position of the receptor along the x_β-axis, and $x_{s\beta}$ is that of the source. Sigma-z does depend on the changes to the time-of-travel. If the receptor lies upwind of the impingement position $x_{o\beta}$, the time-of-travel is given by

$$\tau = \frac{(x_{r\beta} - x_{s\beta})}{S_{\beta\infty}} \int_{x_{s\beta}}^{x_{o\beta}} \frac{S_{\beta\infty}}{S_\beta}\, dx_\beta \, \frac{1}{x_{s\beta}-x_{o\beta}} \tag{74}$$

If the receptor lies beyond $x_{o\beta}$, then the time-of-travel is given by

$$\tau = \frac{x_{r\beta}-x_{o\beta}}{S_{s\beta}} + \frac{1}{S_{\beta\infty}} \int_{x_{s\beta}}^{x_{o\beta}} \frac{S_{\beta\infty}}{S_\beta} dx_\beta \tag{75}$$

where $S_{s\beta}$ is the component of the flow along the x_β-axis at the source position. In this way all travel-time in the interval between the source and the impingement position is adjusted by the time-of-travel factor for the entire interval. This augmented time-of-travel is used to calculate σ_z by means of Equation 50. Note that u_∞ in Equations 65 and 68 is set equal to S_∞.

Two points need to be stated regarding the use of this modeling procedure. First, these adjustments to the flow and dispersion properties are invoked only when the centerline of the plume is less than or equal to the elevation of H_c plus σ_z at $x_{o\beta}$, plus the length σ_{Hc}, which accounts for the variability in H_c over the averaging interval. In this way we distinguish between plumes that

travel primarily in the flow above H_c from those that have a substantial fraction of their material in the flow below H_c.

Second, the time-of-travel is never computed for a mean wind direction that places the source on the stagnation streamline. As discussed earlier, the flow is not expected to be truly steady so plume material will experience a finite residence time on the stagnation streamline. A measure of this residence time is the crosswind turbulence intensity, i_y. For larger values of i_y, the wind direction is less likely to place the source on the stagnation streamline for a long enough period of time to bring it very close to the hill. Therefore, in calculating the time-of-travel, the value of α_w used is never allowed to be any closer to v_s than one half i_y. The choice of the factor one-half is arbitrary at this point in the CTDM development and should receive additional attention in future work.

5.1.3 LIFT

Changes have been made to the LIFT portion of CTDM to simplify the treatment of the horizontal deflection of the plume, to include an estimate of how the turbulence changes over the hill, and to accommodate hills with horizontal cross-sections that are elliptical in shape. Descriptions of these changes are presented below in that order.

Horizontal Deflection: The description of LIFT given by Strimaitis et al. (1984) on page 15 uses one lateral distortion factor to quantify the lateral deflection of a streamline in the flow over a hill as well as to specify changes in the lateral spacing of streamlines. This leads to an expression for the horizontal distribution of plume material in Equation 12 that is not correct. However, a correct specification of the lateral deflection is given in a subsequent section of that report in the discussion of the effective receptor location (section 2.1.3). This situation is rectified in the development presented below.

Hill-induced changes to the horizontal spacing of streamlines are represented by the horizontal distortion factor T_ℓ. This factor does not give the amount of lateral deflection experienced by a particular streamline. LIFT requires the average streamline spacing over the interval $s-s_o$ as well as the lateral position of the plume centerline at the distance s downwind of the source. The former is the average of T_ℓ along the flow over $(s-s_o)$, denoted as $\overline{T_\ell}^{\,x}$. The latter involves the average of T_ℓ, at the downwind distance s, across the flow from the streamline that passes over the center of the hill to the streamline that passes through the source, denoted as $\overline{T_\ell}^{\,y}$. With this notation, the lateral position of the shifted plume centerline becomes $\overline{T_\ell}^{\,y} y_r$ (Figure 85) and the horizontal spread of the plume becomes $\overline{T_\ell}^{\,x} \sigma_{ye}$, where

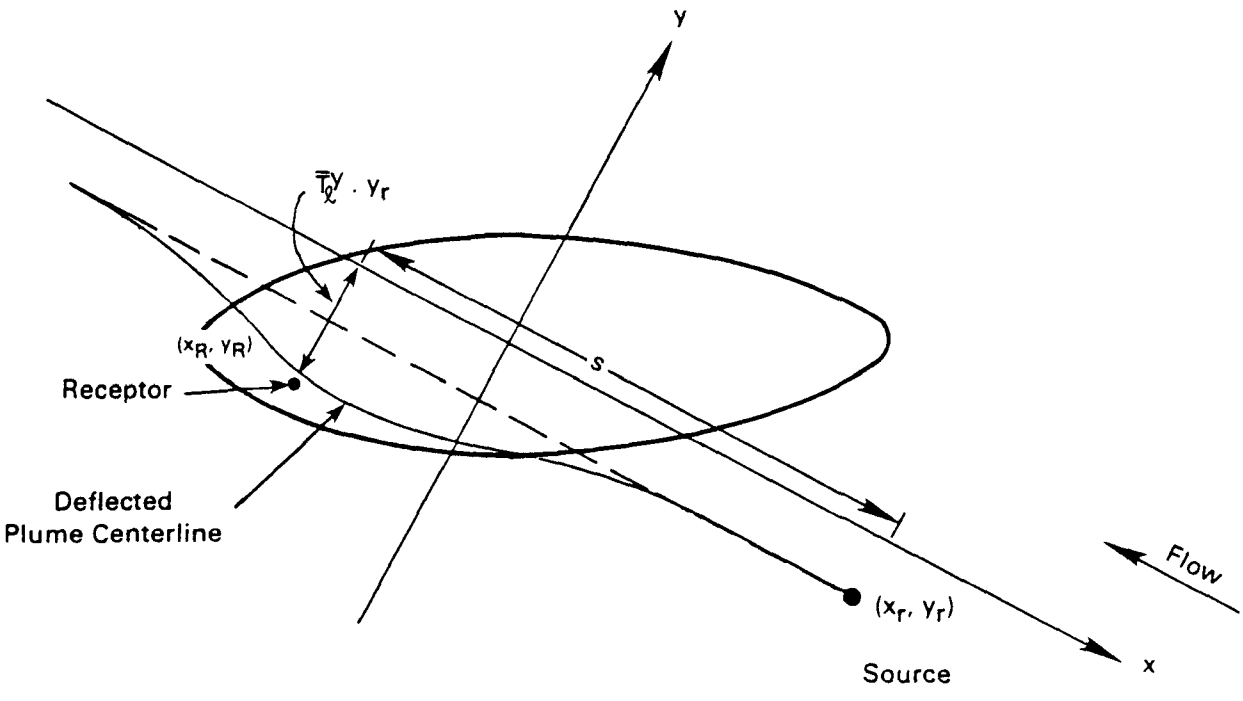

Figure 85. Definition of modeling variables for flow above H_c.

$$\sigma_{ye}^2 = \sigma_{yo}^2 + \sigma_y^{*2}/T_y^2 \tag{76}$$

and T_y is now defined (see Section 2.1.2 in the Fourth Milestone Report) as

$$T_y = \bar{T}_\ell^x / T_{\sigma y} \tag{77}$$

In a coordinate system centered on the hill with the x-axis aligned with the incident flow (see Figure 85), y_r is the lateral position of the plume centerline before deflection. The horizontal distribution function (HDF) then becomes

$$HDF = \frac{e^{-\frac{1}{2}\left(\frac{y_R - \bar{T}_\ell^y\, y_r}{\bar{T}_\ell^x\, \sigma_{ye}}\right)^2}}{\bar{T}_\ell^x\, \sigma_{ye}} \tag{78}$$

where y_R is the lateral position of the receptor. This is the function that simulates a "filament" plume. The equation for concentrations due to a meandering plume becomes

$$C \simeq \frac{F_z(\theta_r^*)}{\sigma_{yT}} \text{ Exp } -0.5 \left(\frac{s_r(\theta_m - \theta_r^*)}{\sigma_{yT}}\right)^2 \tag{79}$$

where F_z is the vertical distribution factor, s_r is the distance from the source to the receptor, θ_m is the mean wind direction for the averaging period, θ_r^* is the wind direction that carries the deflected plume centerline over the receptor, and

$$\sigma_{yT}^2 = \sigma_{ye}^2 (s_r) + \sigma_{ym}^2 (s_m) \tag{80}$$

Note that $\sigma_{ym}(s_m)$ denotes the lateral "meander" plume size at a distance s_m, which is the projection of the distance to the receptor (s_r) onto the trajectory of the 1-hour average plume centerline. This conforms to the usual definition of downwind distance to a receptor. The lateral size of the "filament" plume contains all of the deformation induced by the hill, so that if the meander is large (i.e., if the 1-hour turbulence intensity i_y is dominated by wind direction fluctuations on a time-scale greater than 5 to 10 minutes) $\sigma_{yT} \simeq \sigma_{ym}$, and the hill has no effect on the spread of the plume.

Determination of θ_r^* has been simplified (by approximation) from the iterative method described by Strimaitis et al. (1984). The amount of lateral deflection is now computed on the basis of the path from the source to the receptor in the undistorted flow. For such a path, the y_R equals y_r so that the effective distance between the

centerline of the deflected plume and the receptor is given by Equation 78 as $y_R(1-\overline{T_\ell}^{\,y})/\overline{T_\ell}^{\,x}$. Because we want the deflected plume to pass over the receptor, we must shift the wind direction an amount that "cancels" the deflection given above. Therefore,

$$s_r(\theta_r - \theta_r^*) = y_R(\overline{T_\ell}^{\,y} - 1)/\overline{T_\ell}^{\,x}$$

or

$$\theta_r^* = \theta_r - y_R(\overline{T}_\ell^{\,y} - 1)/s_r\bar{T}_\ell^{\,x} \tag{81}$$

where θ_r is the direction from the receptor to the source in the undistorted flow, y_R is the lateral position of the receptor for a wind direction equal to θ_r, and $\overline{T_\ell}^{\,y}$ is evaluated for a path along the direction θ_r.

Diffusivity Factor T_σ: In assessing the flow above H_c, we assume that the hill slope is small enough that time-of-travel effects can be ignored. Then the relationship between plume spread and diffusivity is

$$\frac{d}{dt}\sigma_z^2(t) = 2K(t) \tag{82}$$

and so (see Equations 9 and 10 in Strimaitis et al. 1984)

$$T_{\sigma z}^2 = \frac{\sigma_z^{*\prime 2}}{\sigma_z^{*2}} = \frac{K_m'}{K_m} \tag{83}$$

where K_m represents the mean diffusivity over the interval $s-s_o$. Because σ_z has the form

$$\sigma_z = \frac{\sigma_w t}{(1 + \frac{t}{2T_L})^{0.5}} \tag{84}$$

the diffusivity is given the approximate form

$$K = \frac{\sigma_w^2 t}{1 + t/T_L} \tag{85}$$

so that

$$T_{\sigma z}^2 = T_{\sigma w}^2 \left[\frac{1 + t_m/T_L}{1 + t_m/T_L'} \right] \tag{86}$$

where t_m is the time-of-travel to the mid-point of the interval $s-s_o$ in the undisturbed flow. Also,

$$1/T_L = \frac{N}{\gamma^2} + \frac{\sigma_w}{\Gamma z} \tag{87}$$

$$1/T'_L = \frac{N}{\gamma^2\sqrt{T_h}} + \frac{T_{\sigma w}\,\sigma_w}{T_h\,\Gamma z} \tag{88}$$

and $T_{\sigma w}$ is the factor for the change in the mean turbulence in the interval.

The turbulence factor can be estimated from rapid distortion theory (RDT) in certain circumstances. RDT describes the effects of straining flows on the turbulence when the straining takes place on a time-scale shorter than the turn-over time of a characteristic eddy. If the straining occurs on a time-scale longer than this, RDT does not apply. In neutral flow, this means that RDT does not apply near the surface in the inner boundary layer. However, in highly stratified flow, the eddy time-scale is inversely proportional to N, so that it grows shorter with increasing stratification. Consequently, there is a point at which RDT is no longer applicable in the outer layer as well. When RDT is applicable, Britter et al. (1981) report an approximate result obtained by Townsend (1976) that is equivalent to

$$T_{\sigma w} = 1 + \sqrt{0.8\,(T_u - 1)} \quad . \tag{89}$$

With the use of this relationship, $T_{\sigma z}$ is expressed solely as a function of T_u and T_h (See Fourth Milestone Report).

If the bulk of the plume is within the inner layer, and if the hill has a moderate slope (say H/L > 0.3, where L is the half-length of the hill at 0.5 H), then

$$T_{\sigma w} = T_u \tag{90}$$

That is, the turbulence intensity remains unchanged over the hill. Britter et al. (1981) estimate the depth of the inner layer as δ:

$$\delta\ \ell n\ (\delta/z_o) = 2k^2\ L \tag{91}$$

where z_o is the roughness length and k is von Karman's constant. For CCB, L ~ 250 m and z_o ~ 5 cm so that δ is approximately 14 m. If we expect that $T_h \leq 0.5$ for CCB, plumes released below 30 m may be influenced by this inner layer. However, the model currently assumes RDT applies to all plumes.

Elliptical Hill Shapes: CTDM has been constructed in a way that allows the degree of flow deformation over a hill to be specified or scaled by the deformation at the crest of the hill. For an

axisymmetric hill, the deformation at the crest does not depend upon the direction of the flow. This is not the case for non-axisymmetric hills.

For an elliptical shape, the deformation or magnitude of terrain-effect depends on the angle of the wind to the major axis of the ellipse. Because the flow is currently modeled on the basis of potential flow calculations, the flow field components along the major and minor axes may be superimposed to obtain the net flow field. For an incident wind speed S_∞ along the major axis, the speed over the crest is defined to be $T_{uoa}\ S_\infty$. For a wind along the minor axis, the speed over the crest is $T_{uob}\ S_\infty$. Therefore, the speed at the crest of the hill (denoted as S_c) for an incident flow of speed S_∞ and direction θ_m, is given by

$$S_c^2 = T^2_{uoa} S_\infty^2 \cos^2(\theta_m - \theta_H) + T^2_{uob} S_\infty^2 \sin^2(\theta_m - \theta_H) \qquad (92)$$

so that the speed factor for a particular wind direction ($T_{uo} = S_c/S_\infty$) is

$$T_{uo}^2 = T_{uoa}^2 + (T_{uob}^2 - T_{uoa}^2) \sin^2(\theta_m - \theta_H) \qquad (93)$$

θ_H is the angle (CW) from north to the major axis. We assume that the vertical compression factor T_{ho} has the same type of dependence on wind direction and that the lateral expansion factor is obtained from flow continuity so that

$$\begin{aligned} T_{ho}^2 &= T_{hoa}^2 + (T_{hob}^2 - T_{hoa}^2) \sin^2(\theta_m - \theta_H) \\ T_{\ell o} &= 1/(T_{ho} T_{uo}) \end{aligned} \qquad (94)$$

with the provision that $T_{\ell o}$ be greater than or equal to the lesser of $T_{\ell oa}$ and $T_{\ell ob}$. If $T_{\ell o}$ falls below this minimum, it is set equal to the minimum, and T_{ho} is recomputed from flow continuity.

The quantities T_{uoa}, T_{uob}, T_{hoa}, and T_{hob} are supplied by the user. In simulating CCB, HBR, and "Beacon Hill" at the FSPS site, we have chosen values based on guidance from potential flow calculations of flow over the crest of an ellipsoid.

The fields of terrain factors are assumed to relax to unity with distance away from the crest as in the previous version of the model, but now the length scale for this relaxation also scales with the two axis lengths, so that it too is a function of direction.

Let (x,y) be a point referenced to a Cartesian coordinate system centered on the ellipse, with the x-axis aligned with the major axis. Then Equation 20 of Strimaitis et al. (1984) becomes (when $x_{sep} = 0$):

$$T(x,y,z_r) = 1 + (T_o(z_r) - 1) \exp\left(-\frac{x^2}{(\alpha a)^2} - \frac{y^2}{(\alpha b)^2}\right) \qquad (95)$$

When the coordinate system is rotated through an angle θ so that the x-axis points into the wind,

$$T(x',y',z_r) = 1 + (T_o(z_r) - 1)\ \exp[-(\frac{x'c - y's}{\alpha a})^2 - (\frac{x's + y'c}{\alpha b})^2] \quad (96)$$

where the primes denote the location of the point in the rotated system, and

$$s = \sin\theta \qquad c = \cos(\theta) \quad (97)$$

Re-arranging the argument of the exponential function in Equation 96,

$$T(x',y',z_r) = 1 + (T_o(z_r)-1)\ e-(\frac{y'R_x}{\alpha ab})^2 \cdot e-[\frac{x'+ y'scR_x^2\ (1/b^2 - 1/a^2)}{\alpha\ R_x}]^2 \quad (98)$$

or

$$T(x',y',z_r) = 1 + (T_o(z_r)-1)\ e-(\frac{x'R_y}{\alpha ab})^2 \cdot e-[\frac{y'+ x'scR_y^2\ (1/b^2 - 1/a^2)}{\alpha\ R_y}]^2 \quad (99)$$

where $R_x^2 = \frac{a^2b^2}{b^2c^2 + a^2s^2}$

$R_y^2 = \frac{a^2b^2}{b^2s^2 + a^2c^2}$

With moderate stratification, x_{sep} is no longer zero, and the T-field is shifted and elongated in the direction of the flow to simulate the appearance of weakly stratified flow.

The elongation and shift now occur in the x' coordinate. The amount of this change, x_{sep}, is added to the length scale in the x' direction to elongate the field (i.e., the denominator of the argument of the exponential function containing x' increases, and this reduces the rate at which the T-factor approaches unity with increasing distance from the crest along x'). And x_{sep} is subtracted from the coordinate position x' to shift the position of the extreme value of the T-factor in the downwind direction:

$$T(x',y',z_r) = 1 + (T_o(z_r) - 1)\ \exp\{-[\frac{y'R_x}{\alpha ab}]^2\} \cdot \exp\{-[\frac{x'-x_{sep} + y'scR_x^2\ (\frac{1}{b^2} - \frac{1}{a^2})}{\alpha\ (R_x + x_{sep})}]^2\} \quad (100)$$

or

$$T(x',y',z_r) = 1 + (T_o(z_r) - 1) \exp\left\{-\left[\frac{x' - x_{sep}}{\alpha\left(\frac{ab}{R_y} + x_{sep}\right)}\right]^2\right\} \cdot \exp\left\{-\left[\frac{y' + x'scR_y^2\left(\frac{1}{b^2} - \frac{1}{a^2}\right)}{\alpha R_y}\right]^2\right\} \quad (101)$$

Although Equations 100 and 101 are not equivalent, the former is more convenient when $T(x',y',z_r)$ must be integrated along x' to obtain $\overline{T}^x$, while the latter is convenient for integrating along y' to obtain $\overline{T}^y$.

5.1.4 LIFT/WRAP Interface

Plumes that approach a hill at elevations less than or slightly greater than H_c are expected to experience a greater horizontal deflection and greater travel time to the hill than are plumes at elevations well above H_c. The WRAP portion of CTDM always computes the horizontal deflection for plume material below H_c, but computes an increased time-of-travel only when the plume centerline is below or near enough to H_c that a significant portion of the plume extends below H_c by the time the plume reaches the hill at the elevation of H_c.

The LIFT portion also incorporates an increased time-of-travel whenever the WRAP portion does. Furthermore, it uses the wind direction computed at "infinity" whenever the time-of-travel is incorporated. Beyond this, LIFT also allows material close to H_c to deflect around the hill if the stagnation streamline at H_c is not directed toward the hill. This adjustment had also been made in the previous version of the model.

In the present version of LIFT, the shift to the side of the hill is introduced into the concentration calculation by changing θ_r* (Equation 79). θ_r* is replaced by θ_r*', where

$$\theta_r{}^{*'} = \theta_r{}^{*} + (\theta_s - \theta_r{}^{*}) \exp\left((H_c - z_R)/\delta H_c\right) \quad (102)$$

and where θ_s is the stagnation wind direction and δH_c is the scale of the transition zone. Equation (102) has a form identical to that used in the previous version of the model.

5.2 CTDM Simulations of Impingement Cases

The current version of CTDM described in Section 5.1 has been applied to the "impingement" hours within the CCB and HBR data sets. The intent of this analysis is to see how the changes made to CTDM, and the WRAP portion in particular, affect model performance.

The "impingement" portion of the CCB data set includes those hours in which the SF_6 plume was released below H_c, or in which it was

released no more than 10 m above H_c. In the terminology of the Fourth Milestone Report, these comprise the impingement (release height = $H_c \pm 10$ m) and stable (release height < H_c - 10 m) hours. Refer to the Fourth Milestone Report for a discussion of the meteorological data for these hours.

For HBR, only the CF_3Br data set from experiment 8 onwards has been considered. Within this data set, we have selected hours in which the mean wind direction is toward the sampler array or in which several 5-minute average wind directions are toward the array.

5.2.1 CCB

The specification of terrain parameters for CCB is noted in Section 5.1. Two other user-provided parameters have been chosen to be consistent with those used in the Fourth Milestone Report. These include the length scale factor for the LIFT-WRAP transition zone ($\delta = 0.1$), and the horizontal scale factor for the terrain-factor fields ($\alpha = 0.67$). The terrain factors for the speed at the hill-crest and the deformation of streamlines in the vertical are:

$$T_{uoa} = 1.16 \qquad T_{hoa} = 0.50$$
$$T_{uob} = 1.22 \qquad T_{hob} = 0.52$$

The 'a' quantities are for flow along the major axis, whereas the 'b' quantities are for flow along the minor axis.

These values of the terrain factors at the crest are estimated from calculations of potential flow over the crest of an ellipsoid. The ellipsoid is determined by matching its shape to the approximate shape of CCB at an elevation of one half its total height. Such an ellipsoid reproduces L along each axis (L = 280 m, 225 m; see 5.1.1). The aspect ratios for the chosen ellipsoid are 3.6 and 2.9. COMPLEX/PFM contains a look-up table of results of calculations of flow over the crest of ellipsoids with aspect ratios of 1, 2, 5, and 10. These results for ellipses described by the cross-wind and along-wind aspect ratio pairs (2,2), (2,5), (5,2), and (5,5) have been used to estimate the factors for CCB. Note that the CCB database primarily contains wind directions aligned approximately with the minor axis so that T_{uob} and T_{hob} will be most important in estimating the flow above H_c. The representative values chosen in the Fourth Milestone Report (Strimaitis et al. 1984) for modeling CCB are $T_{ho} = 0.5$ and $T_{uo} = 1.25$.

Modeling results are presented in Table 13. These results were obtained by averaging the 5 highest observed concentrations (scaled by the emission rate) and the 5 highest modeled concentrations for each hour. Results are presented for the latest version (12185) of CTDM as well as for the version (03184) discussed in the Fourth Milestone Report. The columns labeled C_o and C_p are based on the average of the 5 greatest concentrations. The columns labeled C_o/C_p (Max) show the ratios of the peak observed concentration to the peak modeled concentration. These results essentially reflect the ability of the model to predict the magnitude of the higher concentrations for the hours in which they are observed, but do not reflect the ability of the model to predict the exact locations of the peak observed concentrations.

TABLE 13. COMPARISON OF MODELED AND OBSERVED CONCENTRATIONS FOR STABLE IMPINGEMENT HOURS AT CCB (SF_6 TRACER)

Exp-Hr	$\overline{C_o}$* ($\mu s/m^3$)	CTDM (03184) $\overline{C_p}$* ($\mu s/m^3$)	CTDM (03184) C_o/C_p (Max)	CTDM (12185) $\overline{C_p}$* ($\mu s/m^3$)	CTDM (12185) C_o/C_p (Max)
201-4	13.9	35.8	0.41	36.2	0.39
201-5	19.1	54.0	0.40	44.7	0.49
201-6	14.9	31.3	0.51	15.1	0.77
203-2	4.8	12.8	0.42	9.5	0.65
203-3**	2.1	1.2	1.99	0.9	2.31
203-8	30.4	44.6	1.51	46.4	1.14
205-8	11.9	39.8	0.30	31.2	0.31
206-6	86.5	99.6	0.82	94.6	0.82
206-7	67.2	167.1	0.39	115.4	0.39
206-8	101.0	345.6	0.35	230.9	0.53
209-3	4.7	35.1	0.14	26.7	0.15
209-8	15.2	113.7	0.14	69.4	0.26
211-2	5.0	15.3	0.36	21.5	0.25
211-3**	2.2	17.6	0.15	9.9	0.30
211-5	74.1	39.2	2.30	41.5	2.16
211-6	34.9	18.0	2.37	13.5	2.78
211-7**	6.1	5.6	1.46	0.6	12.70
214-4	43.2	31.2	1.38	25.6	1.70
215-1**	16.7	14.5	1.07	14.1	1.23
215-5	27.4	15.0	2.11	16.1	1.82
204-1	7.4	15.7	0.75	16.2	0.67
204-2	8.2	12.6	0.63	0.2	24.04
204-5	2.9	3.4	1.34	0.8	2.60
204-6	9.5	29.6	0.59	16.4	0.92
204-7	7.0	35.7	0.21	33.0	0.23
204-8	15.1	20.3	0.70	16.4	0.34
205-7	6.6	20.5	0.60	11.9	0.93
213-5	19.6	28.2	0.97	15.4	1.51
213-6	13.6	39.2	0.45	29.3	0.52
213-7	11.0	18.6	0.87	16.2	0.91
213-8	4.2	21.0	0.29	7.9	0.58
214-2	19.3	38.8	0.63	10.1	1.10
214-3	37.2	19.4	2.84	12.4	4.01
215-4	14.4	19.8	0.80	16.7	1.01
215-6	7.6	18.1	0.49	9.4	0.91

*Average of the 5 greatest scaled concentrations ($\mu s/m^3$) for the hour.

**Modeled with the meteorological tower placed 10 km from CCB at a bearing of 127°.

The current CTDM version generally shows a reduction in its tendency to overestimate the observed concentrations. But note that there are now a few hours that are underestimated to a larger degree. Two hours stand out in this regard: 211-7 and 204-2. Apparently, the modeled deflection of the mean flow around the hill keeps the plume too far from the hill. The performance of the models for the remaining hours is as follows:

CTDM Version	"Impingement Hours"	"Stable Hours"
03184	m_g, s_g = 0.54, 2.52	m_g, s_g = 0.49, 1.84
12185	m_g, s_g = 0.66, 2.35	m_g, s_g = 0.84, 2.17

5.2.2 HBR

CTDM has been applied to the CF_3Br dataset from HBR in much the same way as it had been applied to CCB. The scale factors δ and α remain at 0.1 and 0.67, respectively, and the terrain factors for vertical deformation and velocity speed-up at the crest of HBR are:

$T_{uoa} = 1.0$ $\quad$ $T_{hoa} = 1.0$
$T_{uob} = 2.0$ $\quad$ $T_{hob} = 0.5$

These values are obtained from potential flow solutions for flow around a cylinder of circular cross-section. These calculations predict that the streamline that lies along the boundary of the cylinder ($\psi = 0$) is associated with a speed-up factor (T_u) of 2. Because the flow is two-dimensional, the product T_hT_u must be unity so that $T_h = 0.5$ We have used these values of T_u and T_h to approximate those for HBR in this application of CTDM. No attempt has been made as yet to incorporate the results discussed in Section 3 of this milestone report, but this would have a relatively small impact on modeling CF_3Br tracer-hours at HBR because during these hours the plume was virtually always at an elevation less than H_c.

Thirty-six hours were selected from the CF_3Br database at HBR. The principal criterion for selecting an hour was that some of the 5-min average winds be directed toward the sampler network. Of this subset of hours, a few were not modeled because very low CF_3Br concentrations were measured on the ridge.

The 36 hours are listed in Table 14. The highest and second-highest measured CF_3Br concentrations, the hourly averaged H_c value, the release height above local terrain, and the release location are listed. For all but seven of the hours, the release height is below H_c.

Tower A meteorological data in the Modeler's Data Archive were used for the modeling. However, both propeller and sonic measurements were utilized. The values of σ_w measured by the sonic anemometer were used in combination with the wind speeds and directions measured by the props. For releases at locations 203 and 215, model input parameters were interpolated from the Tower A data to the height of the release above sea level rather than height above the ground.

TABLE 14. MODELED HOURS FROM THE HBR MDA

Exp-Hr	Time (MDT)	Measured CF_3Br Concentration ($\mu s/m^3$) High	2nd High	H_c (m)	z_r (m)	Release Location*
8-1	2300-0000	57	40	84	20	215
8-2	0000-0100	34	33	82	10	215
8-5	0300-0400	329	124	65	30	215
8-6	0400-0500	61	48	55	25	215
8-7	0500-0600	72	69	43	25	215
8-8	0600-0700	44	40	45	30	215
8-9	0700-0800	74	41	31	15	215
10-3	0200-0300	19	13	44	30	A
10-5	0400-0500	47	42	63	30	A
10-6	0500-0600	36	34	40	30	A
10-7	0600-0700	42	39	43	30	A
10-8	0700-0800	22	20	47	30	A
10-9	0800-0900	40	27	42	30	A
10-11	1000-1100	11	9	1	30	A
11-1	2300-0000	52	48	77	20	203
11-4	0200-0300	166	166	62	20	203
11-7	0500-0600	9	7	39	25	A
11-8	0600-0700	52	46	28	25	A
11-9	0700-0800	21	20	36	10	A
11-10	0800-0900	9	8	26	10	A
12-2	0200-0300	15	15	50	40	A
12-3	0300-0400	10	9	37	50	A
12-9	0900-1000	23	18	1	40	A
12-10	1000-1100	17	16	1	40	A
14-5	0200-0300	38	33	43	20	203
14-6	0300-0400	117	105	36	20	203
14-7	0400-0500	109	95	39	20	203
14-8	0500-0600	63	61	34	20	203
14-10	0700-0800	6	5	43	35	A
14-12	0900-1000	31	29	25	35	A
15-4	0300-0400	17	15	50	40	A
15-5	0400-0500	58	48	47	40	A
15-7	0600-0700	22	20	39	40	A
15-8	0700-0800	26	24	41	40	A
15-9	0800-0900	36	32	47	40	A
15-11	1000-1100	14	14	1	40	A

*See Figure 49 in Third Milestone Report.

Only data from Experiments 8 through 15 were considered for selection in this model evaluation because no σ_w data from the sonic anemometers are available from Experiment 7 and because noise in the data from Tower A in the earlier experiments swamped the turbulence information. Efforts to reduce the noise were at least partially successful by Experiment 7 but were not completed until Experiment 10.

Table 15 shows the results of running CTDM (12185) at HBR. The data are partitioned into two sets: data for plumes released from Tower A; and plumes released from site 203, located near the intersection of the road to Tower A and "Hogback Highway," the road which parallels HBR at the foot of the ridge, or site 215 which is located roughly one third of the way from the base of HBR down the road toward Tower A. The reasons for making this partition are (1) the meteorological data appropriate to the plume origin are better known for the releases from Tower A, and (2) the Tower A plumes travel roughly twice as far to reach the hillside.

The results presented in Table 15 indicate that the model performs better for the Tower A group than it does for the other group. The geometric mean and standard deviation (m_g and s_g) for the Tower A group are 0.91 and 2.01, respectively, whereas those for the other group are 1.97 and 2.63, respectively. Measuring the meteorological data right at the source position may be partially responsible for this result, but other factors can also be important. For example, the meteorology may not be similar: one of the hours in the Tower A group has a mean wind direction away from the hill, and a simulation of this hour required modeling each 5-minute period. Three hours in the other group had to be simulated in this way.

Excluding these four hours, the modeling results for the Tower A group remain better than those for the releases nearer the hill. The m_g and s_g values for the remaining 22 hours in this group are 0.83 and 1.71, respectively. Those for the 10 hours of releases closer to the hill are 1.53 and 2.22, respectively.

The performance of CTDM (12185) can be compared with the performance of the semi-empirical model (see Table 17) discussed in Section 5.3. When the four hours are removed, values of m_g and s_g from the semi-empirical model for the Tower A group are 0.93 and 1.99, respectively; and those for the other group are 0.77 and 1.78. Therefore CTDM exhibits the least scatter (s_g = 1.71) for the Tower A group, whereas the semi-emipirical model exhibits the least scatter for the other group (s_g = 1.78). These results indicate that although the semi-empirical algorithms do not appear to offer improved modeling performance for the Tower A group, a substantial improvement is seen for those hours in which the plume is released closer to HBR.

5.3 Modeling Freon Releases at HBR

5.3.1 Introduction

In modeling the dispersion of releases around HBR we have adopted two approaches, CTDM (discussed earlier in Section 5.2) and a semi-empirical model that is discussed later in this section. The

TABLE 15. COMPARISON OF MODELED (CTDM) AND OBSERVED CONCENTRATIONS FOR SUBSET OF THE HBR CF_3Br DATA BASE

Tower A Releases				Releases Closer to Ridge			
Exp-Hr	$\overline{C_o}$* ($\mu s/m^3$)	$\overline{C_p}$* ($\mu s/m^3$)	C_o/C_p (Max)	Exp-Hr	$\overline{C_o}$* ($\mu s/m^3$)	$\overline{C_p}$* ($\mu s/m^3$)	C_o/C_p (Max)
10-3	13.1	20.1	0.63	8-1	26.2	62.7	0.86
10-5**	39.5	5.3	8.47	8-2**	30.0	23.5	1.04
10-6	33.0	73.5	0.48	8-5**	160.5	27.1	10.99
10-7	38.3	20.0	2.08	8-6	48.8	42.3	1.38
10-8	18.8	30.0	0.70	8-7	63.7	22.8	2.85
(10-9)	26.9	48.9	0.82	8-8	40.3	18.6	1.88
(10-11)	8.3	12.4	0.70	8-9	45.3	53.9	1.18
11-7	6.3	16.0	0.54	11-1	39.8	54.6	0.94
11-8	43.5	37.7	1.30	11-4**	157.2	12.3	12.65
11-9	17.5	10.3	1.75	14-5	28.1	18.4	1.63
11-10	7.8	12.0	0.66	14-6	90.2	24.0	4.50
12-2	14.7	25.9	0.44	14-7	94.0	16.7	6.22
12-3	8.3	14.0	0.66	14-8	56.0	45.4	1.24
(12-9)	18.3	12.0	1.50				
(12-10)	14.2	11.0	1.33				
14-10	5.6	13.3	0.39				
14-12	23.6	16.4	1.87				
15-4	14.6	40.3	0.34				
15-5	47.9	39.3	1.43				
15-7	18.5	26.1	0.80				
15-8	24.9	33.0	0.83				
15-9	30.0	16.0	1.68				
15-11	13.8	10.1	1.10				

* Average of the 5 greatest scaled concentrations ($\mu s/m^3$) for the hour.

** Concentrations estimated from simulating all 5-minute periods during the hour.

() Turbulence data from the sonic anemometers are incomplete; data from propeller anemometers are substituted.

semi-empirical approach extends the work discussed in Section 4.3 of Fourth Milestone Report. Although the applicability of the semi-empirical model is limited to the observations and complex terrain data used to develop it, the combined use of CTDM and the semi-empirical model can help in understanding dispersion at a ridge site. In particular, the variety of output from CTDM can be used to develop parameterizations required to extend the range of applicability of the semi-empirical model. In short, the model for HBR described in this section should be viewed as a complement of CTDM. It will be improved as we gain more understanding of the behavior of the observations through the more theoretically based model and application of the semi-empirical model to the CCB and Tracy sites.

The basic model is not very different from that described by Strimaitis et al. (1984). The significant modification is related to the use of a probability density function to describe the wind direction and speed data. This change was motivated by the observed variability of the winds measured at Tower A during the majority of the study hours. The next section describes the current version of the semi-empirical model.

5.3.2 The Modified HBR Model

The initial semi-empirical HBR model (Strimaitis et al. 1984) can be represented by the equation,

$$C(x,y,o) = \frac{2Q}{\pi u_r(\sigma_{z\ell}+\sigma_{zu})\sigma_y} \exp\left[-\frac{T_p^2 z_r^2}{2\sigma_{z\ell}^2}\right] \exp\left[-\frac{y_R^2}{2\sigma_y^2}\right] \qquad (103)$$

In Eq. 103, C(x,y,o) is the ground-level concentration, Q is the emission rate, u_r is the hourly averaged mean wind speed at the source height, σ_y is the crosswind spread, $\sigma_{z\ell}$ and σ_{zu} are the parameters that describe the vertical diffusion of the lower and upper portions of the plume, z_r is the release height, and the plume height factor T_p depends upon z_r, H_c, and the source-receptor geometry. Its formulation was described in Subsection 4.3.3 in the Fourth Milestone Report.

The first modification we made was to replace the concept of an hourly averaged mean wind by a probability or frequency distribution derived from the 5-minute averaged wind speeds, directions, and standard deviations. Then, the crosswind term in Eq. (103) becomes

$$\frac{1}{\sqrt{2\pi}\sigma_y u_r} \exp - \frac{y_R^2}{2\sigma_y^2} \rightarrow \frac{P(\theta)}{u_\theta r} \qquad (104)$$

In Eq. 104, $P(\theta)d\theta$ is the probability that the wind blows in the angle $d\theta$ surrounding the direction θ, u_θ is the wind speed associated with θ, and r is the source-receptor distance. Notice that this formulation avoids defining a mean wind direction.

Furthermore, it accounts for the observed distribution of wind directions rather than assuming a Gaussian distribution. The model uses 5-minute average wind directions to construct a probability distribution in 1-degree sectors. In addition, the average wind speed for each sector is calculated and used by the model rather than using the hour-averaged wind speed. The 5-minute average σ_v's are also utilized in the determination of the probability distribution.

Sensitivity studies using this model in a "flat terrain" form ($T_p = 1$) indicated that the inclusion of the upper and lower sigmas for vertical spread made little difference to the ground-level concentrations. Therefore, we adopted the simpler expression for σ_z that is used in CTDM,

$$\sigma_z = \frac{\sigma_w t}{(1 + t/2T_L)^{0.5}} \tag{105}$$

where all the terms on the right hand side are evaluated at source height.

Then the final expression for the ground-level concentration becomes

$$C(x,y,o) = \sqrt{\frac{2}{\pi}} \frac{QP(\theta)}{\sigma_z u_\theta r} \exp\left[\frac{-T_p^2 z_r^2}{2\sigma_z^2}\right] \tag{106}$$

5.3.4 Performance of the Semi-Empirical Model

Before the overall model was evaluated, a considerable amount of time was spent testing the T_p formulation (see Subsection 4.3.3 in the Fourth Milestone Report). Sensitivity studies indicate that for the HBR cases, the current T_p formulation was the best attainable with the available data. It should be stated that the equation for T_p cannot be justified per se on theoretical grounds, although it does have features that are based on observations. It could be modified when the semi-empirical dispersion model is applied to CCB and the Tracy data bases.

As before, the performance of the model is stated in terms of the statistics of the ratio ε defined for each case-hour by

$$\varepsilon = \frac{\text{average of top n observed concentrations}}{\text{average of top n predicted concentrations}} \tag{107}$$

where n has been taken to be 1, 2, and 5. We have analyzed the performance of the model both for the set of 36 hours and for the subset of 29 hours for which the tower data are considered to be of higher quality. Table 16 shows the performance statistics. The model predictions compare reasonably well with the corresponding observations. For all the cases considered, the geometric means of ε are close to the ideal value of unity, and the geometric standard

TABLE 16. SUMMARY STATISTICS FOR HBR MODEL

Experiments 8-15 36 hours

Model	Top 1 m_g	Top 1 s_g	Top 1 r^2	Top 2 m_g	Top 2 s_g	Top 2 r^2	Top 5 m_g	Top 5 s_g	Top 5 r^2
Flat Terrain	2.45	3.60	0.130	2.39	3.64	0.126	2.31	3.73	0.111
Cut-Off Hill	0.46	2.55	0.446	0.47	2.44	0.449	0.48	2.41	0.409
HBR	1.05	2.14	0.347	1.01	2.11	0.350	0.95	2.12	0.331

Experiments 10-15 29 hours

Model	Top 1 m_g	Top 1 s_g	Top 1 r^2	Top 2 m_g	Top 2 s_g	Top 2 r^2	Top 5 m_g	Top 5 s_g	Top 5 r^2
Flat Terrain	2.37	3.57	0.167	2.34	3.72	0.150	2.30	3.88	0.130
Cut-Off Hill	0.50	2.51	0.456	0.51	2.43	0.443	0.52	2.38	0.412
HBR	1.02	1.97	0.413	1.00	2.01	0.388	0.96	2.05	0.362

deviations are approximately 2.0. Although the same cases were not considered in the Fourth Milestone Report, it is clear from an examination of Table 16 and Table 14 (Fourth Milestone Report) that the present model represents a significant improvement over the previous formulation. Clearly, this improvement is directly related to the use of the distribution of 5-minute winds, instead of the Gaussian distribution, to calculate the horizontal concentration distribution. The mean of the 5 greatest observed and modeled concentrations for each of the hours is listed in Table 17, along with the ratio of the peak observed to the peak modeled concentration for each hour.

Table 16 also shows the performance of the empirical T_p formulation relative to a flat-terrain (T_p=1) equation and that corresponding to a cut-off hill, i.e.,

$$\begin{aligned} T_p &= (z_r - H_c)/z_r; \; z_r > H_c \\ &= 0 \qquad\quad ; \; z_r < H_c \end{aligned} \tag{108}$$

As expected, the flat terrain model underpredicts concentrations while the cut-off hill model overpredicts concentrations. However, note that the cut-off hill model results produce r^2-values which are similar to those from the semi-empirical model results. This suggests that the simple device of bringing the plume closer to the hill's surface goes a long way towards explaining the variance of the observed concentrations on the ridge.

Figures 86 and 87 are examples of the behavior of the residuals from the semi-empirical model (the 29-hour subset) as a function of model inputs. In general, the residuals are uncorrelated with the model inputs, which suggests that for the data set and inputs considered, we can do little to improve the performance of this particular model formulation.

Our analysis of the CF_3Br concentration measurements made at HBR suggests that hill "effects" on ground-level concentrations can be accounted through a factor which effectively lowers the plume towards the surface of the hill. Of course, model performance is also affected by the other parameterizations in the model, as evidenced by the improvement of the performance of the HBR model when the Gaussian distribution is replaced by a wind distribution which accounts for the large meandering typical of the wind during stable conditions. The point needs to be reiterated that during stable conditions there is considerable meandering of the wind, and this has to be accounted for in calculating σ_y. Also note that the calculation of σ_z assumes knowledge of turbulence measurements at release height. Because it is not possible to relate these turbulence properties to surface layer variables such as u_* (see Section 3.3), the use of the model requires measurements of the appropriate meteorology at source height.

TABLE 17. COMPARISON OF MODELED (EMPIRICAL) AND OBSERVED CONCENTRATIONS FOR 36-HOUR SUBSET OF THE HBR CF_3Br DATA BASE

Tower A Releases				Releases Closer to Ridge			
Exp-Hr	$\overline{C_o}$* ($\mu s/m^3$)	$\overline{C_p}$* ($\mu s/m^3$)	C_o/C_p (Max)	Exp-Hr	$\overline{C_o}$* ($\mu s/m^3$)	$\overline{C_p}$* ($\mu s/m^3$)	C_o/C_p (Max)
10-3	13.1	40.9	.37	8-1	26.2	66.2	.76
10-5	39.5	10.1	4.54	8-2	30.0	126.2	.20
10-6	33.0	42.1	.82	8-5	160.5	38.5	8.22
10-7	38.3	22.8	1.76	8-6	48.8	76.7	.78
10-8	18.8	27.9	.71	8-7	63.7	38.7	1.61
10-9	26.9	45.1	.84	8-8	40.3	34.1	1.21
10-11	8.3	14.0	.66	8-9	45.3	45.5	1.55
11-7	6.3	20.4	.35	11-1	39.8	128.7	.40
11-8	43.5	46.2	1.04	11-4	157.2	67.1	2.09
11-9	17.5	5.5	3.36	14-5	28.1	59.7	.61
11-10	7.8	18.7	.45	14-6	90.2	71.3	1.51
12-2	14.7	8.1	1.74	14-7	94.0	69.8	1.30
12-3	8.3	11.4	.87	14-8	56.0	95.7	.56
12-9	18.3	10.6	1.82				
12-10	14.2	10.7	1.38				
14-10	5.6	17.0	.30				
14-12	23.6	12.1	2.15				
15-4	14.6	21.9	.71				
15-5	47.9	27.2	1.60				
15-7	18.5	29.5	.72				
15-8	24.9	23.0	1.20				
15-9	30.0	11.9	2.06				
15-11	13.8	10.0	1.19				

* Average of the 5 greatest scaled concentrations ($\mu s/m^3$) for the hour.

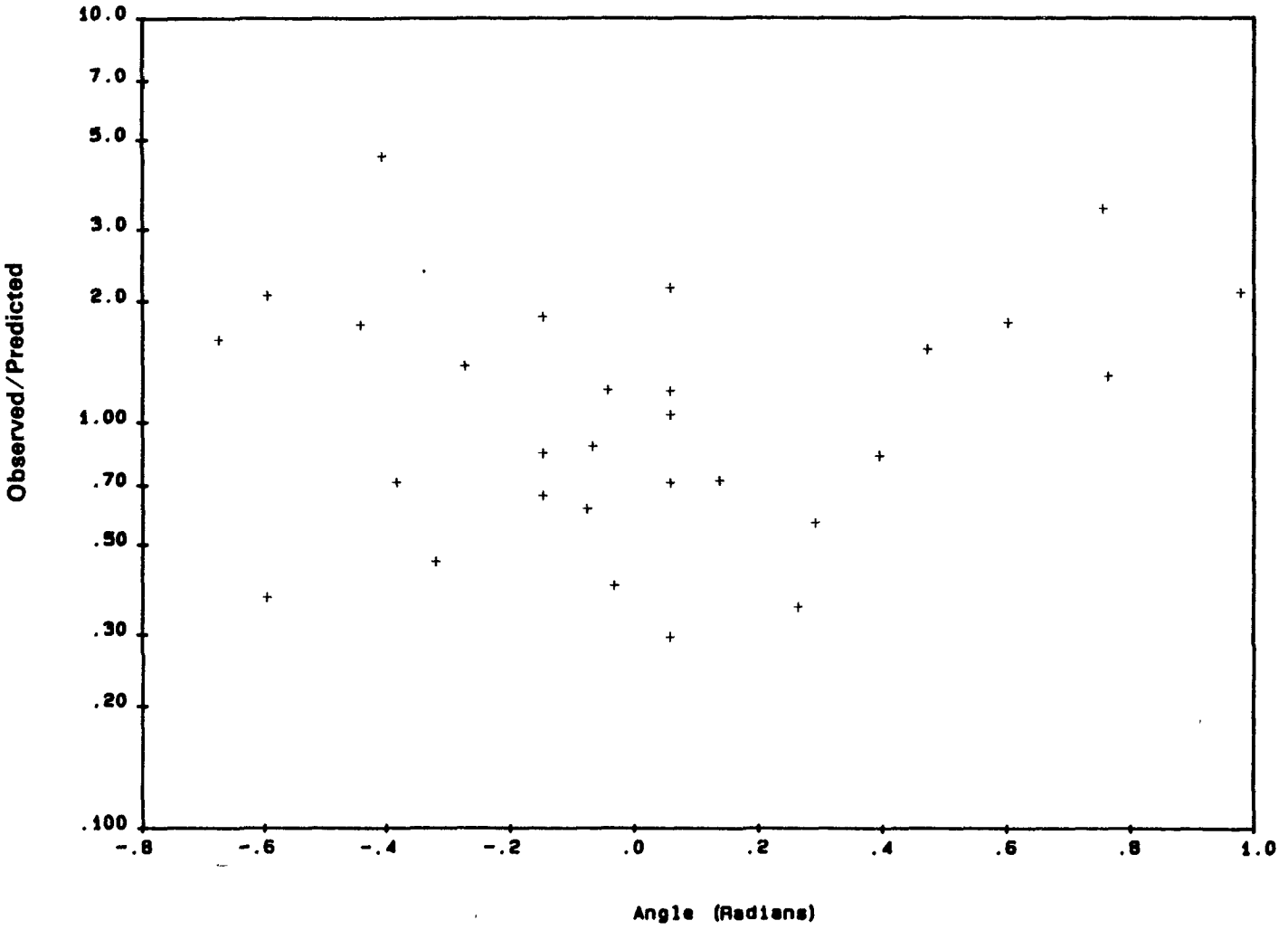

Figure 86. Variation of observed-to-modeled ratios of HBR single maximum hourly concentrations with angle between the stagnation line and line to receptor (29 hours).

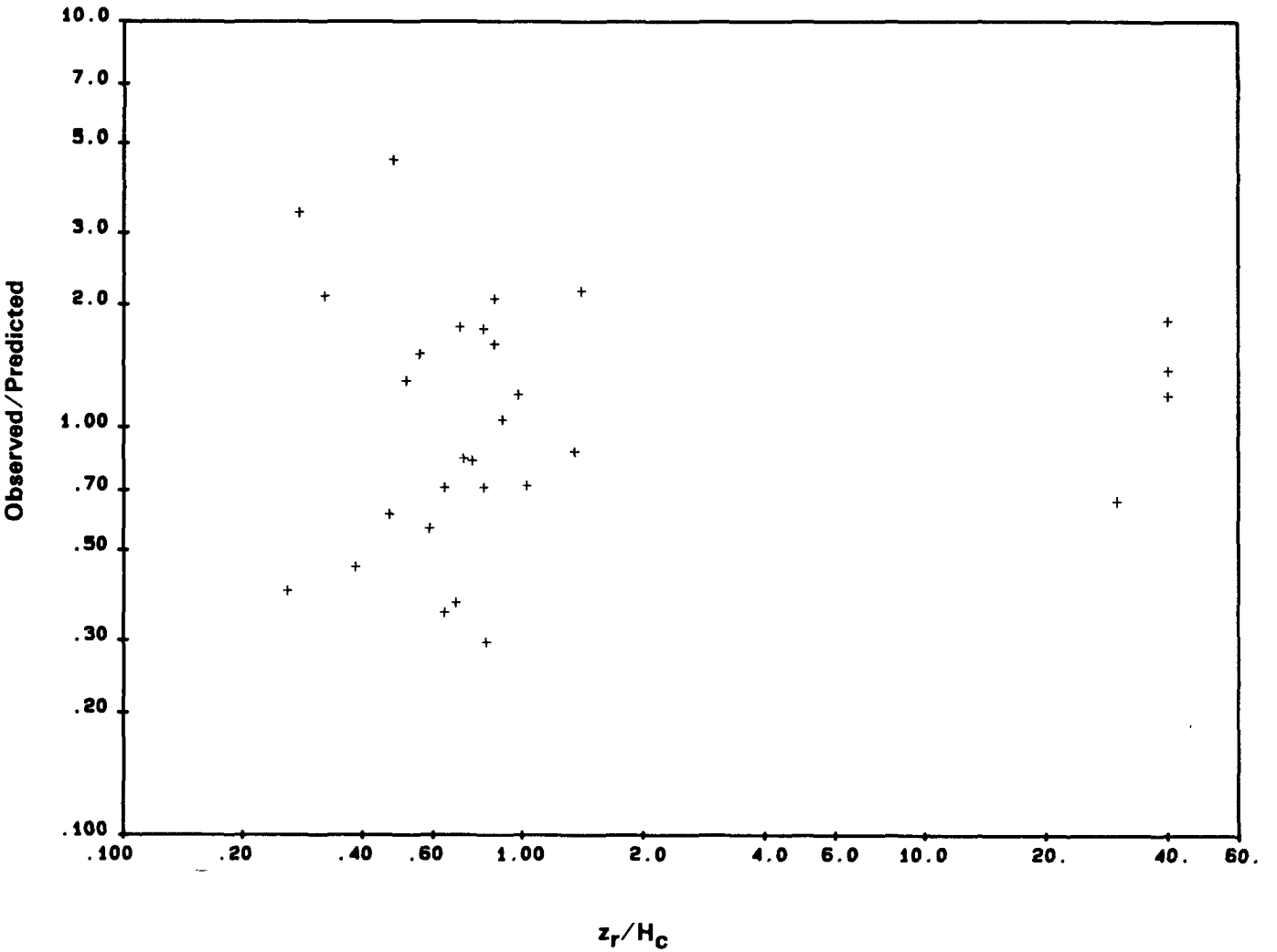

Figure 87. Variation of observed-to-modeled ratios of HBR single maximum hourly concentrations with z_r/H_c (29 hours).

The performance of the model is summarized through the scatterplots of Figure 88. These good results have to be tempered by the fact that the model is only applicable to the limited data set considered in this analysis. This is the limitation of any semi-empirical model. Before the model can provide general guidance on dispersion in complex terrain, it has to be applied to the CCB and Tracy data bases. Furthermore, we have to provide further justification, even if it is only partial, of the formulation for T_p. This has to come from the theoretical models being developed in this project.

5.3.5 Selected Case-Study Results

To provide more information about the modeling than can be derived from the summary of the results, selected hours are described in more detail in this section. The hours are:

- Experiment 11, 0200-0300 MDT
- Experiment 11, 0600-0700 MDT
- Experiment 14, 0500-0600 MDT

These hours were selected because they represent a variety of dispersion conditions and include examples of model underprediction and overprediction.

Experiment 11, Experiment-Hour 4 (0200-0300 MDT)

The tracer gas was released 100 m from the base of the ridge at a release height 20 m above the ground. The winds were light, 1.7 m/s or less, for the entire hour. Four of the 5-minute average wind directions were toward the hill, though only two were within ±60° of the stagnation angle to the ridge. The average value of H_c for this hour was 62 m. The σ_v and σ_w values were 0.227 m/s and 0.107 m/s, respectively.

Figure 89 shows the distribution of observed concentrations for this hour. The distribution of 5-minute winds estimated for the height of release is drawn at the release location. The hourly averaged wind direction is depicted by the long dotted line. Meteorological and source data are listed in the bottom left part of the figure. This hour is distinctive in that the hourly-averaged wind direction is away from the ridge, but relatively high concentrations of CF_3Br were measured at several locations on the hill. The highest and second-highest concentrations were both 166 $\mu s/m^3$.

The predicted concentration spatial distribution is shown in Figure 90. The maximum concentration is 79 $\mu s/m^3$. In this case, the model underpredicts both the maximum and the average concentration ($\overline{C_o}/\overline{C_p}$ = 2.55). However, it should be noted that the PDF approach does far better than the use of a Gaussian horizontal distribution about the hourly averaged wind direction; the latter approach would, of course, yield zero concentrations on the ridge since the hourly averaged wind is directed away from the hill.

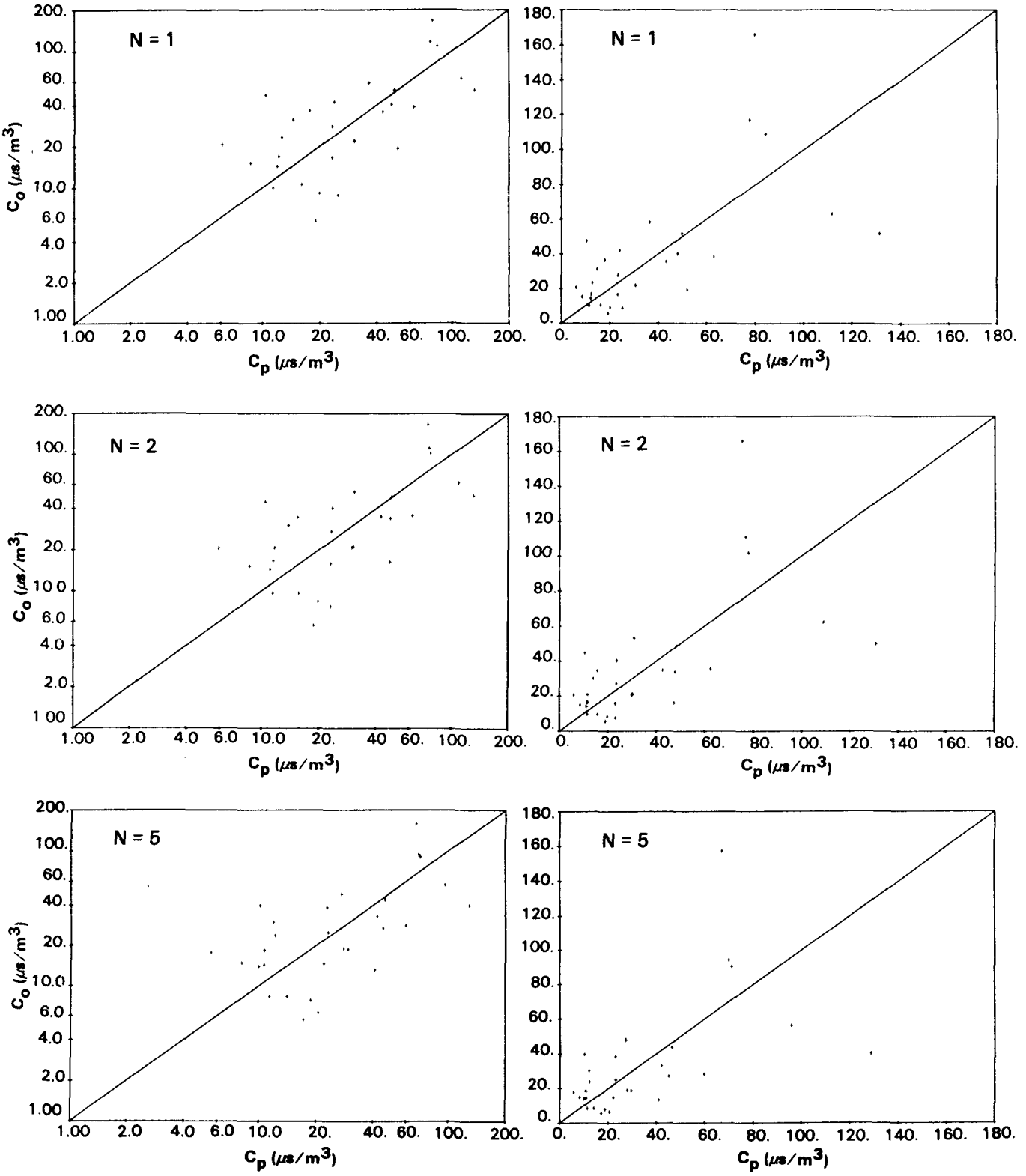

Figure 88. Scatter plot of scaled (C/Q μs/m³) observed and modeled concentrations (peak, top 2, top 5) for 29 hours of HBR data.

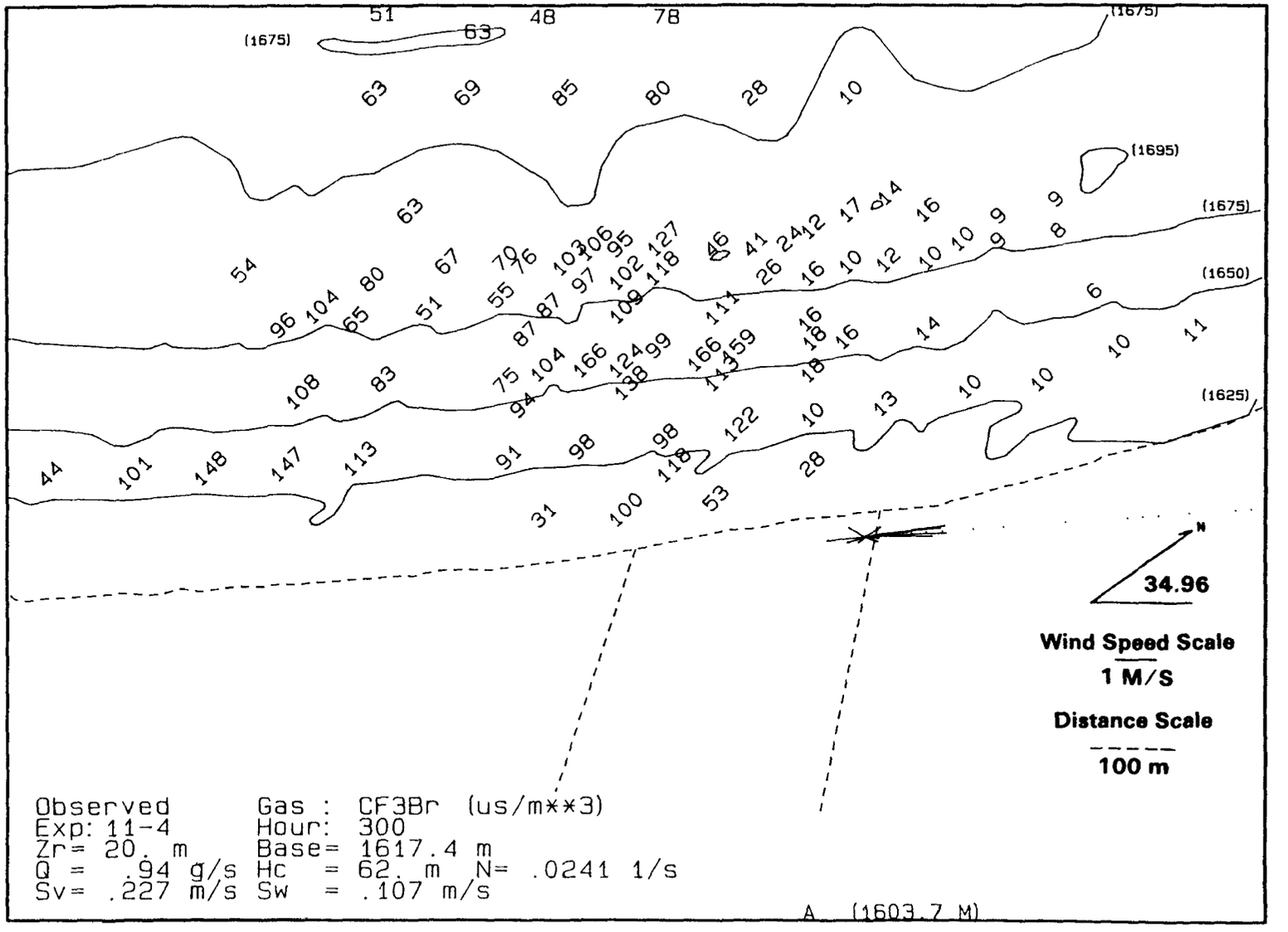

Figure 89. One-hour average observed CF_3Br concentrations scaled by emission rate ($\mu s/m^3$) (Experiment 11, 10/23/82, 0200-0300 MDT).

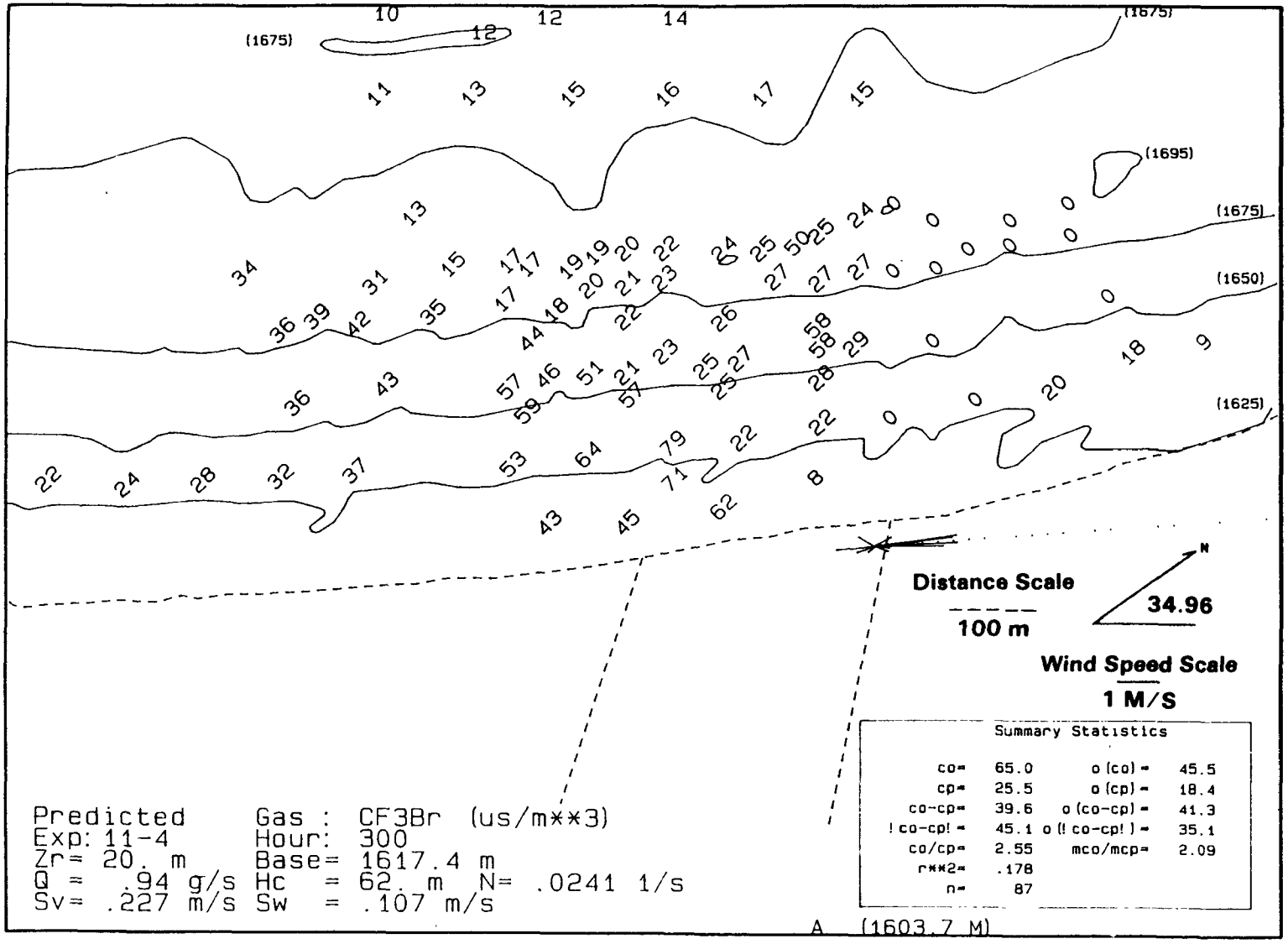

Figure 90. One-hour average predicted scaled concentrations ($\mu s/m^3$) from the HBR model (Experiment 11, 10/23/82, 0200-0300 MDT).

Experiment 11, Experiment-Hour 8 (0600-0700 MDT)

This release was made from Tower A at a height of 25 m. The 5-minute average wind speeds varied from 0.8 to 1.8 m/s; all 12 of the 5-minute average directions were toward the hill. The hourly-averaged value of H_c was 28 m, which is approximately equal to the release height. The hourly-averaged values of σ_v and σ_w were 0.369 m/s and 0.236 m/s, respectively.

The highest and second highest CF_3Br concentrations observed during this hour were 52 $\mu s/m^3$ and 46 $\mu s/m^3$. The spatial distribution of all of the observed CF_3Br concentrations is shown in Figure 91.

The model predicted a maximum concentration of 50 $\mu s/m^3$, which is very close to the maximum observation. On the average, however, the model overpredicts, which can be seen in the summary statistics in Figure 92 ($\overline{C_o}/\overline{C_p}$ = 0.58).

Experiment 14, Experiment-Hour 8 (0500-0600 MDT)

During this hour, the release was made near the base of the ridge at a height of 20 m. The 5-minute average wind speeds ranged from 0.6 m/s to 2.0 m/s. All 12 of the 5-minute average wind directions have a component toward the ridge and 9 of these are within 60° of the stagnation angle. The hourly-averaged H_c value was 34 m. The hourly-averaged value of σ_v and σ_w were 0.620 m/s and 0.293 m/s, respectively.

The spatial distribution of the observed concentrations is shown in Figure 93. The highest and second highest concentrations were 63 $\mu s/m^3$ and 61 $\mu s/m^3$, though the majority of the observations were under 20 $\mu s/m^3$.

As can be seen in Figure 94 the predicted maximum concentration is 112 $\mu s/m^3$, which represents an overprediction of about 78%. On the average the model also overpredicts for this hour, as reflected in the summary statistics given in Figure 94.

5.4 Modeling Tracy

5.4.1 Initial 14-Hour Data Base

The 128 hours of SF_6 tracer gas releases were examined to select the hours for initial model evaluation. The hours with the highest 80 maximum observed concentrations were examined. Of these, lidar data are available for only 14 hours (although more will be available). These 14 hours were selected for initial model evaluation. These hours all represent stable plume impingement conditions with a good distribution of observed concentrations on Beacon Hill or Target Mountain. Five of these are among the top ten highest observed normalized concentrations at Tracy.

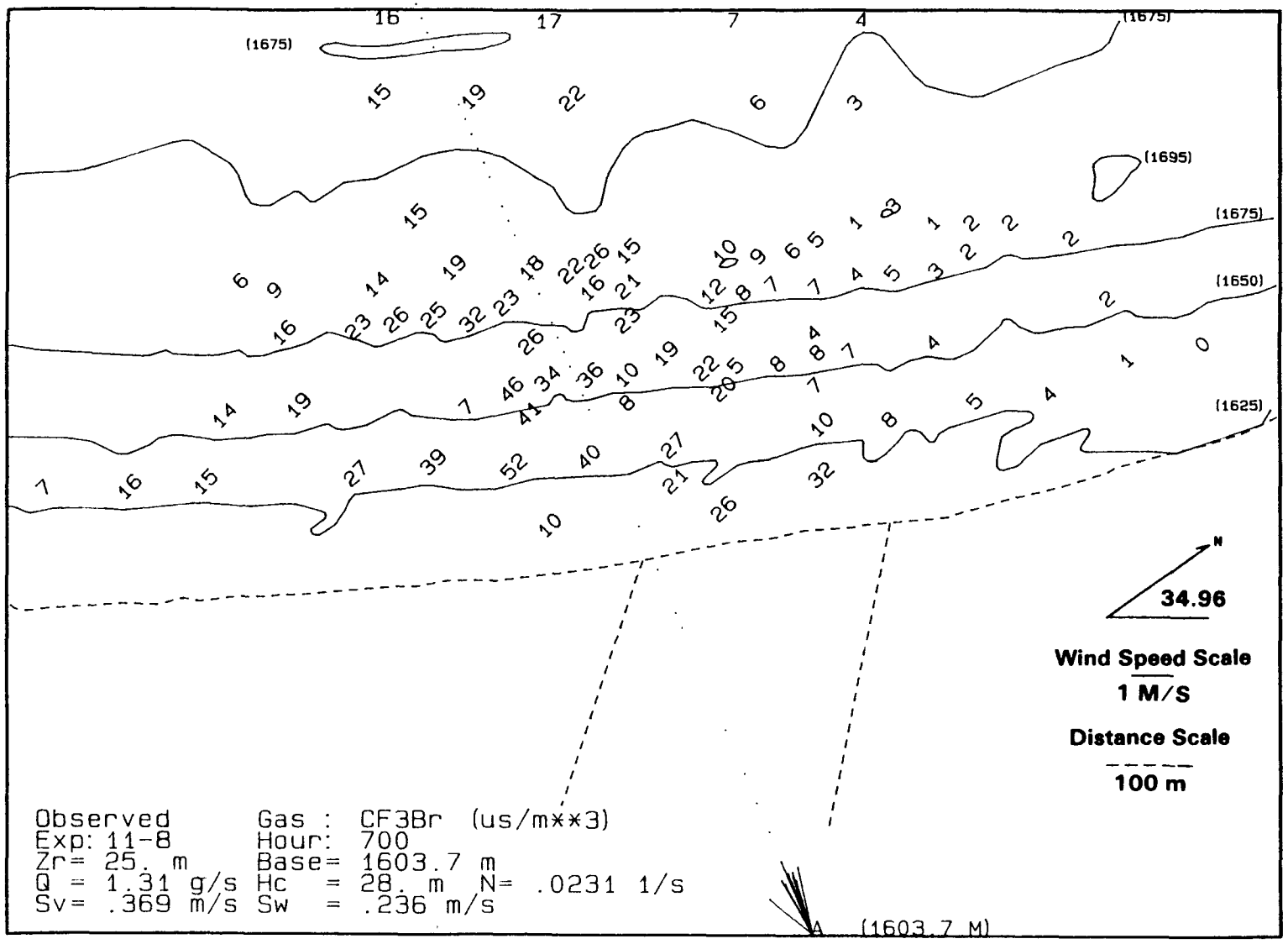

Figure 91. One-hour average observed CF_3Br concentrations scaled by emission rate ($\mu s/m^3$) (Experiment 11, 10/23/82, 0600-0700 MDT).

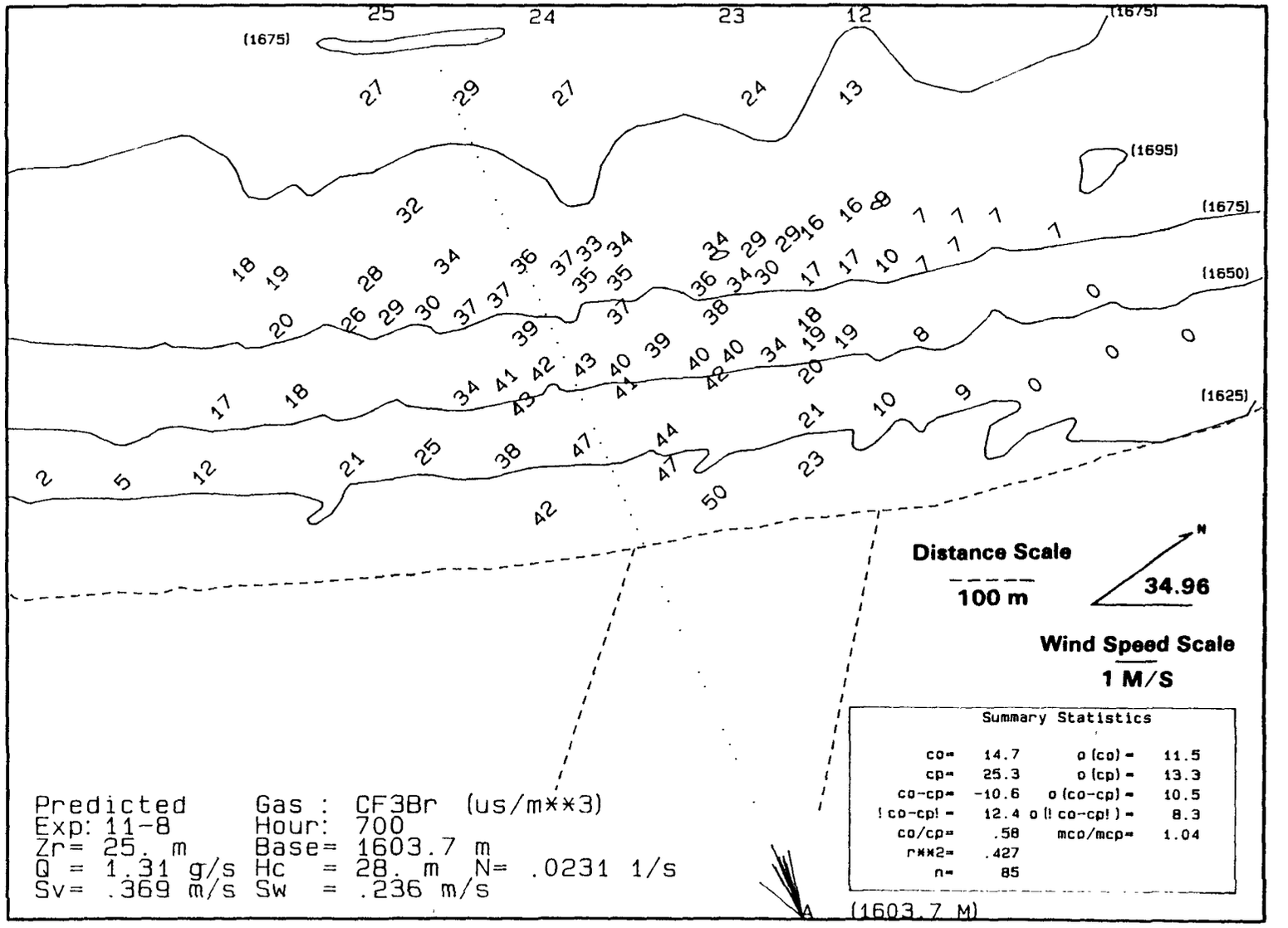

Figure 92. One-hour average predicted scaled concentrations ($\mu s/m^3$) from the HBR model (Experiment 11, 10/23/82, 0600-0700 MDT).

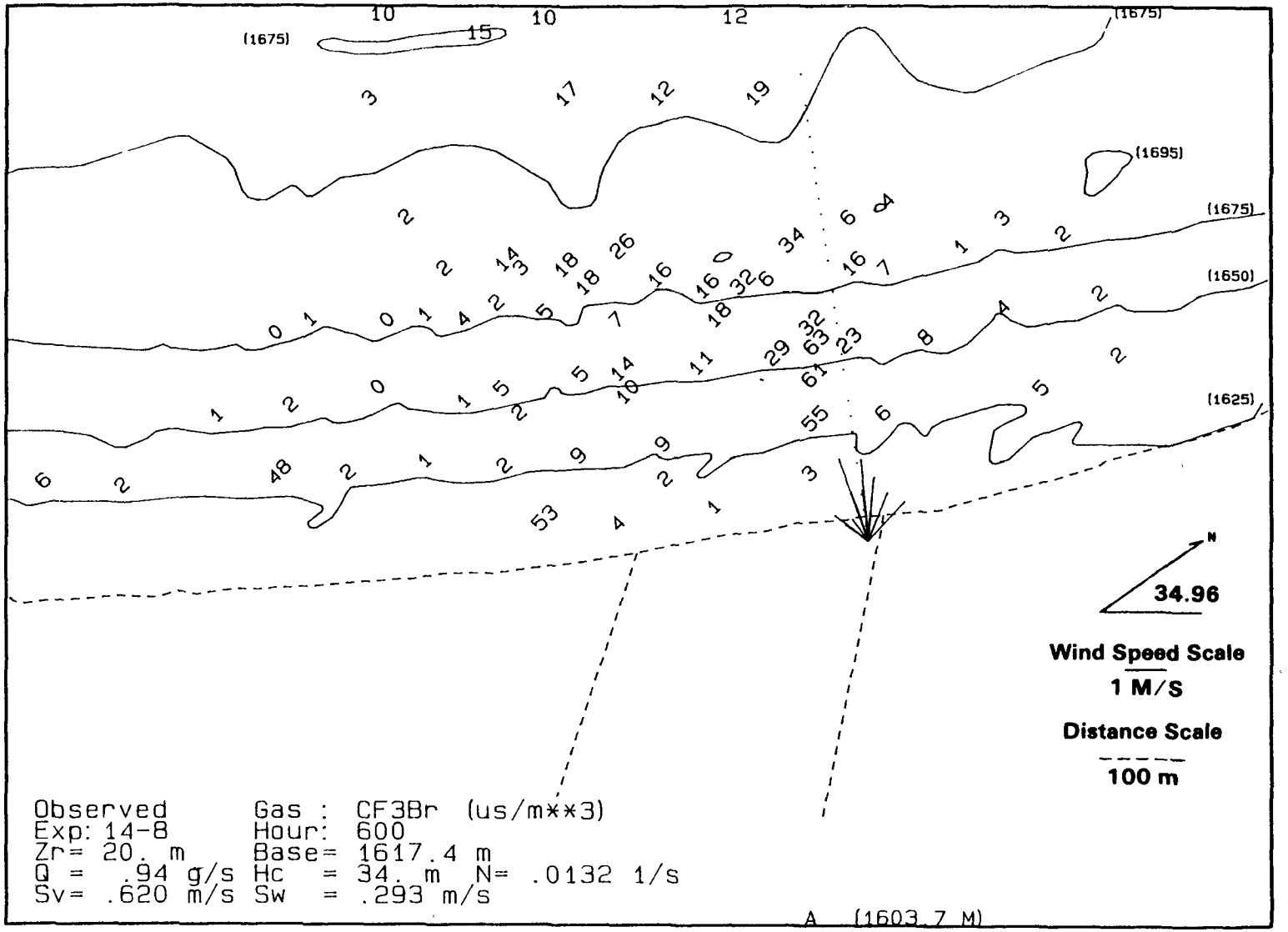

Figure 93. One-hour average observed CF_3Br concentrations scaled by emission rate ($\mu s/m^3$) (Experiment 14, 10/26/82, 0500-0600 MDT).

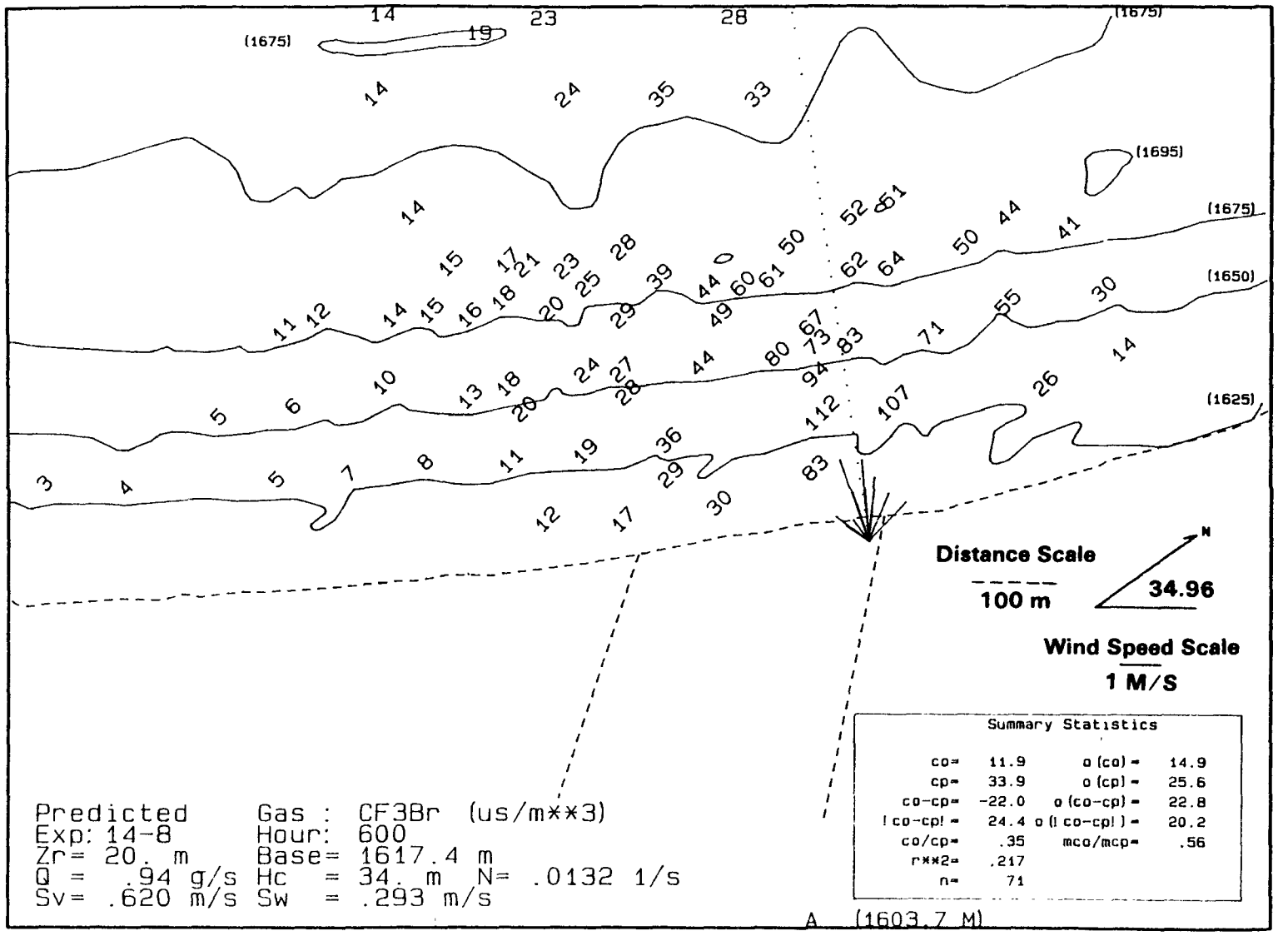

Figure 94. One-hour average predicted scaled concentrations ($\mu s/m^3$) from the HBR model (Experiment 14, 10/26/82, 0500-0600 MDT).

Because the non-cosine response corrections have not yet been applied to the propeller anemometer data, the hourly vector-averaged cup and vane anemometer data from the 150-m level of Tower A are used to represent the wind speed and direction at the height of the plume. In addition to CTDM, three conventional complex terrain models (RTDM, Complex I and II) were run. Wind data collected at 150 m were used, rather than the 10-m wind data extrapolated to stack top with a power law relationship.

The stability class was calculated from net radiation and wind speed data by means of the method of Williamson and Krenmayer (1980). The hourly scalar-averaged wind speeds measured by the cups at the 10-m level on Tower A and the hourly averaged net radiation data measured at the 1-m level on Tower A were used to compute the stability.

The vertical turbulence (σ_w) used to represent dispersion conditions at plume height was obtained from the hourly averaged 150-m vertical intensity of turbulence measured by the props and the hourly vector averaged propeller wind speed measured at the 150-m level on Tower A. The prop response correction suggested by Horst (1973) has been applied to the hourly averaged estimate of σ_w.

The local Brunt-Vaisala frequency (N) was estimated at the release height by using the hourly averaged temperature difference between the 125-m and 150-m level on Tower A. The critical dividing-streamline height (H_c) was calculated by the method discussed in Subsection 4.3.1.

The observed concentration distribution, the wind data estimated at plume height, and the travel time to the location of the observed maximum concentration were used to determine whether the meteorology representative of the experiment-hour should be shifted in time. A one-half to one-hour shift of the 5-minute meteorology was applied to 11 of the modeling hours based on an examination of the concentration pattern, wind direction, and travel time. An appropriate one-hour average was then calculated from the shifted 5-minute data.

Table 18 lists for each experiment-hour all of the inputs to the models that were tested with the FSPS data in this report. The experiment number, date, and hour ending for each of the 14 experiment-hours are followed by the effective plume elevation above the base of the stack ($z_r + \Delta h$), the critical dividing-streamline height (H_c), the 150-m hourly average wind speed and direction, the Brunt-Vaisala frequency (N), sigma-w (σ_w), and the stability class. The hourly averaged lidar scans made in the vicinity of the stack were used to estimate the hourly average plume rise (Δh).

The stability classification scheme suggested that all of the modeling hours except one were stable (Class F). The one-hour average net radiation data and the 10-m wind speeds gave stability class C for Experiment 13, Hour Ending 09. A detailed case study of this hour is presented in Subsection 4.3.1. For this hour, RTDM, Complex I, and

TABLE 18. SUMMARY OF FSPS MODEL INPUT DATA

Experiment No. (Date 1984)	Hour Ending (PDT)	$z_r + \Delta h$ (m)	H_c (m)	Average Wind Speed (m/s)	Average Wind Direction (°)	N (1/s)	σ_w (m/s)	Stability Class
2 (8/7)	4	156	180	2.8	238.	.0288	.227	F
2	5	134	177	3.2	231.	.0280	.210	F
2	6	148	200	2.3	250.	.0258	.173	F
2	7	163	223	1.7	244.	.0260	.145	F
3 (8/10)	6	186	184	2.3	254.	.0217	.288	F
5 (8/12)	4	171	245	1.2	239.	.0267	.183	F
6 (8/16)	5	110	184	5.6	257.	.0209	.268	F
6	7	152	48	3.7	246.	.0185	.322	F
7 (8/17)	7	163	143	2.7	236.	.0239	.230	F
11 (8/23)	6	198	243	1.3	241.	.0273	.168	F
13 (8/25)	7	208	220	1.9	256.	.0266	.093	F
13	8	206	246	1.1	229.	.0250	.125	F
13	9	211	225	1.6	238.	.0239	.148	C*
14 (8/27)	3	184	24	3.2	234.	.0195	.425	F

*Also modeled as stability class F.

Complex II were run using stability class F as well. Predicted concentration plots for both stability classes are presented in the next subsection.

5.4.2 Application of Conventional Complex Terrain Models

Valley

The maximum 1-hour tracer concentrations (scaled by the emission rate) from the EPA Valley screening model are presented in Table 19 for each of the 14 case hours. The observed maximum concentrations and the ratios of the hourly calculated to observed concentrations paired in time but unpaired in space are also included. Two sets of predicted concentrations are presented for each experiment-hour. The first set includes Valley calculations without buoyancy enhancement and the second set is based on a buoyancy enhanced estimate of σ_z. Equation 52 was used to calculate the ambient σ_{za}. The constants used in this equation are applicable for P-G stability Class F over a distance greater than 1,000 m, which includes all of the downwind distances for the 14 case hours. For the buoyancy enhanced Valley calculations,

$$\sigma_{zb} = \frac{\Delta h}{3.5} \tag{108}$$

where Δh is the lidar-derived hourly averaged plume rise. The resultant value of σ_z^2 is then expressed as the sum of the squares of the ambient and buoyant σ_z components $\sigma_z^2 = \sigma_{za}^2 + \sigma_{zb}^2$.

The non-buoyancy enhanced Valley concentrations appreciably overestimate the maximum observed normalized concentrations for all case-hours. Valley overestimates by as much as a factor of nine for two case-hours. The closest the non-buoyant Valley prediction comes to the maximum observed concentration is for Experiment 13-9 where the (C_o/C_p) Max is 0.42.

Similarly, the buoyancy enhanced Valley concentrations also overestimate the maximum observed normalized concentrations for all case-hours. However, three of the case-hour predictions are now within a factor of two of the maximum observed. For Experiment 13-9, (C_o/C_p) Max is now 0.74. In any event, both sets of Valley calculations substantially overestimate the observed SF_6 concentrations.

COMPLEX I and COMPLEX II

COMPLEX I is a univariate Gaussian plume model with 22.5° sector averaging in the horizontal, while COMPLEX II computes off-plume-centerline concentrations according to a bivariate Gaussian distribution function. Terrain treatment in the COMPLEX models varies with stability class. A 0.5 terrain adjustment is used for neutral and unstable classes, while no terrain adjustments (with a 10-m "miss" distance) are used for stable classes.

TABLE 19. SUMMARY χ/Q STATISTICS FOR VALLEY CALCULATIONS

Experiment Number	Hour Ending	Max C_o (μs/m³)	Max C_p (μs/m³)	(C_o/C_p) Max	Max C_p* (μs/m³)	(C_o/C_p) Max
2	4	3.4	24.7	0.14	18.8	0.18
2	5	8.0	26.4	0.30	22.9	0.35
2	6	3.2	25.5	0.13	20.4	0.16
2	7	5.1	24.3	0.21	17.7	0.29
3	6	3.2	22.0	0.15	14.2	0.23
5	4	5.1	23.5	0.22	16.4	0.31
6	5	3.7	28.3	0.13	27.4	0.14
6	7	2.7	25.1	0.11	19.6	0.14
7	7	5.5	24.2	0.23	17.7	0.31
11	6	7.5	21.4	0.35	12.8	0.59
13	7	4.1	20.1	0.20	11.5	0.36
13	8	6.7	20.3	0.33	11.7	0.57
13	9	8.3	19.8	0.42	11.2	0.74
14	3	2.4	22.4	0.11	14.5	0.17

*Buoyancy Enhanced.

In order to use the buoyancy induced dispersion option, the model must first calculate the plume rise. The hourly averaged lidar-observed plume rise (Δh) and a constant stack temperature (T_s) are used to estimate the exit velocity as

$$V_{ex} = \frac{4T_s F}{g d_s^2 (T_s - T_a)} \tag{109}$$

where g is the acceleration due to gravity, d_s is the stack diameter, and T_a is the ambient temperature. Given measured values of plume rise (Δh) and meteorological parameters, the buoyancy flux for stable conditions can be estimated from

$$F = \left(\frac{\Delta h}{2.6}\right)^3 \frac{u g \partial\theta/\partial z}{T_a} \tag{110}$$

where u is the 150-m wind speed and $\partial\theta/\partial z = .035$ °K/m for stability class F. For unstable conditions, the buoyancy flux is

$$F = \left(\frac{u\Delta h}{21.425}\right)^{4/3} \qquad F < 55 \text{ m}^4/\text{s}^3 \quad , \tag{111}$$

$$F = \left(\frac{u\Delta h}{38.71}\right)^{4/3} \qquad F \geq 55 \text{ m}^4/\text{s}^3 \tag{112}$$

Thus, the exit velocity input to the model is specified such that the modeled plume rise will match the lidar-observed plume rise. This plume rise is then used to calculate the buoyancy induced dispersion as $\Delta h/3.5$.

The performance statistics for the average of the top two concentrations paired in time but unpaired in space for the COMPLEX models are presented in Tables 20 and 21. Because there are a limited number of samplers in the area of the maximum observed concentration, the top two statistics are used rather than the top five statistics. The average of the highest two observed and predicted normalized concentrations, their residuals, the maximum predicted concentrations, and the ratios of maximum observed to the maximum predicted are listed. Experiment 13-9 was modeled using stability classes C and F.

The average top-two COMPLEX I concentrations are in fair agreement with the average top-two observed concentrations. The average top-two residuals indicate that COMPLEX I overpredicts for 11 of the case-hours. The ratio of the maximum observed to predicted concentrations indicate that 10 of the case-hours lie within a factor of two.

The COMPLEX I predicted concentration distribution (as normalized χ/Q in units of $\mu s/m^3$) for Experiment 13-9 using stability class C is presented in Figure 95. The observed concentration distribution (as normalized χ/Q) is presented in Figure 96. The 5-minute vector averaged wind distribution estimated at the height of the plume is

TABLE 20. SUMMARY χ/Q STATISTICS FOR COMPLEX I CALCULATIONS[+]

Experiment Number	Hour Ending	$\overline{C_o}$ (μs/m³)	$\overline{C_p}$ (μs/m³)	$\overline{C_o - C_p}$ (μs/m³)	Max C_p (μs/m³)	(C_o/C_p) Max
2	4	3.4	6.5	-3.1	6.7	0.52
2	5	7.3	5.8	1.5	6.0	1.34
2	6	3.0	8.0	-5.0	8.2	0.39
2	7	4.8	10.5	-5.7	10.8	0.47
3	6	2.5	5.4	-2.9	5.9	0.54
5	4	4.7	14.5	-9.8	14.9	0.34
6	5	3.0	2.9	0.1	3.1	1.20
6	7	2.6	4.9	-2.3	5.1	0.53
7	7	5.0	6.6	-1.6	6.8	0.81
11	6	5.9	9.3	-3.4	9.3	0.80
13	7	3.5	4.9	-1.4	5.5	0.75
13	8	4.5	8.9	-4.4	9.3	0.72
13	9	8.2	1.5	6.7	1.5	5.69
13	9*	8.2	6.0	2.2	6.2	1.35
14	3	2.0	4.1	-2.1	4.9	0.49

[+]Refer to Table 19 for Max C_o values.

*Modeled with Stability Class F.

TABLE 21. SUMMARY χ/Q STATISTICS FOR COMPLEX II CALCULATIONS[+]

Experiment Number	Hour Ending	$\overline{C_o}$ (μs/m³)	$\overline{C_p}$ (μs/m³)	$\overline{C_o - C_p}$ (μs/m³)	Max C_p (μs/m³)	(C_o/C_p) Max
2	4	3.4	14.1	-10.7	17.4	0.20
2	5	7.3	8.6	-1.3	14.8	0.54
2	6	3.0	21.9	-18.9	27.6	0.12
2	7	4.8	15.9	-11.1	22.9	0.22
3	6	2.5	4.5	-2.0	4.7	0.68
5	4	4.7	40.5	-35.8	42.9	0.12
6	5	3.0	5.4	-2.4	6.9	0.54
6	7	2.6	14.1	-11.5	15.0	0.18
7	7	5.0	7.4	-2.4	8.1	0.68
11	6	5.9	39.0	-33.1	44.8	0.17
13	7	3.5	10.5	-7.0	13.0	0.32
13	8	4.5	34.8	-30.3	46.1	0.15
13	9	8.2	2.1	6.1	2.5	3.35
13	9*	8.2	23.4	-15.2	28.8	0.29
14	3	2.0	13.3	-11.3	14.1	0.17

[+]Refer to Table 19 for Max C_o values.

*Modeled with Stability Class F.

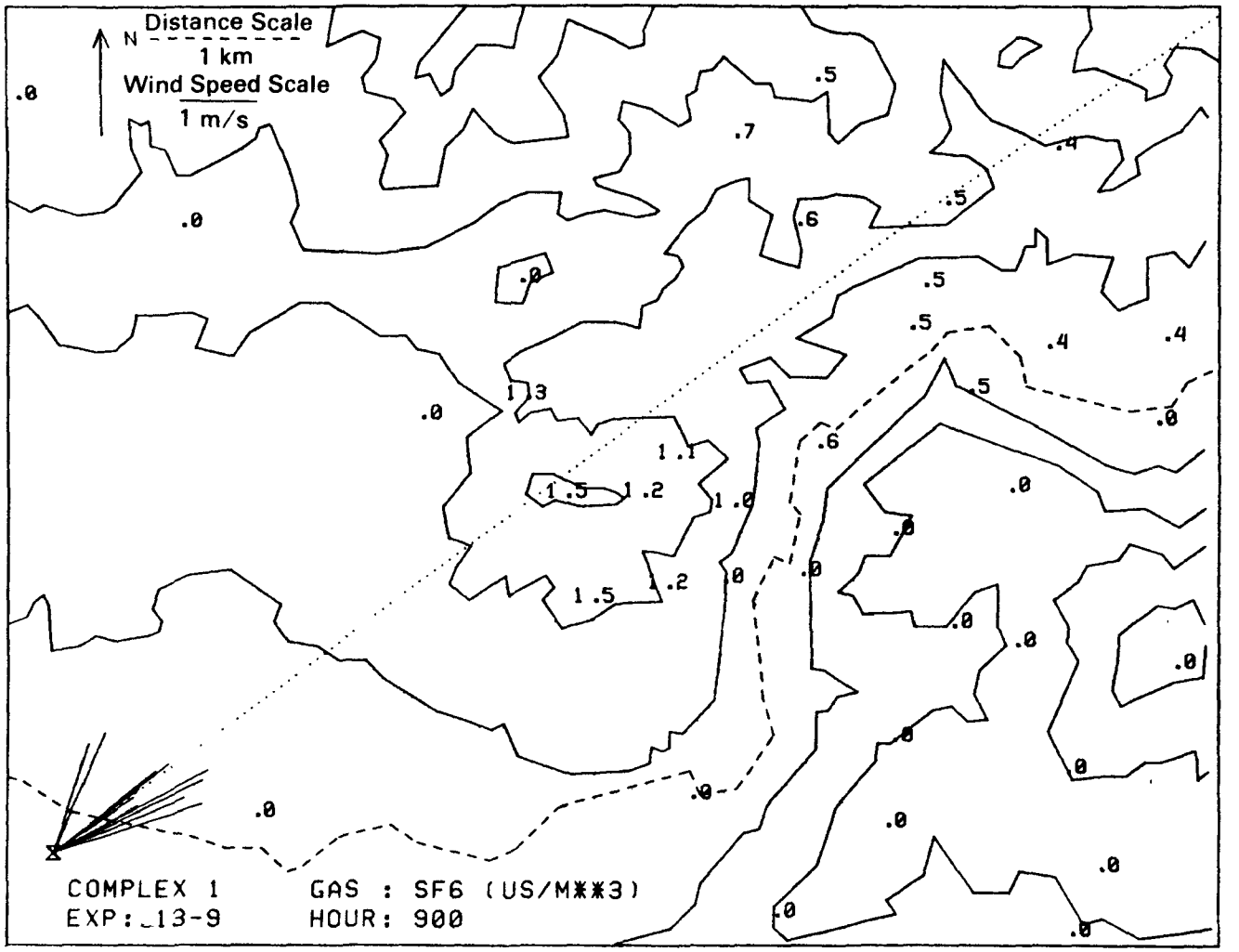

Figure 95. One-hour average predicted scaled concentrations ($\mu s/m^3$) from COMPLEX I, Stability Class C (Experiment 13, 8/26/84, 0800-0900 PDT).

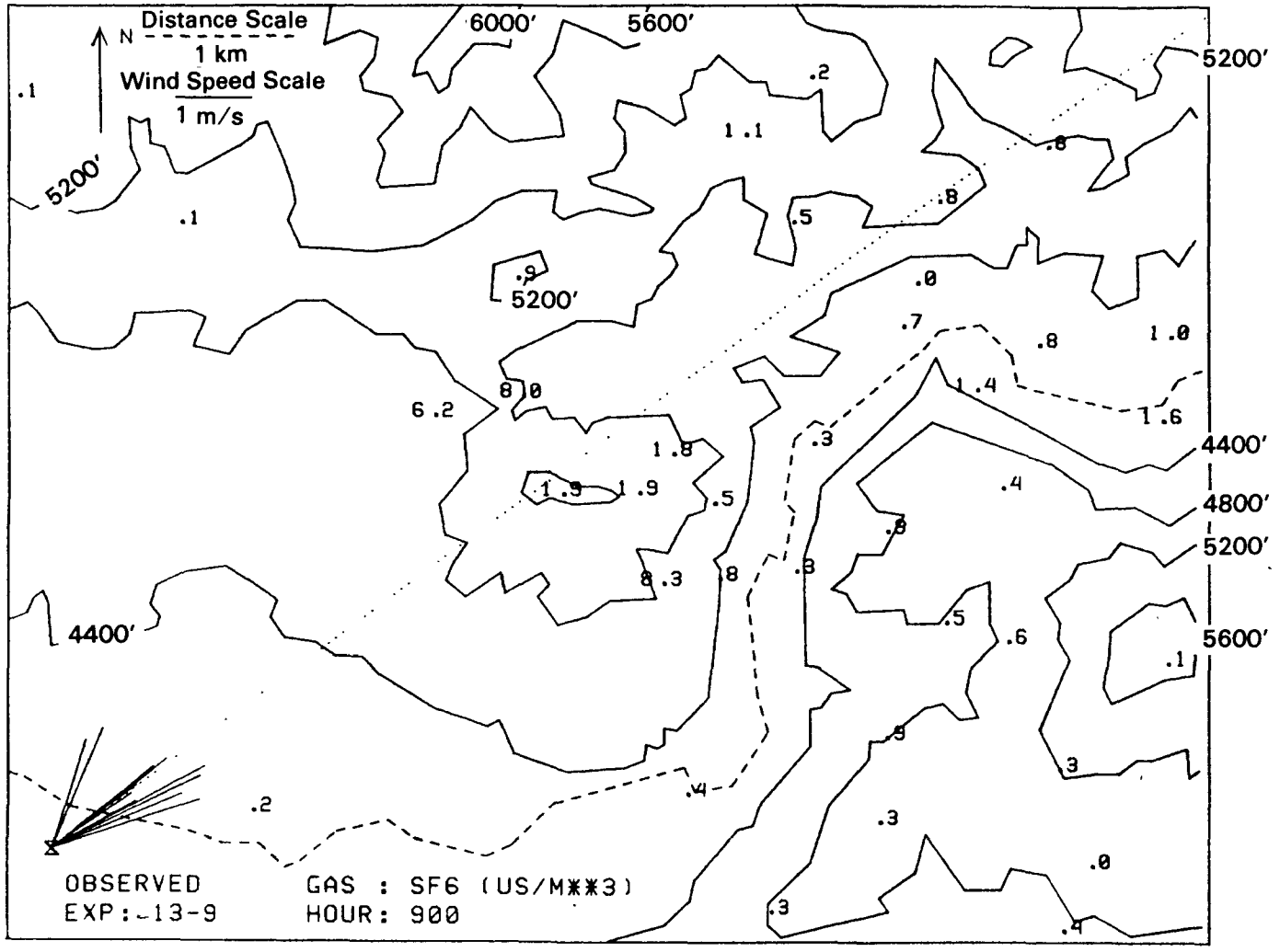

Figure 96. One-hour average observed scaled concentrations ($\mu s/m^3$) (Experiment 13, 8/26/84, 0800-0900 PDT).

drawn at the stack position. The hourly vector averaged wind direction is depicted by the long dotted line. Using stability class C, COMPLEX I grossly underpredicts the maximum observed concentrations. The predicted COMPLEX I concentration distribution using stability class F is presented in Figure 97. The predicted concentrations are now more than four times larger than those COMPLEX I calculations using stability class C. However, the peak predicted concentrations are still less than the maximum observed concentrations. Also, the predicted concentration distribution shows a horizontal spread that appears too small.

The COMPLEX II results indicate an overprediction of all case-hours except for Experiment 13-9 when stability class C was used. The residual statistics indicate that four of the case-hours have predicted concentrations within 2 $\mu s/m^3$; however, nine of the case-hours show overpredictions of more than 10 $\mu s/m^3$. The ratios of the maximum observed to predicted concentrations show that only four of the case-hours lie within a factor of two.

The COMPLEX II predicted concentration distribution (as normalized χ/Q in units of $\mu s/m^3$) for Experiment 13-9 using stability class C is presented in Figure 98. The predicted concentrations are much lower than the observed concentrations. When stability class F is used, as shown in Figure 99, COMPLEX II grossly overpredicts the maximum observed concentrations. Also, the spatial distribution pattern shown in the COMPLEX II run is much narrower in the crosswind direction (than the observed scatter).

RTDM

The Rough Terrain Diffusion Model (RTDM) is a sequential Gaussian plume model designed to estimate ground-level concentrations in rough (or flat) terrain in the vicinity of one or more collocated point sources (ERT, 1982). It is specifically designed for applications involving nonreactive gases and is best suited for evaluation of buoyant plume behavior within about 15 km of the source.

Rather than assuming full reflection (Valley-like computations) for cases of plume impingement, RTDM uses a partial plume reflection algorithm that takes into account the slope of the terrain. Off-plume centerline concentrations are computed according to a bivariate Gaussian distribution.

In stable conditions, the dividing-streamline height (H_c) is computed from the wind speed, the terrain height, and the strength of the ground-based inversion. Plumes below H_c are allowed to impinge on the terrain. During neutral or unstable conditions, or above H_c in stable conditions, a "half-height" correction simulates the effect of terrain-induced plume modifications on ground-level concentrations.

As used in the COMPLEX I and COMPLEX II analysis, the hourly averaged lidar-derived plume rise (Δh) and a constant stack temperature are used to estimate the exit velocity. Thus, the exit

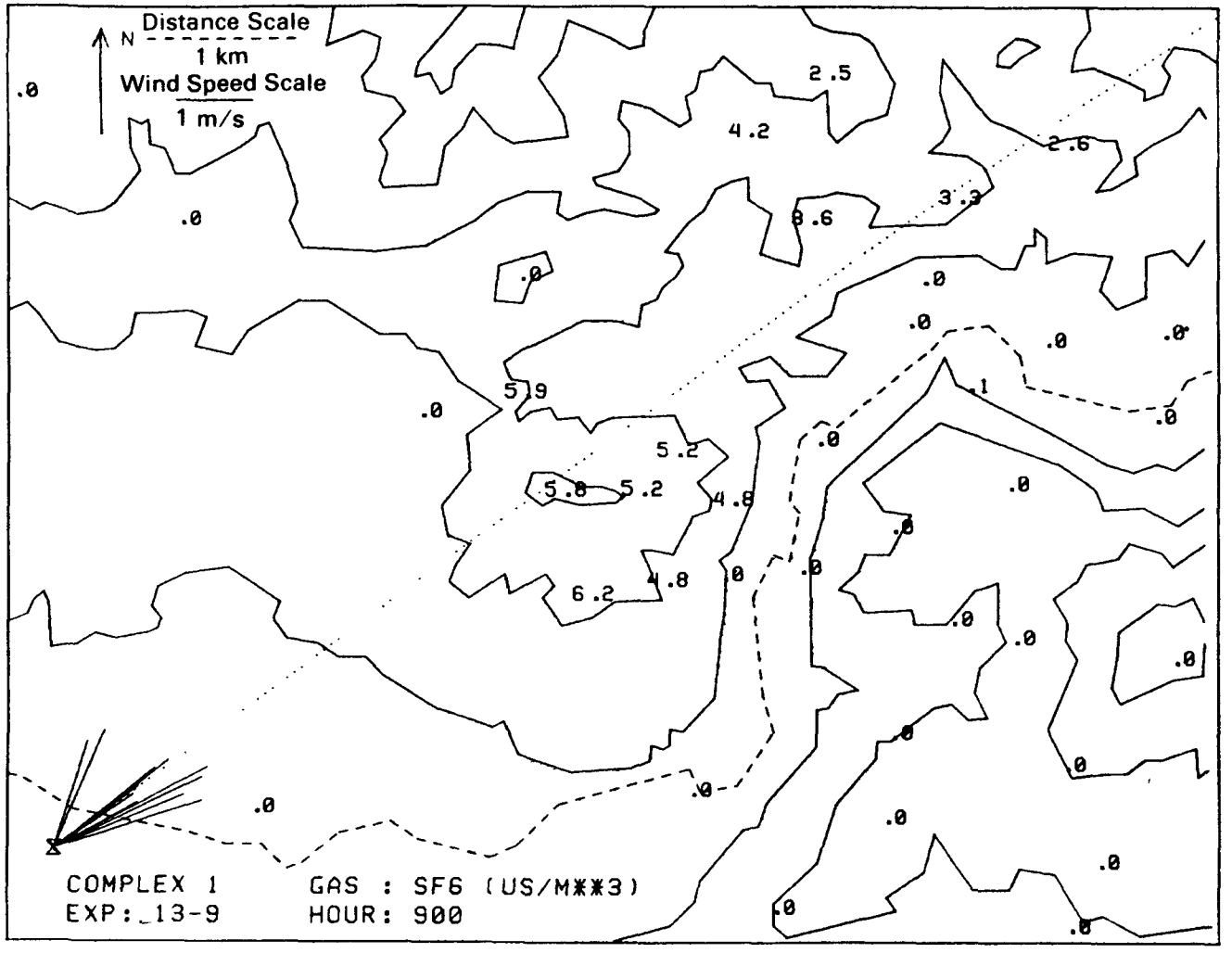

Figure 97. One-hour average predicted scaled concentrations ($\mu s/m^3$) from COMPLEX I, Stability Class F (Experiment 13, 8/26/84, 0800-0900 PDT).

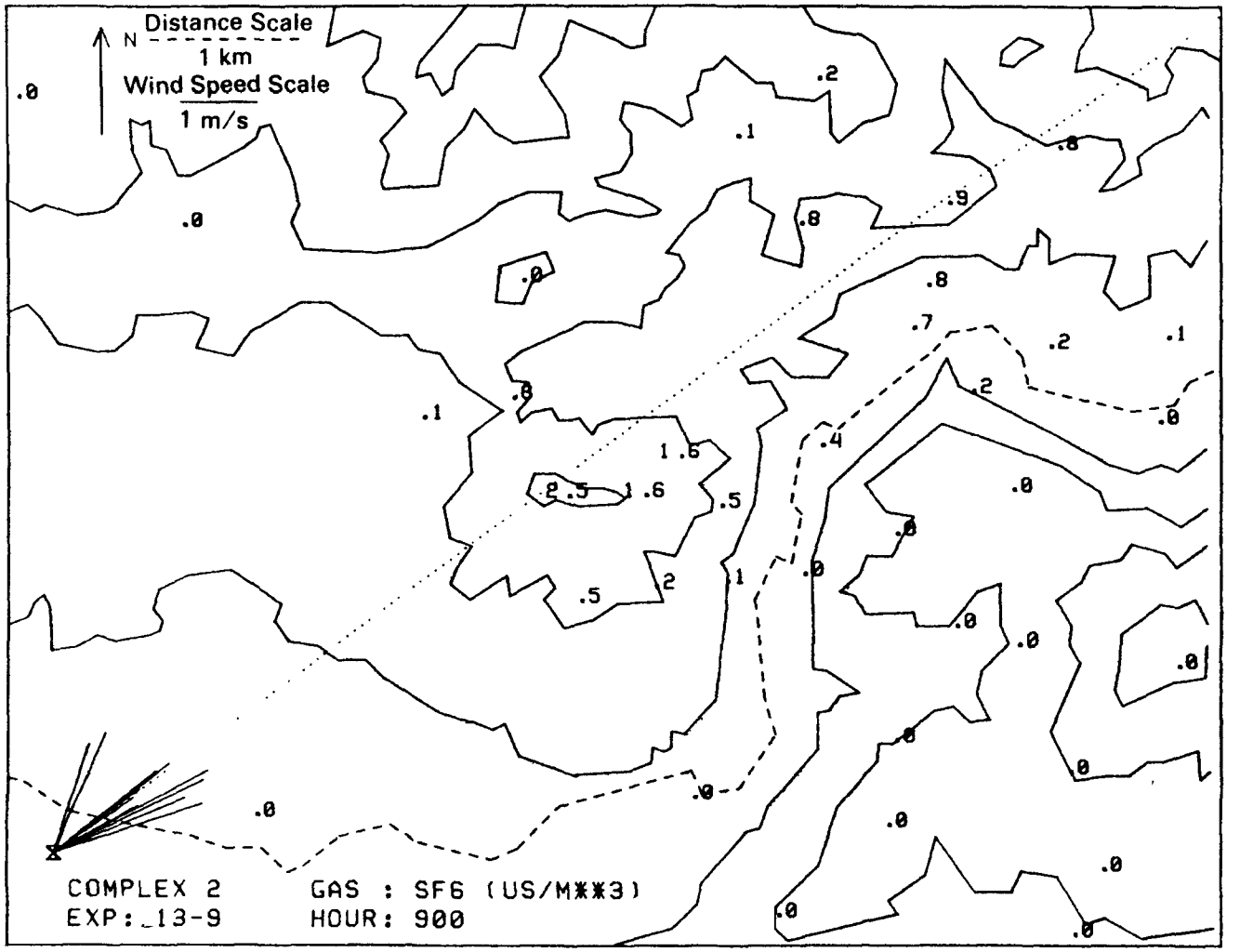

Figure 98. One-hour average predicted scaled concentrations ($\mu s/m^3$) from COMPLEX II, Stability Class C (Experiment 13, 8/26/84, 0800-0900 PDT).

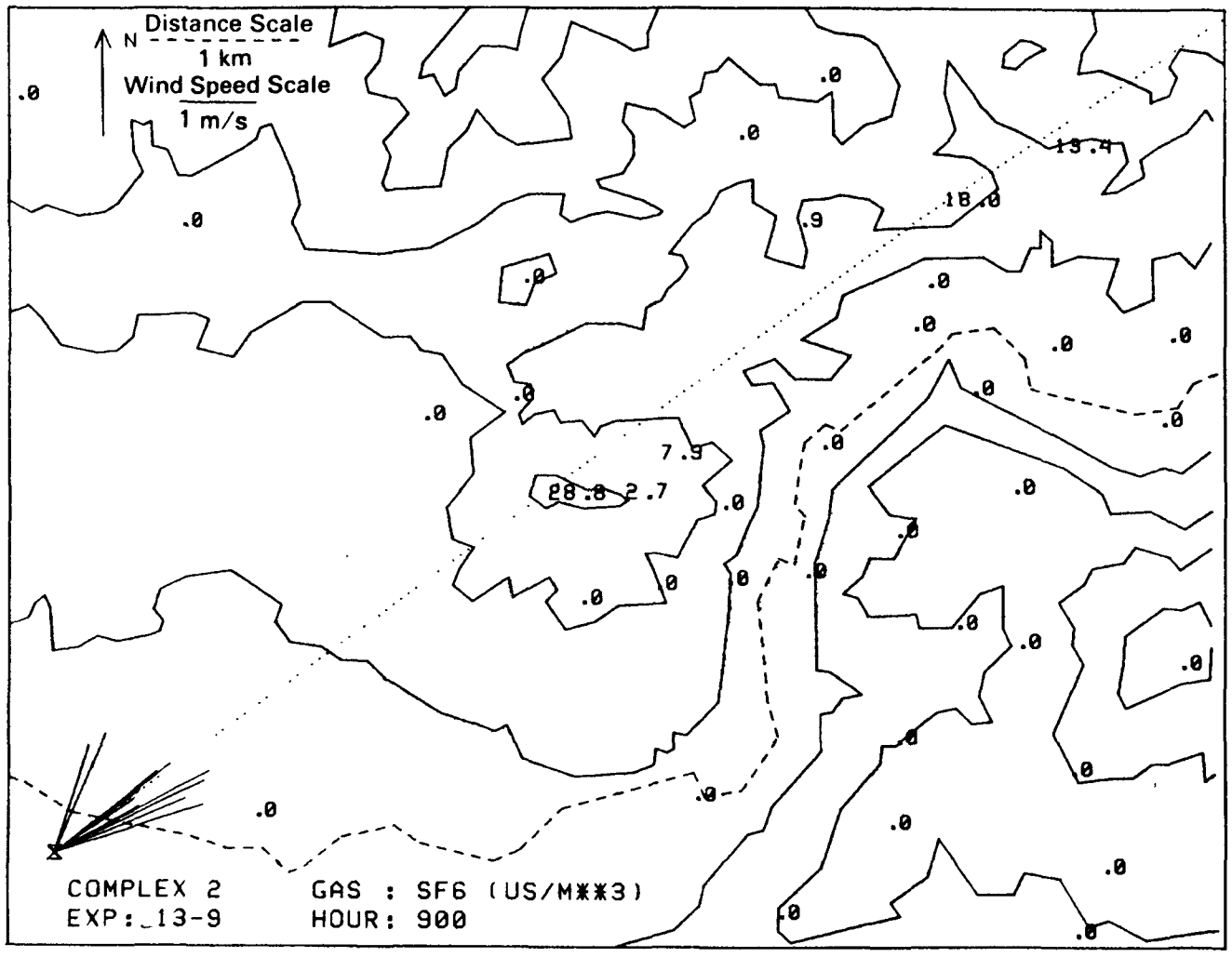

Figure 99. One-hour average predicted scaled concentrations ($\mu s/m^3$) from COMPLEX II, Stability Class F (Experiment 13, 8/26/84, 0800-0900 PDT).

velocity input to RTDM is such that the modeled plume rise will match the lidar-derived plume rise. This plume rise is then used to calculate the buoyancy-induced dispersion as $\Delta h/\sqrt{10}$.

RTDM was first run using the hourly values of the vertical and horizontal components of the turbulence intensity estimated at plume height to calculate σ_y and σ_z. The top-two normalized concentration statistics paired in time but unpaired in space for this version of RTDM are presented in Table 22. The average top-two concentrations underpredict the observations for all case-hours. The ratio of the maximum observed to predicted concentrations indicate that none of the case-hours lie within a factor of two.

The RTDM predicted concentration distribution (as normalized χ/Q in units of $\mu s/m^3$) for Experiment 13-9 using the measured turbulence data and stability class C is presented in Figure 100. The observed concentration distribution was presented in Figure 96. For unstable conditions, RTDM sets H_c to zero and σ_z is only a function of the vertical intensity of turbulence and downwind distance expressed as

$$\sigma_z = i_z x \quad . \tag{113}$$

RTDM grossly underpredicts the maximum observed concentrations. The results do not change much when stability class F is used, as shown in Figure 101. As discussed in Subsection 3.4.3, the values of σ_z are overpredicted when the measured values of turbulence are used in conjunction with the RTDM expression for stable σ_z.

RTDM was then tested using the Briggs rural (ASME, 1979) dispersion coefficients and these results are presented in Table 23. The top-two average predicted concentrations are now much larger than those predicted from RTDM's algorithm that use the measured turbulence data. The ratios of the maximum observed to predicted concentrations indicate that six of the case-hours now lie within a factor of two.

The RTDM predicted concentration distribution (as normalized χ/Q in units of $\mu s/m^3$) for Experiment 13-9 using the ASME dispersion parameters and stability class C is presented in Figure 102. RTDM still underpredicts the maximum observed concentrations. The predicted concentrations increase substantially when stability class F is used, as presented in Figure 103. The (C_o/C_p) Max is now 0.92; however, the maximum concentration occurs much further downwind than the maximum observed concentration. Also, compared to the observed concentrations, the spatial distribution pattern is extremely narrow in the crosswind direction.

5.4.3 Application of CTDM

CTDM (12185) has been applied to the initial modeling dataset. All but one of the 14 hours has been included; only "Beacon Hill" receptors have been explicitly included in the modeling, so the single hour of the dataset in which "Target Mountain" was the primary impact zone was not modeled.

TABLE 22. SUMMARY χ/Q STATISTICS FOR RTDM CALCULATIONS USING ON-SITE TURBULENCE DATA[+]

Experiment Number	Hour Ending	$\overline{C_o}$ (μs/m³)	$\overline{C_p}$ (μs/m³)	$\overline{C_o - C_p}$ (μs/m³)	Max C_p (μs/m³)	(C_o/C_p) Max
2	4	3.4	0.9	2.5	1.0	3.4
2	5	7.3	1.0	6.3	1.4	5.8
2	6	3.0	1.0	2.0	1.1	2.9
2	7	4.8	0.8	4.0	0.8	6.1
3	6	2.5	0.8	1.7	1.1	2.9
5	4	4.7	0.8	3.9	1.1	4.8
6	5	3.0	0.9	2.1	0.9	4.1
6	7	2.6	0.5	2.1	0.5	5.3
7	7	5.0	1.5	3.5	1.8	3.1
11	6	5.9	0.6	5.3	0.7	11.3
13	7	3.5	1.1	2.4	1.1	3.7
13	8	4.5	0.4	4.1	0.4	16.7
13	9	8.2	0.6	7.6	0.6	12.9
13	9*	8.2	0.7	7.5	0.7	11.6
14	3	2.0	0.7	1.3	0.8	2.9

[+]Refer to Table 19 for Max C_o values.

*Modeled with stability class F.

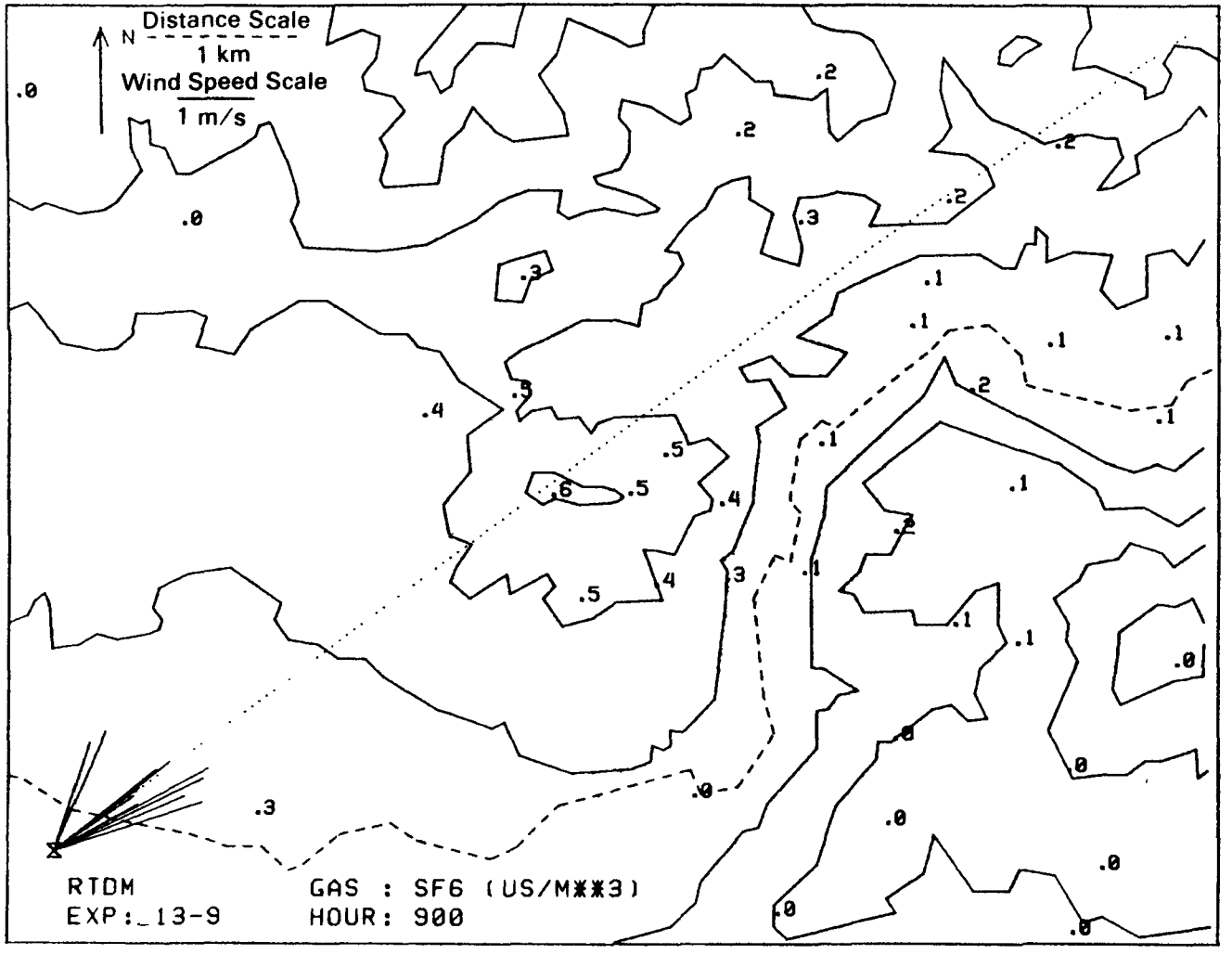

Figure 100. One-hour average predicted scaled concentrations ($\mu s/m^3$) from RTDM, Stability Class C using measured turbulence (Experiment 13, 8/26/84, 0800-0900 PDT).

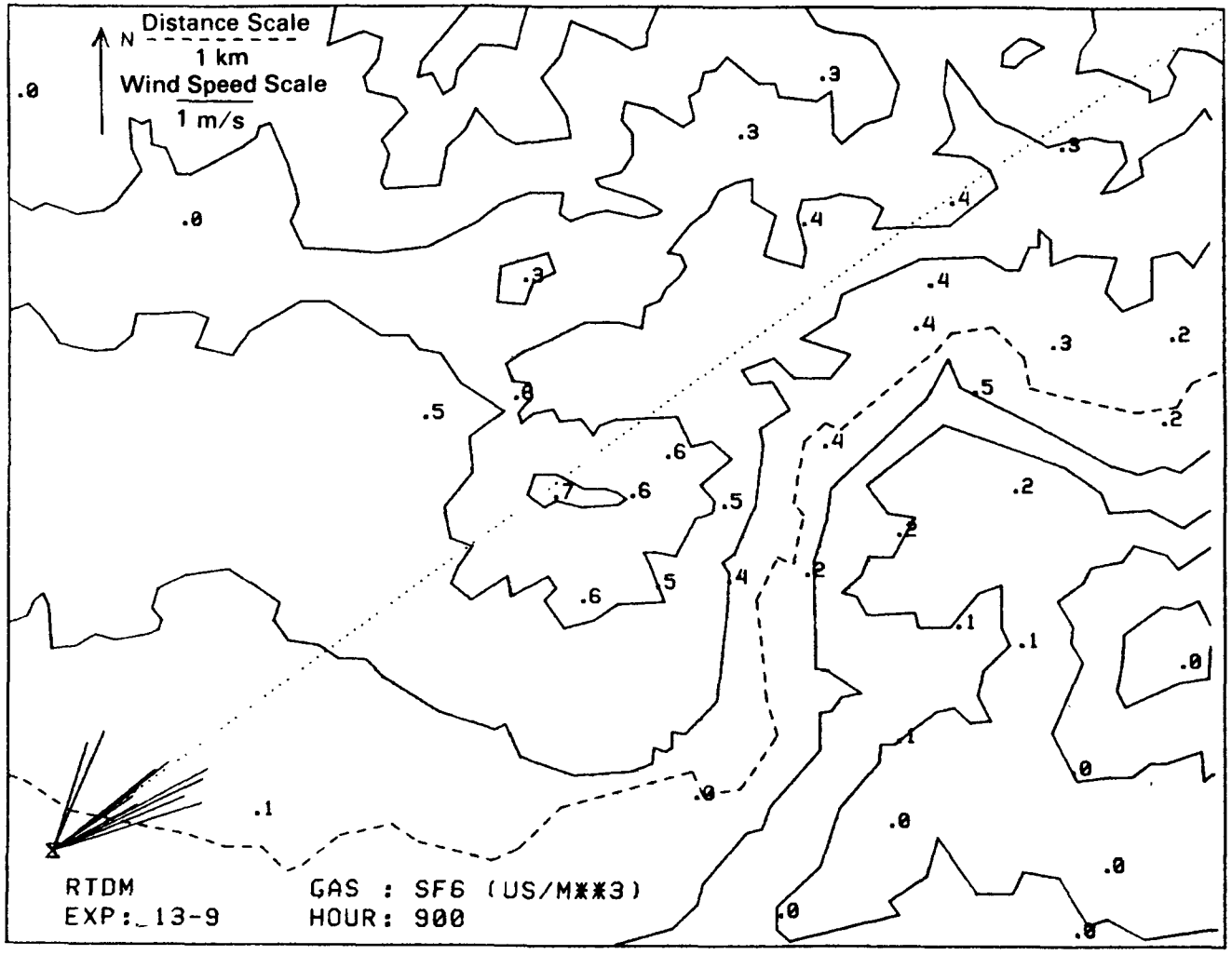

Figure 101. One-hour average predicted scaled concentrations ($\mu s/m^3$) from RTDM, Stability Class F using measured turbulence (Experiment 13, 8/26/84, 0800-0900 PDT).

TABLE 23. SUMMARY χ/Q STATISTICS FOR RTDM CALCULATIONS USING BRIGGS-RURAL/ASME - 1979 DISPERSION COEFFICIENTS[+]

Experiment Number	Hour Ending	$\overline{C_o}$ ($\mu s/m^3$)	$\overline{C_p}$ ($\mu s/m^3$)	$\overline{C_o - C_p}$ ($\mu s/m^3$)	Max C_p ($\mu s/m^3$)	(C_o/C_p) Max
2	4	3.4	3.5	-0.1	5.1	0.68
2	5	7.3	3.6	3.7	5.6	1.44
2	6	3.0	12.5	-9.5	14.2	0.23
2	7	4.8	9.5	-4.7	12.9	0.40
3	6	2.5	4.1	-1.6	4.5	0.72
5	4	4.7	16.4	-11.7	22.0	0.23
6	5	3.0	1.1	1.9	1.1	3.48
6	7	2.6	4.4	-1.8	4.9	0.55
7	7	5.0	5.4	-0.4	6.7	0.82
11	6	5.9	19.5	-13.6	25.7	0.29
13	7	3.5	7.7	-4.2	9.6	0.43
13	8	4.5	17.3	-12.8	23.0	0.29
13	9	8.2	1.2	7.0	1.4	5.84
13	9*	8.2	8.4	-0.2	9.0	0.92
14	3	2.0	6.4	-4.4	7.1	0.34

[+]Refer to Table 19 for Max C_o values.

*Modeled with stability class F.

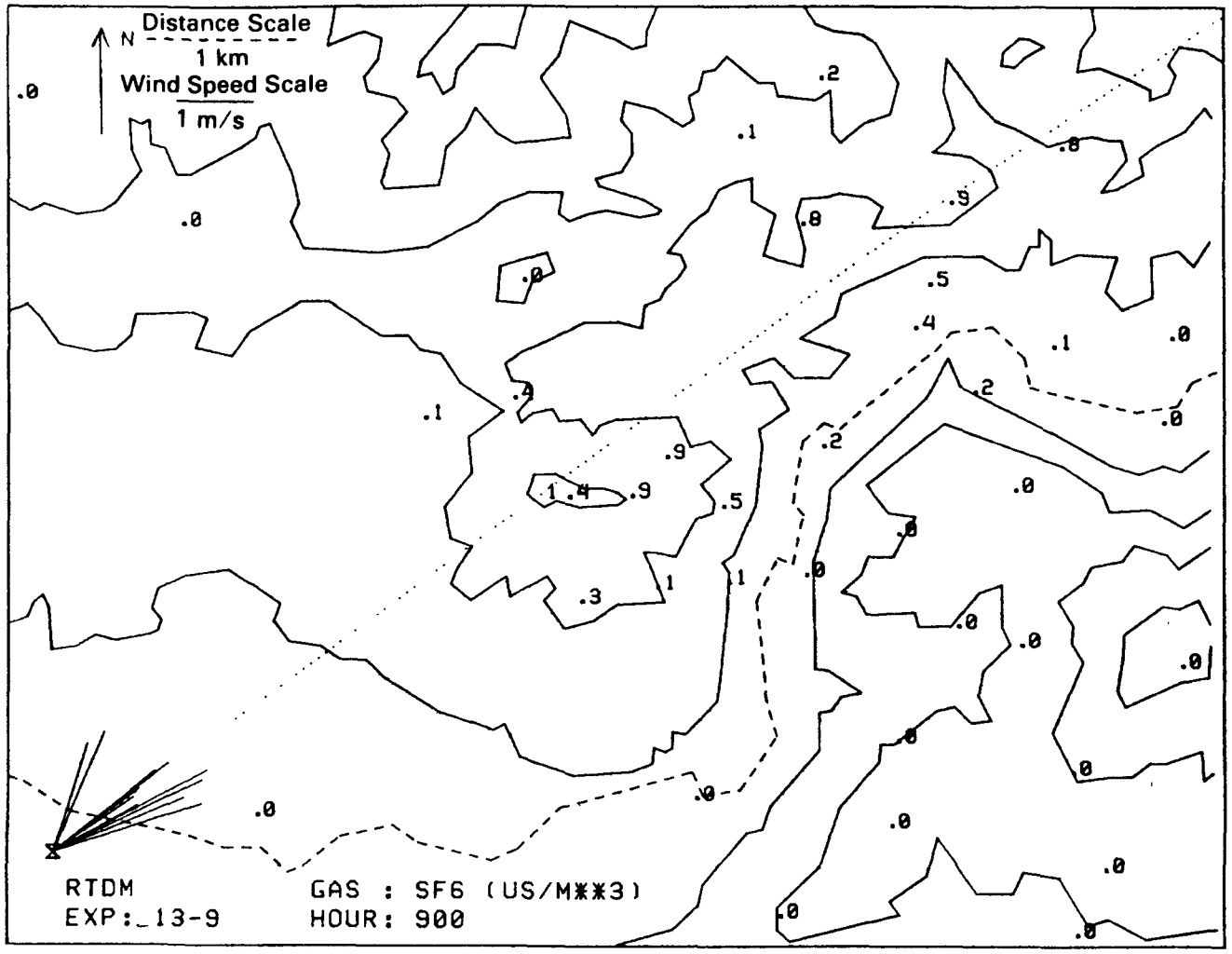

Figure 102. One-hour average predicted scaled concentrations ($\mu s/m^3$) from RTDM, Stability Class C using Briggs rural (ASME, 1979) dispersion coefficients (Experiment 13, 8/26/84, 0800-0900 PDT).

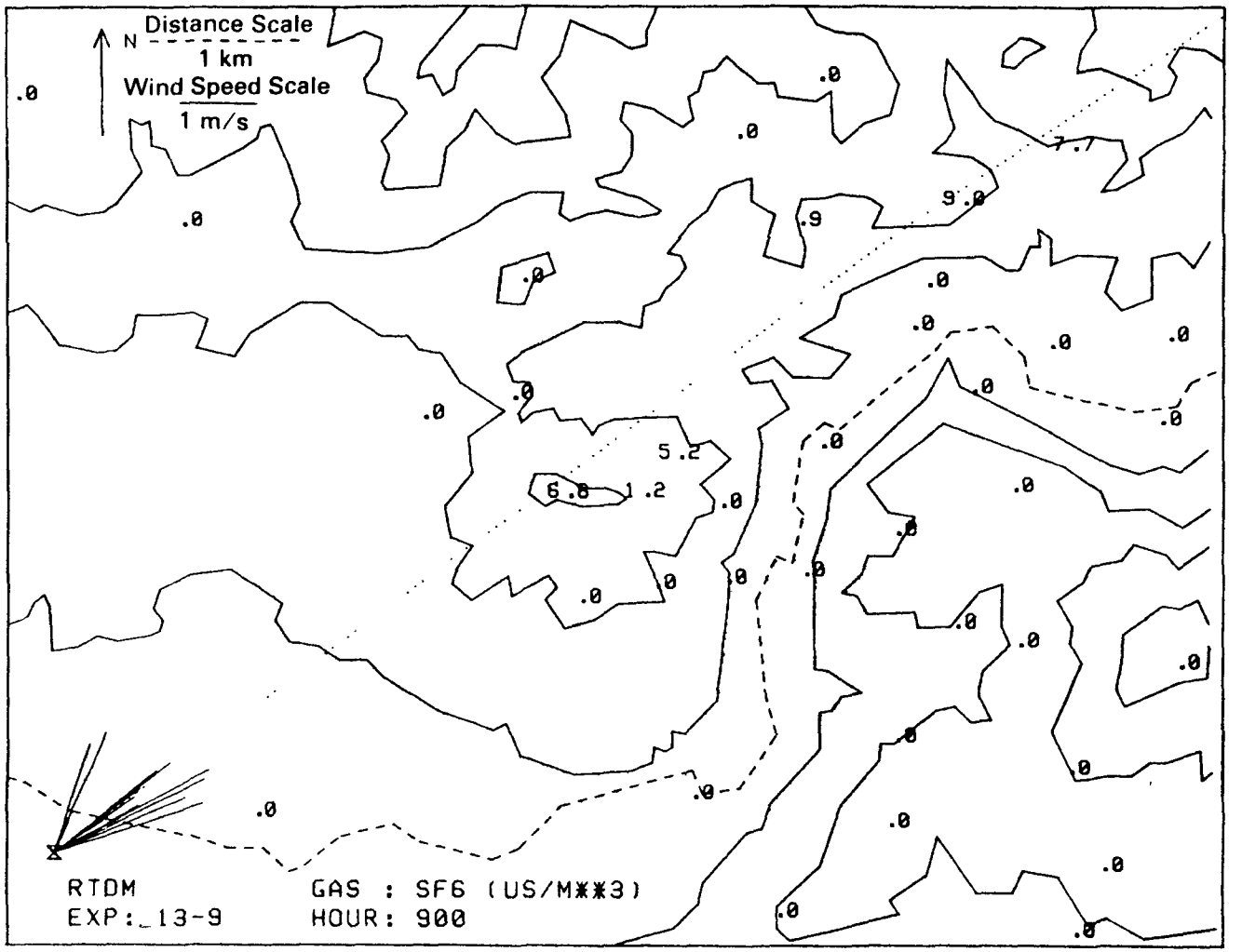

Figure 103. One-hour average predicted scaled concentrations ($\mu s/m^3$) from RTDM, Stability Class F using Briggs rural (ASME, 1979) dispersion coefficients (Experiment 13, 8/26/84, 0800-0900 PDT).

"Beacon Hill" is represented in CTDM by the following parameters:

Height (H) = 300 m
Base Elevation (h_o) = 1299 m (MSL)

	Major Axis	Minor Axis
Semi-length (L)	1062 m	708 m
Inverse Polynomial Power (p)	2.5	1.5

Orientation of the major axis (degrees CW from north) is 66°. The length scale factors for the transition region above H_c and the terrain factor fields are the same as those used in the modeling of CCB:

$\delta = 0.1$
$\alpha = 0.67$

The terrain factors for the vertical deformation and speed-up of the flow at the crest are taken to be

$T_{hoa} = 0.50$ $\quad$ $T_{hob} = 0.60$
$T_{uoa} = 1.15$ $\quad$ $T_{uob} = 1.30$

where "a" refers to flow along the major axis, and "b" refers to flow along the minor axis. These terrain factors are consistent with what one might expect for potential flow over Beacon Hill. They are obtained from estimates of potential flow over an ellipsoid as discussed in Subsection 5.2.1.

Modeling results are presented in Table 24. CTDM underestimates all but one of the peak observed concentrations, but six of the thirteen are within a factor of two. The geometric mean and standard deviation for this dataset are 2.32 and 1.86, respectively. For comparison, the geometric mean and standard deviation for the COMPLEX I results presented in Table 20 (using Class F for Experiment 13-9) are 0.59 and 1.53. Therefore, CTDM tends to underestimate the observed concentrations to a greater degree than COMPLEX I overestimates them, and the scatter in the CTDM estimates is somewhat larger than the scatter in the COMPLEX I estimates.

Approximate centerline values of the χ/Q have been calculated as $1/(2\pi u\sigma_y\sigma_z)$ from representative hourly plume spread parameters from CTDM. They are compared with peak modeled and observed values of the χ/Q in Table 25. In most cases, the tendency for CTDM to underestimate the observed peak concentrations arises from the size of the computed values of σ_y and σ_z, and not from the impact assumptions. The analysis of Section 3.4 indicates that σ_z is generally overestimated by the CTDM algorithm, and so an improvement in CTDM performance will require better performance from the σ_z algorithm.

The performance of the σ_y algorithm has not been assessed. This algorithm may also be overestimating the spread of the plume in a time-averaged sense over an hour, but it is also possible that the use of a Gaussian distribution for the horizontal spread also leads to an

TABLE 24. SUMMARY χ/Q STATISTICS FOR CTDM CALCULATIONS[+]

Exp No.	Hour Ending	$\overline{C_o}$* (ms/m^3)	$\overline{C_p}$* (μs/m^3)	Max C_p (μs/m^3)	(C_o/C_p) Max
2	4	3.4	3.3	3.4	1.02
2	5	7.3	1.7	2.8	2.84
2	6	3.0	3.3	3.3	0.96
2	7	4.8	3.7	3.8	1.33
3	6	2.3	1.1	1.3	2.55
5	4	4.7	2.7	2.8	1.86
6	5	3.0	–	–	–
6	7	2.6	0.4	0.4	6.33
7	7	4.2	2.4	2.7	1.60
11	6	5.9	1.6	1.6	4.62
13	7	2.1	1.4	1.7	1.46
13	8	4.2	1.5	1.7	4.07
13	9	8.2	2.2	2.3	3.64
14	3	2.0	0.5	0.5	4.70

[+]Refer to Table 25 for Max C_o values.

*Average of the 2 greatest scaled concentrations at receptors near "Beacon Hill" for the hour.

TABLE 25. COMPARISON OF PEAK MODELED AND OBSERVED SCALED CONCENTRATIONS WITH CENTERLINE CONCENTRATIONS ESTIMATED FROM PLUME SPREAD PARAMETERS FROM CTDM

Exp-Hr	σ_z (m)	σ_y (m)	u (m/s)	Centerline ($\mu s/m^3$)	CTDM χ/Q(peak) ($\mu s/m^3$)	OBS χ/Q(peak) ($\mu s/m^3$)
2-4	30	380	2.8	5.0	3.4	3.4
2-5	33	290	3.2	5.2	2.8	8.0
2-6	32	380	2.3	5.7	3.3	3.2
2-7	28	880	1.7	3.8	3.8	5.1
3-6	61	1240	2.3	0.9	1.3	3.2
5-4	54	860	1.2	2.9	2.8	5.1
6-7	70	770	3.7	0.8	0.4	2.7
7-7	52	330	3.4	3.4	2.7	4.3
11-6	62	1070	1.3	1.8	1.6	7.5
13-7	32	600	1.9	4.4	1.7	2.4
13-8	43	1970	1.9	1.9	1.7	6.7
13-9	44	850	1.6	2.7	2.3	8.3
14-3	90	360	3.2	1.5	0.5	2.4

underestimate of the peak observed concentrations. Consider experiment 13-9. Modeled concentrations for this hour are shown in Figure 104, as are the 5-minute average wind vectors used in the modeling. The distribution of winds is not Gaussian, and exhibits a dominant lobe towards "Beacon Hill." In effect, this lobe defines a narrower plume than that estimated by the model, and yet this lobe is most important in determining the peak observed concentrations for the hour. Consequently, a type of PDF approach may be important in modeling the FSPS.

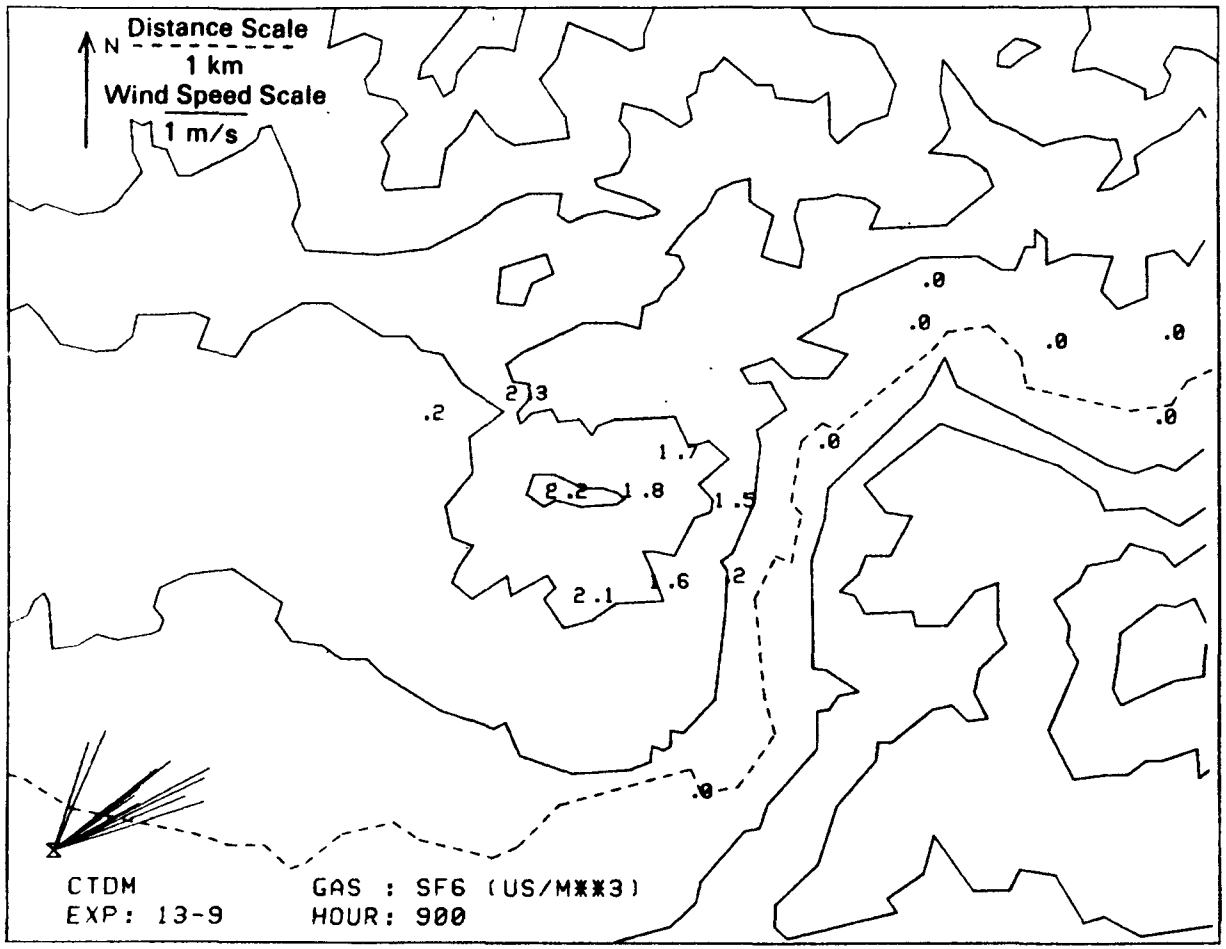

Figure 104. One-hour average predicted scaled concentrations ($\mu s/m^3$) from CTDM (12185) (Experiment 13, 8/26/84, 0800-0900 PDT).

SECTION 6

CTDM - IMPROVEMENTS AND MODIFICATIONS

Several modifications to CTDM are under development. These activities involve the scientific basis of the model and the need for a practical regulatory tool. They address the need for specifying the influence of the hill on diffusion in the flow above H_c (i.e., the LIFT module). It is important for the model to be able to distinguish among hill shapes and the structure of the incident flow in calculating the flow deformation caused by the hill. The results reported in Section 3.2 are encouraging in that streamline heights observed over the crest of HBR tend to follow theoretical expectations. Additional aspects of developing the theory for flow over two- and three-dimensional hills are discussed in 6.1.

In Section 6.2, a connection is made between the terrain factor for σ_z contained in CTDM and the theory of thin plumes embedded in a deformed flow presented by Hunt and Mulhearn (1973). A modification to how the average diffusivity is calculated over the hill allows the CTDM calculation to simulate the results of the theory.

A discussion of how CTDM, or the basic concepts of CTDM, can be transferred to other sites is contained in Section 6.3. This discussion explores several topics raised in contemplating the eventual use of CTDM in the air quality permitting process.

6.1 Stratified Airflow over a Three-Dimensional Hill

Hunt and Richards (1984) describe a quite general approach for approximating the flow over arbitrary three-dimensional hills in terms of multi-layered flows in the neutral, $s \equiv NL/u << 1$, and strongly stratified, $s >> 1$, limits. Their results are generally presented in the form of various convolution integrals over the hill shape function or its derivative; but these integrals can be quite difficult to evaluate for hill shapes other than the inverse polynomial hill. On the other hand, Smith (1980) keeps the integrals in their Fourier representations and presents approximate, closed-form results for flow near the surface for a symmetric inverse polynomial hill. In this section a somewhat intermediate path is taken and results are developed for an arbitrary hill shape and evaluated for the asymmetric inverse polynomial hill as well as the bivariate Gaussian hill shape function

$$h(x,y) = h \exp[-\frac{1}{2}[(x/\sigma_x)^2 + (y/\sigma_y)^2]] \qquad (114)$$

where the hill sigmas are related to the more conventional half-widths at half maximum by

$$L = \sigma(2\ell n2)^{1/2} \simeq 1.18\ \sigma \quad . \tag{115}$$

Paralleling the development in Subsection 3.2.2 one can write the solution for the vertical displacement, $\delta(x,y,z)$, as

$$\delta(x,y,z) = \mathrm{Re}\left(\frac{1}{2\pi}\right)^2 \int dk \int d\ell \int dx' \int dy' h(x',y') e^{imz'} \cdot e^{ik(x-x') + i\ell(y-y')}, \tag{116}$$

where Re denotes the real part, k, ℓ are the x, y wave numbers, respectively, $z' = z - h(x,y)$, all integrals are over the domain $-\infty$ to $+\infty$ unless otherwise noted, and

$$m^2 = \left(\frac{k^2 + \ell^2}{k^2}\right)\left(\frac{N^2}{u^2} - k^2\right) \quad . \tag{117}$$

All of the physics are contained in the definition of m and yet its simplification is required if Eq. (116) is to be evaluated easily and without numerical quadrature (e.g., FFT) routines. No single approximation to Eq. (117) can cover the full range of ℓ, k, and N/u of relevance but

$$m \simeq m' + ik + i|\ell| \quad , \tag{118}$$

where $m' = (1 + L_x^2/L_y^2)^{1/2}(N/u)$

has attractive properties that include

- recovery of the 2-d form (i.e, as $\ell \to 0$, $L_y \to \infty$) that provided reasonable results for HBR lidar measurements in Subsection 3.2.2,
- reasonable approximation of the integrand maximum corresponding to $\ell/k = L_x/L_y$, and
- the ability to evaluate Eq. (116).

It is also worth noting that the errors incurred in the imaginary part of m are not so critical because the limit $z' \to 0$ will be invoked for this part. Inserting (118) into (116) gives rise to two integral expressions that have simple results in the limit of $z' \to 0$. These are

$$\frac{1}{2\pi} \int dk\ e^{-kz' + ik(x-x')} = \Delta(x-x') + \frac{i}{\pi}\frac{1}{x-x'} \tag{119}$$

and $$\frac{1}{2\pi} \int d\ell\ e^{-|\ell|z' + i\ell(y-y')} = \Delta(y-y') \tag{120}$$

where $\Delta(x-x')$ is the Dirac delta function and the absence of an imaginary term in (120) is due to the presence of the absolute value $|\ell|$ as contrasted with the k term in Eq. (119). Inserting these results back into (116) and performing the remaining y' and x' integrations yields

$$\delta(x,y,z) = \text{Re } e^{im'z'}[h(x,y) + J(x,y)] \tag{121}$$

where J(x,y) is the principal value of an integral that can be expressed alternatively as

$$J(x,y) = \frac{i}{\pi} \int \frac{dx'h(x',y)}{x-x'} \quad , \tag{122a}$$

$$= \frac{-2ix}{\pi} \int_0^\infty \frac{dx'h(x',y)}{(x'-x)(x'+x)} \quad , \tag{122b}$$

or

$$= \frac{i}{\pi} \int_0^\infty \frac{dx'}{x'} [h(x-x',y) - h(x+x',y)] \quad . \tag{122c}$$

The latter form is suggestive of the derivative of the hill shape function term of Hunt et al. (1981). Selection of the particular form of Eq. (122) depends mostly on the assumed form of h(x,y). For example, the case of the asymmetric 3-d inverse polynomial hill,

$$h(x,y) = \frac{h}{1 + x^2/L_x^2 + y^2/L_y^2} \quad , \tag{123}$$

yields

$$J(x,y) = i(x/L_x)h(x,y)/(1 + y^2/L_y^2)^{1/2} \tag{124}$$

after evaluation of either Eq. (122a) or (122b) by contour integration. It is also encouraging to note that the limit $L_y \to \infty$ gives back the 2-d ridge, and (124) combined with (123) gives back Eq. (18): the original Queney (1947) result. This result also shows that Eq. (121) is correct in the limit $z'/L_x << 1$ and that correction factors of order (1 + z'/L) could be used to extend the usefulness of Eq. (121) to larger z'; however, this is not a critical point since the principal interest is in narrow plumes approaching close to the hill so that z' << L. The final form for the vertical deflection for the 3-d inverse polynomial hill is

$$\delta(x,y,z) = h(x,y)[\cos m'z' - \frac{(x/L_x)}{(1+y^2/L_y^2)^{1/2}} \sin m'z'] \tag{125}$$

where h(x,y) is given by Eq. (123) and m' is defined by Eq. (118).

The bivariate Gaussian hill function given by Eq. (114) is more readily evaluated using (122c) and conventional integration techniques since the integrand is not well behaved at large imaginary values of x'. After some algebraic manipulation one obtains

$$\begin{aligned} J(x,y) &= \frac{i}{\pi} h(x,y)\ 2 \int_0^\infty \frac{dx'}{x'} e^{-\frac{1}{2}(x'/\sigma_x)^2} \sinh(xx'/\sigma_x^2) \\ &= i(2/\pi)^{1/2} h(x,y)(x/\sigma_x) M(\tfrac{1}{2},\tfrac{3}{2},\tfrac{1}{2}(x/\sigma_x)^2) \\ &\simeq i(2/\pi)^{1/2} h(x,y)(x/\sigma_x) \end{aligned} \qquad (126)$$

where M is a Kummer function that is then approximated to lowest order in x/σ_x. As with the inverse polynomial hill, this result can be easily combined with Eq. (121) to yield a complete description of $\delta(x,y,z)$.

Once the vertical deflections are available, the z' integration necessary to obtain the pressure fluctuation, p', is obtained as

$$p'(x,y,z) = -g\frac{d\rho}{dz} \cdot \mathrm{Re}\frac{i}{m'} e^{im'z'} [h(x,y) + J(x,y)] \quad , \qquad (127)$$

where $\rho(z)$ is the unperturbed density profile. As discussed in Smith (1980), this then immediately yields the downstream velocity perturbation, u', as

$$u' = -p'/(\rho_0 u) \quad . \qquad (128)$$

Computation of lateral velocities and displacements are somewhat more difficult as successive integrations in the x direction are required; however, these are not expected to present major problems. This then provides a complete description of the plume centerline path (or any other streamline) in stratified flow. The secondary effects of speed shear with height are then factored in as described in Subsection 3.2.2. Arbitrary wind directions may be handled by a rotation of the hill shape function and a slight redefinition of m'. In addition, an inner boundary layer may be added by displacing the hill shape function by the desired amount.

6.2 Connection between the Hunt and Mulhearn (1973) Approach and CTDM

In CTDM, the distortion in the flow over a hill and the response of the diffusion process to that distortion are treated consecutively to simplify the computation. The mean distortion in the flow along the path to a particular receptor is specified, and then the diffusion of plume material in that altered flow takes place with an altered

mean diffusivity. Physically, the plume growth is altered locally at each position along the path, and can be approximated by a line integral (along the trajectory) involving the diffusivity and the local straining of the flow (Hunt and Mulhearn 1973). The CTDM approach can give results more like the line integral by altering the way the mean diffusivity is calculated.

The streamline height above the ground is denoted by η, where

$$\eta(z,t) = z + \delta_z(z,t) - Hf(t) \quad . \tag{129}$$

The vertical deflection of the plume streamline is δ_z, H is the height of the hill, and f(t) is the shape of the hill along the wind direction. Note that the distance coordinate "x" has been transformed into a time-of-travel, t, and that z denotes the elevation of the streamline far upwind of the hill. Also note that far upwind of the hill, $f(t) = 0$, and $\delta_z(z,t) = 0$, so that the spacing between streamlines in the vertical is a constant:

$$\frac{\partial \eta}{\partial z} = 1$$

The key parameter in the vertical distribution factor in the Gaussian plume equation is the ratio of the plume centerline height above the ground to the spread of the plume in the vertical. Denote this ratio as R. For low-slope hills in the limit that the travel-time is greater than the Lagrangian time-scale (T_L), R can be written as:

$$R^2 = \frac{\eta^2(z_c,\, t)}{\left(\frac{\partial h\,(z,t)}{\partial z}\Big|_{z_c}\right)^2 \int_0^{t_2} \frac{K(t')\,dt'}{\left(\frac{\partial \eta\,(z,t)}{\partial z}\Big|_{z_c}\right)^2}} \tag{130}$$

where t is the travel time, z_c is the initial height of the plume upwind of the terrain, and K is the diffusivity. If we take the straining of the flow ($\partial\eta/\partial z$) to be constant with height, as does Hunt and Mulhearn (1973), but equal to its average value between the plume centerline and the surface rather than its value at plume centerline height, then the streamline height above the surface is approximated by

$$\eta(z,t) = z\,\overline{\frac{\partial h(t)}{\partial z}} \tag{131}$$

so that

$$R^2 = \frac{z_c^2}{\int_o^t \frac{2K(t')\,dt'}{(\overline{\frac{\partial \eta\,(t')}{\partial z}})^2}} \tag{132}$$

Assume that the initial time-of-travel "t_o" takes place before the hill has a significant influence on the flow. Then

$$\int_o^{t_o} \frac{2K(t')dt}{(\overline{\frac{\partial \eta(t')}{\partial z}})^2} = \int_o^{t_o} 2K_F(t')dt' = \sigma_z^2\,(t_o) \tag{133}$$

where K_F is the diffusivity in the absence of the hill. This allows R to be rewritten as

$$R^2 = \frac{z_c^2}{\sigma_z^2\,(t_o) + \int_{t_o}^t \frac{2K(t')\,dt'}{(\overline{\frac{\partial n(t')}{\partial z}})^2}} \tag{134}$$

The mean rate-of-strain for the layer of air between the surface and the centerline of the plume is denoted in CTDM by

$$T_h\,(z_c,t) = \overline{\frac{\partial n(t)}{\partial z}} \tag{135}$$

That is, the height of the streamline over the hill is related to its initial height upwind of the hill by T_h:

$$\eta\,(z_c,t) = z_c\,T_h\,(z_c,t) \tag{136}$$

In this notation, R^2 becomes

$$R^2 = \frac{z_c^2}{\sigma_z^2\,(t_o) + \int_{t_o}^t \frac{2K(t')\,dt'}{T_h^2\,(z_c,t')}} \tag{137}$$

The ratio R is given in CTDM as

$$R^2 = (\frac{z_c}{\sigma_{zc}})^2 = \frac{z_c^2}{\sigma_z^2\,(t_o) + (\frac{\sigma_z}{T_h})^2 \int_{t_o}^t 2K_F(t')dt'} \tag{138}$$

This equation approximates the diffusion process in the interval $(t-t_o)$ with a mean diffusivity factor $\overline{T}_{\sigma z}$ and a mean strain factor T_h.

Therefore, the two approaches are consistent if

$$\left(\frac{\overline{T}_{\sigma z}}{\overline{T}_h}\right)^2 = \int_{t_o}^{t} \frac{2K(t')dt'}{T_h^2(z_c,t)} + \int_{t_o}^{t} 2K_F(t')\,dt' \qquad (139)$$

Because Equation (130) is valid for $t >> T_L$, K_F is independent of t in the interval $t-t_o$ so that

$$\int_{t_o}^{t} 2K_F(t')\,dt' = (t-t_o)\,2K_F \qquad (140)$$

If we assume that the time dependence of $T_h(z_c,t)$ is contained in a function $\phi(t)$ so that

$$T_h(z_c, t) \equiv \phi(t)\,\overline{T}_h \qquad (141)$$

then

$$T_{\sigma z}^2 = \frac{1}{K_F} \int_{t_o}^{t} \frac{K(t')\,dt'}{\phi^2(t')} = \frac{\overline{K/\phi^2}}{K_F} \qquad (142)$$

Therefore, the factor $\overline{T}_{\sigma z}$ is related to a weighted average of the diffusivity over the interval $(t-t_o)$, where the weighting function is essentially the square of the amount of straining in the flow. The spatial distribution of the straining of the flow can be obtained from the analysis presented in 6.1.

An interesting situation arises when the diffusivity is very small. Mixing of plume material across streamlines towards the hill surface proceeds at a slow pace even in the presence of hill-induced distortion. Consequently, the effect of the hill on ground-level pollutant concentrations appears minimal if the plume is far enough above H_c (i.e., no impingement potential). However, a new inner boundary develops over the surface of the hill at elevations above H_c and if this layer extends high enough to intercept plume material, pollutant concentrations at the surface can increase markedly. Under these circumstances, the speed-up of the flow is important in establishing the depth of this new inner layer, and the elevation of the plume above the surface in the deformed flow is important in determining how much plume material can be mixed through the inner layer to the surface.

This type of terrain effect is not included in applications of the Hunt and Mulhearn theory, and it is not included in CTDM. However, because of the importance of the elevation of the plume in the deformed flow relative to the depth of the inner layer, the effect might be viewed as a plume-height correction analogous to the terrain correction factor or partial height factor contained in simpler models. Specification of the inner layer depth is being pursued so that this concept can be included in CTDM and tested.

6.3 Applicability of CTDM to Other Sites

A fundamental objective of the CTMD project has been to develop a model which, to the largest extent possible, would be applicable to a variety of terrain settings where direct impaction of a plume during stable atmospheric conditions could be expected. The best way to accomplish this objective is to simulate correctly the dominant physical processes involved in the transport and diffusion algorithms. The overall CTMD project design, which called for field experiments at three different topographic settings, including one at a "full scale" power plant location, emphasized the importance of obtaining a physical understanding of the phenomena of importance by observing plume behavior at different scales and different topography. The heavy reliance of the CTMD project on the use of physical modeling results is a further manifestation of the concept that properly scaled and interpreted results from small scale experiments can be used to provide insight on the importance of and effects of specific physical variables. At this point, we have a clearer understanding of the similarities and differences of flow behavior observed at small and large physical scales and at the different topographic settings. It is therefore appropriate to comment on these findings and how they are related to the applicability of CTDM to more general locations. It should be stated, however, that while every effort, within the constraints of the project, has been made to develop a generalized model, the diversity of the topography near existing or anticipated emission sources is large and, generally, one should expect some degradation of the reliability of the model predictions as one applies CTDM to very different settings.

In the discussion that follows, we will identify different physical phenomena that affect the generality of CTDM and provide some guidance on the proper interpretation of this knowledge to future applications of CTDM.

6.3.1 Dividing Streamline Height

One of the more important findings of the work performed to date from the physical modeling and field studies is the general applicability of the method for estimating H_c, the dividing streamline height. Snyder et al. (1985) provide a comprehensive and up-to-date documentation of these findings, including discussions of cases and circumstances where some modifications of the approach have been suggested.

Towing tank experiments with a model of CCB showed good agreement of dividing streamline heights normalized by hill height with the '1-Fr' rule. Experiments with truncated triangular ridges showed agreement for Fr < .25 but deviation from the rule for greater values of Fr. This deviation was associated with the formation of an upwind vortex which produced a downflow on the front face of the ridge. The experiments confirmed, however, that the dividing streamline height was independent of the width of the hill. Other experiments with truncated sinusoidal ridges at various angles to the mean flow provide further substantiation of the '1-Fr' rule for angles of 60° and 90° to the ridge axis. At a 30° angle, the streamline followed a '1-.7 Fr' relationship -- indicating that a path of lower potential energy was found. This is consistent with the notion that the kinetic energy of a parcel provides a necessary but not sufficient basis for predicting that the parcel will travel up and over a terrain obstacle. In this sense the dividing streamline height calculated from the integral energy equation provides a lower limit to the actual dividing streamlines.

As discussed elsewhere the use of the dividing streamline height to define flow patterns has been important to the understanding of flow at CCB, HBR, and at the Tracy power plant. Other investigators (Rowe et al., 1982 and Ryan et al., 1984) have confirmed the applicability of the concept to large scale settings. Because it is applicable to a range of physical scales, the dividing streamline concept is one of the cornerstones of the general applicability of CTDM.

6.3.2 Terrain Correction Factors

Previous sections of this report have addressed the formulation of T-factors that characterize turbulence changes and flow distortion as a function of the three-dimensional geometry of terrain objects and characteristics of the incident flow. The development of these formulations has been based on physical concepts which should be, and which appear to be, valid for a range of topographic shapes and scales. Whereas terrain correction factors commonly used in today's models are arbitrary (e.g., 10 meters in the Valley model) or oversimplifications (e.g, the half-height concept), the CTDM formulations represent factors which will adjust the various parameters in a manner consistent with our knowledge of the physical processes.

We believe that further work will be required to specify corrections to the streamline heights, dispersion coefficients, etc. associated with multiple hill interactions. For example, the present formulations cannot be expected to give good results in predicting the peak concentration on the front side of a hill downwind of another hill unless the plume-terrain interaction for the first hill is weak. More generally, the sensitivity of the peak predicted concentrations as a function of specific variations of the topographic descriptors needs to be explored mathematically and with comparisons to other applicable data sets.

6.3.3 Effects of Upwind Terrain

Both the CCB and HBR experimental sites were selected because of the existence of relatively flat fetches upwind of the primary terrain obstacles. It was desirable to study the impingement phenomena without the complications expected from the effects of upwind terrain obstacles. On the other hand, at Tracy, the surrounding topography undoubtedly affected the approach flow to the various terrain features. It is our view that the effect of upwind terrain is primarily to (1) affect the horizontal dispersion rates through the formation of large eddies which subsequently break up in the approach flow; and (2) creation of lee waves under stable conditions which affect the vertical motion of the plumes. The magnitude of these effects is very much site specific -- depending upon the shapes, relative heights, and complexity of the surrounding terrain. For this reason site specific meteorological measurements are the best way to quantify their influence on dispersion rates. The first effect, on horizontal dispersion, can be estimated from wind fluctuation data just upwind of the source. Such measurements can be directly input to CTDM and the model calculations will be altered in accordance with the magnitude of the crosswind dispersion.

How to treat the second effect, the formation of waves, needs further analyses. Vertically oriented anemometers cannot distinguish between wave motion and turbulent motions. The wave motions, of course, have a finite effect on the vertical displacements possible of fluid parcels while the turbulent motions result in continuous diffusion. While spectral analysis of the vertical wind fluctuation data could presumably allow some separation of wave effects from turbulence effects, it is not clear that this will resolve the issues. For example, the wave motions will induce vertical motion of an elevated plume on a hillside where impingement is taking place. This will, in effect, leave the signature of a plume with greater vertical dimensions than would be implied from "snapshot" views or by eliminating the wave motions from the turbulence data. However, the effect of these motions on time-averaged concentrations will not be as large as would be implied if the contribution of the waves were treated as turbulence. Whether spectral analysis should be applied may depend upon the amplitude of the wave motions encountered. If their amplitude is large in comparison to the characteristic scale of the plume resulting from buoyancy induced dispersion, and/or the ambient turbulence, such analysis will probably be desirable. This is a technical area which will receive further study this year through analysis of the Tracy data set. The results will provide further information on the magnitude of wave effects and on the need to make adjustments to turbulence data for dispersion model use.

6.3.4 Importance of Drainage Flows

An issue raised in the early design of the CTMD project (Hovind et al., 1979) was the importance of drainage flows in full scale topographic settings. There are two aspects to this issue. First of all is the question of whether stable air flow in mountainous areas will commonly carry an elevated plume toward high terrain. Because

drainage winds are shallow compared to terrain heights in many areas and because such flows will prefer to pass around the sides of a terrain obstacle rather than to climb up the surface, the question of whether stable plume impingement occurs in reality is a valid one. The way to address this issue definitively for any location is through direct observation of the local flows either through wind measurements or flow visualization. At the Tracy power plant, drainage flows, which had origins in the Sierras to the west, clearly were sufficiently deep to dominate the approach flow to Beacon Hill and Target Mountain. Similarly, at CCB and HBR, large scale drainage flows created relatively predictable deep and stable winds toward the terrain objects. Of course, this was an important aspect of these areas which made them attractive experimental sites. In fact, this was the principal reason why they were selected. There are settings (narrow canyons or valleys) where systematic flow toward the high terrain (sidewalls) is not expected. Meteorological measurements at these settings will probably indicate frequent up-down valley flows and rare cross valley flows.

The second aspect of the drainage flow issue is what the effect of very local drainage flows, induced by the immediately encountered terrain, will have on plume trajectories and dispersion. McNider and Arritt (1984) have outlined some concerns on the transferability of the dividing streamline concept to large scale topography because of the increased importance of drainage winds. They argue that if a terrain feature protrudes above the nocturnal surface inversion, drainage winds will develop more strongly because the temperature gradient will not suppress the formation of the drainage flow. Independent of that effect, large features will develop deeper drainage flows. From some numerical simulations of a two-dimensional terrain feature, McNider and Arritt postulate that the drainage flow from a 1,000 m high hill extended to 250 m in depth. While we feel that the influence would be much smaller for three-dimensional features (the drainage flow will be shallower for a three-dimensional feature), this is clearly an area for further investigation with the Tracy data.

The influence of such local drainage flows on concentration patterns observed at CCB and HBR is minimal. These "small hills" are not tall enough to generate deep slope flows, although very shallow slope flows at low elevation on these hills were occasionally observed. Near terrain of greater relief, one would expect drainage flows to exert a greater influence on the distribution of plume material, and this was observed at Tracy. However, the effect of drainage flows, or slope flows, on the peak observed concentrations at Tracy does not appear to be important. For concentrations averaged over an hour, peak values are characteristically found near plume elevation. However, some tracer material from the location of the higher concentrations is apparently carried downslope and produces nonzero concentrations at lower elevations. These concentrations are typically much less than those at plume elevation. The significance of these concentrations might increase with averaging time, and it would be interesting to look at available 3-hour averages of the observed tracer concentrations to see if this is so.

SECTION 7

SUMMARY, CONCLUSIONS, AND RECOMMENDATIONS FOR FURTHER STUDY

This Fifth Milestone Report describes in detail the FSPS that was performed in August 1984 at the Tracy Power Plant. The FSPS produced a 128-hour data base of SF_6 and CF_3Br concentrations, ground-based and airborne lidar data, photographs, 8-mm movies, videotapes, and extensive meteorological measurements. This report describes the final refinement of the HBR meteorological data base. It also presents a variety of data analyses that were performed in support of the model development. The highest ground-level tracer concentrations measured at the CCB, HBR, and FSPS sites are discussed.

The further development of CTDM is described. Mathematical descriptions of the modifications to the model are presented. The latest version of the model has been tested using a subset of impingement hours from the CCB, HBR, and FSPS data bases. The initial 14-hour FSPS data base was also used to test four existing complex terrain models -- COMPLEX I and II, Valley, and RTDM.

7.1 Principal Accomplishments and Conclusions

Refinement of the HBR Meteorological Data Base

The refinement of the meteorological data collected during SHIS #2 is now complete. The refinement process involved the filtering and flagging of the raw 1-sec counts data to reduce the effects of noise on the calculated measurements. Corrections were also made on the basis of the audit results and the cosine response characteristics of the fixed propeller anemometers. Five-minute and one-hour averaged values of meteorological measures were calculated from the corrected and flagged 1-sec data. The success of the refinement efforts is demonstrated by the improvement in consistency between collocated measurements.

An overall assessment of the quality of the HBR meteorological (and tracer gas) data base can be found in the Quality Assurance Project Report (Greene 1985). It presents estimates of the precision and accuracy of all the measurements. The bottom line of this assessment is that the data from Experiments 10 through 15 are

completely useful for modeling purposes. The data from the other experiments are still somewhat noisy, especially the turbulence data from Experiments 4, 5, and 6. The HBR data base is available from the EPA Project Officer.

HBR Streamline Analysis

Lidar data collected at HBR have been used to compare streamline heights upwind and over the crest of HBR to calculations from potential flow theory and from a linearized perturbation analysis. The comparisons suggest that for releases above H_c at HBR a substantial portion of the streamline deflection near the crest can be explained by potential flow of the air above H_c over a cylinder. This approach assumes the terrain is "cut-off" below H_c. The perturbation analysis shows some improvement in the simulation of the streamline height when stratification is included in the calculations.

Representativeness of Stable Boundary Layer Similarity Theory

Modeling the dispersion of an elevated plume requires meteorological data representative of plume height. Since this information is not always available, it is useful to consider if near-surface measurements can be used to infer information at plume elevations. This issue was addressed by using stable boundary layer similarity relationships to predict wind and temperature data at 40 m and 150 m from data obtained at 10 m and 2 m. The predictions were compared to measurements taken at CCB and HBR. The results indicate that the similarity relationships reproduce the observations fairly well to elevations less than about 10L. Above 10L the predictions have little reliability. Since L is typically a few meters during stable conditions, near-surface measurements will not be useful for estimating meteorological conditions above, say, 50 m. Most major sources generate plumes whose equilibrium heights are well above 50 m. Therefore, proper modeling of these sources will require meteorological data collected on tall towers or via acoustic sodar.

Strimaitis et al. (1984) demonstrated that the performance of CTDM deteriorates when the model input data were constructed from sparse data sets using near-surface measurements, rather than the wind and temperature profiles available from the 150-m tower. These model performance tests and the fact that the similarity relationships are useful to heights of less than 10L corroborate the need for onsite measurements of turbulence intensity near the release height and detailed vertical profiles of wind and temperature.

Investigations of Vertical Plume Growth

CTDM uses the expression:

$$\sigma_z = \frac{\sigma_w t}{(1 + \frac{t}{2T_L})^{0.5}}$$

to simulate the vertical diffusion of an elevated plume. Hourly-average lidar data from 14 FSPS impingement hours were used to perform an initial evaluation of the expression for σ_z. In particular, the evolution of σ_z after plume rise was investigated.

The initial growth (σ_{zb}) of the plume due to entrainment associated with its buoyant rise was estimated from the hourly-averaged lidar scan made in the vicinity of the stack, once the plume had leveled off. Typically, σ_{zb} was measured at a distance of 700 m from the stack. The lidar scans taken downwind of this distance were then used to evaluate the subsequent growth of σ_z.

The observed values of σ_z beyond σ_{zb} suggest that the model for T_L and σ_z overestimates the lidar estimates of vertical plume growth. This tendency of the observed plume growth to be overestimated could be the result of modeling T_L incorrectly, not screening out the wave contribution to σ_w, or not accounting for a collapse of the plume in the vertical after plume rise. None of these possibilities has been investigated in detail as yet.

An Analysis of the Highest Ground-Level Concentrations Observed at CCB, HBR, and the FSPS

The ten highest SF_6 and CF_3Br concentrations observed at CCB, HBR, and Tracy were presented in order to illustrate the associated meteorological conditions. The distributions of the tracer concentrations and the lidar and photographic data support the concept of a critical dividing streamline that separates stable air flow into two layers. At CCB the highest concentrations were observed most often when the tracer gas was emitted at an elevation near the calculated dividing streamline height. At the Hogback the highest concentrations were observed when the tracer gas was released below H_c. Evidently, at a long ridge setting like HBR, the flow below H_c is impeded by the ridge, thereby giving the tracer gas an opportunity to impinge on its windward side. At the isolated, three-dimensional CCB site the air flow below H_c is not constrained, but "escapes" by flowing around the sides of the hill, effectively dispersing the tracer gas. At both sites tracers released above H_c tended to flow over the terrain and the higher concentrations were produced near the top or on the lee side.

Initial analysis of the Tracy data base suggests the full-scale site exhibits dispersion characteristics similar to both small scale sites. The observed concentrations show that nine of the ten highest normalized concentrations occurred when the tracer gas was released below H_c. We have not yet analyzed the meteorological data to ascertain if the low-level flow at Tracy was blocked or constrained. For the hours with the ten highest SF_6 concentrations, five have estimates of the plume height. All five plume heights (or effective release heights) are near the calculated height of the dividing streamline.

The Complex Terrain Dispersion Model (CTDM)

The Fourth Milestone Report provides a detailed description of CTDM. Most of the basic structure of the model described therein has not been changed. The current version (12185) is considered a working version that has been and will continue to be revised before the initial submittal to EPA in October 1985. Over the last year the major revisions include:

- a generalization of the treatment of terrain so that now hills are simulated as ellipsoids;
- a reformulation of WRAP to simulate the effects of travel time on vertical plume growth; and
- changes to LIFT to simplify the treatment of the horizontal deflection of the plume, to include an estimate of how the turbulence changes over the hill, and to accommodate hills with horizontal cross-sections that are elliptical in shape.

Upcoming revisions to the model are also discussed in this milestone report.

The current version of CTDM has been tested using a subset of "impingement" hours from the CCB and HBR data bases and 13 hours from an initial 14-hour data set from the FSPS. A comparison of the modeled concentrations with the values observed at CCB suggests a reduction in the tendency of the model to overestimate the observed concentrations (see Table 7 in the Fourth Milestone Report). The model does reasonably well in simulating the HBR concentrations.

CTDM underestimates the concentrations measured during the FSPS although many (6 of 13) are within a factor of two. This tendency toward underprediction arises primarily from the size of the computed hourly values of σ_y and σ_z, and not from the impingement assumptions. An examination of 5-minute wind vectors for some of the hours suggests a PDF approach might improve the modeling of the FSPS.

The Semi-Empirical HBR Model

A simple plume model in which the horizontal distribution of tracer gas is determined by a probability distribution function (PDF) developed from wind direction observations, and in which wind speed is associated with wind direction as well, was applied to a subset of CF_3Br cases from HBR. With the vertical terrain correction factor described in the Fourth Milestone Report and the σ_z formulation from CTDM, this model simulated the observed concentrations reasonably well (i.e., $m_g \approx 1.0$ and $s_g < 2.0$).

Comparative Model Evaluations Using the 14-Hour FSPS Data Base

Valley, COMPLEX I and II, and RTDM were run using the 14-hour FSPS data set. CTDM was run for 13 of these hours in which the primary plume impact is on "Beacon Hill." Valley and COMPLEX II substantially overestimate the observed SF_6 concentrations.

The average top-two COMPLEX I concentrations are in fair agreement with the average top-two observed concentrations paired hourly. The average top-two residuals indicate that COMPLEX I overpredicts for 11 of the case-hours. The ratio of the maximum observed to predicted concentrations indicate that 10 of the case-hours lie within a factor of two.

RTDM was first run with the hourly values of the vertical and horizontal components of the turbulence intensity estimated at plume height to calculate σ_y and σ_z. The average top-two concentrations underpredict the observations for all case-hours. The ratio of the maximum observed to predicted concentrations indicate that none of the case-hours lie within a factor of two.

RTDM was then tested with its default Briggs rural (ASME, 1979) dispersion coefficients. The top-two average predicted concentrations are now much larger than those predicted from RTDM's algorithm that uses the measured turbulence data. The ratios of the maximum observed to predicted concentrations indicate that six of the case-hours now lie within a factor of two.

Again, CTDM was run using 13 hours of the initial FSPS data base. The averages of the highest two modeled concentrations for all but one of the hours underestimated the observations. Six of the modeled concentrations were within a factor of two of the observations.

7.2 Recommendations for Further Study

7.2.1 Data Analysis and Model Formulation

High priority will be given to expanding the analysis of the vertical growth of the Tracy plume because it is apparent that a proper specification of σ_z(and σ_y) is critical to modeling concentrations at Tracy. More hours, including a wider range of meteorological conditions, will be included. It is particularly important to provide as complete a description of the effects of waves, as possible. Data from the sonic anemometers will be particularly important in evaluating the model of Pearson et al. (1983) for this data set, and in attempting to identify wave-dominated events.

High priority will also be given to investigating the performance of a PDF formulation of CTDM. Such a formulation appears important for adequate simulation of some of the hours in the HBR dataset and may improve the ability to simulate the peak observed concentrations at Tracy. While formulating the PDF version of CTDM, we will learn more about the elements of the semi-empirical model that control its performance at HBR, and how these elements can be related to theory and incorporated in CTDM.

Of particular importance at Tracy are the issues of averaging time and time-of-travel from the stack to the terrain. A 1-hour averaging period for the concentration field may be too short a period for many important impingement events in which the time-of-travel to the impingement zone is nearly equal to or actually exceeds one hour. Long travel times must be treated carefully if a plume model is to be applied correctly. To assess this, impingement calculations will be made for various averaging periods and compared with the corresponding measured concentration averages. Various lag times for the meteorological data will also be included in the study, and comparisons with traditional averages of hourly Gaussian plume calculations will be made to investigate the significance of averaging and lag times for current regulatory modeling practice.

An algorithm for calculating the terrain effect factors for the LIFT portion of CTDM, based on the theory developed and described in this report, will be formulated and implemented. Included in this algorithm will be the effects of streamline displacement, flow deformation, changes in turbulence, and an inner boundary layer over the top of the hill, on the evolution of the plume, and on the resulting concentration of plume material at the surface of the hill. Once implemented, the algorithm will be tested for its sensitivity to hill shape and the structure of the approach flow.

Work will be performed on the problem of how to "decompose" an array of hills into hill segments that will reflect the degree of flow deformation expected in the neighborhood of each receptor in a model application. This will aid in the generalization of CTDM and its transferability to arbitrary terrain settings.

The algorithm in LIFT that provides a transition region between the LIFT and WRAP portions of the code will be modified to reflect the towing tank data obtained at the EPA FMF, and reported in the Appendix. Essentially, the issue to be addressed is how quickly the steering tendency of the terrain below H_c is reduced above H_c.

The WRAP model requires further scrutiny. At present, its primary effect on concentrations at ground-level arises from its time-of-travel adjustments, and its "terrain steering" (i.e., the relationship between the mean streamline through the source and the stagnation streamline of the mean flow.) Each of these is quite dependent on the scale of the hill (or hills) in horizontal cross-section compared to the distance of the source from the hill, and the suitability of the notion of a steady, mean flow. At HBR, where the scale of the hill is much greater than the distance from the hill to the source, the model calculations appear to be too sensitive to the hill shape, and notions about a mean flow are at times inappropriate. At CCB, the degree of steering seems to be overestimated at times. Some of these problems may arise from how wind directions measured at towers near the hill are "adjusted" to obtain the wind direction "at infinity."

Once the modifications to the model are complete, CTDM will undergo a systematic series of sensitivity studies. These will help identify the conditions in which the terrain effects contained in CTDM have the greatest and least impact on the magnitude of the ground-level concentrations. The effects of uncertainties of the model input data on concentrations will also be analyzed. These will include direct input (wind speed, etc.), the various terrain parameters, and the location of the meteorological tower.

An analysis of the FSPS data will be undertaken to provide a description of the observed flow throughout the experiment area. The behavior of the visible plume from the Tracy stack and the corresponding tracer-gas concentrations measured at the ground will be characterized as a function of area-wide meteorological measurements. This analysis will serve to identify the roles of the upper-level flow and the local drainage flow in determining the character of the flow and turbulence in the valley.

7.2.2 Development of FSPS Meteorological Data Base

Because the height of the SF_6/oil-fog plume at Tracy was often greater than 150 m, and because the flow in the Truckee Valley was sheared at these elevations in very stable conditions, meteorological data relevant to the plume will have to be derived for many periods from measurements made by tethersonde, Doppler sodar, and rabals. The tethersonde flown west of the power plant was apparently faulty, and little data are available from the east Doppler system as well, so the best sources of data above 150 m are the tethersonde flown near the tall tower and the west Doppler. Both of these systems can provide good estimates of wind speed and direction, but vertical turbulence estimates must come from the Doppler. The rabal data extend the vertical range of wind observations well above plume height on a quasi-instantaneous basis and will be most useful for evaluation of spatial variability within the valley. These considerations imply that the development of a Modeler's Data Archive for FSPS will be somewhat more complex than those for CCB and HBR.

The audit of the meteorological tower systems indicated that the quality of data from these instruments is excellent and no major noise problems have been discovered. The principal effort in the refinement of these data will be the correction of the averaged speeds and directions from UVW propellers for non-cosine response.

REFERENCES

American Society of Mechanical Engineers 1979. Recommended Guide for the Prediction of Airborne Effluents. M. Smith, New York, NY.

Batchelor, G.K. 1970. An Introduction to Fluid Dynamics. Cambridge University Press, London NW1, England.

Briggs, G.A. 1973. Diffusion Estimation for Small Emissions. ATDL Contribution File No. 79, Atmospheric Turbulence and Diffusion Laboratory.

Britter, R.E., J.C.R. Hunt, and K.J. Richards 1981. Airflow Over a Two-Dimensional Hill: Studies of Velocity Speed-up, Roughness Effects and Turbulence. Quart. J.R. Met. Soc., 107: 91-110.

Businger, J.A. 1973. Turbulent Transfer in the Atmospheric Surface Layer. In Workshop on Micrometeorology, AMS, Boston, 67-100.

Csanady, G.T. 1964. Turbulent Diffusion in a Stratified Fluid. J. Atmos. Sci., 21: 439-447.

Environmental Research and Technology, Inc. 1982. User's Guide to the Rough Terrain Diffusion Model (RTDM). ERT No. M2209-585, Environmental Research and Technology, Inc., Concord, MA, 225 pp.

Greene, B.R. 1985. Complex Terrain Model Development Quality Assurance Project for Small Hill Impaction Study No. 2. ERT No. P-B876-350.

Greene, B.R. and S. Heisler 1982. EPA CTMD Quality Assurance Project Report for SHIS #1. ERT #P-B348-350.

Holzworth, G.C. 1980. The EPA Program for Dispersion Model Development for Sources in Complex Terrain. Second Joint Conference on Applications of Air Pollution Meteorology, New Orleans, LA. AMS, Boston.

Horst, T.W., 1973. Corrections for Response Errors in a Three-Component Propeller Anemometer. J. Appl. Met., 12: 716-725.

Hovind, E.L., M.W. Edelstein, and V.C. Sutherland, 1979. Workshop on Atmospheric Dispersion Models in Complex Terrain. EPA-600/9-79-041. U.S. EPA. Research Triangle Park, N.C.

Hunt, J.C.R., and R.J. Mulhearn 1973. Turbulent Dispersion from Sources Near Two-Dimensional Obstacles. J. Fluid Mech., 61: 245-274.

Hunt, J.C.R., S. Leibovich, and J.L. Lumley 1981. Prediction Method for the Dispersal of Atmospheric Pollutant in Complex Terrain. Flow Analysis Associates. Report P85-81-04, Ithaca, NY, 14850.

Hunt, J.C.R. 1982. Diffusion in the Stable Boundary Layer. Chapt. 6 in Atmospheric Turbulence and Air Pollution Modelling. F.T.M. Nieuwstadt and H. von Dop, Eds., Reidel, Dordrecht, Holland.

Hunt, J.C.R. and K.J. Richards 1984. Stratified Airflow Over One or Two Hills. Boundary-Layer Met., 30: 223-259.

Hunt, J.C.R. 1985. Diffusion in the Stably Stratified Atmospheric Boundary Layer. J. Clim. Appl. Meteor. (to appear).

Lavery, T.F., A. Bass, D.G. Strimaitis, A. Venkatram, B.R. Greene, P.J. Drivas, and B.A. Egan, 1982. EPA Complex Terrain Model Development Program: First Milestone Report - 1981. EPA-600/3-82-036, U.S. Environmental Protection Agency, Research Triangle Park, NC.

Lavery, T.F., D.G. Strimaitis, A. Venkatram, B.R. Greene, D.C. DiCristofaro, and B.A. Egan, 1983. EPA Complex Terrain Model Development Program: Third Milestone Report - 1983. EPA-600/3-83-101, U.S. Environmental Protection Agency, Research Triangle Park, NC.

Lilly, D.K. and J.B. Klemp 1979. The Effect of Terrain Shape on Nonlinear Hydrostatic Mountain Waves. J. Fluid Mech., 95-2: 241-261.

Long, R.R. 1953. Some Aspects of the Flow of Stratified Fluids, I. A Theoretical Investigation. Tellus, 5: 42-57.

McNider, R.T. and R.W. Arritt 1984. Transferability of Critical Dividing-Streamline Models to Larger Scale Terrain. Conference Volume Fourth Joint Conf. on Applications of Air Pollution Meteorology. Oct. 16-19, Portland, OR. Amer. Meteor. Soc., Boston, MA.

Panofsky, H.A. and J.A. Dutton 1984. Atmospheric Turbulence. John Wiley and Sons, Inc., New York, NY.

Pasquill, F. 1976. Atmospheric Dispersion Parameters in Gaussian Plume Modeling: Part II. Possible Requirements for Change in the Turner Workbook Values. EPA-600/4-76-306, U.S. Environmental Protection Agency, Research Triangle Park, NC.

Pearson, H.J., J.S. Puttock, and J.C.R. Hunt 1983. A Statistical Model of Fluid-Element Motions and Vertical Diffusion in a Homogeneous Stratified Turbulent Flow. J. Fluid Mech., 129, 219-249.

Queney, P. 1947. Theory of Perturbations in Stratified Currents with Applications to Airflow Over Mountain Barriers. Dept. of Met., Univ. of Chicago Report No. 23, Univ. of Chicago Press. Also described in Dynamic Meteorology, P. Morel (ed.), D. Reidel Publishing Co., Boston, 622 pp., 1970.

Rowe, R.D., S.F. Benjamin, K.P. Chung, J.J. Harlena, and C.Z. Lee 1982. Field Studies of Stable Air Flow Over and Around a Ridge. Atmospheric Environment 16,643-653.

Ryan, W., B. Lamb, and E. Robinson, 1984. An Atmospheric Tracer Investgation of Transport and Diffusion around a Large Isolated Hill. Atmospheric Environment 18,2003-2021.

Scorer, R.S. 1949. Theory of Waves in the Lee of Mountains. Quart. J.R. Met. Soc., 75: 41-56. Also described in Environmental Aerodynamics, R.S. Scorer, Halsted Press, New York, 488 pp, 1978.

Sheppard, P.A. 1956. Airflow Over Mountains. Quart. J. R. Meteor. Soc., 82: 528-529.

Skibin D. and J.A. Businger 1985. The Vertical Extent of the Log-Linear Wind Profile Under Stable Stratification. Atm. Env., 19: 27-30.

Smith, R.B. 1980. Linear Theory of Stratified Hydrostatic Flow Past an Isolated Mountain. Tellus, 32: 348-364.

Snyder, W.H., R.S. Thompson, R.E. Eskridge, R.E. Lawson, I.P. Castro, J.T. Lee, J.C.R. Hunt, and Y. Ogawa 1985. The Structure of Strongly Stratified Flow Over Hills: Dividing-Streamline Concept. J. Fluid Mech., 152: 249-288.

Strimaitis, D.G., T.F. Lavery, A. Venkatram, D.C. DiCristofaro, B.R. Greene, and B.A. Egan, 1984. EPA Complex Terrain Model Development Program: Fourth Milestone Report - 1984. EPA-600/3-84-110, U.S. Environmental Protection Agency, Research Triangle Park, NC.

Strimaitis, D.G., A. Venkatram, B.R. Greene, S. Hanna, S. Heisler, T.F. Lavery, A. Bass, and B.A. Eagan, 1983. EPA Complex Terrain Model Development Program: Second Milestone Report - 1982. EPA-600/3-83-015, U.S. Environmental Protection Agency, Research Triangle Park, NC.

Stull, R.B. 1983. A Heat-Flux History Length Scale for the Nocturnal Boundary Layer. Tellus, 35A: 219-230.

Townsend, A.A. 1976: The Structure of Turbulent Shear Flow, Cambridge Univ. Press, Cambridge, England, p. 315.

van Ulden, A.P. and A.A.M. Holtslag 1985. Estimation of Atmospheric Boundary Layer Parameters for Diffusion Applications. J. Clim. Appl. Meteor. (to appear).

Venkatram, A., D. Strimaitis, and D. DiCristofaro 1984. A Semiempirical Model to Estimate Vertical Dispersion of Elevated Releases in the Stable Boundary Layer. Atmospheric Environment, 18: 923-928.

Webb, E.K. 1970. Profile Relationships: The Log-Linear Range, and Extension to Strong Stability. Quart. J. R. Met. Soc, 96: 67-90.

Williamson, H.J. and R.R. Krenmayer 1980. Analysis of the Relationship Between Turner's Stability Classifications and Wind Speed and Direct Measurements of Net Radiation. 2nd Joint Conference on Applications of Air Pollution Meteorology, March 24-27, AMS, Boston.

Wurtele, M. 1957. The Three Dimensional Lee Wave. Beitr. Phys. frei Atmos., 29: 242-252.

Yamada, T. 1979. Prediction of the Nocturnal Surface Inversion Height. J. Appl. Meteor., 18: 526-531.

Yamartino, R.J. 1984. A Comparison of Several "Single-Pass" Estimators of the Standard Deviation of Wind Direction. J. Climate and Appl. Met., 23:1362-1366.

APPENDIX

STREAMLINE TRAJECTORIES IN NEUTRAL AND STRATIFIED FLOW OVER A THREE-DIMENSIONAL HILL

Streamline Trajectories in Neutral and Stratified Flow Over a Three-Dimensional Hill

by

William H. Snyder*

Roger S. Thompson

Meteorology and Assessment Division
Atmospheric Sciences Research Laboratory
U.S. Environmental Protection Agency
Research Triangle Park, NC 27711

and

Michael S. Shipman
Northrop Services, Inc.
Research Triangle Park, NC 27709

May 1985

ATMOSPHERIC SCIENCES RESEARCH LABORATORY
OFFICE OF RESEARCH AND DEVELOPMENT
U.S. ENVIRONMENTAL PROTECTION AGENCY
RESEARCH TRIANGLE PARK, NC 27711

*On assignment from the National Oceanic and Atmospheric Administration, U.S. Department of Commerce

1. INTRODUCTION

In attempting to predict the maximum ground-level concentration from a source upwind of a hill, the most important feature of the flow is the displacement of the mean streamline through the source, because that displacement determines how near to the surface the centerline of the plume will reach. The exact path taken by the plume in circumventing the hill and the plume's closeness of approach to the hill surface are critical in determining the location and magnitude of the ground-level concentrations. These displacements are known to be strongly affected by the hill shape and by the stratification in the approach flow (Hunt et al., 1979; Hunt and Snyder, 1980; Snyder and Hunt, 1984; Snyder et al., 1985).

The purpose of the work described herein was to characterize the effects of stability on the horizontal and vertical deflections of streamlines around an isolated hill. A large set of streamline trajectories over an axisymmetric hill was measured using the stratified towing tank of the EPA Fluid Modeling Facility. Three-dimensional coordinates of the streamlines (86 independent trajectories) were determined through stereographic analysis of photographs of dye streak lines released at a matrix of source positions (heights and lateral offsets from the hill/flow centerline), and at stabilities ranging from strongly stable to neutral (Froude number of 0.6, 1.0, 2.0, and ∞). The general features of these measurements are presented, but the primary value lies in the fact that a relatively complete data set is available for testing mathematical models and algorithms of the detailed structure of stratified flow over hills. As an example use of the data set, a particular mathematical model using linear theory and a Fast Fourier Transform (FFT) technique to predict these streamline trajectories is evaluated.

Section 2 describes the experimental details and the photographic analysis technique. Example results are presented and discussed in Section 3, and a description and evaluation of the mathematical model are presented in Section 4. A data tape containing the coordinates of the trajectories is available from the authors upon request.

2. APPARATUS, INSTRUMENTATION AND TECHNIQUES

2.1 The Towing Tank

The EPA towing tank (1.2 m X 2.4 m X 25 m) is elevated approximately 3.5 m above the building floor. The walls and floor are made of clear acrylic plastic (2.54 and 3.17 cm thick respectively), providing maximum visual access. The model hill is mounted on a flat, square baseplate. This apparatus is turned upside down and suspended from a towing carriage so that the baseplate is submerged approximately 6 mm below the water surface. The apparatus is then towed the length of the tank. Further details may be obtained from Thompson and Snyder (1976).

Figure A-1 shows the arrangement of the model and cameras about the tank. The coordinate system originates at the hill base center. The longitudinal coordinate, x, increases downstream from the hill axis. The cross-stream coordinate, y, is measured from the hill centerline, positively toward the camera. The vertical coordinate, z, is taken to be positive downward from the baseplate level. Since the model is upside down, the depth z is directly interpreted as height in the atmosphere.

Mixing and distribution systems permit the tank to be filled with any desired shape of stable density profile. In these experiments, the maximum uniform density gradient was used--that is, the tank was initially filled with fresh water at the surface and saturated salt water at the bottom. The density profile tended to erode toward neutral at the surface and bottom of the tank because of the towing operations and molecular diffusion. In order to maintain the desired stratification in the vicinity of the hill, the neutral layer (nominally 3 cm) near the surface was "skimmed" off between tows, and the original level was restored by introducing an additional layer of saturated brine at the bottom of the tank. Thus, successive experiments had slightly different density profiles as an increasingly deep layer of nearly constant density fluid was accumulated at the bottom. This gradual change in the bottom boundary condition does not appear to significantly affect the study results, since the depth of the uniform gradient extended from the surface to at least four hill heights in elevation. When the depth of the neutral layer reached 40-50 cm, the tank was emptied and refilled. Figure A-2 shows the evolution of the density profile over a time period of 16 days and a series of 15 tows.

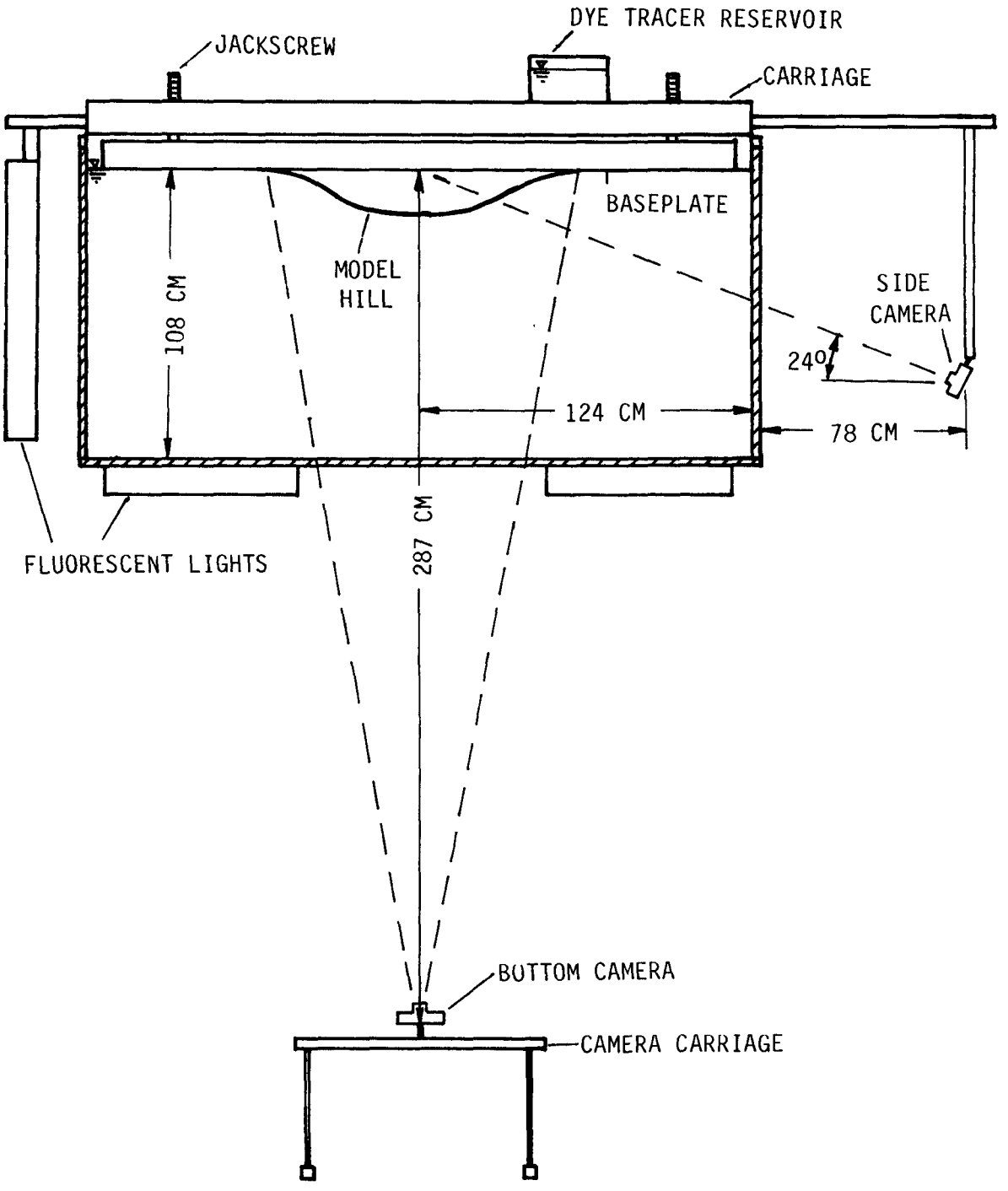

Figure A-1. Cross-section of the towing tank showing the arrangement of the model and cameras.

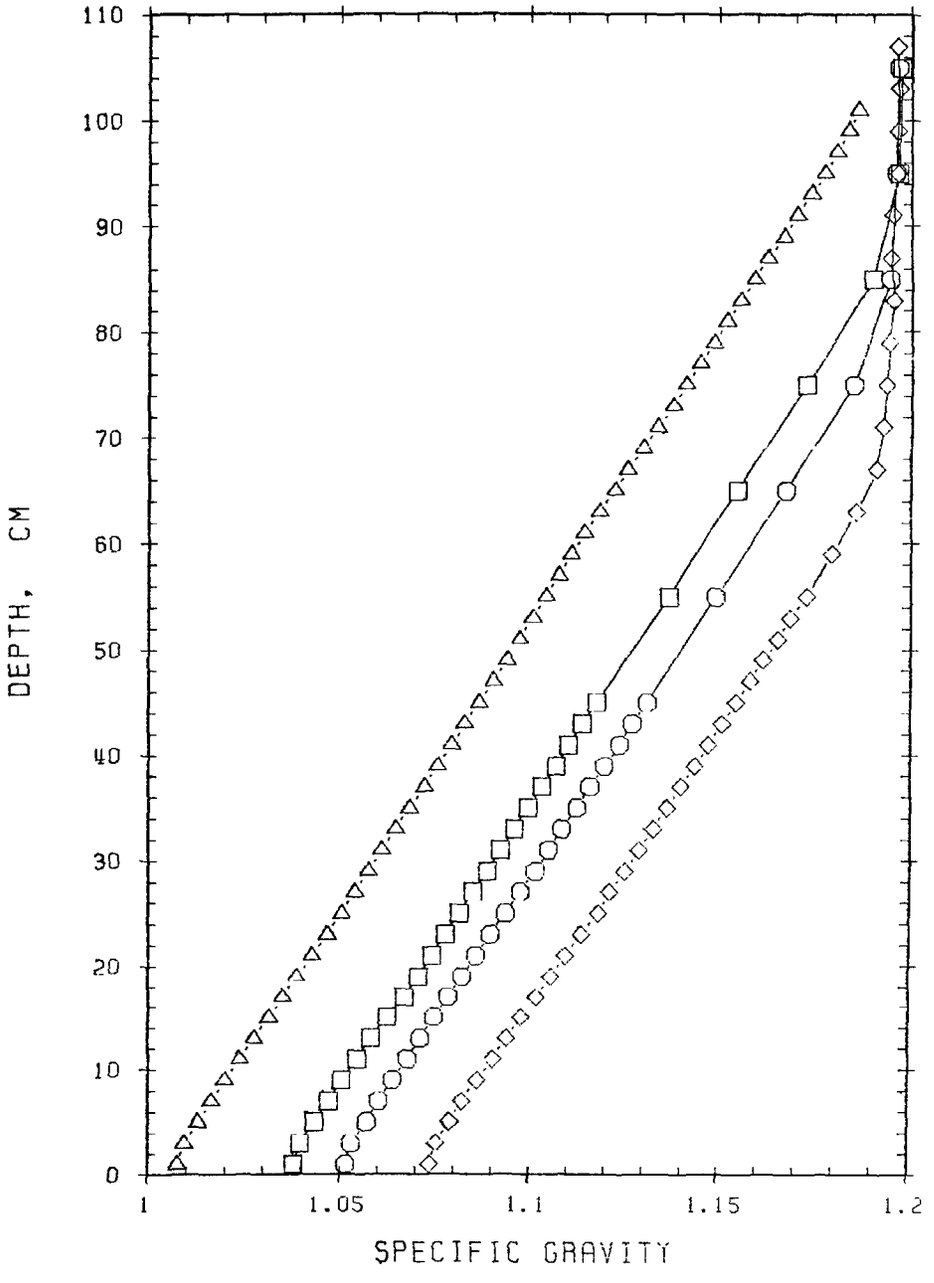

Figure A-2. Evolution of density profiles over the course of 16 days and 15 tows.

The tracer used in these experiments was a blue food dye diluted with sufficient salt water to produce a plume that was neutrally buoyant at the release height. This mixture was released from a bent-over stack located near the upstream edge of the baseplate (x = -7.5H, where H is the hill height). For these experiments, a narrow plume was desired, so that a thin tube (1.5 mm ID) was used for the stack and the dye mixture was emitted nearly isokinetically to form a streamtube.

2.2 The Model

The model used in this study was an idealized representation of Cinder Cone Butte in Idaho. The axisymmetric model shape is given by

$$h(r) = (H + c)/[1 + (r/L)^4] - c,$$

with H = 15.45 cm, L = 38.75 cm, and c = 0.97 cm. As shown in the figures, the model had a fairly flat top and a maximum slope of 0.45 or 24.4°. The model was mounted on the towing-tank baseplate such that the hill blended smoothly into the flat surface at a radius of 5H. Reference circles were painted on the model at various elevations to aid in the flow visualization.

Density profiles were measured before each tow. Water samples from various levels in the towing-tank were drawn into test tubes. The specific gravity of each sample was determined by the weight of a submerged object relative to its weight in fresh water. The resulting density profile was used to set the tow speed U to obtain the desired Froude number

$$Fr = U/(gH\Delta\rho/\rho)^{1/2},$$

where $\Delta\rho$ is the density difference between the base and top of the model hill and g is the gravitational acceleration.

The density profile was also used to specify how the refractive index varied with depth. For this purpose, the density profile, which was typically measured with a spacing of 2 cm down to 45 cm, and 10 cm spacing below 45 cm, was filled-in using interpolation techniques; a detailed profile of refractive index was derived from that. The refractive index ranged from 1.333 for fresh water to 1.378 for saturated brine.

2.3 Photographic Technique

The purpose of this section is to describe the technique developed to measure the three-dimensional plume trajectories (streaklines). Basically, the technique is an application of the common stereographic process in which two simultaneous photographs taken from different vantage points are combined to provide a three-dimensional representation. The plume centerlines on side- and bottom-view photographic prints were digitized and input to a PDP

11/44 minicomputer. In reconciling these disparate views, the computer algorithm accounted for parallax and refraction. Light rays were bent significantly by the salt water gradient in the tank and at the water-wall and wall-air interfaces.

Both side- and bottom-view cameras moved with the model as it was towed so that several photos were obtained during each tow. The side-view camera was hung from the towing carriage itself. It was held at the lowest practical level--looking obliquely upwards through the layers of salt water to avoid internal reflections. The bottom-view camera was mounted on a second carriage below the tank. This vertically facing camera was aligned with the model. The cameras were fired simultaneously by radio command. Both cameras were equipped with lenses with focal lengths of 43 mm and were operated at aperture settings of f/5.6.

2.4 Photographic Analysis

In the analysis of the photographs, the camera was treated as a point source/receptor of light rays which were traced through the walls of the tank and the layers of salt water. The photographic print is thought of as a screen between the virtual camera and the wall of the tank. Together, the virtual camera and a point in the photograph determine a light ray which can be projected into the tank to recover the actual location of the feature in question.

The location of the virtual-point camera must be determined. Also, the orientation angle of the side-view camera must be specified to greater precision than can be easily measured.

The side-view camera was aimed so that a reference mark on the wall of the tank was aligned with a hash mark on the model. The incident angle at the wall of the light ray passing through these two points was determined by a predictor-corrector method - given the density profile. This angle was taken as the vertical orientation of the camera. The line of sight of the side-view camera was assumed to be perfectly aligned in the $x = 0$ plane, and the bottom-view camera was taken to be directly below the hill center.

The location of the virtual-point camera was determined by a least-squares fitting technique. A grid (10 cm mesh) was photographed at five lateral positions with the tank ($y = -40, -20, 0, 20, 40$ cm). The actual positions of the grid intersections (473 points total) were compared to the positions projected from the photographs. Both the virtual-camera location and a scale factor (depending on the relative positions of the photograph and camera) were varied. The combination giving the best fit was determined. The virtual location of the side camera was found to be 199 cm from the centerline and the bottom camera was found to be 277 cm below the free surface. In comparison, the physical positions were 209 and 287 cm, respectively.

Generally, six pairs of photographs were taken during each tow. Depending upon the variability of the plume path, two, three, or four pairs were selected for processing. Photos from the first half of the tow were favored as they were believed to be more representative of the prescribed flow conditions (i.e., less influenced by the columnar-mode reflections from the upstream end-wall of the tank; see Snyder et al., 1985).

The centerline of the plume was estimated and marked on each 8 X 10 inch photographic print. Points along this line were digitized in addition to several reference points. Eight reference points were used for the side view--three on the model surface and five on 5 cm-long pointers spaced along the model centerline. Eleven reference points were available for the bottom view--all on the model surface--although often either the extreme upstream of downstream point was obscured by a support member.

Given the virtual position and orientation of the camera, the locations of reference points, and the density profile, the computer determined the paths of light rays to each of the reference points using a predictor-corrector method. By computing the points where these rays intersected an arbitrary plane (perpendicular to the line of sight of the camera), the positions at which the reference points were expected to appear on the photograph were determined--to within a constant scale factor. Figure A-3 illustrates this projection. The length and slope of line segments connecting reference points were calculated for the computed digitized sets. The scale factor required to project points in the photograph to the arbitrary plane was found by comparing these line lengths. This scale factor was computed separately for each photograph to allow for possible differences in the printing process. In a similar manner, a rotation angle and offset were found to correct for the orientation of the photograph on the digitizer board. The coordinates of the digitized plume centerline were transformed by this offset, rotation angle, and scale factor.

The result of this transformation was that coordinates from the photograph were properly oriented and projected to a known plane. Then a ray from the "point camera" through any point of interest on the photograph was traced as it passed through the water-channel walls and saltwater layers. The intersection of the rays from a point observed in both side- and bottom-view photographs is an estimate of the actual three-dimensional position of the feature.

Combining the two views of the plume centerline was a bit more complicated because the independently digitized curves were made up of different points. An interactive procedure was used, interpolating within both sets of points, to finally find rays that intersected at the same (x,y,z) coordinates. For convenience, interpolation was again used to find y and z values for a set of points spaced uniformly in x.

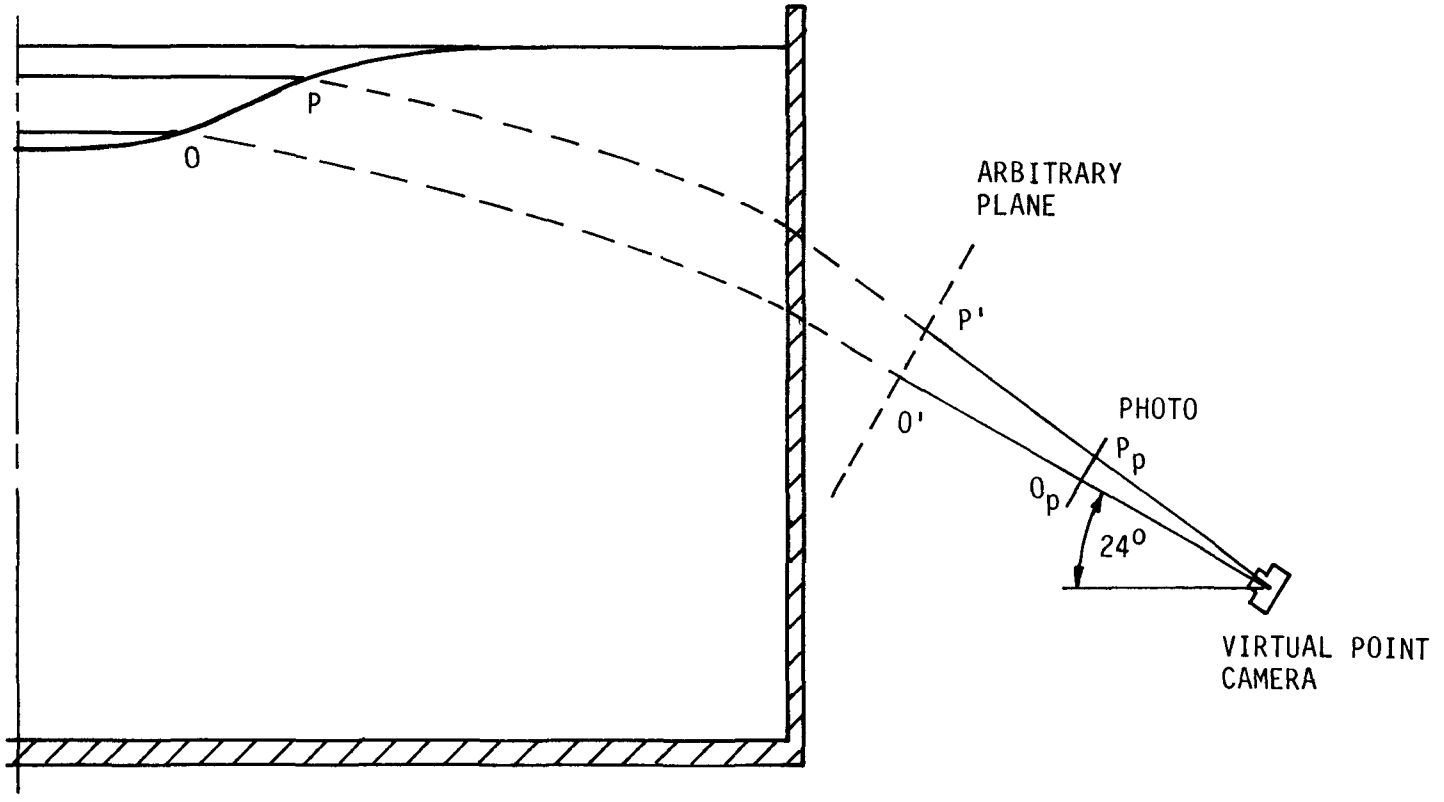

Figure A-3. Schematic representation showing the projection of reference points from the tank and from the photograph to an arbitrary plane for the side view camera.

The streamwise extent of the observed/computed streaklines was -60 to +60 cm (-4 to 4H), although the range was smaller for plumes with large lateral offsets, that is, closer to the camera.

In the most stable cases, the plume's behavior was observed to vary during the tow. Low stacks, just above the dividing-streamline height (Snyder et al., 1985), were especially sensitive to changes in flow conditions during the tow. Also, a few plumes in neutral conditions had some significant meanders (secondary flows in the tank due to wind tunnel operations and instabilities at the source are possible explanations for these deviations). In order to increase the representativeness and smoothness of the derived trajectories, several trajectories from a single tow were averaged together. Interpolation was used to obtain y and z values at specified x values. A simple independent average of the y and z values was used.

As a final step, the averaged trajectory was normalized by the hill height and expressed in several other coordinate systems. The parameters listed below were calculated and are listed in the data tape.

Horizontal radius	$R = (x^2 + y^2)^{1/2}$
Total deflection	$D = [(z - z_s)^2 + (y - y_s)^2]^{1/2}$
Deflection angle	$\phi = \tan^{-1} ((z - z_s)/(y - y_s))$
Horizontal distance to hill	$R - r(z)$
Vertical distance to hill	$z - h(x,y)$
Normal distance to hill surface	η

The maximum vertical ($z - z_s$) and lateral ($y - y_s$) deflections are reported along with the x location at which they occurred. The plume's closest approach to the hill surface (minimum η) was also estimated. Finally, the values of D, ϕ, and η at the side of the hill ($x = 0$) were evaluated. Figure A-4 illustrates the interpretation of several of these parameters.

2.5 Error Estimates

There are several sources of error in the photo analysis method used in this study. The geometric treatment using the concept of a "virtual-point camera" is questionable. The cameras were assumed to be perfectly aligned, and distortion inherent in the photographic processing was ignored. Numerically, a fit to derived coordinates of reference points was used to scale and orient digitized points. The use of a discrete density profile caused some discontinuity--an infinitesimal change in position at the side wall that moves a ray across a density interface causes a finite change in position near the model. The resolution of the digitizer was 0.01 inch, which translates to 0.2 cm in the towing tank (bottom view).

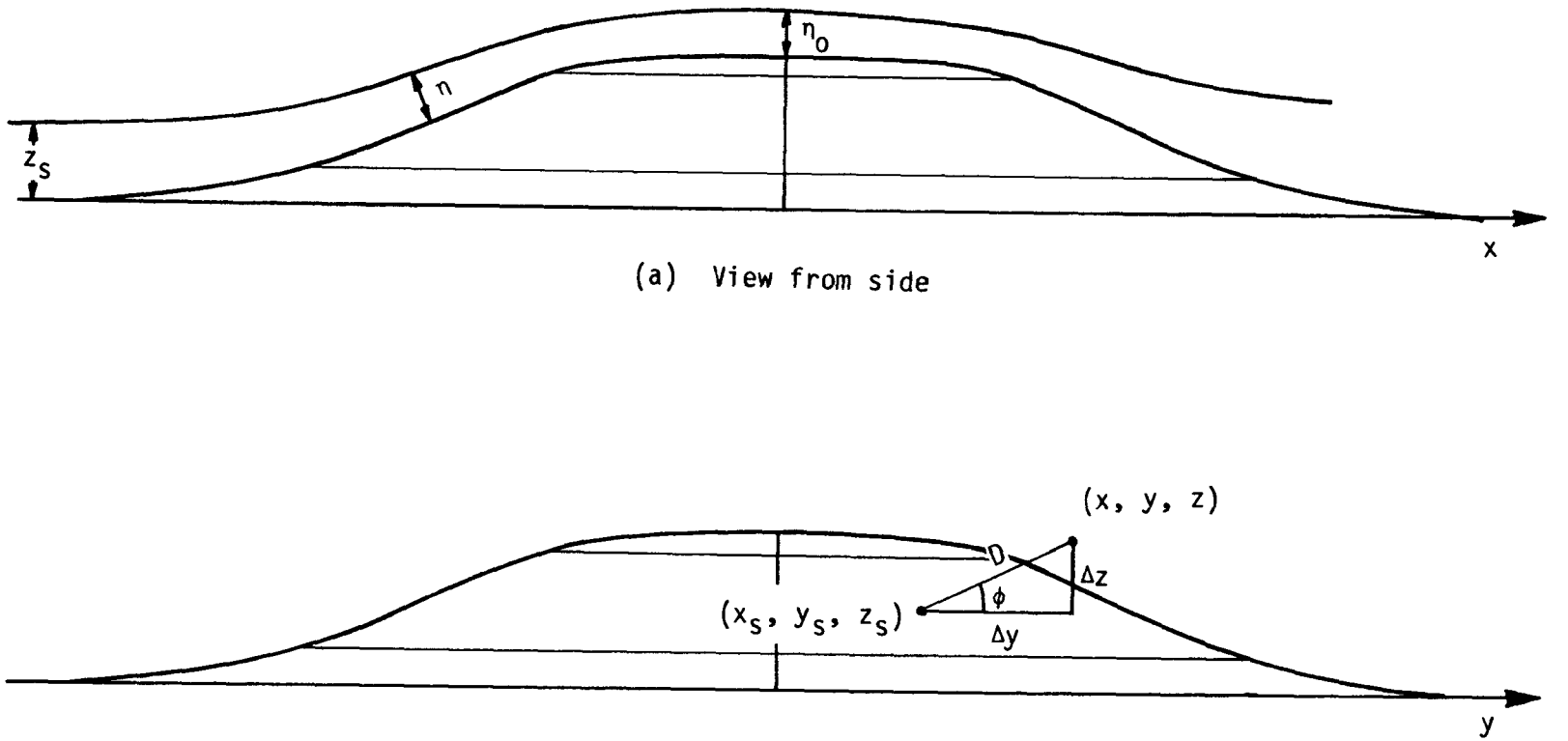

Figure A-4. Illustration of measured parameters.

A measure of the cumulative magnitude of these errors was obtained in the fitting process and in independent verifications. A preliminary experiment was conducted to test the feasibility of measuring plume trajectories in the towing tank. A different model hill was used. The "Polynomial Hill" was higher (H = 23.4 cm), and had a greater maximum slope (45°) than the Axisymmetric Cinder Cone model. This model had several pointers attached which served as verification marks independent of the reference points. Specific, identifiable points were used, but the positions were determined without extrinsic knowledge. That is, the rays from the side and bottom views were traced to their intersection and not to a known plane.

The results of this verification test are shown in Figure A-5. The relatively large discrepancy shown for one pair of points (near x=0) was due to difficulty in seeing the pointer against the hash mark in its background. It should be noted that the "measured" coordinates were partially determined from the photographs. The radial distance was physically measured, but the azimuthal angle was taken from the bottom view photograph because of the difficulty in accurately measuring such angles on the model. The largest error in the radial distances of the verification marks was 0.23 cm and the remaining values were less than 0.1 cm. This test was conducted with the model stationary. A second test in which the model was towed produced essentially identical results. This indicates that the disturbed density field did not dramatically alter the apparent positions of objects for the chosen vantage points.

These tests showed that the stereographic technique had sufficient resolution to locate fixed, identifiable points on and near the model. In practice, other sources of error occurred. First, the centerline of the plume had to be estimated. Except for a few cases in which the plume remained quite narrow, this was probably the greatest source of error. In some cases with meandering or looping plumes, some smoothing was necessary. The plume centerline was drawn on the photograph with a felt-tipped pen. Then the curve was traced with a cursor using the digitizer table. In carefully tracing the curve, it was impossible to keep the crosshairs from wandering about the line. When many plumes were digitized at a sitting, the operator's care may have varied. The variability was estimated to be on the order of the line width (0.03 inch), which translates to 0.6 cm at the model.

Also, the curves obtained for the side and bottom views were digitized independently and therefore were made up of different points. Interpolation and interaction were required to obtain rays that could be traced to the same (x,y,z) coordinates.

In conclusion, it is believed that plume trajectories were measured in the towing tank to within one centimeter. The general behavior of plumes which closely approached the hill surface confirmed this conclusion; that is, very few of the measured/computed trajectories were seen to violate the hill surface.

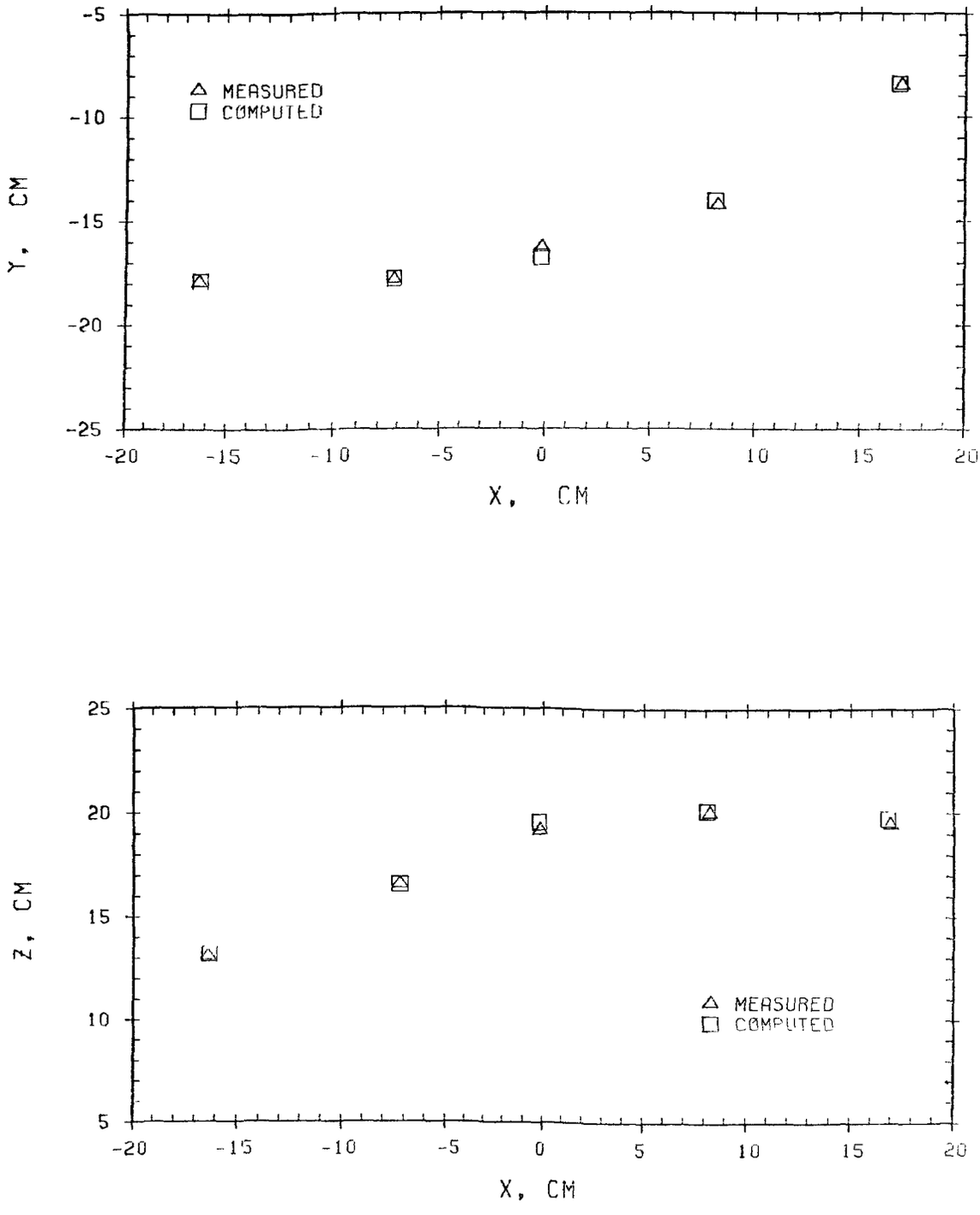

Figure A-5. Verification of photographic technique: comparison of photoderived locations of fixed, identifiable points in the flow field with actual locations.

3. EXPERIMENTAL RESULTS

Figure A-6 shows the source locations in the y-z plane used in the experiments with the axisymmetric Cinder Cone model. Beginning with tow number 73, two plumes were released simultaneously, and the two trajectories were identified with suffixes A and B. The x-coordinate for all the releases was -7.5H. The major parameters measured are listed in Tables A-1 through A-4. In these Tables, all lengths have been normalized by the hill height of 15.45 cm.

Figure A-7 shows examples of (a) side- and (b) bottom-view photographs taken during tow number 51 ($F = 0.6$, $y_s/H = z_s/H = 0.50$).

As mentioned earlier, six pairs of photographs were generally taken during each tow and, depending upon the variability of the plume path during the tow, two to four pairs were selected for digitization and analysis. These individual realizations were then averaged together to obtain the averaged trajectory. Figure A-8 shows a typical example of the variations in the trajectories obtained from the digitization of three pairs of photographs; the variation from one trajectory to the next is observed to be generally well within 0.1H. The averaging process, however, was clearly inappropriate in a very few cases where the plume behavior was not steady during the length of the tow. Figure A-9 shows an example ($F = 0.6$, $z_s = 0.5H$, $y_s = 0$) where the release height was only very slightly above the dividing-streamline height ($H_D = 0.4H$). The plume initially traveled directly up and over the hill, but perhaps due to secondary (horizontal) flows in the tank, it was later observed to deviate widely around the side of the hill. Averaging was done in all cases, however, as averaging was inappropriate in only a very few cases.

Figure A-10 shows the lateral and vertical displacements and displacement angles for streamers originating on the centerline at half the hill height under the various stabilities. The lateral deflections were essentially zero for all stabilities except for $F = 0.6$ in which, as shown in Figure A-9 and discussed above, the plume path was not steady. The vertical deflections show a monotonic increase with increasing F (decreasing stability). Note that because of the lateral deflection observed at $F = 0.6$, the maximum height reached by that streamer was less than the hill height. The displacement angle changed sign when the streamer descended below its initial elevation. Note that this happened in the stratified cases, but not in the neutral case. In the stratified cases, the streamers

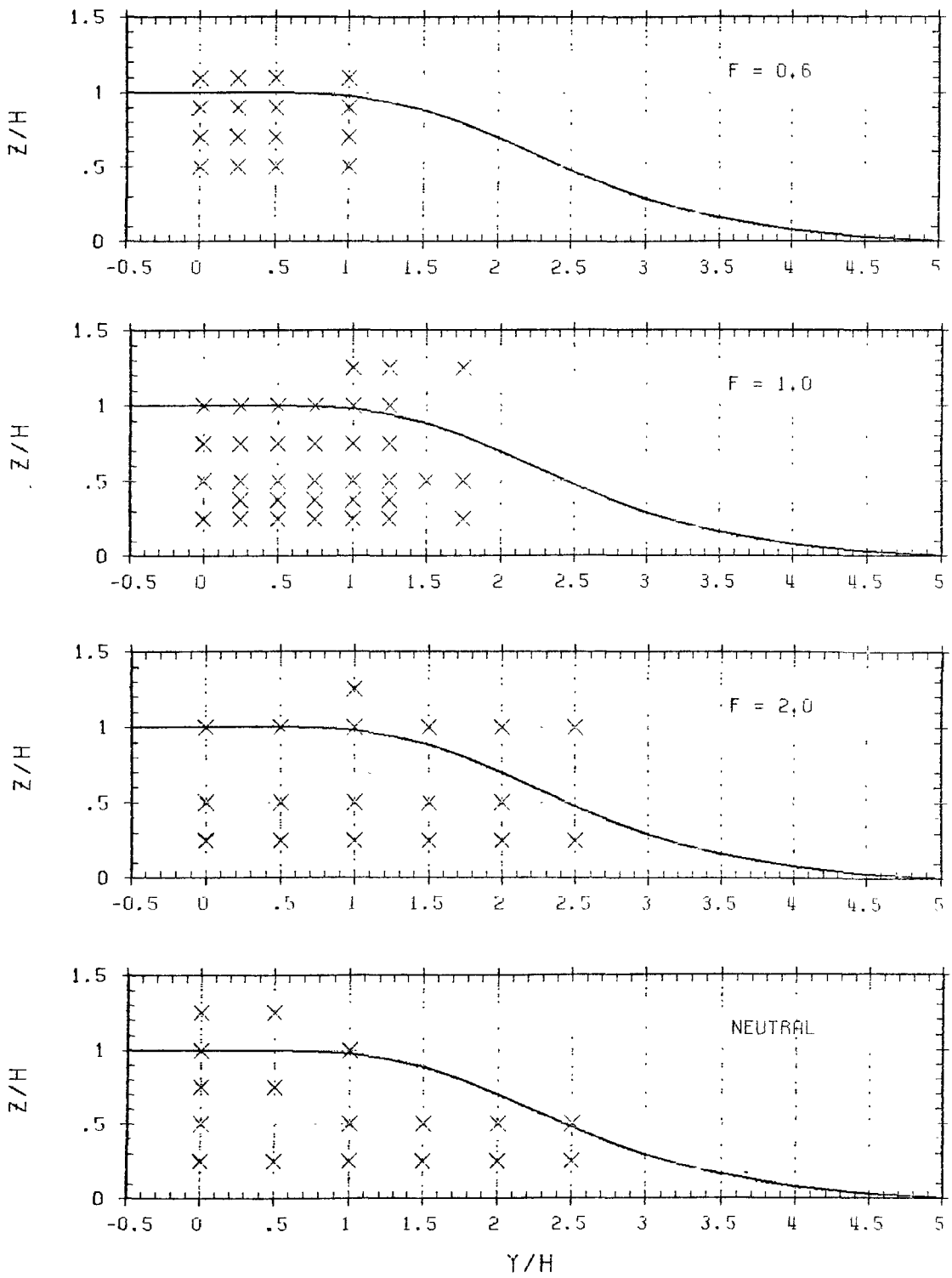

Figure A-6. Source positions used in experiments with ACC model.

TABLE A-1. MAIN PARAMETERS OF TRAJECTORIES, F = 0.6.

TOW NO.	y_s	z_s	$x(\Delta y_{mx})$	Δy_{mx}	$x(\Delta z_{mx})$	Δz_{mx}	$x(\eta_{mn})$	η_{mn}	D(x=0)	η(x=0)	ϕ(x=0)
8	0.00	0.50	1.92	1.40	-0.68	0.47	2.06	0.00	0.98	64.51	25.09
9	0.00	0.70	1.48	0.35	-0.72	0.38	0.85	0.01	0.40	0.06	62.12
13	0.00	0.90	1.23	0.17	-0.87	0.27	0.82	0.06	0.25	0.12	61.28
20	0.00	1.10	1.48	0.18	-0.93	0.10	0.77	0.09	0.14	0.14	16.73
50	0.25	0.50	1.81	2.37	-0.89	0.39	0.03	0.00	1.48	56.02	11.28
53	0.25	0.70	2.06	1.56	-0.75	0.33	-0.01	0.02	0.78	0.02	22.40
56	0.25	0.90	2.32	0.53	-0.62	0.27	1.01	0.08	0.34	0.13	41.96
59	0.25	1.10	2.06	0.27	-0.98	0.14	0.95	0.12	0.16	0.19	35.35
51	0.50	0.50	1.81	2.71	-1.46	0.18	-0.82	0.00	1.97	0.06	0.60
54	0.50	0.70	2.06	1.96	-0.98	0.24	-0.24	0.04	1.15	0.04	8.48
57	0.50	0.90	2.32	0.69	-0.70	0.27	0.77	0.11	0.48	0.16	30.61
60	0.50	1.10	2.32	0.71	-1.01	0.10	1.24	0.13	0.37	0.18	9.39
52	1.00	0.50	1.81	2.15	-3.52	0.14	-0.75	0.10	1.63	0.13	1.19
55	1.00	0.70	2.13	1.60	-1.35	0.16	0.28	0.14	1.18	0.15	2.61
58	1.00	0.90	2.32	1.09	-0.85	0.11	0.54	0.18	0.83	0.20	4.27
61	1.00	1.10	1.77	0.69	-0.99	0.10	1.21	0.25	0.51	0.26	4.55

TABLE A-2. MAIN PARAMETERS OF TRAJECTORIES, F = 1.0.

TOW NO.	y_s	z_s	$x(\Delta y_{mx})$	Δy_{mx}	$x(\Delta z_{mx})$	Δz_{mx}	$x(\eta_{mn})$	η_{mn}	D(x=0)	η(x=0)	ϕ(x=0)
72	0.00	0.25	-1.06	0.03	-0.97	0.81	-1.35	0.06	999.90	999.90	999.90
73A	0.00	0.50	3.79	0.14	-0.54	0.60	0.93	0.00	0.54	0.04	90.73
74A	0.00	0.50	3.87	0.29	-0.54	0.58	1.01	0.01	0.55	0.05	89.31
75A	0.00	0.75	2.88	0.06	-0.83	0.44	3.55	0.05	0.38	0.12	85.41
76A	0.00	1.00	-2.98	0.03	-0.98	0.31	3.33	0.12	0.27	0.27	85.80
78A	0.00	1.00	1.77	0.04	-1.13	0.31	3.47	0.12	0.26	0.26	89.44
76B	0.25	0.25	3.23	2.54	-2.17	0.47	3.23	0.00	1.92	73.83	10.13
88A	0.25	0.37	3.87	1.80	-0.31	0.62	-0.77	0.03	1.10	0.03	33.73
78B	0.25	0.50	3.55	0.96	-0.16	0.58	0.73	0.05	0.74	0.09	52.11
81A	0.25	0.75	3.55	0.43	-0.46	0.46	0.95	0.12	0.47	0.18	66.25
77A	0.25	1.00	3.18	0.25	-0.83	0.32	3.55	0.16	0.27	0.24	63.26
75B	0.50	0.25	2.90	2.88	-2.25	0.37	-0.48	0.02	2.10	0.07	6.42
87A	0.50	0.37	3.55	2.12	-0.75	0.49	3.33	0.04	1.38	0.08	19.86
77B	0.50	0.50	3.55	1.54	-0.16	0.50	-0.46	0.07	0.94	0.07	31.86
82A	0.50	0.75	3.40	0.74	-0.90	0.46	0.80	0.16	0.63	0.20	42.49
79A	0.50	1.00	2.58	0.46	-1.05	0.34	1.47	0.22	0.41	0.29	42.08
81B	0.75	0.25	3.23	2.65	-1.67	0.40	2.73	0.10	2.06	0.15	6.70
86A	0.75	0.37	3.55	2.34	-0.98	0.37	3.55	0.06	1.61	0.11	9.74
79B	0.75	0.50	3.47	1.50	-0.83	0.46	3.47	0.11	1.15	0.15	20.78
84A	0.75	0.75	2.25	0.80	-0.93	0.39	3.87	0.16	0.71	0.20	30.97

TABLE A-2. (Continued)

TOW NO.	y_s	z_s	$x(\Delta y_{mx})$	Δy_{mx}	$x(\Delta z_{mx})$	Δz_{mx}	$x(\eta_{mn})$	η_{mn}	D(x=0)	η(x=0)	φ(x=0)
80A	0.75	1.00	2.36	0.57	-1.13	0.31	3.55	0.24	0.52	0.31	29.16
82B	1.00	0.25	3.23	2.43	-1.25	0.35	3.23	0.14	1.83	0.20	9.10
73B	1.00	0.25	3.08	2.65	-2.74	0.27	-1.10	0.08	2.05	0.13	4.01
74B	1.00	0.25	3.23	2.63	-2.03	0.30	-0.68	0.09	1.89	0.12	5.26
84B	1.00	0.37	3.03	1.74	-1.27	0.38	-0.01	0.15	1.38	0.15	12.69
80B	1.00	0.50	2.88	1.46	-1.35	0.39	3.47	0.16	1.22	0.20	14.67
83A	1.00	0.75	2.09	0.85	-1.08	0.37	0.70	0.25	0.77	0.27	26.21
90A	1.00	1.00	1.32	0.62	-1.32	0.25	3.87	0.26	0.56	0.33	21.04
85A	1.00	1.25	1.01	0.38	-1.24	0.18	0.93	0.40	0.37	0.45	19.00
83B	1.25	0.25	3.10	2.24	-1.42	0.32	3.55	0.18	1.69	0.21	9.06
89A	1.25	0.37	2.73	1.89	-1.87	0.27	3.40	0.17	1.56	0.24	7.82
85B	1.25	0.50	2.48	1.33	-1.24	0.34	3.64	0.25	1.21	0.27	13.27
86B	1.25	0.75	2.09	1.13	-1.63	0.23	3.79	0.22	0.95	0.26	7.80
87B	1.25	1.00	1.24	0.66	-1.08	0.22	3.72	0.32	0.58	0.37	14.80
88B	1.25	1.25	1.16	0.44	-1.24	0.16	0.85	0.39	0.39	0.46	8.77
91A	1.50	0.50	1.86	1.43	-1.39	0.25	3.79	0.20	1.25	0.29	7.62
91B	1.75	0.25	0.97	1.91	-0.73	0.19	-1.40	0.22	1.71	0.27	6.00
90B	1.75	0.50	1.78	1.32	-2.09	0.25	3.87	0.27	1.19	0.40	10.12
89B	1.75	1.25	0.57	0.41	-1.77	0.15	3.55	0.54	0.40	0.63	6.91

TABLE A-3. MAIN PARAMETERS OF TRAJECTORIES, F = 2.0.

TOW NO.	y_s	z_s	$x(\Delta y_{mx})$	Δy_{mx}	$x(\Delta z_{mx})$	Δz_{mx}	$x(\eta_{mn})$	η_{mn}	D(x=0)	η(x=0)	ϕ(x=0)
92A	0.00	0.25	4.19	0.09	-0.59	0.87	1.09	0.04	0.85	0.10	89.23
94A	0.00	0.50	-0.61	0.02	-0.46	0.72	2.06	0.10	0.71	0.21	90.93
95A	0.00	0.50	0.54	0.05	-0.46	0.72	1.16	0.10	0.69	0.18	86.43
97A	0.00	1.00	-2.79	0.02	-0.70	0.52	1.70	0.35	0.47	0.47	88.31
93A	0.50	0.25	3.87	0.87	-0.46	0.83	1.08	0.11	0.99	0.11	56.63
96A	0.50	0.50	3.87	0.51	-0.08	0.71	0.85	0.18	0.78	0.22	65.31
98A	0.50	1.00	2.94	0.27	-0.54	0.49	1.39	0.38	0.51	0.47	66.41
94B	1.00	0.25	2.87	1.21	-0.45	0.61	3.55	0.13	1.16	0.16	31.05
95B	1.00	0.25	3.79	1.20	-0.54	0.63	3.79	0.14	1.15	0.15	31.40
97B	1.00	0.50	2.17	0.80	-0.39	0.61	3.87	0.28	0.92	0.29	41.81
92B	1.00	1.00	0.46	0.38	-0.62	0.52	0.70	0.54	0.60	0.56	53.29
99A	1.00	1.25	1.41	0.30	-0.59	0.37	1.11	0.61	0.44	0.66	53.09
96B	1.50	0.25	3.87	1.24	-0.46	0.47	3.87	0.15	1.12	0.24	23.70
98B	1.50	0.50	3.87	0.93	-0.21	0.44	-0.36	0.36	0.93	0.37	27.64
93B	1.50	1.00	1.49	0.50	-0.50	0.42	0.78	0.63	0.62	0.66	40.84
99B	2.00	0.25	3.26	1.18	-0.28	0.31	-3.55	0.21	1.02	0.27	17.71
101A	2.00	0.50	1.57	0.87	-0.36	0.36	3.87	0.45	0.86	0.48	24.40
100A	2.00	1.00	0.64	0.54	-0.64	0.33	3.55	0.77	0.61	0.80	30.93
100B	2.50	0.25	1.09	0.97	-0.48	0.22	-3.55	0.23	1.00	0.31	12.01
101B	2.50	1.00	1.35	0.55	-0.19	0.27	3.23	0.94	0.59	0.96	27.42

TABLE A-4. MAIN PARAMETERS OF TRAJECTORIES, NEUTRAL

TOW NO.	y_s	z_s	$x(\Delta y_{mx})$	Δy_{mx}	$x(\Delta z_{mx})$	Δz_{mx}	$x(\eta_{mn})$	η_{mn}	D(x=0)	η(x=0)	ϕ(x=0)
32	0.00	0.25	-1.32	0.04	-0.39	0.92	0.88	0.15	0.92	0.16	89.29
28	0.00	0.50	-0.48	0.04	-0.55	0.80	1.23	0.26	0.80	0.30	87.43
31	0.00	0.75	-0.89	0.03	-0.25	0.71	1.03	0.44	0.71	0.46	87.91
29	0.00	1.00	3.87	0.03	0.23	0.64	-0.77	0.60	0.63	0.63	91.41
30	0.00	1.25	-3.79	0.02	0.23	0.57	-1.08	0.78	0.57	0.82	90.60
33	0.50	0.25	-1.86	0.17	0.39	0.93	-0.93	0.15	0.93	0.17	82.72
36	0.50	0.75	-0.70	0.22	-0.23	0.74	1.08	0.46	0.76	0.49	74.65
38	0.50	1.25	3.87	0.26	0.08	0.56	1.01	0.76	0.58	0.82	75.84
62	1.00	0.25	1.03	0.46	0.58	0.88	-0.46	0.16	0.95	0.20	62.45
66	1.00	0.50	0.72	0.37	0.18	0.71	-0.57	0.27	0.78	0.28	63.37
70	1.00	1.00	0.38	0.25	0.99	0.52	-0.16	0.55	0.55	0.56	66.07
71	1.00	1.00	-1.85	0.16	0.07	0.50	-0.28	0.53	0.51	0.54	75.03
63	1.50	0.25	0.25	0.34	0.85	0.67	-0.09	0.15	0.74	0.16	63.18
68	1.50	0.50	-0.45	0.38	0.06	0.59	-0.39	0.31	0.69	0.33	58.89
64	2.00	0.25	0.71	0.40	0.06	0.51	-0.13	0.23	0.63	0.23	54.29
67	2.00	0.50	0.84	0.38	0.32	0.51	-0.39	0.43	0.62	0.45	52.94
65	2.50	0.25	0.26	0.44	0.52	0.33	-1.23	0.24	0.54	0.28	37.18
69	2.50	0.50	-0.26	0.47	0.52	0.32	-0.84	0.50	0.57	0.52	34.18

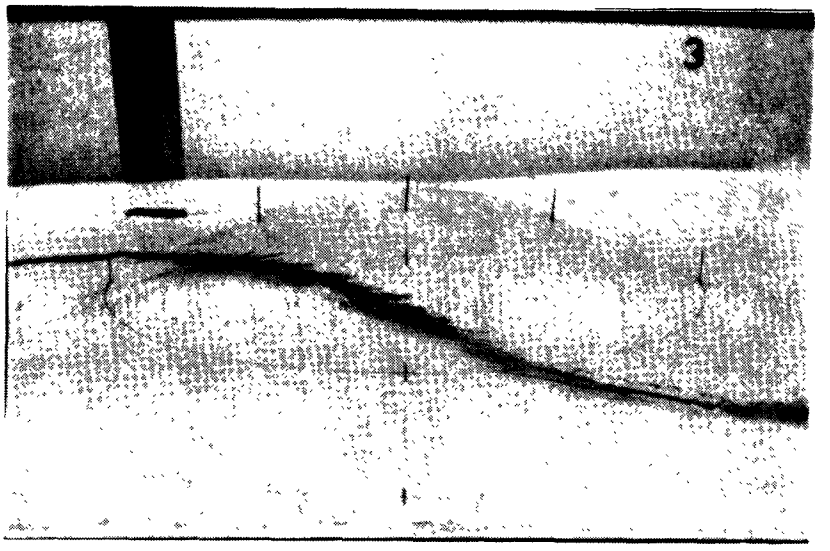

(a) Side view.

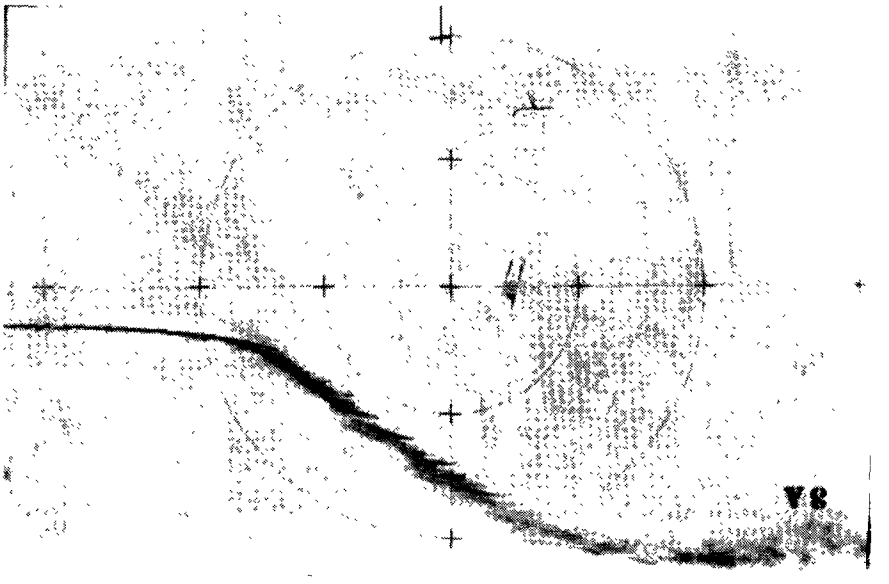

(b) Bottom view.

Figure A-7. Examples of photographs digitized to estimate plume trajectories in three dimensions. Tow 51, F = 0.6, y_s/h = 0.5, z_s/h = 0.5. Flow from left to right.

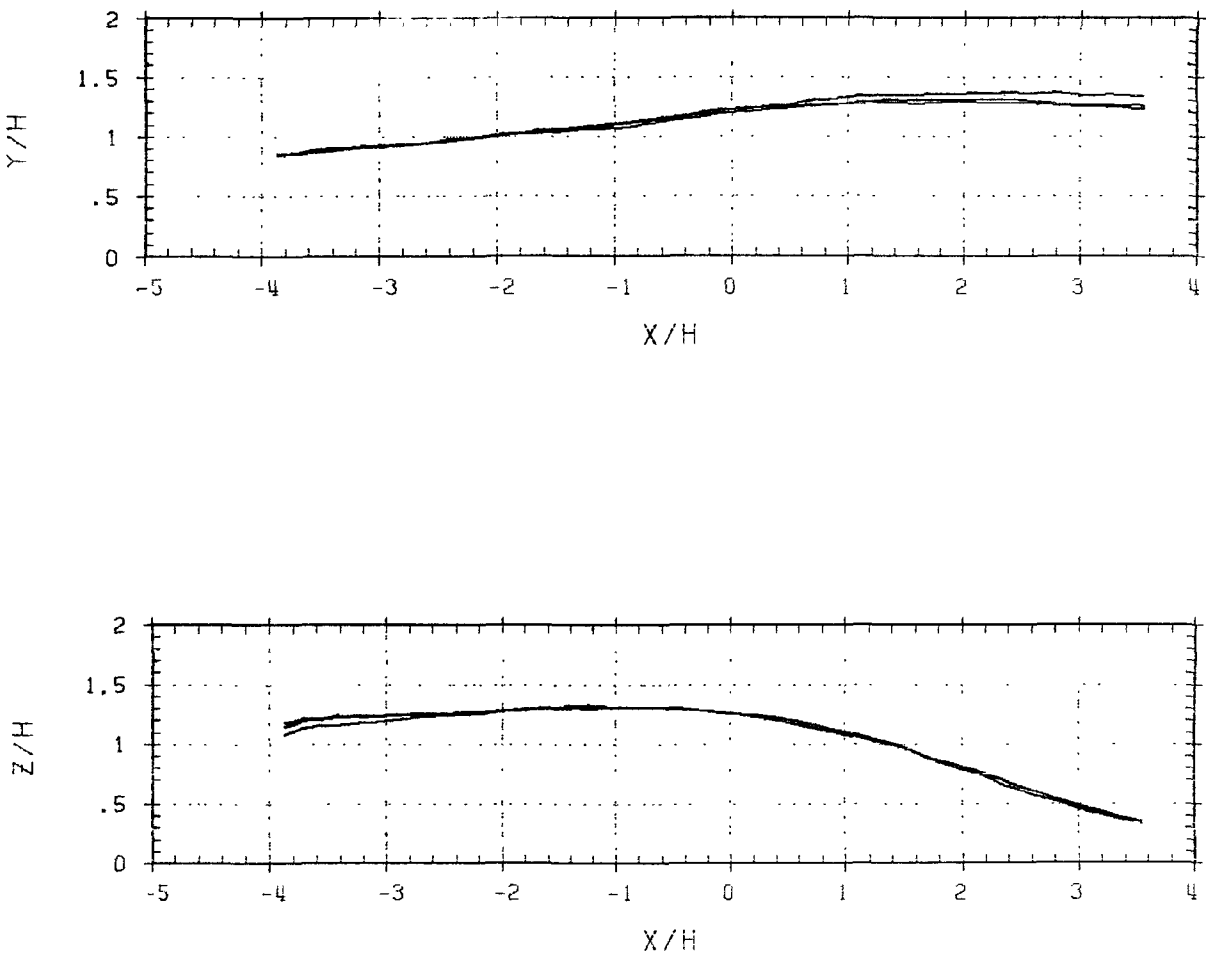

Figure A-8. Typical example of plume variation during a tow. Tow 80, F = 0.2, z_s/h = 1.0, y_s/h = 0.75.

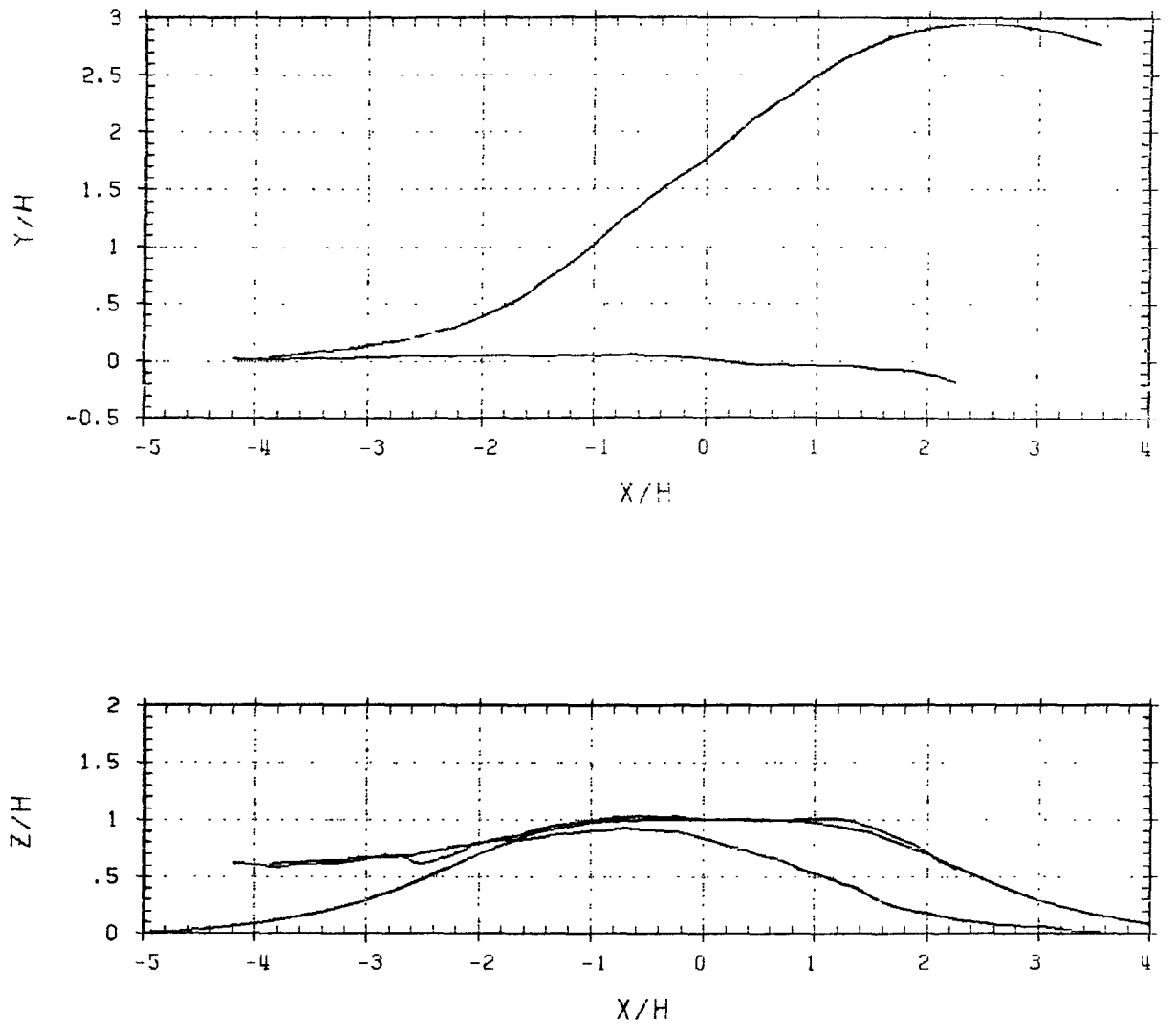

Figure A-9. Example of experiment during which the plume's path varied markedly and averaging was perhaps inappropriate. Tow 8, F = 0.6, y_s=0, z_s = 0.5.

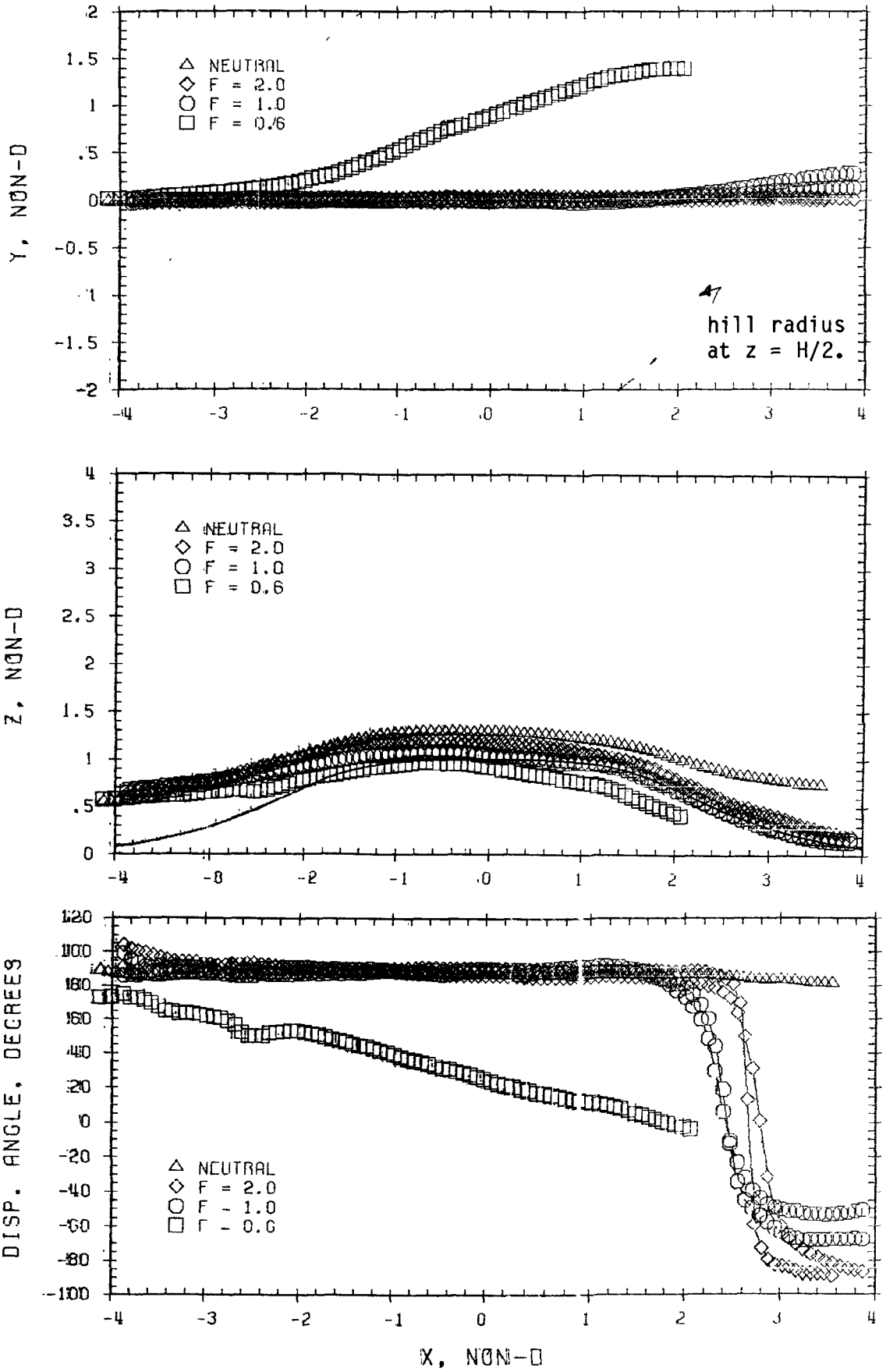

Figure A-10. Elevations and lateral displacements and displacement angles for plumes originating at y = 0, z = 0.5h for various stabilities.

obviously "hugged" the hill surface as they swept down the lee side. In the neutral case, however, separation occurred on the lee side, and the streamer remained well aloft of the surface.

Figure A-11 shows similar trajectory parameters, but where the lateral offset of the source was $y_s/H = 1.0$. In this, the lateral deflections increased dramatically with increasing stability, from 0.35H in neutral flow to 1.6H at F = 0.6 (deflections at hill center, x = 0). Note that the lateral deflections are roughly symmetrical fore and aft of the hill in neutral flow, but far from symmetrical in the stable cases. The vertical deflections are obviously inhibited by the stable stratification; the maximum vertical deflection at F = 0.6 appears to occur at x = -4H and has a value of 0.1H, whereas the maximum under neutral conditions occurs near x = 0, with a value of 0.7H.

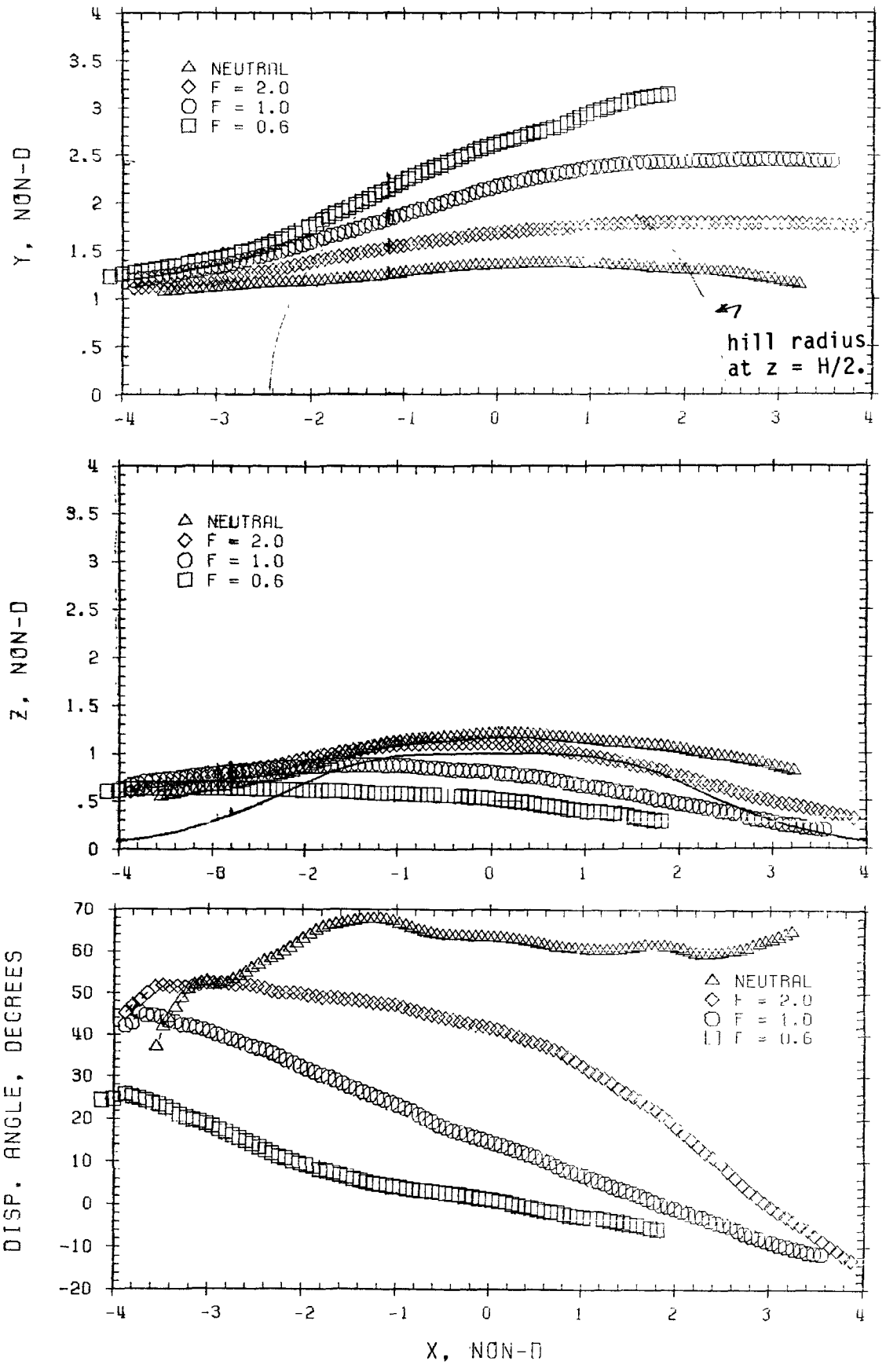

Figure A-11. Vertical and lateral displacements and displacement angle for plumes originating at y = 1.0h, z = 0.5h for various stabilities.

4. MATHEMATICAL MODEL

A method of predicting streamline trajectories for arbitrary hill shapes is necessary in the application of complex terrain dispersion models that use the idea of a Gaussian plume following a streamline (Hunt et al., 1983). One such method is described and evaluated here, using the data described in Section 3. This method used linear theory and the Fast Fourier Transform (FFT) technique.

4.1 Description of Model

A linear theory of stratified flow past a three-dimensional, isolated hill was presented by Crapper (1959). He applied his theory to an axisymmetric hill which had a known Fourier transform and obtained an analytic solution for the vertical deflection of streamlines. Smith (1980) used Crapper's ideas but made use of modern computers in performing FFT calculations to determine the deflections. Both Crapper and Smith were interested primarily in lee waves. However, the vertical deflections of streamlines applied to the flow upwind of the hill, as computed with their techniques, are directly applicable to plume trajectory estimation.

Although Crapper (1959) allowed a vertical shear in the approach velocity profile, Smith (1980) did not. Since the flow in the EPA Towing Tank is for a linear stratification and uniform approach velocity, all calculations presented here were made assuming such conditions.

The approach outlined by Smith (1980) can be briefly described as follows. The steady flow of a stratified Boussinesq fluid can be described by linearized equations of motion for the perturbation quantities u, v, w, ρ, p, and η (where $\partial\eta/\partial x = w/U$, η is the vertical displacement of a streamline above its far upstream height). The system of equations can be reduced to a single equation for η

$$[\partial^2/\partial x^2]\ \nabla^2\eta + [H^2N^2/U^2]\ \nabla^2_{\text{horiz}}\ \eta = 0,$$

where

$$N^2 = -(g/\rho)(d\rho/dz),$$

and all lengths have been normalized by the hill height H. By taking a double Fourier integral (transformed variable indicated by a $\wedge$), the equation becomes

$$\hat{\eta}_{zz} + m^2\hat{\eta} = 0,$$

with

$$m^2 = [(k^2 + \ell^2)/k^2]\ [(H^2N^2/U^2) - k^2].$$

For constant N^2/U^2, the solution is

$$\hat{\eta}(k, \ell, z) = \hat{\eta}(k, \ell, 0)\ e^{imz}.$$

The boundary condition required for solution is $\eta(x, y, 0) = h(x, y)$ which gives, through Fourier transform,

$$\hat{\eta}(k, \ell, 0) = \hat{h}(k, \ell).$$

This boundary condition requires streamlines originating at $z = 0$ to follow the hill surface. The computation method then consists of obtaining the FFT of the hill shape, multiplying by e^{imz} for the height z of interest, and inverting to obtain the streamline deflections. Smith provides some suggestions for optimizing the two-dimensional FFT procedure.

A Digital Equipment Corporation PDP 11/44 computer was used for the numerical computations. The largest two-dimensional array (actually a pair of arrays for the real and imaginary parts) that may be easily used for calculations with this machine is 128 X 128, and this array size was used exclusively. The hill was centered at grid point (64,64) in this array.

To provide a suitable upstream and downstream area for the flow to adjust, an interval of $\Delta = 0.5H$ was used; that is, the terrain extended from 31.5H upstream to 32H downstream of the hill center. The digitized representation of the hill cross-section can be seen in Figure A-12.

Each run of the model, corresponding to a prescribed height z above the datum, produced an array of the amount the streamlines have been deflected from their far upstream level z_o to arrive at points (x,y,z). To obtain streamline trajectories from such data would require making model runs for several z values and performing some sort of contouring method for various z_o values. Under the assumption that deflections are small, each model run can be interpreted as corresponding to a given upstream level z_o; that is, $\eta(x,y,z) \sim \eta(x,y,z_o)$. Linear theory presumes that deflections are small, so that this interpretation is warranted. Large differences between the two interpretations indicate the inapplicability of the theory. Thus, the result of each model run was used directly even though some of the deflections were not small.

Smith's solution and numerical method were followed closely. However, the solution of the differential equation in transform space has a singular point at longitudinal wave number equal to zero. In the discrete solution, the Fourier coefficients for $k = 0$ in the transform array were arbitrarily set to zero to avoid the difficulties of the singular behavior. This resulted in a shift of the mean

heights of the calculated streamlines which were then adjusted to originate at the correct level; that is, to pass through the locations of the point sources in the towing tank experiments (7.5H upstream of the hill center).

In addition, an equation for the transform of lateral deflections was derived, and lateral deflections were obtained through the inverse FFT algorithm. Together, the lateral and vertical deflections provided predictions of three-dimensional trajectories originating away from the hill centerline.

4.2 Comparison with Experimental Results

The linear theory was derived for small deflections which can be expected to result from flow over gentle hills. The axisymmetric CCB model, however, was quite steep (maximum slope of 0.45 or 24.4°). Also, very stable flow (Fr = U/NH less than 1.0) is known to divide and pass around the hill at lower elevations. The linear theory cannot be expected to be applicable to such situations. Two questions are to be considered for this relatively steep hill: how well do the calculated streamlines match the streamlines observed in neutral flow and how does increasing stability affect the results?

Experimental and predicted streamline trajectories for streamlines originating directly upstream of the hill center for neutral flow are shown in Figure A-13. There is very good agreement between the experimental results and predictions for all heights for the flow upstream and over the hill top. The heights of the trajectories are underpredicted in the lee of the hill where flow separation was observed. The linear theory cannot predict separation. The vertical deflection of streamlines originating at lateral offsets of 1H are shown in Figure A-14. The agreement is not quite as good as was observed for the centerline cases.

The lateral deflections of the streamlines for neutral flow are shown in Figures A-15 to A-18 for streamlines that originate at heights of 0.25, 0.50, 0.75, and 1.0 H, respectively. Overall, the comparisons with most of the experimental observations are very good. Where there is a discrepancy between calculated and experimental result, the neighboring cases usually are in good agreement, which indicates experimental variability rather than inadequacy of the calculation technique.

Trajectories were also calculated for stable flow with Fr = 1.0. Comparison with the towing tank results were poor even on centerline where the calculated streamlines originating as high as 1.0 H intersected the hill near the top of the lee side. This low Froude number in combination with the steepness of the hill was clearly beyond the capabilities of the linear theory approach.

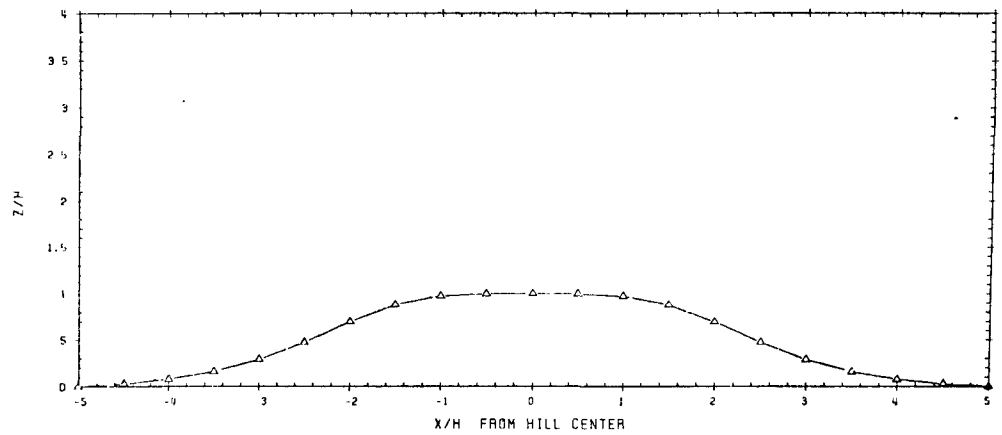

Figure A-12. The discrete representation of the hill along the x-axis.

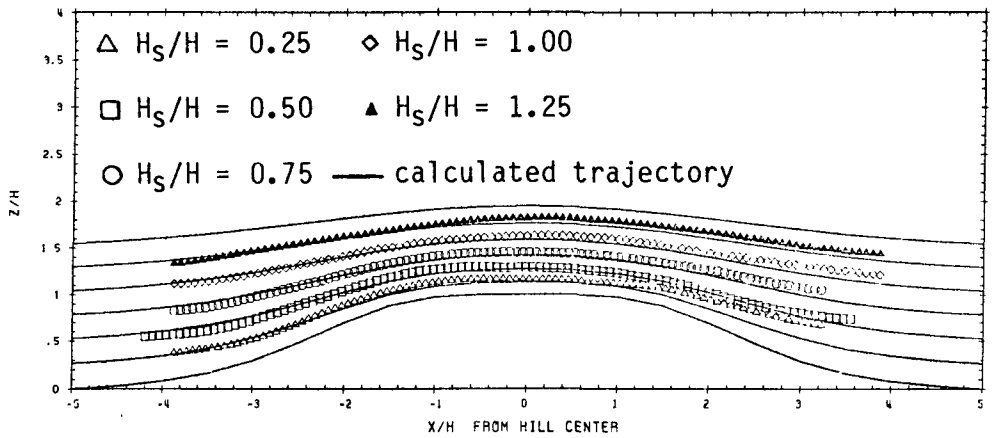

Figure A-13. Streamline trajectories for neutral flow over the hill center; $y_S/H = 0$.

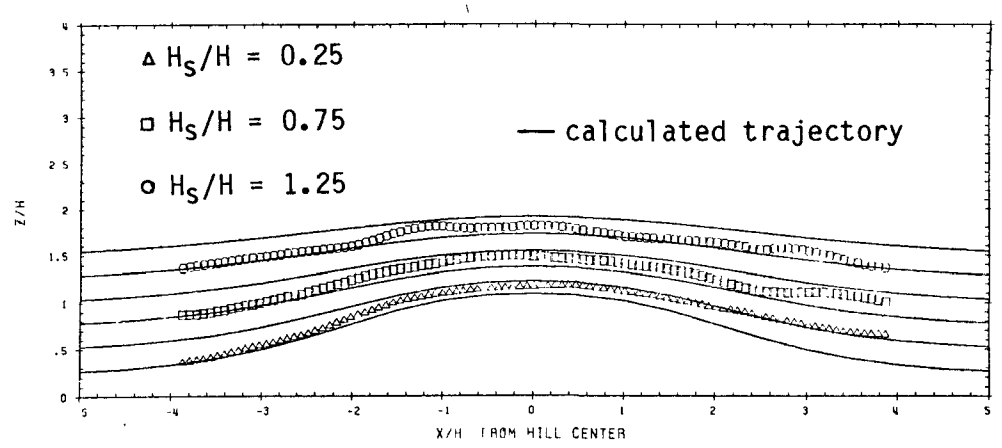

Figure A-14. Streamline trajectories for neutral flow. Vertical deflection for streamlines originating at offset of $y_S/H = 1.0$

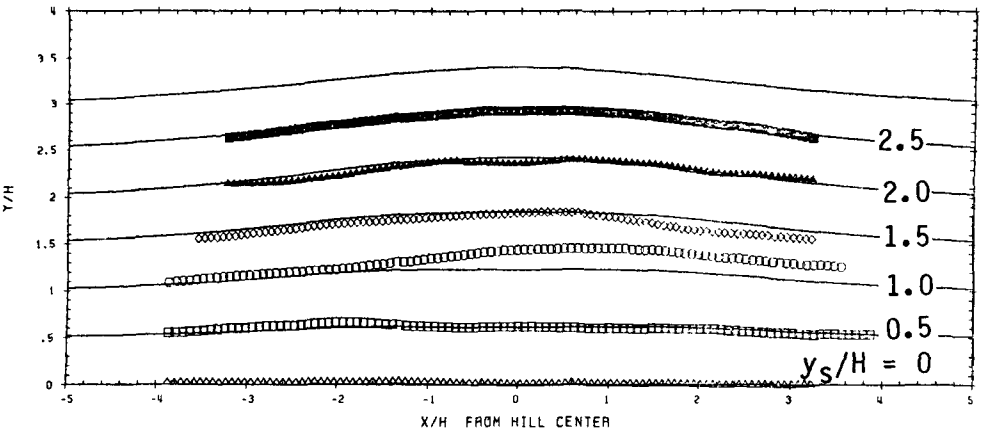

Figure A-15. Streamline trajectories for neutral flow. Lateral deflection for streamlines originating at $H_s/H = 0.25$.

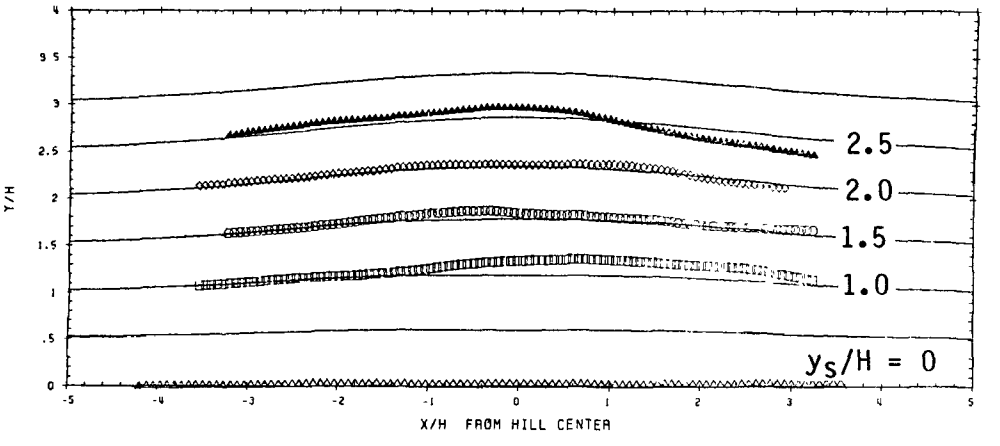

Figure A-16. Streamline trajectories for neutral flow. Lateral deflection for streamlines originating at $H_s/H = 0.50$.

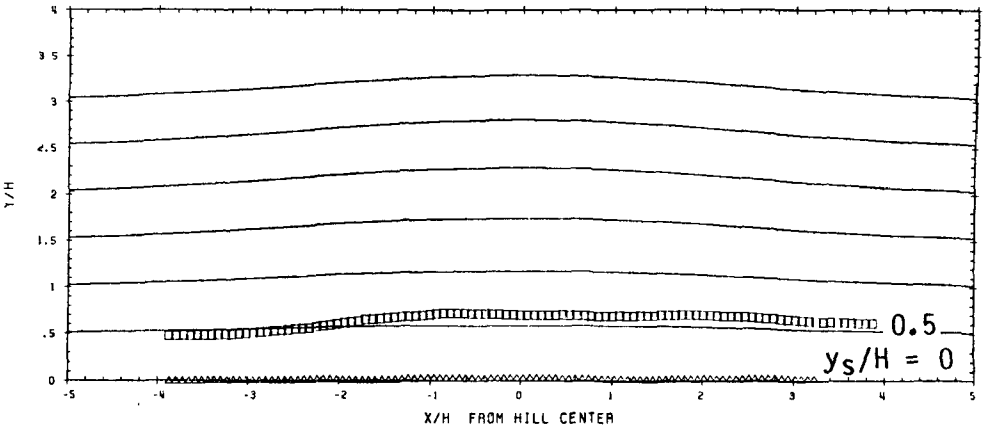

Figure A-17. Streamline trajectories for neutral flow. Lateral deflection for streamlines originating at $H_s/H = 0.75$.

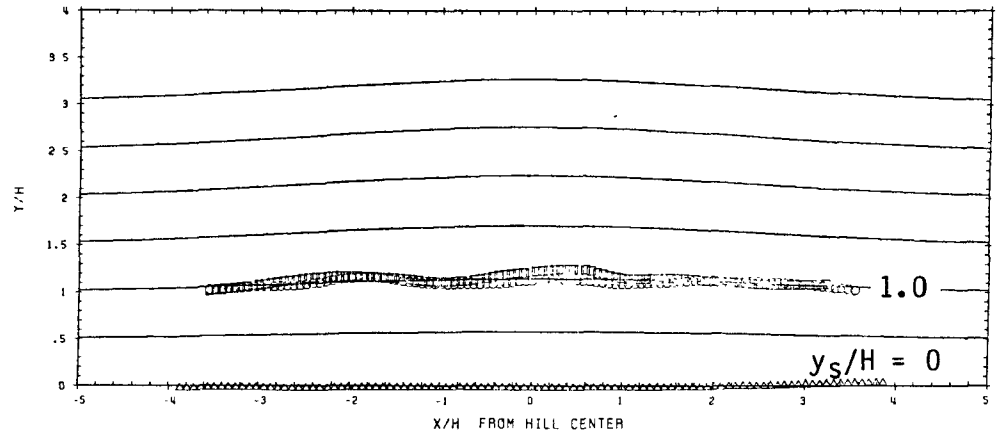

Figure A-18. Streamline trajectories for neutral flow. Lateral deflection for streamlines originating at $H_S/H = 1.0$.

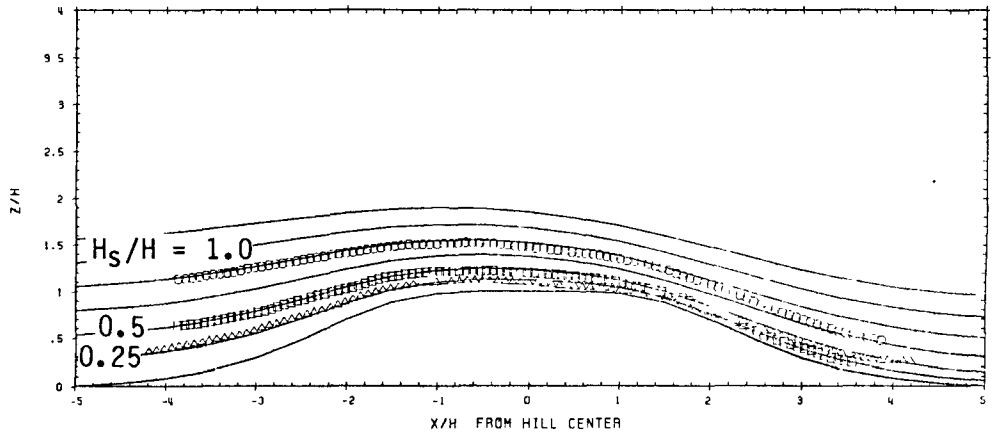

Figure A-19. Streamline trajectories for stable flow, Fr = 2.0, over the hill center, $y_S/H = 0$.

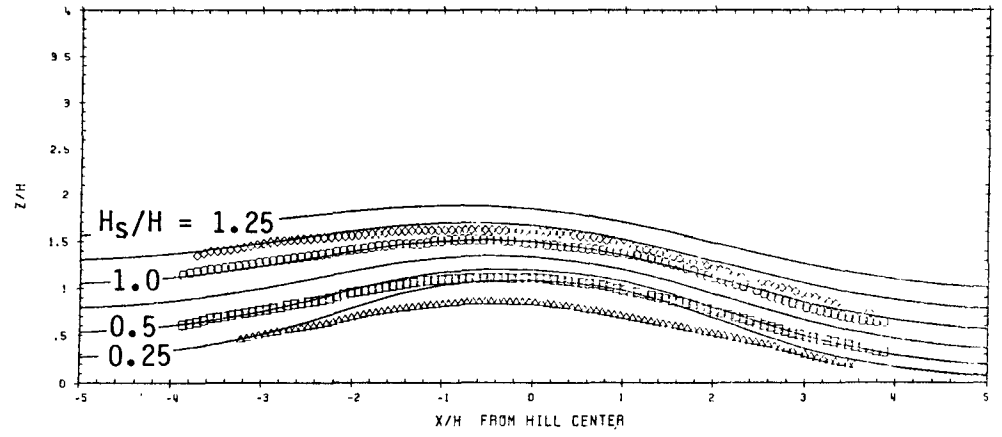

Figure A-20. Streamline trajectories for stable flow, Fr = 2.0. Vertical deflections for streamlines originating at offset of $y_S/H = 1.0$.

Comparisons are also made at a Froude number of 2.0. The vertical deflections of streamlines originating directly upstream of the hill center and at lateral offsets of y_s/H = 1.0 and 2.0 are shown in Figures A-19, A-20, and A-21, respectively. The streamline trajectories for sources on the centerline show quite good agreement between the predictions and experimental results, at least upwind of the hill center. However, the comparisons are not as good for streamlines originating at laterally offset positions. The predicted vertical deflections are much too large especially for the streamlines originating at the lower levels. The lateral deflections, Figures A-22 to A-25, are underpredicted for this stable flow, again, especially at the lower levels. The experimental results exhibit substantially more lateral and less vertical deflection than the predictions.

4.3 Conclusions

Streamline trajectories calculated using a linear theory model and FFT computations were compared with those obtained in towing tank experiments for a three-dimensional hill.

The calculated trajectories compared quite well with the experimental results for neutral flow. Both vertical and lateral deflections of the flow as it passed the hill showed good agreement except in the small region to the lee of the hill where the flow separated in the towing tank experiments. The model does not handle separation.

However, for stable flow, Fr = 2.0, the linear theory did not predict the streamline trajectories well except for those on the centerline that passed directly over the hill. The calculated streamlines that originated at points offset from the centerline did not deflect as much in the lateral and deflected more in the vertical than the experimentally measured trajectories. That is, the model results correspond to what would be expected for a less stable situation.

The approximations made in the linear theory approach are most appropriate for very large Froude numbers. Smith (1980) provided some estimations of limiting Froude numbers for which this method should be applicable. He showed that the linear theory will break down as a result of a collapse of the vertical distribution of density at Froude numbers near 2.0. The boundary condition used in the analysis restricts ground-level streamlines to pass over the hill in a direct downstream direction, that is, with no lateral deflection. This boundary condition is consistent with the other approximations made for shallow hills and small deflections. However, it is known that as the stability of the flow increases, streamlines near the hill surface experience larger lateral deflections. The failure of the computations for Froude numbers of 2.0 in matching the experimental results are consistent with these approximations. The vertical deflections over the center of the hill where lateral deflections were small showed good agreement with experimental results. Streamlines originating at points offset from the center did not match as well.

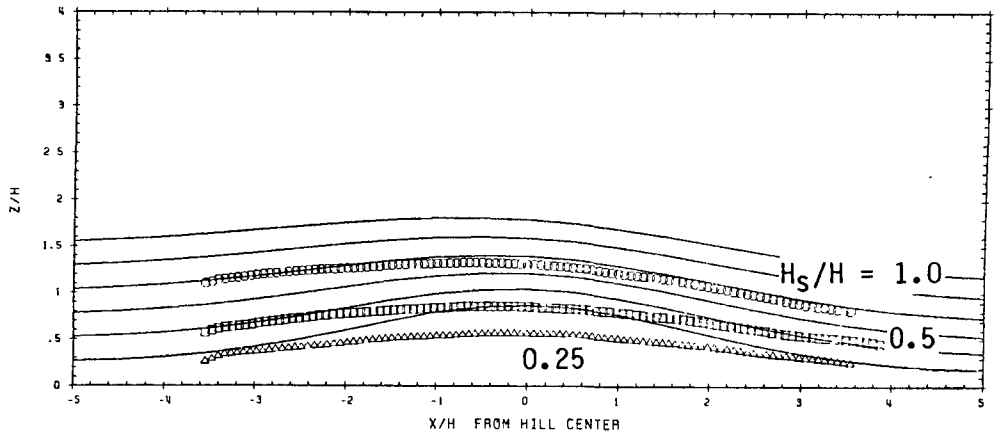

Figure A-21. Streamline trajectories for stable flow, Fr = 2.0. Vertical deflections for streamlines originating at offset of y_S/H = 2.0.

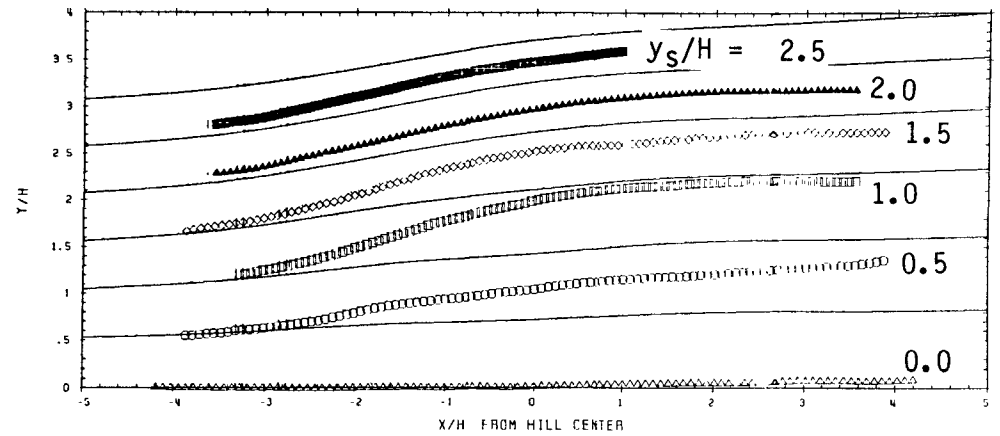

Figure A-22. Streamline deflections for stable flow, Fr = 2.0. Lateral deflections for streamlines originating at H_S/H = 0.25.

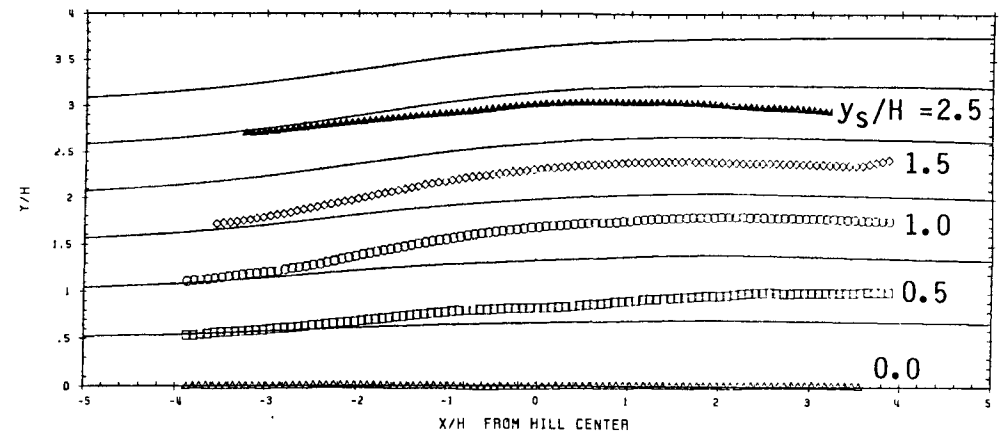

Figure A-23. Streamline trajectories for stable flow, Fr = 2.0. Lateral deflections for streamlines originating at H_S/H = 0.50.

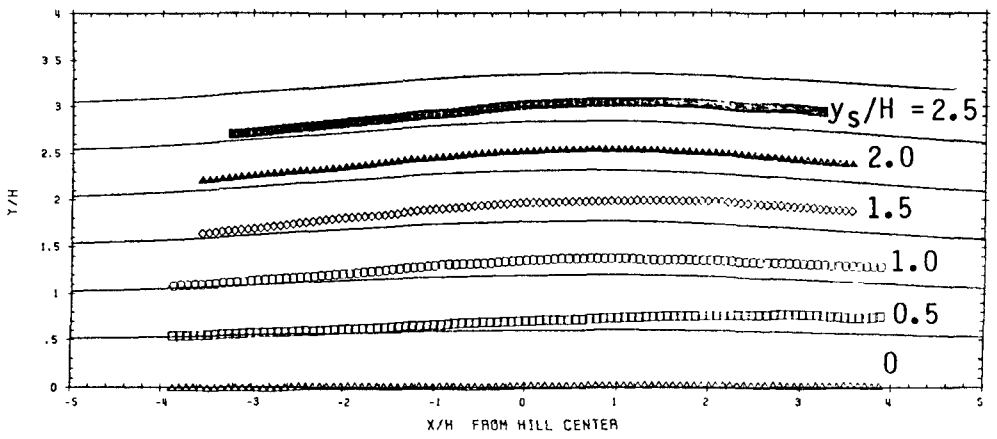

Figure A-24. Streamline trajectories for stable flow, Fr = 2.0. Lateral deflections for streamlines originating at H_s/H = 1.0.

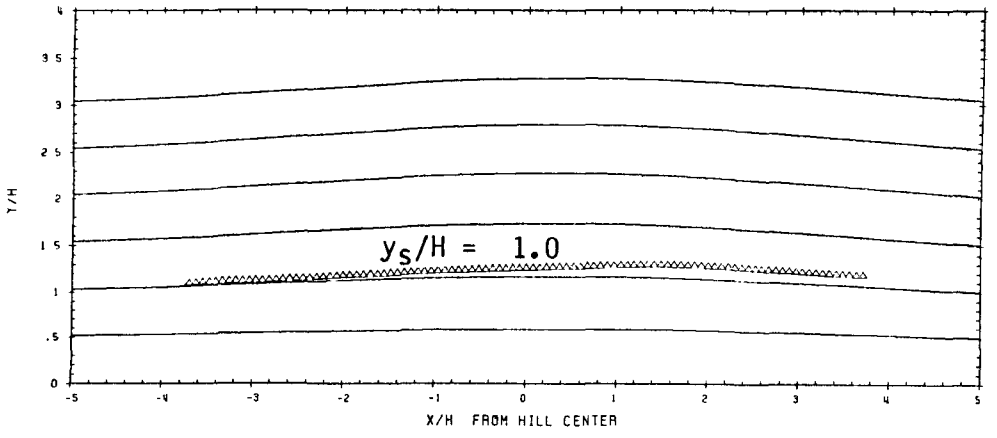

Figure A-25. Streamline trajectories for stable flow, Fr = 2.0. Lateral deflections for streamlines originating at H_s/H = 1.25.

That the linear theory predicted reasonably well in neutral flow and showed the correct trends with stability is encouraging. Further tests of the calculation method should be made for less steep hills under neutral and stable conditions. For a less steep hill, for which there is no flow separation, the method may be expected to work quite well for neutral flow. Hopefully, stable flow results would also improve for hills with less steep slopes. Finally, further experimental results in the range $2.0 < F < 10$ would prove useful in delineating the range of applicability of the linear theory.

The streamline trajectories obtained for neutral flow over the axisymmetric CCB hill can be used to predict ground-level concentrations using a Gaussian plume following the streamline approach with the results to be compared with available wind tunnel data.

REFERENCES

Crapper, G.D., 1959. A Three-Dimensional Solution for Waves in the Lee of Mountains, J. Fluid Mech., 6, 51-76.

Hunt, J.C.R., Leibovich, S. and Lumley, J.L., 1983. Prediction Methods for the Dispersal of Atmospheric Pollutants in Complex Terrain, Rpt. No. PPRP-78 to Maryland Power Plant Siting Program by Flow Analysis Associates, Ithaca, NY, 177p.

Hunt, J.C.R., Puttock, J.S. and Snyder, W.H., 1979. Turbulent Diffusion from a Point Source in Stratified and Neutral Flows around a Three-Dimensional Hill: Part I: Diffusion Equation Analysis, Atmos. Envir., 13, 1227-39.

Hunt, J.C.R. and Snyder, W.H., 1980. Experiments on Stably and Neutrally Stratified Flow over a Model Three-Dimensional Hill, J. Fluid Mech., 96, pt. 4, 671-704.

Smith, R.B., 1980. Linear Theory of Stratified Hydrostatic Flow Past an Isolated Mountain, Tellus, 32, 348-64.

Synder, W.H. and Hunt, J.C.R., 1984. Turbulent Diffusion from a Point Source in Stratified and Neutral Flows around a Three-Dimensional Hill; Part II: Laboratory Measurements of Surface Concentrations, Atmos. Envir., 18, 1969-2002.

Snyder, W.H., Thompson, R.S., Eskridge, R.E., Lawson, R.E., Jr., Castro, I.P., Lee, J.T., Hunt, J.C.R. and Ogawa, Y., 1985. The Structure of Strongly Stratified Flow over Hills; Dividing-Streamline Concept, J. Fluid Mech., 52, 249-88.

Thompson, R.S. and Snyder, W.H., 1976. EPA Fluid Modeling Facility, Proc. Conf. on Modeling and Simulation, EPA-600/9-76-016, U.S. Environmental Protection Agency, Washington, D.C.

☆U.S.Government Printing Office: 1986 — 646-014/40002